BARRIER DISTRIBUTIONS IN HEAVY ION INDUCED FUSION REACTIONS

BY

JIAN XIN WEI

A thesis submitted for the degree of
Doctor of Philosophy
at the Australian National University

Canberra, July 1993

To my family

and to the memory of my father.

It is my father who guided me on the road to science...

奉献给我亲爱的妈妈，妻子和女儿；

并志以记念我敬爱的父亲，

是他引导我走上了科学的道路.....

Preface

This thesis describes the results of an experimental investigation of the distributions of barriers and angular momenta involved in fusion reactions, which was carried out at the Department of Nuclear Physics in the Australian National University. The reactions studied were $^{154}Sm + ^{16}O$ and $^{186}W + ^{16}O$ at the beam energies from 58 to 110 MeV.

Experimental techniques were developed to enable the determination of evaporation residue cross-sections to a high precision. A large portion of the time in the course of this PhD study was spent on the development of a compact velocity filter involving crossed magnetic and electric fields, and a position sensitive multiwire proportional counter (MWPC). To build such an apparatus was suggested by Dr. J.R. Leigh. The filter and the MWPC were designed, constructed and tested by myself with some useful advice from Dr. D.C. Weisser and assistance from the technical staff in the Department. Although the construction of the experimental apparatus was very difficult and very time consuming, and the date when it finally worked was almost at the end of my PhD course, the achievements using this apparatus are great. It has been shown that it works extremely efficiently and has enabled measurements of evaporation residues cross-sections to be made with unprecedented precision (~1%, about one order of magnitude higher than before). Until now, it is the only apparatus in the world that has made fusion measurements to such a high precision.

Fortuitously, when the apparatus was just ready to work Dr. N. Rowley proposed a new technique of analysing fusion excitation functions in terms of the "barrier distribution"; this technique required high precision data which was not available then. Unlike many proposals which can not be exploited because of experimental difficulties, my experimental apparatus made this proposal viable almost at the same time when it was "born". The data I obtained not only gave my thesis its title, the results of the analyses of the data have also proved that this proposal is a useful tool for "looking" the fusion process.

The bulk of the experimental work was carried out by Dr. J.R. Leigh, Professor J.O. Newton, Dr. D.J. Hinde, Dr. S. Elfstrom, Dr. J.X.

Chen, R.C. Lemmon and myself. Dr. D.G. Popescu, Dr. J. P. Lestone contributed at various stages.

The reduction of most of the raw data was performed by me with some assistance from R.C. Lemmon in part of the ^{186}W data. All the subsequent analysis and interpretation of the data was carried out by myself. Various programs were written by me for these purposes. Dr. N. Rowley's code CONTACT was used to extract the deformation parameters of the target nuclei.

I was helped at all the stages of this course of work by many discussions with Dr. J. R. Leigh, Professor J.O. Newton and Dr. D.J. Hinde. I also gained useful discussions with Dr. N. Rowley when he was visiting this laboratory in 1992 and 1993.

Some of the work described in this thesis have appeared or will appear in the following publications:

(1) A Compact Velocity Filter For Evaporation Residue Measurements

J.X. Wei, J.R. Leigh, D.C. Weisser, J.O. Newton, S. Elfstrom, J.P. Lestone, J.X. Chen, D.G. Popescu and D.J. Hinde

Nucl. Instr. & Meth. in Phys. Res. **A306** (1991) 557-562.

(2) Experimental Determination of The Fusion Barrier Distribution For The $^{154}Sm + ^{16}O$ Reaction

J.X. Wei, J.R. Leigh, D.J. Hinde, J.O. Newton, R.C. Lemmon, S. Elfstrom, J.X. Chen and N. Rowley

Phys. Rev. Lett. **67** (1991) 3368-3371.

(3) Reconciling Deformation Parameters From Fusion With Those From Coulomb Excitation

J.R. Leigh, N. Rowley, R.C. Lemmon, D.J. Hinde, J.O. Newton, J.X. Wei, J. Mein, C.R. Morton, S. Kuyucak and A. Kruppa

Phys. Rev. **C47** (1993) R437-R440.

(4) High Precision Fusion Excitation Function Measurements; What Can We Learn From Them?

J.R. Leigh, M. Dasgupta, C. Morton, D.J. Hinde, R.C. Lemmon, J.O. Newton, J.X. Wei, and N. Rowley

Invited talk to RIKEN International Workshop, 18-22 February, 1993, Tokyo, Japan. Proceedings of RIKEN

International Workshop On Heavy-Ion Reaction with Neutron-Rich Beams, to be published by World Scientific Press.

(5) Obtaining Average Angular Momenta From Fusion Excitation Functions

N. Rowley, J.R. Leigh, J.X. Wei, and R. Lindsay

Submitted to Phys. Lett. **B**.
Daresbury Laboratory, UK; preprint, May 1993, (DL/NUC/P339T).

(6) Strong Dependence of Sub-barrier Fusion On The Nuclear Hexadecapole Deformation

R.C. Lemmon, J.R. Leigh, J.X. Wei, C.R. Morton, D.J. Hinde, J.O. Newton, J.C. Mein, M. Dasgupta and N. Rowley

Submitted to Phys. Lett. **B**.
Australian National University, Canberra; preprint, June 1993, (ANU-P/1134).

(7) Experimental Determination of The Distribution of Barriers For Fusion of $^{154}Sm + ^{16}O$

J.X. Wei, J.R. Leigh, J.O. Newton, D.J. Hinde, J.P. Lestone, R.C. Lemmon, J.X. Chen, S. Elfstrom and N. Rowley

International Symposium "Towards a Unified Picture of Nuclear Dynamics", June 1991, Nikko, Japan.

(8) Fusion Barrier Distributions In The Reactions $^{186}W + ^{16}O$ and $^{144,154}Sm + ^{16}O$

J.X. Wei, D.J. Hinde, J.R. Leigh, R.C. Lemmon, and J.O. Newton

International Nuclear Physics conference, July 26 - August 1, 1992, Wiesbaden, Germany.

The remaining material in this thesis is being prepared for publication.

No part of this thesis has been submitted for a degree at any other university.

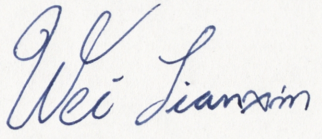

Jian Xin Wei
Canberra, July 1993

Acknowledgements

I would like to express my sincere gratitude to my supervisors Jack Leigh and John Newton for many constructive discussions and their critical reading of the draft and revisions of this thesis. I am grateful to David Hinde for his critical reading of some parts of this thesis as well.

I am indebted to David Weisser for his advice in designing and building the velocity filter and the MWPC which have contributed a lot to my experiments. I would like to thank the technical staff in the School for their help in the construction of the experimental apparatus.

My thanks go to John, Jack, David, Jinxiang, Dom, Nami, Sven, John Lestone and Roy Lemmon for their assistance in running experiments.

I would like to thank people who helped me in the preparation of this thesis, particularly Gavin for the photography and Anne for assisting me to get used to the word processing package in the Macintosh. Special thanks are due to Bernhard Fabricius and his program "MultiFig" which I used to produce most of the figures. Special thanks also to Nanda, Clyde and Jason for their proof reading of this thesis in such a short time.

I am grateful to A.N.U. for offering me this research scholarship.

Finally a special thank to my wife Shaohua for her great encouragement and support, and I wish she will hand in her Ph.D thesis in Linguistics next year; and also thanks to my lovely little daughter Beina to whom I owe so much time for her kids games; and thanks to my mother who misses me so much in China while I have been in Canberra.

Abstract

Fusion excitation functions for the reactions $^{154}Sm + ^{16}O$ and $^{186}W + ^{16}O$ have been accurately measured at small energy intervals around the Coulomb barrier. The accurate fusion cross-sections were obtained by measuring the evaporation residue cross-sections to an unprecedented precision (~1%); about one order of magnitude higher than that of the measurements available earlier. The measurements were made with the help of a compact velocity filter and a MWPC developed by me during this work. These high precision measurements have not only improved the quality of the fusion data but challenged the common view that the fusion excitation functions are featureless and do not provide a good test of models.

The excitation functions are sensitive to the details of the structure of the interacting nuclei. This has been clearly demonstrated by the well defined fusion barrier distributions extracted from these data, using a recently proposed analysis technique. The extracted barrier distributions are in good agreement with those expected from the static deformations of the target nuclei. The shapes of the two barrier distributions from ^{154}Sm and ^{186}W are different, reflecting the different hexadecapole deformations of the two nuclei. It is shown that the extracted barrier distribution provides a good test for fusion models.

High precision fusion data can now be used to give a "snapshot" of the important channels in reactions where sub-barrier fusion enhancement cannot be explained using simple geometric models.

This will give insight into the couplings which may be dominant. Such results will surely stimulate new interest in sub-barrier fusion.

These high precision data can also be used to extract the fusion angular momentum distribution as proposed a few years ago. Distributions of angular momentum have been quantitatively extracted, for the first time, directly from fusion excitation function. The limitations of this method have been studied.

CONTENTS

Chapter 1
Introduction

One of the major challenges in nuclear physics is to understand the dynamical processes during the reactions of heavy ion induced fusion on a time scale of ~10^{-21}s or shorter. These processes are strongly dependent on the barrier between the interacting nuclei, formed by the combination of Coulomb force, nuclear force and the centrifugal force. These processes are difficult to describe because the interaction is so complicated when the projectile is tunnelling/overcoming the mutual internuclear barrier. Despite the complex process involved in fusion, in energy region well above the fusion barrier, the quantum mechanical effects of tunnelling through the barrier are insignificant, and a classical picture of overcoming a single fusion barrier is adequate to describe this process. However, at bombarding energies around and below the fusion barrier, quantum mechanical tunnelling through the barrier becomes important and becomes the major process contributing to fusion. Theoretically, the Hill-Wheeler formula of barrier penetration [Hil53] is routinely used to calculate the fusion at the energies around the barrier.

In the late 1970s and early 1980s, Stokstad et al, published their systematic measurements of fusion cross-section for the reactions of ^{16}O on targets of Sm isotopes [Sto78, Sto80] at the energies around the conventional barrier (known as the Coulomb barrier). They found that fusion cross-sections were up to several orders of magnitude higher

than expected from simple barrier penetration model. Subsequently, this enhancement has been observed by many other groups in the measurements of fusion cross-sections at energies around the Coulomb barrier [Bec80, Eve81, Bec82, Rei82, Löb83, Alj84]. The enhancement has, therefore, been recognised as a global phenomenon. It was suggested that the enhancement may be understood if there is a set of barriers encountered in fusion rather than the single conventional Coulomb barrier [Vaz74, Rei85, Ste88].

A distribution of barriers may result, for example, classically from the permanent deformation [Sto78, Sto80] of the target and/or the projectile and quantum mechanically from the effects of coupling the fusion channel to other channels such as inelastic scattering and particle transfer [Bec80, Pen83]. Calculation shows that for a given fusion barrier height B, at bombarding energies around this barrier the fusion cross-section falls very quickly as the energy decreases; an exponential dependence on the difference between the bombarding energy E and barrier height B is predicted. Thus, if a set of barriers is involved in fusion, only the barriers whose heights are smaller than the bombarding energy contribute to fusion significantly.

The shape of barrier distribution therefore becomes important in affecting fusion and some arbitrary type of barrier distributions, such as flat and Gaussian distributions, have been introduced in order to fit fusion excitation functions. These distributions were successful to some degree but often a number of different barrier distributions provided equally good fits within the typical experimental uncertainties of ~10%. This supported the common view that fusion excitation functions are featureless and can be reproduced by a range of different models.

Contrasting with this common view, a recent theoretical development in the middle of 1990 [Row91, Row91a], showed that considerable information about dynamical processes in fusion can indeed be extracted directly from experimental fusion excitation functions. In particular, the distribution of barriers involved in fusion can be extracted directly from the measured experimental fusion data without reliance on models; the curvature of fusion excitation function $d^2(E\sigma)/dE^2$ is related to the distribution of fusion barriers. This represents a major advance in the understanding of heavy-ion fusion. However, to take advantage of this development, the measurement of the fusion excitation function to much higher precision (essentially ~1%) and in very fine energy steps (~0.5 MeV) is required. The data previously available were not measured in such detail, partially due to the limitation of experimental methods used and partially due to the common view that there was no need to measure the data to better than 10% because of the little use of the details of fusion excitation functions. The new method of analysing the fusion excitation function essentially leads the study of heavy ion fusion into a new dimension and raises a new task and challenge for the experimentists to measure fusion cross-sections to much higher precision, by an order of magnitude, than before.

This experimental challenge has been answered and the validity of the proposed analysis technique has been tested in the work presented in this thesis.

A velocity filter with crossed electric and magnetic fields and a position sensitive multiwire proportional counter (MWPC) have been developed by me during the course of this PhD study [Wei91]. The filter is compact (~20 cm long and ~10 cm wide), and is capable of

transmitting evaporation residues from heavy ion fusion reactions and suppressing elastic scattering, even at angles as close as 0.5° to the beam direction. The measured efficiency of the filter is very close to 100%. The transmitted evaporation residues were then detected by the MWPC behind the filter.

Using this apparatus the fusion cross-sections can be easily and quickly measured and unprecedented precision (~1%) in evaporation residue cross-section measurements has been obtained. Details of the experimental method and the apparatus will be given in Chapter 3.

The measurements were performed using a doubly closed shell spherical projectile ^{16}O, which is not expected to contribute to the barrier distributions significantly, and target nuclei ^{154}Sm and ^{186}W, which are known to have permanent deformations. These deformations are expected to give rise to a continuous distribution of barriers to fusion. Hence the extraction of these barrier distributions from measured fusion data provides a test of the validity of the proposed analysis technique.

However, the results of these tests proved to be even more exciting than anticipated. Not only were well-defined barrier distributions extracted from data but the shapes of these barrier distributions for the two reactions with different targets of ^{154}Sm and ^{186}W were quite different. These difference were assigned to the difference in the hexadecapole deformation of the two nuclei. Thus as well as proving the utility of the new method these data have shown that the measurement of fusion excitation functions can be a powerful tool for measuring nuclear deformation properties [Lei93]. In particular, the signs of hexadecapole nuclear deformation parameter, which are

notoriously difficult to determine by other methods, are determined. More importantly, this sensitivity to relatively small effects suggests that fusion data may be used as delicate probe of weak couplings. Through the barrier distribution the important channels which are responsible for enhancing fusion may then be identified.

Another important aspect in studies of fusion is the angular momentum distribution of the fused system which plays an important role in governing the details of the decay processes of the hot, rapidly rotating compound nucleus, particularly in competition between fission and particle emission. The angular momentum distribution has therefore been extensively studied experimentally and theoretically.

Experimentally, the angular momentum distributions are usually estimated using measurement of γ-ray multiplicities [Van83, Gil85, Lei86, Gil90, Wuo91, Bie93], isomer ratios [Dig90], fission fragment angular distributions [Bac85, Mur86, Van86], α-particle angular distributions [Bor86] and elastic scattering [Uda85, Lei86, Kon87]. However, none of these methods directly measures the angular momentum distribution in fusion. They generally rely on the measurements of one or other decay products following fusion, and all require interpretation using various models or recipes. This model dependence introduces large uncertainty in extracted angular momentum distribution in the compound nucleus.

Another method, pointed out by various authors [Bal83, Rei85, Bal86, Das86], is that the fusion angular momentum may be extracted from the slope of fusion excitation function. Thus the transmission coefficient T_l at $l = 0$ can be written as $T_0(E) = [d(E\sigma)/dE]/R^2$ and T_l can

be obtained by $T_l(E) = T_0(E')$, where R is the fusion radius and $E' = E - l(l + 1)\hbar/2\mu R^2$, μ is the reduce mass of projectile. However, this method has not been used practically because of the relatively poor precision of the existing data though some authors [Das91, Ste92] have tried to extract the mean angular momentum from fusion excitation function by interpreting the experimental fusion data with various methods and models. As it has been point out by Stefanini [Ste92], that only qualitative results can be obtained from their analyses and quantitative deductions cannot be made due to the difficulties of obtaining the fusion data to the required precision. The availability of the high precision fusion data, measured in small energy steps, presented in this thesis made this technique viable quantitatively for the first time.

Using this method, the distributions of fusion angular momentum for the reactions of ^{154}Sm and $^{186}W + ^{16}O$ have been extracted. The errors relating to the replacement of the fusion radius, which varies with the barrier and the angular momentum, by an average fusion radius have been studied. The extracted mean angular momenta have been compared with those converted from γ-ray multiplicities measurements [Bie93]. Details of these are presented in the last Chapter of this thesis.

In summary, for the first time, well defined fusion barrier distributions have been extracted directly from experimental data, and fusion angular momentum distributions have also been extracted from the data. It has been demonstrated that, contrary to the commonly held view, fusion excitation function itself does contain a considerable amount of information about the fusion process. However, this information can only be explored when the fusion

excitation function is measured to very high precision and in very small energy intervals.

The analysis methods for the extraction of the fusion barrier and angular momentum distributions have been shown to work extremely well. It is with confidence that we can now expand this analysis to more complex reaction systems in which the quantum mechanical coupling effects are dominant [Lei93a], rather than the classical barrier distribution associated with deformed nuclei. These would lead us to other new insights into the dynamical process in heavy ion induced fusion.

Chapter 2
Theoretical Background

2.1 FUSION

Fusion is a process in which two nuclei, a projectile and a target, come together with sufficient kinetic energy to overcome their mutual electrostatic and centrifugal repulsion to form a new nucleus. Fusion is classified as complete or incomplete depending on whether the final charge Z_c, and atomic mass A_c, of the newly formed compound nucleus (CN) are equal to the sum of those of the projectile and target or not. It has been shown experimentally (e.g. in [Wil80]) that incomplete fusion becomes significant once the bombarding energy is above a certain energy threshold corresponding to a critical angular momentum. This threshold is far above the barrier region, thus we expect that incomplete fusion is insignificant at the energies used here and hence can be ignored in this work. The term fusion in all that follows refers only to a complete fusion.

Because of the large amount of energy and angular momentum involved in fusion, the newly formed CN is a "hot" and rapidly "spinning" system. In the energy region studied in this work, the CN decays mainly by evaporating particles and γ-rays, resulting in an evaporation residue, or by fission (the CN splits into two roughly equal fragments). Thus, the fusion cross-section can be determined experimentally by measuring evaporation residues and fission

fragments, and assuming that it is the sum of the cross-sections for these two decay processes. However, fission only becomes important in the decay process when the fission barrier is equal to or less than the neutron bounding energy of CN [Van73]. In this work the decay processes of evaporating particles are dominant and the fusion cross-sections are equal to those for evaporation residues. For the reaction of $^{186}W + ^{16}O$ at the bombarding energies well above the fusion barrier there is a small fission probability and this has been taken into account. Since the process of fission is not studied in this thesis, the fission cross-sections of $^{186}W + ^{16}O$ were taken from reference [Bem87].

2.1.1 The Fusion Barrier

The internuclear potential V, of the colliding projectile and target is a function of the distance r, between the centres of the two nuclei. In a head on collision V is the sum of an attractive nuclear potential $-V_{nuc}$, and a repulsive Coulomb potential V_{Coul}, thus:

$$V(r) = -V_{nuc}(r) + V_{Coul}(r) \qquad (2\text{-}1\text{-}1)$$

V_{nuc} is the strong, short range potential, and thus, it is only important when the surfaces of the two nuclei are very close to each other. The nuclear potential is not yet fully understood in detail, but a good and simple approximation, successful in describing elastic scattering for example, is a Woods-Saxon potential which can be written as:

$$-V_{nuc}(r) = -V_0 \left[1+\exp\left(\frac{r - R_N}{a}\right)\right]^{-1} \qquad (2\text{-}1\text{-}2)$$

Where V_0 and a are the depth and diffuseness of the potential, and R_N is the sum of the two nuclear radii.

The Coulomb potential can be written exactly if the shapes of the two nuclei are known and the the two nuclei are separated from each other. If the two nuclei are spherical then V_{Coul} is simply

$$V_{Coul}(r) = \frac{Z_1 Z_2 e^2}{r} \qquad (2\text{-}1\text{-}3),$$

where Z_1, Z_2 are the nuclear charges. For a deformed projectile and/or target, V_{Coul} and V_{nuc} also depend on angle of the orientation of two colliding nuclei; this will be discussed in §2.2.2.

For non-head on collision, the internuclear potential becomes angular momentum l dependent,

$$V_l(r) = V(r) + \frac{l(l+1)\hbar^2}{2\mu r^2} \qquad (2\text{-}1\text{-}4)$$

where μ is the reduced mass of the projectile. The angular momentum is conserved during the collision and is determined by the asymptotic impact parameter of the projectile and target.

A plot of the internuclear potential V_l vs r is shown in Fig 2-1-1. For l=0, one can see that there is a peak in V(r) along the r axis and a repulsive region to the right side of the peak, where the Coulomb potential is dominant. To the left side of the peak, for smaller distances, the attractive nuclear potential is dominant and an absorptive well is formed. Classically, the colliding system of the projectile and target must have sufficient energy to overcome the potential peak in order to reach the absorptive well and thus to fuse. The height of the peak and the distance at which it occurs are therefore defined as the fusion barrier (frequently called the Coulomb barrier) B_0 and the fusion radius R_0. As will be discussed later, these

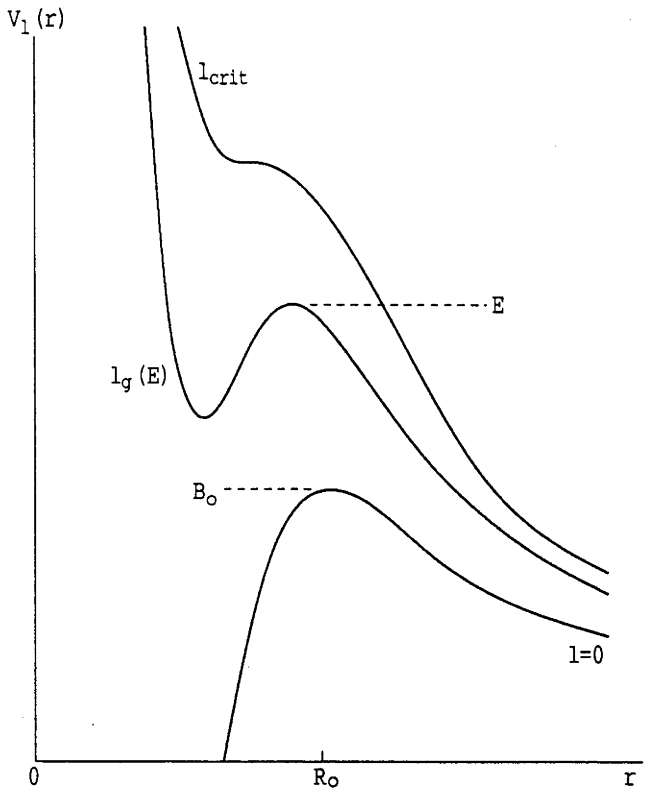

Fig. 2-1-1:
Illustration of the angular moment dependence of internuclear potential (adapted from [Pof83]). Theoretically the barrier height and the position can be found at the stationary point for all potentials of $l \leq l_{crit}$, and there is no absorption well when $l > l_{crit}$ (see text for details). The potential at the grazing angular momentum l_g is indicated for a given incident energy E.

are two fundamental parameters in the study of the fusion process. Values of B_0 and R_0 can be found by finding the stationary point in the first differential of V(r), thus

$$\left[\frac{dV(r)}{dr}\right]_{r=R_0} = 0 \qquad (2\text{-}1\text{-}5),$$

and

$$B_0 = -V_{nuc}(R) + \frac{Z_1 Z_2 e^2}{R_0} \qquad (2\text{-}1\text{-}6)$$

However, since the form of nuclear potential is not exactly known, B_0 and R_0 cannot be precisely determined by theory alone. Instead they are usually extracted from the measured fusion cross-sections, as discussed in §2.1.2.

When $l \neq 0$, the centrifugal term is taken into account, both the barrier height and fusion radius become l dependent (denoted as B_l and R_l). Thus

$$B_l = -V_{nuc}(R_l) + \frac{Z_1 Z_2 e^2}{R_l} + \frac{l(l+1)\hbar^2}{2\mu R_l^2} \qquad (2\text{-}1\text{-}7)$$

Calculation shows that the R_l decreases as l increases. However R_l is not very sensitive to l, and to the first order it is not a bad approximation [Won73] to take R_l independent of l. Thus

$$R_l \approx R_0 = R \qquad (2\text{-}1\text{-}8)$$

The barrier height B_l is then approximately

$$B_l \simeq B_0 + \frac{l(l+1)\hbar^2}{2\mu R^2} \qquad (2\text{-}1\text{-}9)$$

As l increases, the absorptive well of the potential becomes shallower and eventually vanishes. The value of l at which the absorption well vanishes, is the so-called critical angular momentum, l_{crit}. Classically, there is no fusion when the $l \geq l_{crit}$, because no absorption region exists in the potential of $V_{(l \geq l crit)}$, and the large angular momentum will disrupt the interacting system before a compound nucleus is formed.

2.1.2 Fusion Cross-Sections

Starting from a geometric view of the collision of two nuclei, one can get the expression for the fusion cross-section σ as

$$\sigma(E) = \pi \lambda\!\!\!^{-2} \sum_{l=0}^{\infty} (2l+1) T_l(E)\, P_l \equiv \sum_{l=0}^{\infty} \sigma_l \qquad (2\text{-}1\text{-}10)$$

where the T_l and σ_l are the transmission coefficients, and partial cross-sections at angular momentum l respectively. The P_l are the fusion probabilities which are generally taken to be unity in the energy range used in this work [Row91]. The reduced wave length is given by

$$\lambda\!\!\!^{-2} = \frac{\hbar^2}{2\mu E} ,$$

where E is the kinetic energy of the projectile in the centre of mass system.

In the sharp cutoff model the T_l is given by:

$$T_l = \begin{cases} 1 & l \leq l_g \\ 0 & l > l_g \end{cases} \qquad (2\text{-}1\text{-}11)$$

where l_g is the maximum angular momentum which can fuse, often referred to as the grazing angular momentum, defined by

$$E = B_0 + \frac{\hbar^2}{2\mu R^2} l_g(l_g+1) \qquad (2\text{-}1\text{-}12)$$

Inserting (2-1-11) into (2-1-10) and replacing the sum over l by an integration, the fusion cross-section becomes

$$\sigma(E) = \begin{cases} \pi \lambda\!\!\!^{-2} \sum_{l=0}^{l_g} (2l+1) = \pi \lambda\!\!\!^{-2} \int_{l=0}^{l_g} (2l+1)dl = \pi \lambda\!\!\!^{-2} l_g(l_g+1) & E \geq B_0 \\ 0 & E < B_0 \end{cases} \qquad (2\text{-}1\text{-}13)$$

which, using (2-1-12), gives

$$\sigma(E) = \begin{cases} \pi R^2 (1 - \frac{B_0}{E}) & E \geq B_0 \\ 0 & E < B_0 \end{cases} \qquad (2\text{-}1\text{-}14)$$

This equation is commonly known [Wei37, Gut73, Sco76] as the sharp cutoff expression. It predicts that the fusion cross-section varies linearly with 1/E, with intercept B_0 and slope πR^2. For the convenience of the discussions about the barrier distributions later, the above equation, multiplied by E on both side, can be written as:

$$E\sigma(E) = \begin{cases} \pi R^2 (E - B_0) & E \geq B_0 \\ 0 & E < B_0 \end{cases} \qquad (2\text{-}1\text{-}15)$$

The function $E\sigma$ is, now, linear in E.

Shown in Fig. 2-1-2 is a plot of $E\sigma$ vs E for the reaction of $^{74}Ge + ^{74}Ge$. The fusion barrier height B_0 and the fusion radius (the fusion radius is defined as the barrier radius R) can be extracted from such a plot by fitting the experimental data. This type of analysis was first performed by Gutbord et al. [Gut73] and has been used since then by many authors in their analyses of heavy ion induced fusion reactions [Eis77, Jah82, Bec83, Mos84].

However, as expected, the sharp cutoff model fails at energies near to the barrier regime. This is evident in Fig. 2-1-2 in which the data deviate significantly from the straight line at low energies. Details of this phenomena will be discussed in §2.2.

As shown in Fig. 2-1-1, the absorptive well of the internuclear potential vanishes at the angular momentum $l_{crit.}$ In a simple classical model which relies on trapping the nuclei inside the potential well, no partial waves $l \geq l_{crit}$ can lead to fusion. Hence the l_g in Eq. 2-1-2 should be replaced by l_{crit} if the energy $E \geq E_1$, where

$$E_1 = B_0 + \frac{\hbar^2}{2\mu R^2} l_{crit}(l_{crit}+1) \qquad (2\text{-}1\text{-}16)$$

The region of energy $E \geq E_1$ is defined as high energy region, and the region $B_0 < E < E_1$ is defined as intermediate energy region. While the energy $E \leq B_0$ is so-called sub-barrier region. Since the beam energies used in this work are much lower than E_1 the limit of l_{crit} is not reached, and hence it is not taken into account in our analyses of the experimental fusion cross-section data.

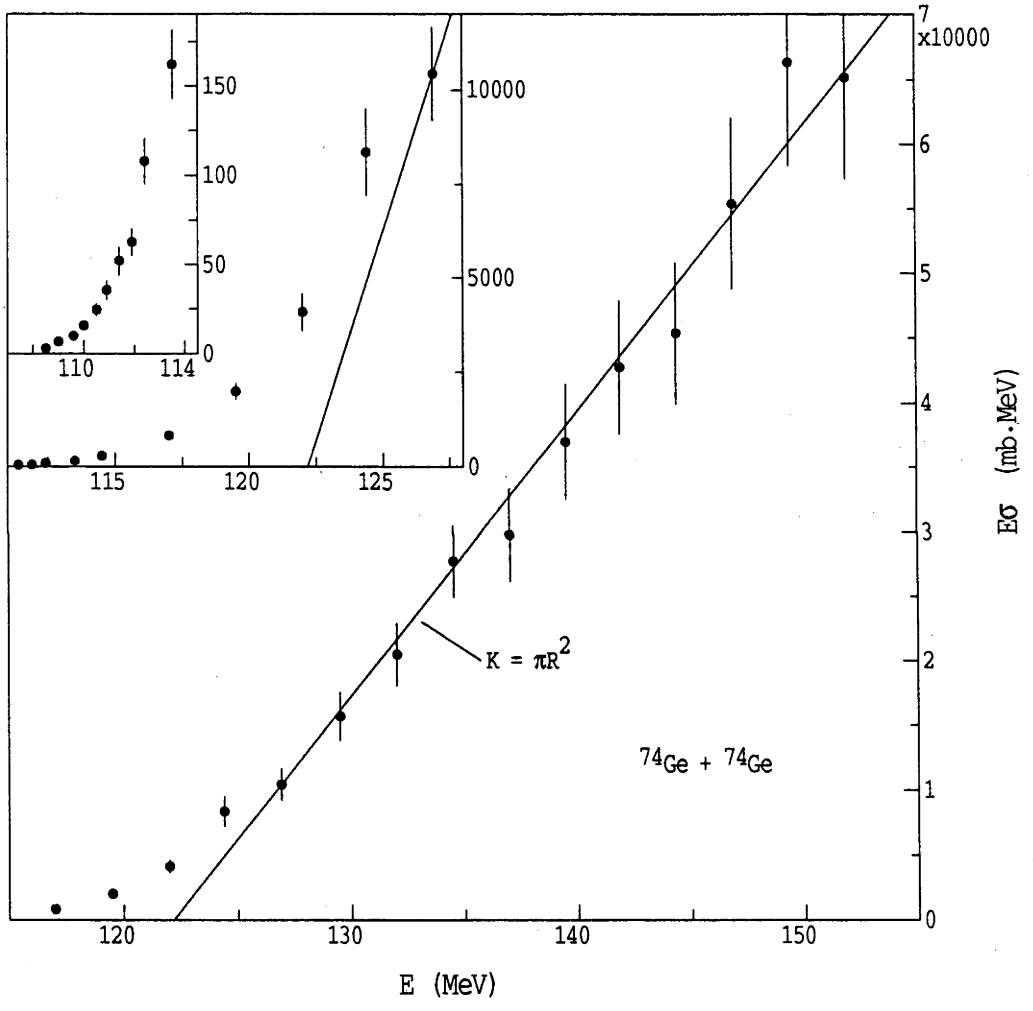

Fig. 2-1-2: Plot of Eσ vs E (in centre of mass) for the reaction of $^{74}Ge + ^{74}Ge$ (adapted from [Bec88]). At the energies above fusion barrier, Eσ is essentially linear. The intercept of the linear fit and the abscissa gives the fusion barrier height B_0 while the slope K of the straight line gives the fusion radius (πR^2). The inserts expand the view at the energies near and below the barrier.

2.2 SUB-BARRIER FUSION

2.2.1 Barrier Penetration

The sharp cutoff model discussed in §2.1.2, given its simplicity, has had great success in describing fusion cross-sections at energies above the potential barrier. It is, however, not appropriate at energies near and below the barrier where the barrier penetration effect becomes important. Thus, Eq. 2-1-11 is no longer a good approximation. To take into account the barrier penetration, WKB approximation [Kem35, Fro65] is often used to calculate the transmission coefficients T_l . The T_l for a projectile to tunnel through a barrier can be written as

$$T_l(E) = \frac{1}{1 + \exp\left(\mp \int_{r_a}^{r_b} \sqrt{\frac{2\mu}{\hbar^2} |V_l(r) - E|}\, dr\right)} \qquad (2\text{-}2\text{-}1)$$

where r_a and r_b are the inner and outer turning points of the potential barrier, the minus/plus signs in front of the integral refer to above/below barrier energies, the $V_l(r)$ is defined in Eq. (2-1-4).

In principle, the $T_l(E)$ and hence the fusion cross-section, can be calculated if the $V_l(r)$ is known. However, because the nucleus-nucleus potential is not known, as discussed before, some assumptions about the $V_l(r)$ have to be made. The usual assumption is that the potential barrier is nearly parabolic in shape [Tho59, Hui61, Ras71]. The Coulomb and nuclear potentials can then be replaced by an inverted harmonic oscillator potential to give

$$V_l(r) = B_o - \frac{1}{2}\mu\omega_o^2(r - R_o)^2 + \frac{l(l+1)\hbar^2}{2\mu r^2} \qquad (2\text{-}2\text{-}2)$$

For an energy E, the transmission coefficients $T_l(E)$ can then be calculated analytically and are given by the Hill-Wheeler formula [Hil53]

$$T_l(E) = \frac{1}{1 + \exp[\frac{2\pi}{\hbar\omega_l}(B_l - E)]} \qquad (2\text{-}2\text{-}3)$$

where B_l and $\hbar\omega_l$ are the barrier height and barrier curvature for the lth partial wave.

B_l and the ω_l are calculated numerically, from the total potential by finding the stationary point R_l of the first differential of the potential, thus

$$B_l = V_l(R_l) \qquad (2\text{-}2\text{-}4)$$

and

$$\hbar\omega_l = -\frac{\hbar}{\sqrt{\mu}}\left[\frac{d^2V_l(r)}{dr^2}\right]^{1/2}_{r=R_l} \qquad (2\text{-}2\text{-}5)$$

By inserting Eq. (2-2-3) into Eq. (2-1-10) the fusion cross-section σ can be found.

Further theoretical studies have been carried out by Wong [Won73] and it was found that the R_l and $\hbar\omega_l$ are rather insensitive to l. Hence, it can be assumed that the barrier positions and curvatures are independent of angular momentum, thus

$$R_l \approx R_0 = R \qquad \hbar\omega_l \approx \hbar\omega_0$$

and

$$B_l \approx B_0 + \frac{l(l+1)\hbar^2}{2\mu R^2}$$

Then

$$T_l(E) = \frac{1}{1 + \exp[\frac{2\pi}{\hbar\omega_0}(B_0 + \frac{l(l+1)\hbar^2}{2\mu R^2} - E)]} \qquad (2\text{-}2\text{-}6)$$

and

$$\sigma(E) = \frac{R^2\hbar\omega_0}{2E} \ln\{1 + \exp[\frac{2\pi}{\hbar\omega_0}(E - B_0)]\} \qquad (2\text{-}2\text{-}7)$$

This is a very useful theoretical approximation for the fusion cross-section and it forms the basis of many other models which will be discussed later.

At energies well above the barrier where $E \gg B_0$ the logarithmic expression (2-2-7) reduces to the well-known classical formula (2-1-14).

For low energies such that $E \ll B_0$, the cross-sections are given by

$$\sigma(E) = \frac{R^2\hbar\omega_0}{2E} \exp[\frac{2\pi}{\hbar\omega_0}(E - B_0)] \qquad (2\text{-}2\text{-}8)$$

showing that the fusion cross-section decreases exponentially with decreasing E.

One of the successful applications of this penetration model is for the reaction of $^{144}Sm + ^{16}O$ [DiG86]. DiGregorio et al, measured the fusion cross-section for this system at bombarding energies in the range of 63 MeV to 72 MeV in lab. The fusion cross-sections ranged from 0.3 mb to 400 mb. They extracted the B_0 and R from the data measured above the Coulomb barrier and then adjusted $\hbar\omega_0$ to fit all the measured fusion cross-sections. The model fitted the data within the experimental error (~10%) using a value of 3.9 MeV for $\hbar\omega_0$. However, extending the analysis to the ^{16}O induced fusion reactions on the other even Sm isotopes ($^{148,150,152,154}Sm$), they found that at sub-barrier

energies the cross-sections for the different isotopes varied far more than would be expected from simple $A^{1/3}$ variations of the radii [Sto78, Sto80, Sto81, DiG86].

The enhancement of sub-barrier fusion cross-sections, in these cases, is mainly due to the permanent deformations of the Sm isotopes which vary from spherical ^{144}Sm (closed neutron shell) to well deformed ^{154}Sm. However, such enhancement is a common phenomenon observed in essentially all heavy ion reactions at sub-barrier energies [Bec80, Rei82, Pen83, Ste84, Bec85, Ste86]; the fusion cross-sections are orders of magnitude larger than those expected from simple barrier penetration models. A number of possible theoretical explanations of this phenomenon have been developed and investigated. These approaches consider effects of zero-point motion [Esb81], coupling to inelastic excitation [Das83, Das83a, Bro83], particle transfer [Bro83a, Ste90], neck formation [Vaz81, Jah82, Ste90], and the static deformation of the reacting nuclei [Sto81]. Details of some of these theoretical approaches will be discussed.

2.2.2 Static Deformation of Nuclei

The penetration models discussed above assume that the projectile and target are spherical. However, if one (or both) of the nuclei is deformed the interaction potential becomes strongly dependent on the mutual orientation of the two nuclei. For example, when a spherical projectile approaches a deformed prolate target, the fusion barrier is lower if the symmetry axis is along the beam direction ($\theta = 0°$ in Fig. 2-2-1) and is higher if it is perpendicular to it. The transmission coefficient T_l varies very quickly (exponentially) with bombarding energy near the barriers (for example in the (spherical) $^{16}O + ^{144}Sm$

case, when $E - B_0 = 1.5$ MeV, $T_0 \sim 0.9$ and when $E - B_0 = -1.5$ MeV, $T_0 \sim 0.08$). Hence only the barriers which are lower than the bombarding energy contribute significantly to fusion. These orientation effects should thus critically affect the sub-barrier fusion cross-sections.

Expanding the nuclear radius in terms of spherical harmonics $Y_{\lambda 0}(\theta)$ [Sto81], one gets

$$R_t(\theta) = R_t [1+\sum_{\lambda}\beta_\lambda Y_{\lambda 0}(\theta)] \qquad (2\text{-}2\text{-}9)$$

where β_λ (λ = 2,4,6,...) are the parameters describing the deviation of the nuclear surface from a sphere with a radius R_t.

Replacing R_N with $R_N(\theta) = R_p + R_t(\theta)$ (R_p is radius of projectile) in the potential in Eq. 2-1-2 and replacing the monopole Coulomb potential with multipole potential $V_{Coul}(r,\theta)$, the θ dependent internuclear potential becomes

$$V_l(r,\theta) = -V_{nuc}(r,\theta) + V_{Coul}(r,\theta) + \frac{l(l+1)\hbar^2}{2\mu r^2} \qquad (2\text{-}2\text{-}10)$$

Where θ is the angle between the axis of symmetry of the deformed target nucleus and the initial direction of the spherical projectile as in Fig. 2-2-1.

From this equation, the fusion barrier height $B(\theta)$ and transmission coefficients $T_l(E,\theta)$ can be calculated. Instead of a single fusion barrier B_0, as in the spherical case, there is a continuous distribution of barriers $B(\theta)$. Fig. 2-2-1 shows the barriers for the interaction of $^{154}Sm + ^{16}O$ for $l = 0$ as a function of the angle θ describing the orientation of the deformed ^{154}Sm [Sto81]. The fusion barriers heights change by about 9 MeV as θ varies from 0° to 90°. The potential at 52.5° shown in this figure is close to that for a spherical case.

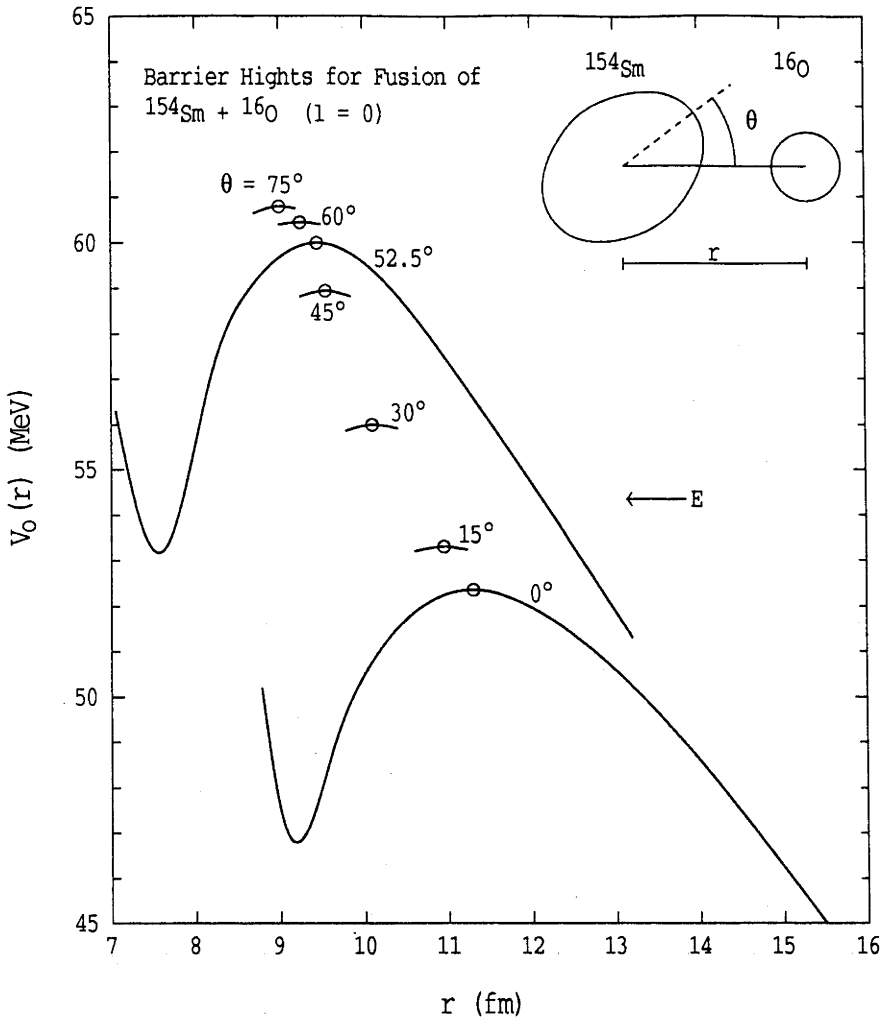

Fig. 2-2-1: Barriers (l = 0) of ^{154}Sm + ^{16}O vary with the angles of orientation (adapted from [Sto81]). An incident energy of 54.3 MeV (60 MeV lab) is indicated, from which it is evident that the incident energy is much lower than the heights of most of the barriers but it is still higher than the lowest barriers. Only those lowest barriers significantly contribute to fusion (see Fig. 2-2-2 for details).

The fusion cross-section for an orientation θ is given by

$$\sigma(\theta) = \pi \lambda\!\!\!^{-2} \sum_{l=0}^{\infty} (2l+1) T_l(\theta) \qquad (2\text{-}2\text{-}11)$$

Fig. 2-2-2 shows the calculated σ(θ) for ^{154}Sm + ^{16}O at centre of mass energy of 54.3 MeV (60 MeV bombarding energy). The partial cross-sections σ(θ) span three order of magnitude. This bombarding energy

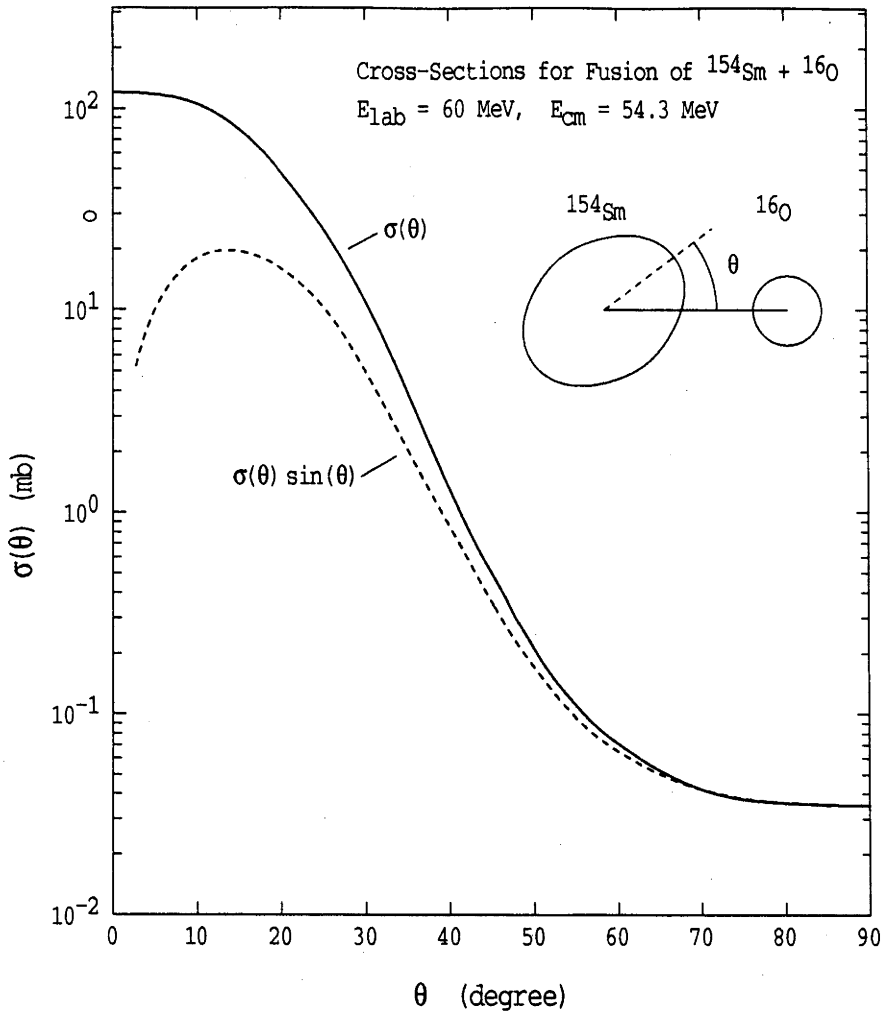

Fig. 2-2-2: Calculated fusion cross-sections as a function of the angle of orientation (adapted from [Sto81]). Only the smallest angles, hence the lowest barriers, significantly contributed to fusion at E_{cm} 54.3 MeV.

is equivalent to the barrier height, B(θ), at θ ~ 20°. One can see that the σ(θ) drops dramatically as the barrier height B(θ) becomes larger than the incident energy as θ exceeds 20°.

The total fusion cross-sections have to be averaged over all θ values since the nucleus in the target have random orientation, thus

$$\sigma = \int_0^{\pi/2} \sigma(\theta) \sin\theta d\theta \ . \qquad (2\text{-}2\text{-}12)$$

In the analysis of the ^{A}Sm + ^{16}O reactions, by Stokstad et al and DiGregorio et al, ^{144}Sm was treated as spherical and for the other isotopes β_2 was used as a free parameter (the values of the β_4, β_6, ..., were set equal to zero) to minimise the χ^2 of the theoretical fits to the data. They found that the best fits occurred when β_2 ~ 0.15, 0.18, 0.19, 0.22 for ^{148,150,152,154}Sm respectively (see Fig. 2-2-3 adapted from [DiG86]). However these extracted β_2 values are systematically

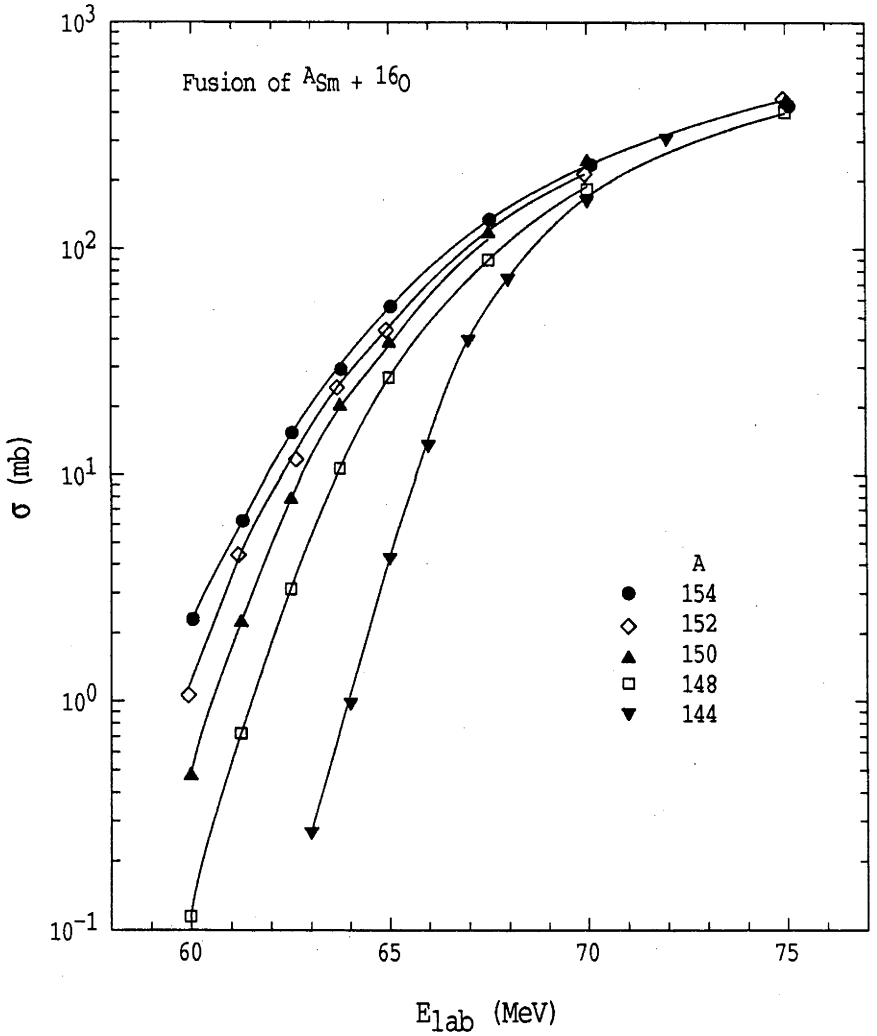

Fig. 2-2-3: Fusion cross-sections for ^{A}Sm + ^{16}O (adapted from [DiG86]). The solid curves are calculated cross-sections by Wong model, (see text for detail).

smaller than those extracted from the α-particle inelastic scattering and other reactions [Hen68, Hen73, Bru74, Sha74, Lee74, Lee75]. For example, the value of the β_2 of ^{154}Sm, extracted from the inelastic scattering, ranged within 0.27 to 0.33, roughly 30% larger than that extracted from fusion data. The reason for this remained unknown until recently when the high precision fusion data for this reaction, obtained during the course of this work, were re-analysed [Lei93], as discussed in the Chapter 5.

2.2.3 Vibration of Nucleus

Just as the different orientations of a deformed nucleus result in a distribution of barrier, the fluctuation of the surface-to-surface distance originating from collective vibrational motion (zero-point motion) of a nucleus [Esb78, Bro79, Bro79a, Esb81] also results in a distribution of fusion radii, hence a distributions of barrier heights. Although these two barrier distributions may be quite different to each other, both of them produce significant enhancement of fusion at the energies near and below the Coulomb barrier.

It can be shown that the distribution of the nuclear radius has a Gaussian form, if one assumes that the surface vibrations are independent harmonic vibrations [Boh75, Bro76]. Using this radius distribution, Esbensen [Esb81] parameterised the nuclear potential and calculated fusion cross-sections. He investigated the fusion excitation functions of ^{16}O + ^{148,150,152,154}Sm and ^{40}Ar + ^{144,148,154}Sm, measured by Stokstad, et al [Sto78,Sto80a]. The fusion cross-sections were calculated assuming that there are quadrupole and octupole vibrations for the "lighter" targets of ^{144,148,150}Sm, and quadrupole

deformations and octupole vibrations for ^{152,154}Sm. A quantitative agreement with experimental data (measured to about ±10%) was obtained at the energies below the Coulomb barrier. As a comparison, he calculated the fusion cross-sections of ^{40}Ar + Sm by including the quadrupole ZPM of ^{40}Ar, based on the low-lying 2^+ state in ^{40}Ar. It was found that including the ZPM of ^{40}Ar improves the agreement between experiment and calculation at the energies below the barrier. However, the calculations overestimated the fusion cross-sections in the intermediate energy region. This overestimation was larger for the ^{40}Ar than for ^{16}O induced fusion. It was suggested [Esb81] that this may result from the lack of consideration of the dynamical effect, such as formation of a "neck" between the interacting nuclei during the fusion process. After investigating many fusion excitation functions Vaz et al and Jahnke et al [Vaz81, Jah82] have qualitatively predicted that such a dynamical effect would be proportional to the Z_1Z_2 of the interacting nuclei. However, because of the difficulties in parameterising the "neck" formation dynamically, no quantitative calculations have been provided to testify this proposition.

However, Reisdorf, et al, had claimed that "there is no need to invoke additional degrees of freedom such as neck formation", after they reinvestigated the reactions of ^{40}Ar + ^{144,148,154}Sm and measured the reactions of ^{40}Ar + ^{112,116,122}Sn [Rei82]. They showed that the experimental data (overall accuracy of 15%) can be interpreted by the barrier fluctuations correlated with the collective surface zero point motion of nuclei. To fit the data, they found that the largest fluctuation parameter is required for the target nucleus ^{148}Sm and larger fluctuations are required for ^{40}Ar than for ^{16}O induced fusion. The first observation is consistent with the fact that the ^{148}Sm is a

transitional nucleus and has the largest vibration; ^{154}Sm is known as static deformed and this has been taken into account in their calculation. The latter one might relate to the fusion channel coupling with the inelastic channel at the low lying 2^+ state (1.46 MeV) in ^{40}Ar but not in ^{16}O. More detailed analyses were carried out later by the same authors [Rei85]. It was found that the experimental data can be well reproduced by simplified coupled channel calculations, which will be discussed in the following section.

2.2.4 Coupled Channels Calculations

It was found by Beckerman et al [Bec80] in an investigation for reactions involving ^{58}Ni and ^{64}Ni nuclei, that the enhancement of fusion cross-sections for $^{58}Ni + ^{64}Ni$ is much larger (up to 1 or 2 orders of magnitude) than that for either of the reactions $^{58}Ni + ^{58}Ni$ and $^{64}Ni + ^{64}Ni$, and this cannot be simply explained by static deformations or surface vibrations. For example, if the enhancements were caused by a static deformation of only one of the nuclei, the largest enhancement should occur when both the projectile and target are deformed. Beckerman et al [Bec82, Bec83] have explored further the complex variation of the sub-barrier fusion cross-sections in their series of fusion studies of $^{58,64}Ni$ and ^{74}Ge projectiles on a target of ^{74}Ge.

In 1983, Dasso et al [Das83, Das83a] and Broglia et al [Bro83,Bro83a] published a series of papers and introduced a new idea that fusion may be enhanced by coupling the entrance channel to a non-fusion channel such as inelastic excitation or transfer.

Using particle transfer reaction as an example, for instance, if a particle, such as a neutron or proton is exchanged between the

interacting nuclei before fusion, the kinetic energy (or say the effective bombarding energy) of the fusing system is changed because of the Q-value of the transfer reaction. Also the barrier height is changed because of the changes of the fusion radius and/or the redistribution of the charges after proton transfer. For simplicity, assuming there is only a single transfer channel, the probability of the transfer reaction is P(E). If the Coulomb barrier height of entrance channel minus that of exit channel is ΔE_c, then the net gain [Bro83] for the bombarding energy after the particle transfer is $Q + \Delta E_c$ and the total fusion cross-section $\sigma(E)$ is

$$\sigma(E) = [1 - P(E)]\sigma^0(E) + P(E)\,\sigma^1(E + Q + \Delta E_c)$$

Where the σ^0 is the fusion cross-section for the normal fusion entrance channel, and the σ^1 is the fusion cross-section for the transfer channel. Since the fusion cross-section is very sensitive to the bombarding energy at energies below the Coulomb barrier, there would be a considerable contribution from σ_1 if the value of $Q + \Delta E_c$ is positive.

Notice that there is a positive value of $Q + \Delta E_c$ in the transfer channel when two neutrons are picked up by the projectile ^{58}Ni from both targets ^{64}Ni and ^{74} Ge in the reactions mentioned above; the values of $Q + \Delta E_c$ are +3.9 and +3.5 MeV for the targets of ^{64}Ni and ^{74}Ge respectively. Broglia et al have calculated the enhancements of the fusion cross-sections of these two reactions. They found that the experimental data can be fitted reasonably well when the P(E) = 0.06 for the reaction ^{58}Ni + ^{64}Ni and when the P(E) = 0.1 for the reaction of ^{58}Ni + ^{74}Ge. Fig. 2-2-4 shows the results of their calculations. The calculated σ_0, for reactions of ^{58}Ni + ^{58}Ni and ^{64}Ni + ^{74}Ge, are also shown in the figure by dashed lines.

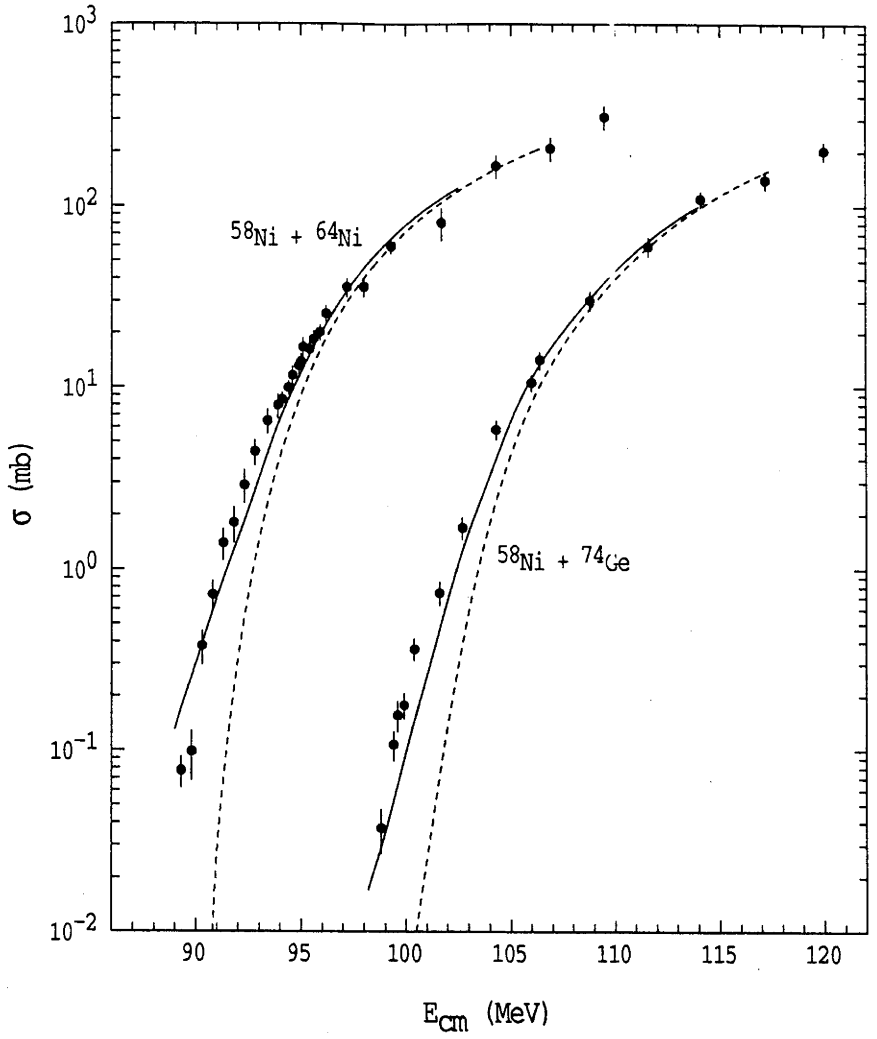

Fig. 2-2-4: Fusion cross-sections for ^{58}Ni + ^{64}Ni and ^{58}Ni + ^{74}Ge (adapted from [Bro83]). The solid curves and the dashed curves show the calculated fusion cross-sections with and without the inclusion of transfer channels respectively.

This simple example shows that how other reaction channels can affect fusion. The real situation however is much more complicated. The reaction channels can couple to each other, resulting in enhancement at sub-barrier energies even if negative Q-values are involved. The total Hamiltonian for the interacting nuclei can be written as a normal term without coupling plus a coupling term V_{cpl} [Das83a], thus

$$H = H_0 + K + V + V_{cpl} \qquad (2\text{-}2\text{-}13)$$

where the H_0 is an intrinsic Hamiltonian for two colliding nuclei, the K and V are relative kinetic and potential energies of the interacting system.

Assuming that there are only two channels, the problem is reduced to solving the following two coupled Schrödinger equations in a single spatial dimension x [Das83, Lan85],

$$\left[\frac{-\hbar^2}{2\mu} \frac{d^2}{dx^2} + V(x) - E_0 \right] u_0 = -F(x)\, u_1 \qquad (2\text{-}2\text{-}14)$$

$$\left[\frac{-\hbar^2}{2\mu} \frac{d^2}{dx^2} + V(x) - E_1 \right] u_1 = -F(x)\, u_0 \qquad (2\text{-}2\text{-}15)$$

where μ is the reduced mass of projectile and E_α is the energy of the particular channel α. F(x) is the coupling strength which depends on the details of the interaction. For simplicity, F(x) has been taken as a constant F for the following discussion.

The boundary conditions are

$$u_\alpha = \begin{cases} \delta_{\alpha o} e^{-ik_\alpha x} + r_\alpha e^{ik_\alpha x} & x \to +\infty \\ t_\alpha e^{-ik_\alpha x} & x \to -\infty \end{cases} \qquad (2\text{-}2\text{-}16)$$

where $k_\alpha = \sqrt{2\mu E_\alpha/\hbar^2}$ is the asymptotic wave number, the r_α and t_α are the reflection and transmission coefficients.

Then equations (2-1-14) and (2-1-15) can be solved by diagonalising a matrix

$$M = \begin{bmatrix} 0 & F \\ F & -Q \end{bmatrix} \qquad (2\text{-}2\text{-}17)$$

where $Q = E_1 - E_0$ is the reaction Q value.

The eigenvalues of M are

$$\lambda_{\pm} = \frac{1}{2}(-Q \pm \sqrt{4F^2 + Q^2}) \qquad (2\text{-}2\text{-}18)$$

The transmission probability for a given l is given by

$$T_l = \sum |t_\alpha|^2 = \sum_i P_i T_l[E, V_l(x) + \lambda_i] \qquad (2\text{-}2\text{-}19)$$

where $T_l[E, V_l(x) + \lambda_i]$ are the transmission probabilities for the potential barriers of $V_l(x) + \lambda_i$ at the energy E, and

$$P_i = \frac{F^2}{F^2 + \lambda_{\pm}^2} \qquad (2\text{-}2\text{-}20)$$

are the weight factors for individual channels.

Taking the parabolic barrier approximation, $T_l[E, V_l(x) + \lambda_i]$ for each channel can be written analytically as (refer to Eq. (2-2-6))

$$T_l[E, V_l(x) + \lambda_i] = \frac{1}{1 + \exp[\frac{2\pi}{\hbar\omega_0}(B_0 + \frac{l(l+1)\hbar^2}{2\mu R^2} + \lambda_i - E)]} \qquad (2\text{-}2\text{-}21)$$

The fusion cross-section can then be written as

$$\sigma(E) = \frac{R^2\hbar\omega_0}{2E} \sum_i P_i \ln\{1 + \exp[\frac{2\pi}{\hbar\omega_0}(E - B_0 - \lambda_i)]\} \qquad (2\text{-}2\text{-}22)$$

In the cases of coupling to inelastic channels, for instance the 2^+ state of the rotational band in a deformed nucleus, the Q value ($Q = E_1 - E_0 \sim$ keV) is very small compared to the $\frac{\hbar\omega_0}{2\pi}$ (~ MeV), taking Q = 0 is a good approximation [Lin84] equations (2-2-18) and (2-2-20) reduce to

$$\lambda_{\pm} = \pm F, \qquad P_{\pm} = \frac{1}{2}$$

The total transmission probability is simply equal to the sum of two transmission probabilities through two split barriers with the heights of $B_0 \pm F$. Thus

$$T = T_+ + T_-$$

$$= \frac{1}{2}\left[\{1 + \exp[\frac{2\pi}{\hbar\omega_0}(B_0 + F - E)]\}^{-1} + \{1 + \exp[\frac{2\pi}{\hbar\omega_0}(B_0 - F - E)]\}^{-1}\right]$$

Fig. 2-2-5, in panels a and b, illustrates the splitting of the barrier heights and the changes of the transmission function as a result of the coupling. The transmission function is mainly affected around the initial barrier B_0, T is increased in the region below the barrier B_0 and reduced above B_0. Panels c and d of this figure show the effects of a non zero Q- value on the transmission function and the weight factor $P_\pm$. In the case of positive Q-value both the effective barriers are at lower energies than in the case of Q = 0; however the weight factor P_- is reduced and the P_+ is increased. In the case of negative Q value the changes of effective barriers and the weight factors are all reversed compared with the case of positive Q-value. This gives us a picture of a distribution of discrete fusion barrier heights. The weight factors P_i may be interpreted as the probability of encountering the fusion barrier of height $B_0 + \lambda_i$. Details of the distribution of fusion barrier heights will be discussed in the next section.

In general, the entrance channel can couple to more than one reaction channel. The matrix M in Eq. (2-2-17) becomes NxN dimensional matrix [Das83a], where N is the number of reaction channels. There are N eigenvalues λ_i and hence N effective fusion barriers. Details of the N excited states of the reacting nuclei are required to uncouple the equations. The distribution of barriers

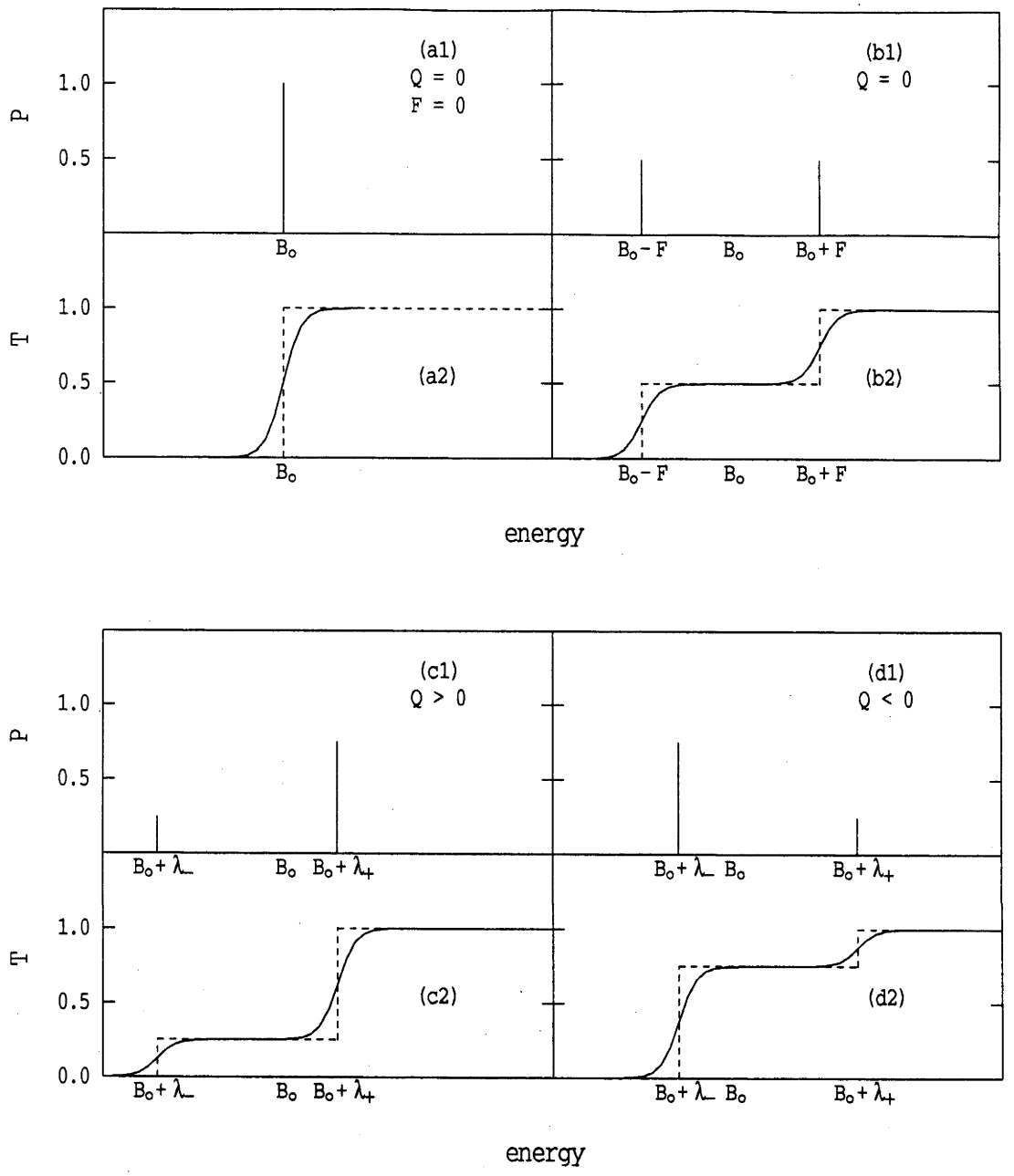

Fig. 2-2-5: Discrete barrier distributions resulting from coupling reaction channels. P indicates the probabilities of encountering the barriers during fusion and T illustrates the transmission coefficients (l = 0). See text for the details.

becomes more complicated as N increases. However, as pointed out [Bec88], there is always at least one negative eigenvalue, hence a lower barrier compared to B_0. Due to the exponential dependence of the transmission probability upon the energy difference (E - $B_0+\lambda_i$), at

sub-barrier energies, the net effects of the barrier splitting is always to enhance the sub-barrier fusion. It can be shown [Lan84] that the fusion cross-section at energies below the Coulomb barrier is enhanced, compared with that of no coupling, by a factor of

$$\sum_{i}^{N} P_i \exp(-\lambda_i \frac{2\pi}{\hbar\omega_0}) . \qquad (2\text{-}2\text{-}23)$$

At energies $E \gg B_0 + \lambda_i$, there is little effect on the total fusion cross-section resulting from the channel coupling, and the classical formula of (2-1-14) is again appropriate [Lin84].

2.3 FUSION BARRIER AND ANGULAR MOMENTUM DISTRIBUTIONS

Many different models have been proposed to explain sub-barrier fusion cross-sections. Some of the models may have quite different physics input and hence give different barrier distributions. The coupled channels approach, for example, gives a series of discrete fusion barriers, whilst static deformation and ZPM models give continuous barrier distributions. Some arbitrary barrier distributions, such as flat [Vaz74, Vaz78, Ste88, Ste89, Ste90, Ste91] and Gaussian [Rei85] distributions, have also been introduced at various times for specific reasons. Even though the barrier distribution predicted by different models is very different, they often yield similar cross-sections and reproduce the data within experimental uncertainties (typically ~10%). The question then arises as to whether the fusion excitation function carries all information about the fusion barrier distribution. Rowley et al [Row91, Row91a, Wei91a] published papers which demonstrated that the distribution of

fusion barriers can be determined uniquely from high precision experimental fusion excitation function at energies around the Coulomb barrier.

2.3.1 Fusion Barrier Distributions

As mentioned above Reisdorf et al, Vaz et al and Stelson et al introduced the concept of continuous barrier distributions in their analyses of the fusion cross-sections for heavy ion systems, the fusion cross-section, then, can be written as

$$\sigma(E) = \int_0^\infty \sigma(E,B)\, D(B)\, dB \qquad (2\text{-}3\text{-}1)$$

where $\sigma(E,B)$ is the cross-section for barrier B. For instance, $\sigma(E,B)$ can be taken from expression (2-2-7) in Wong model [Won73], or from the classical formula of Eq. (2-1-14) in sharp cut off model. The quantity D(B) is the barrier distribution, which represents the probability of encountering a barrier at height of B for the interacting nuclei, and

$$\int_0^\infty D(B)\, dB = 1 \qquad (2\text{-}3\text{-}2)$$

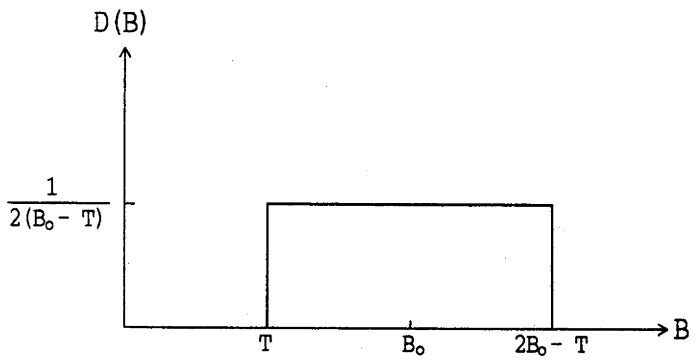

Fig. 2-3-1: Illustration of the "flat" barrier height distribution.

Fig 2-3-1 shows a flat barrier height distribution [Ste88, Ste89, Ste90, Ste91], and D(B) can be written as

$$D(B) = \begin{cases} \dfrac{1}{2(B_0 - T)} & T \le B \le 2B_0 - T \\ 0 & \text{elsewhere} \end{cases} \qquad (2\text{-}3\text{-}3)$$

Using the classical model, for given energy E, and barrier B we have

$$\sigma(E,B) = \begin{cases} \pi R^2 (1 - \dfrac{B}{E}) & E \ge B \\ 0 & E < B \end{cases} \qquad (2\text{-}3\text{-}4)$$

then the fusion cross-section is

$$\sigma(E) = \begin{cases} 0 & E < T \\ \dfrac{\pi R^2}{2(B_0 - T)} \displaystyle\int_T^E (1 - \frac{B}{E})\, dB = \frac{\pi R^2 (E - T)^2}{4(B_0 - T)E} & T \le E \le B_0 - T \\ \dfrac{\pi R^2}{2(B_0 - T)} \displaystyle\int_T^{2B_0 - T} (1 - \frac{B}{E})\, dB = \pi R^2 (1 - \frac{B_0}{E}) & E > 2B_0 - T \end{cases} \qquad (2\text{-}3\text{-}5)$$

which shows that at energies higher than $2B_0 - T$ the cross-sections revert to the classical expression of (2-1-14), and hence $E\sigma$ is linear to E. However, at energies around the Coulomb barrier, $T \le E \le 2B_0 - T$, the $\sqrt{E\sigma}$ is linear in E, not $E\sigma$. Thus

$$\sqrt{E\sigma} = \sqrt{\frac{\pi R^2}{4(B_0 - T)}}\,(E - T) \qquad (2\text{-}3\text{-}6)$$

Hence, if the experimental data $\sqrt{E\sigma}$ vs E is plotted around the barrier region (particularly cross-sections from ~10 mb to ~200 mb), T can be found from the zero intercept point of a straight line fit to the data. B_0

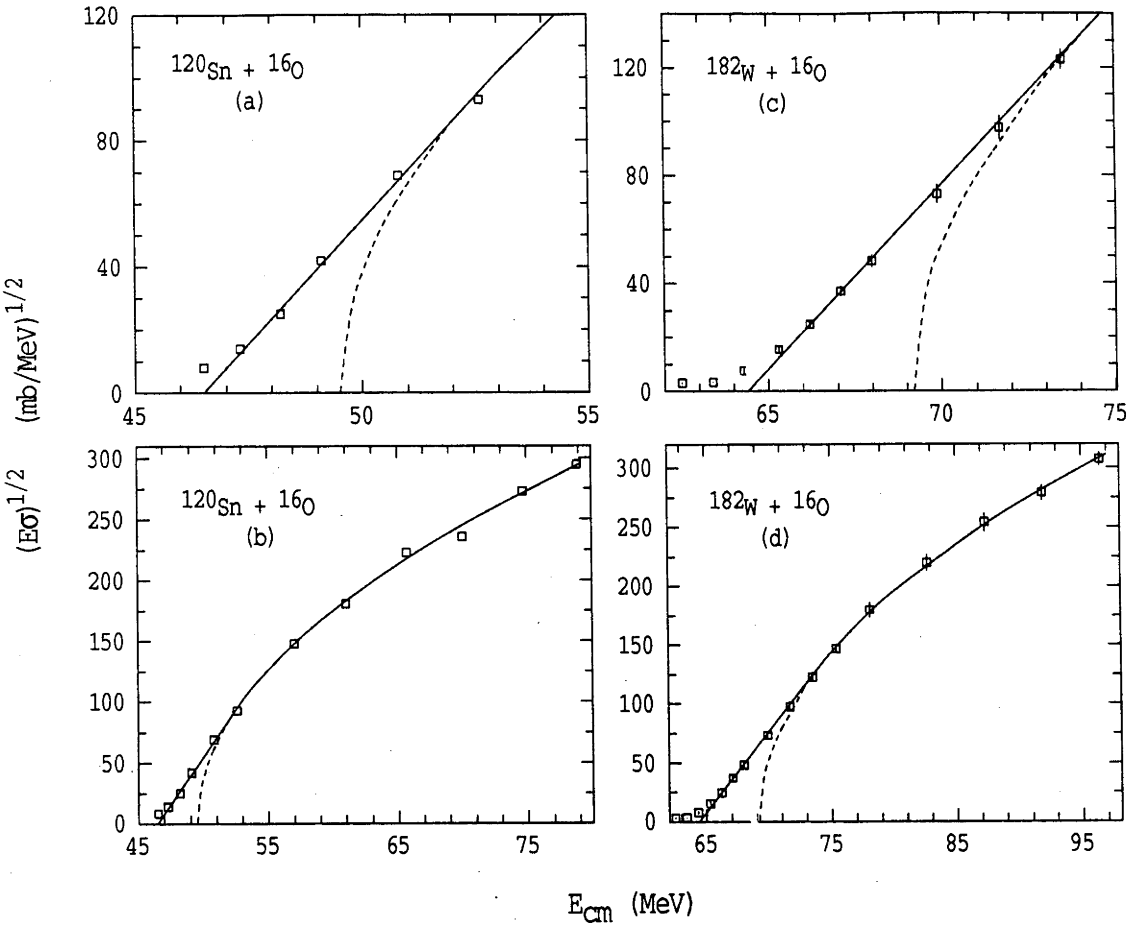

Fig. 2-3-2: plots of $(E\sigma)^{1/2}$ vs E for reactions of ^{120}Sn and ^{182}W + ^{16}O (adapted from [Ste91]). They show expanded views in the "barriers" regime. The solid lines show the calculations using "flat" barrier height distributions. The dashed curves show the calculations with a single barrier.

and R can be found at the energies well above the barrier as discussed in §2.1.

Fig 2-3-2 illustrates this approach to the fusion of ^{16}O + ^{120}Sn, ^{182}W, measured by Jacobs et al and Bemis et al [Jac86, Bem87]. One can see that the cross-sections calculated under the assumption of a flat distribution of barrier represent the data well in the region between

~10 mb to ~200 mb level. There are still large variations in the far sub-barrier region (< 10 mb). It may be due to the sharp cut off of the barrier distribution at the threshold energy T. A Gaussian modulation has been introduced [Ste90] to smooth the barrier distribution. Instead a single T there is a distribution, thus

$$M(T' - T) = (2\pi\Omega^2)^{-1/2}\exp[-\frac{(T' - T)^2}{2\Omega^2}] \qquad (2\text{-}3\text{-}7)$$

and

$$D(B) = \int_{-\infty}^{B} \frac{M(T' - T)}{2(B_0 - T')}\, dT' \qquad (2\text{-}3\text{-}8)$$

where T is obtained from expression (2-3-6) described above, and Ω is the width of the modulation to be adjusted to fit the data. When $\Omega \rightarrow 0$, $D(B) \rightarrow 1/2(B_0 - T)$ reduces to the flat barrier distribution expression (2-3-4).

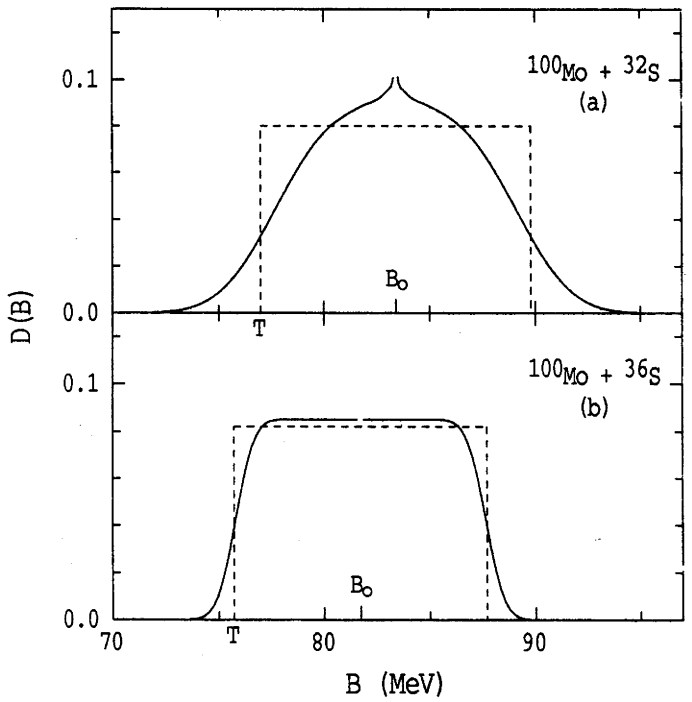

Fig. 2-3-3: Flat (dashed lines) and modulated flat (solid curves) barrier height distributions for the reactions of ^{100}Mo + ^{32}S and ^{36}S (adapted from [Row91]).

Fig. 2-3-3 shows the modulated flat barrier distribution with which the calculated cross-sections fit the experimental data (~10%) for the reactions of $^{32,36}S + {}^{100}Mo$ [Pen83].

Using the modulated flat barrier distributions, Stelson et al successfully reproduced the fusion cross-sections for a number of reactions [Ste90]. However, as they pointed out in their paper, some other barrier distributions, such as a Gaussian distribution or the classical distribution resulting from static deformation, fit the data equally well.

2.3.2 Experimental Determination of The Distribution of Fusion Barrier Heights

Starting with the classical model [Row91, Row91a], see equation (2-1-15), with a distribution of barriers, one obtains

$$E\sigma(E) = \pi R^2 \int_0^E (E - B)\, D(B)\, dB \qquad (2\text{-}3\text{-}9)$$

Differentiating both sides of the above equation with respect to E, we get

$$\frac{d(E\sigma)}{dE} = \pi R^2 \int_0^E D(B)\, dB \qquad (2\text{-}3\text{-}10)$$

Differentiating again, we get

$$\frac{d^2(E\sigma)}{dE^2} = \pi R^2\, D(E) \qquad (2\text{-}3\text{-}11)$$

or

$$\frac{1}{\pi R^2}\,\frac{d^2(E\sigma)}{dE^2} = D(E) \qquad (2\text{-}3\text{-}11a)$$

This tells us that the barrier distribution can be found if the fusion excitation function is known. In other words the probabilities of encountering a barrier B can be determined by the second derivative of $E\sigma$ at energy $E = B$.

For the simple case of a single barrier B_0, the cross-section is given by Eq. (2-1-14) for energies higher than B_0, and is zero for energy less than B_0, we have

$$\frac{d(E\sigma)}{dE} = \begin{cases} \pi R^2 & E \geq B_0 \\ 0 & E < B_0 \end{cases} \qquad (2\text{-}3\text{-}12)$$

then

$$\frac{1}{\pi R^2}\frac{d^2(E\sigma)}{dE^2} = \delta(E - B_0) \qquad (2\text{-}3\text{-}13)$$

hence

$$D(E) = \delta(E - B_0) \qquad (2\text{-}3\text{-}14)$$

which obviously represents the barrier distribution in this single barrier case.

It has been shown [Row91, Row91a] that the above consideration can easily be extended to a set of discrete barriers, thus

$$\frac{1}{\pi R^2}\frac{d^2(E\sigma)}{dE^2} = \sum_i w_i \delta(E - B_i) \qquad (2\text{-}3\text{-}15)$$

and

$$\sum_i w_i = 1 \qquad (2\text{-}3\text{-}16)$$

where w_i are the probabilities of encountering fusion barrier heights B_i, and the D(B) can be written as

$$D(B) = \sum_i w_i \delta(B - B_i) \qquad (2\text{-}3\text{-}17)$$

Thus in the simple sharp cut off model the double differential of $E\sigma$ reproduces the discrete set of barriers.

Fig. 2-3-4 illustrates the above procedure of determining the barrier distribution in the simple cases; one barrier (left panel) and two barriers (right panel) with equal weight.

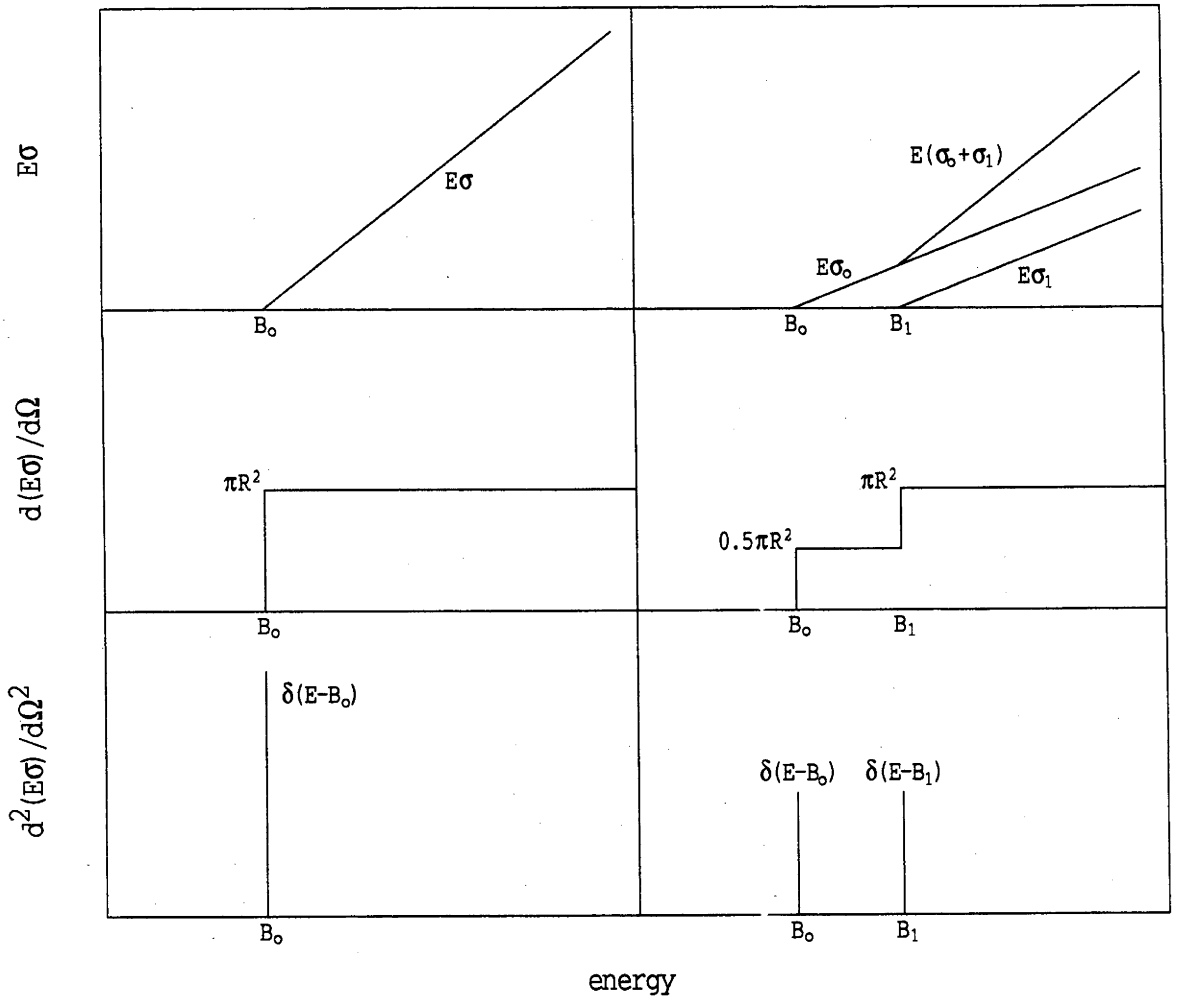

Fig. 2-3-4: In the sharp cutoff model the barrier height distributions can be extracted [Row91a].

However, the above did not consider barrier penetration effects, which smooths the function $\frac{d^2(E\sigma)}{dE^2}$.

Starting with the cross-section expression (2-2-7) of Wong model which considered the quantum tunnelling, we now obtain

$$\frac{1}{\pi R^2}\frac{d^2(E\sigma)}{dE^2} = G(x) = (\frac{2\pi}{\hbar\omega})\frac{e^x}{(1+e^x)^2} \qquad (2\text{-}3\text{-}18)$$

where

$$x = \frac{2\pi}{\hbar\omega}(E - B) \qquad (2\text{-}3\text{-}19)$$

It can be shown that

$$\int_0^\infty G(x)\,dx = 1$$

and when $\hbar\omega \rightarrow 0$, the $G(x) \rightarrow \delta(E - B)$, hence the expression (2-3-18) becomes the sharp cut off expression (2-3-13). Fig. 2-3-5 shows G(x) for

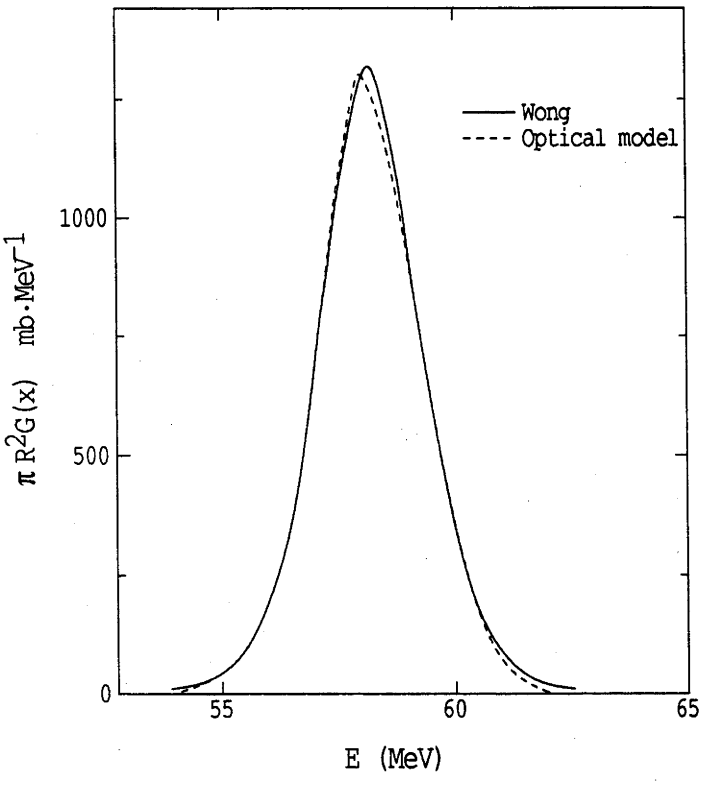

Fig. 2-3-5: The single barrier height distribution has been smoothed by barrier penetration (adapted from [Row91a]).

the reaction of $^{32}S + ^{64}Ni$. From this figure one can see that the δ distribution of the single barrier has been smeared by quantum tunnelling over an energy region with a FWHM of $0.56\hbar\omega$.

For a distribution of barriers, the σ is given by the Eq. (2-3-1), then the second derivative of $E\sigma$ gives

$$\frac{1}{\pi R^2}\frac{d^2(E\sigma)}{dE^2} = \bar{D}(E) = \int_0^\infty G(x)\, D(B)\, dB \qquad (2\text{-}3\text{-}20)$$

where $\bar{D}(E)$ is barrier height distribution smoothed by quantum tunnelling.

In terms of the discrete barrier height distribution

$$\bar{D}(E) = \sum_i w_i\, G(x_i) \qquad (2\text{-}3\text{-}21)$$

where

$$x_i = \frac{2\pi}{\hbar\omega}(E - B_i) \qquad (2\text{-}3\text{-}22)$$

Hence, the smoothed barrier height distribution $\bar{D}(E)$ can be extracted directly if the fusion excitation function is known.

Rowley et al have extracted the barrier height distribution for fusion of $^{154}Sm + ^{16}O$, using the data measured by Stokstad et al [Sto80]. This is illustrated in Fig. 2-3-6 along with the calculated barrier height distributions, derived from coupled channels and classical static deformation models. One can see that the barrier distribution of the smoothed three-channel coupling approaches the classical one. More generally, Nagarajan et al [Nag86] have shown that, in the limit of including all members of rotational band, the coupled channel model

gives the same barrier distribution as that from the classical static deformation model.

However, as pointed out in [Wei91a], to extract the barrier height distribution with sufficient accuracy requires high statistical accuracy together with small, precisely determined energy steps. A comparison of the extracted barrier height distributions for reactions of $^{154}Sm + ^{16}O$ from two sets of fusion data with different precisions and energy steps is illustrated in Fig. 2-3-7. The errors on the points in (a) and (b) are associated with random error of ~5% and ~1% respectively [Sto80, Wei91a]. The fusion data used in (a) and (b) were

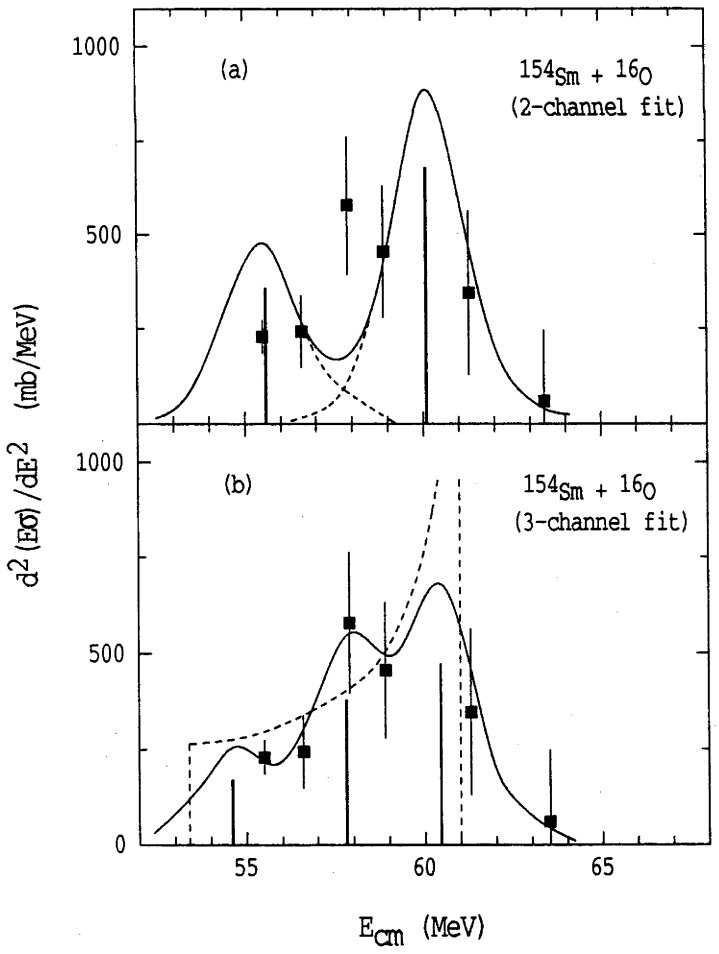

Fig. 2-3-6: Calculated fusion barrier height distributions compared with the experimental value of $d^2(E\sigma)/dE^2$ (adapted from [Row91]). (a), the two-coupled-channel; (b), the three coupled-channel (solid curve) and classical barrier distribution (dashed curve) due to the static deformation of the target ^{154}Sm.

measured in energy steps of 2 to 10 MeV, and 0.5 MeV in Lab respectively. A clearly asymmetric barrier height distribution is shown in (b), whilst in (a) a number of different distributions with different shapes, flat, Gaussian and asymmetric can fit the data equally well within the errors. Details of the requirements of fusion data to extract the barrier height distribution will be given in Chapter 4.

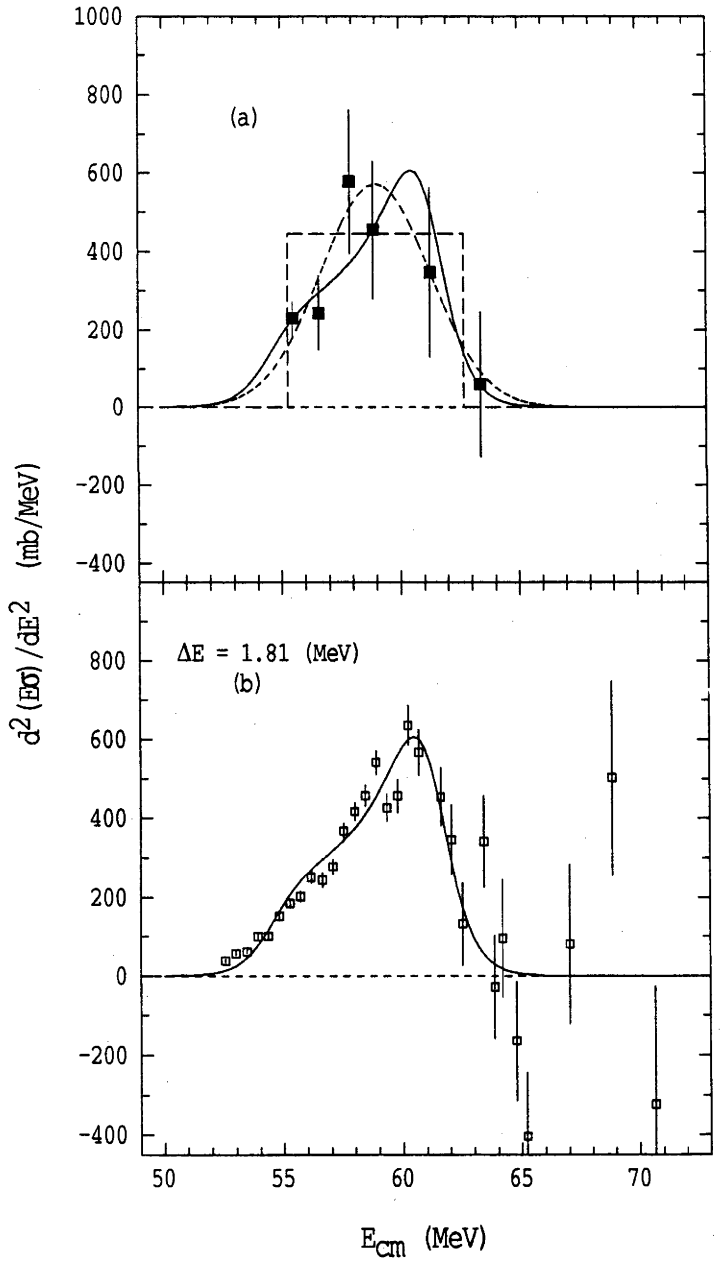

Fig. 2-3-7: (a), experimental barrier height distributions, $d^2(E\sigma)/dE^2$, for $^{154}Sm + ^{16}O$ (adapted from [Row91]). (b), $d^2(E\sigma)/dE^2$, extracted from newly measured excitation function of this reaction in this work [Wei91a]. See text for the details of theoretical explanation.

2.3.3 Fusion Angular Momentum Distributions

Different fusion models predicted different angular momentum distributions. For instance, in the sharp cut off model, as discussed in §2.12, the angular momentum is sharply cut and the distribution is a triangular, whereas in the Wong model the edge of the triangle is smoothed due to the penetration of the fusion barrier (see Fig. 2-3-8).

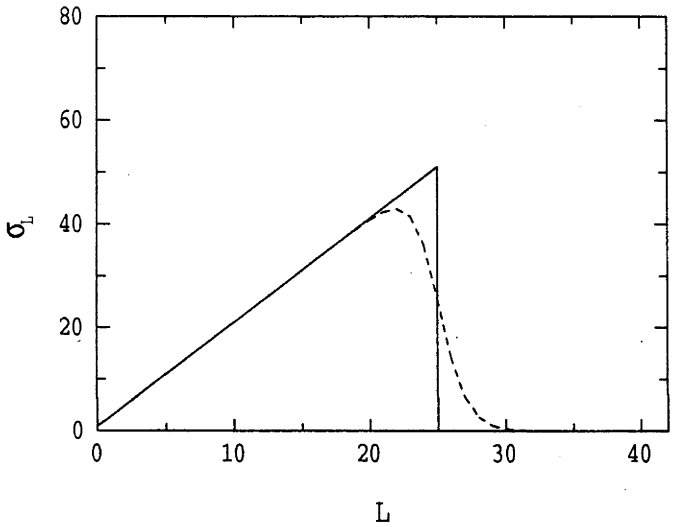

Fig. 2-3-8: Calculated partial-wave distributions in sharp cutoff model (solid line), and with the barrier penetration (dashed line).

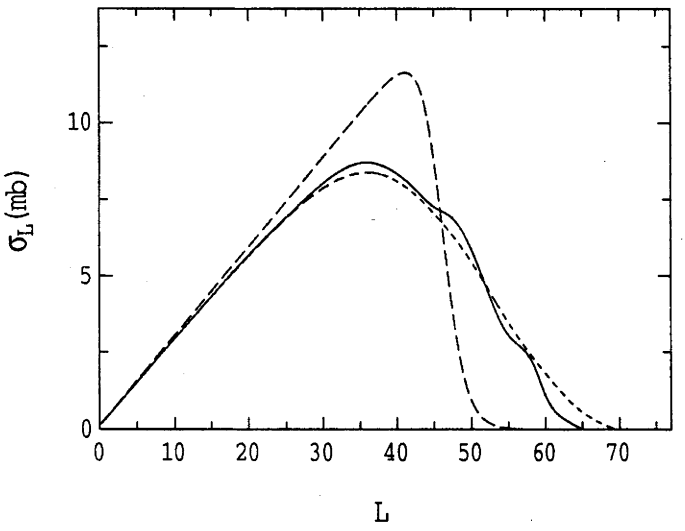

Fig. 2-3-9: Calculated partial-wave distributions for fusion of $^{144}Sm + ^{40}Ar$ at incident energy of 178.9 MeV with different models: coupled-channels (solid line), WKB with a Gaussian barrier distribution (dashed line) and WKB without barrier fluctuation or coupling (dotted line). All the calculations yield the same fusion cross-section of 330 mb. Adapted from [Rei85].

This smoothing results in higher angular momentum being brought into the fused system, which may substantially change the decay mode of the CN; for example, the probability of fission can be increased significantly [Cha86, New88]. However, for a given bombarding energy, the fusion cross-section may be equally well reproduced by a number of fusion models with different fusion angular momentum distributions. Shown in Fig. 2-3-9 are the calculated fusion angular momentum distributions with different models for the reaction of $^{40}Ar + ^{144}Sm$ at the energy of 178.9 MeV and all the models yield about the same total fusion cross-section of 330 mb. Therefore, it has been generally considered that angular momentum distribution provide a much more sensitive test of the models [Wuo91].

However, it should be noticed that if a complete excitation function is available the range of applicable models is restricted and became more restricted for high precision data.

2.3.4 Experimental Determination of Angular Momentum Distributions of Fusion

Considerable effort has been invested in determining fusion angular momentum distributions experimentally, through measurements of γ-ray multiplicities [Wuo91, Van83, Gil85, Gil90, Lei86], isomer ratios [DiG90], fission fragment angular distributions [Van86, Mur86, Bac85], α-particle angular distributions [Bor86] and elastic scattering [Lei86, Kon87, Uda85].

However, none of the above methods directly yields the spin distribution in fusion. For instance, the first two measure properties of evaporation residues, after several particles have been emitted.

There are also problems in converting γ-ray multiplicities into angular momenta. The fission and α-decay studies measure only a part of the CN decay, and again (as discussed below) rely on models to interpret the angular distribution. Details of the decay processes are, therefore, required in the transformation of measured data to the fusion angular momentum (usually the mean values $<l>$ and $<l^2>$). For instance, to obtain the $<l^2>$ from the measured fission fragment angular distributions W(θ), the following expression of standard transition-state theory is used

$$\frac{W(180°)}{W(90°)} \simeq 1 + \frac{<l^2>}{4K_0^2} \qquad (2\text{-}3\text{-}23)$$

where the K_0 is the width of the distribution of the spin projection along the symmetry axis. However, this can only determine the ratio of $<l^2>/K_0^2$. To deduce $<l^2>$ one has to assume, or otherwise determine, a value for K_0^2 which is dependent on the fusion-fission decay process at the saddle point (or alternatively to deduce the K_0^2 by assuming a value of $<l^2>$). Since the extraction of the angular momentum depends on K_0, which depends on the temperature of CN, details of the dynamical process of fission are then required. For example, the number of particles emitted before fission, which is often determined by the nuclear viscosity, affects the temperature. Strictly speaking, this method does not deduce the angular momentum brought into the compound nucleus in fusion but the angular momentum at the saddle point just before fission. This method, of course, is only valid when fission is the dominant decay process. Similarly, the methods of measuring γ-ray multiplicities and isomer ratios relate to the angular momenta of the residues, and are only valid when the fusion-evaporation decay process is dominant.

The method of deducing the fusion angular momentum distribution from elastic scattering does not rely on the decay channels. However, it measures the total reaction cross-section, including quasi-elastic processes in addition to fusion. The reduced l-distribution thus also includes the effect of peripheral collisions. To deduce the angular momentum of fusion, an assumption that the shapes of fusion l-distribution and the total reaction l-distribution are the same has to be taken. Uncertainty in the fusion l-distribution is again introduced by this assumption.

Another method, introduced by [Bal83, Rei85, Bal86, Das86], is to deduce the fusion angular momentum distribution directly from fusion excitation functions. Even though this method was proposed a number of years ago, it has not been successfully used because of a lack of fusion data with sufficient high precision [Rei85]. Details of this method are given as follows.

Starting with the expression (2-1-10) for the fusion cross-section at centre of mass energy E, the first derivative of $E\sigma$ with respect to E is

$$\frac{d(E\sigma)}{dE} = \frac{\hbar^2}{2\mu}\int_0^\infty (2l+1)\frac{dT_l(E)}{dE}\,dl \qquad (2\text{-}3\text{-}24)$$

where the sum in expression (2-1-10) has been replaced by an integral.

Now consider $dT_l(E)/dE$. Notice that for a given l the transmission coefficient depends on energy E, and the variables E and l in $T_l(E)$ are correlated to some degree. For instance, in the sharp cut-off model, the transmission coefficients are determined only by constant Δ, the difference between the incident energy and the height of the l-dependent barrier:

$$\Delta = B_l - E = B_0 + \frac{l(l+1)\hbar^2}{2\mu R^2} - E \qquad (2\text{-}3\text{-}25)$$

When $\Delta > 0$, $T_l(E) = 0$, for $\Delta \leq 0$, $T_l(E) = 1$, as shown in Eq. (2-1-11).

In a more general case, for example, in the WKB approximation, $T_l(E)$ can be written as

$$T_l(E) = \frac{1}{1 + \exp\left(\mp \int_{r_a}^{r_b} \sqrt{\frac{2\mu}{\hbar^2} |\Delta(r)|}\, dr\right)} \qquad (2\text{-}3\text{-}26)$$

where

$$\Delta(r) \simeq V_0(r) + \frac{l(l+1)\hbar^2}{2\mu r^2} - E \qquad (2\text{-}3\text{-}27)$$

If we assume that there is only a constant term $\frac{l(l+1)\hbar^2}{2\mu R^2}$ relating B_l to B_0, in other words, the shape of the potential and position of barrier are independent of l, we get

$$\Delta_l(r,E) = V_0(r) + \frac{l(l+1)\hbar^2}{2\mu R^2} - E \qquad (2\text{-}3\text{-}28)$$

and

$$\frac{dT_l(E)}{dE} = \frac{dT_l(E)}{d\Delta_l(r,E)} \frac{d\Delta_l(r,E)}{dE} = -\frac{dT_l(E)}{d\Delta_l(r,E)} \qquad (2\text{-}3\text{-}29)$$

and

$$\frac{dT_l(E)}{dl} = \frac{dT_l(E)}{d\Delta_l(r,E)} \frac{d\Delta_l(r,E)}{dl} = \frac{(2l+1)\hbar^2}{2\mu R^2} \frac{dT_l(E)}{d\Delta_l(r,E)} \qquad (2\text{-}3\text{-}30)$$

From (2-3-29), (2-3-30) we have

$$\frac{dT_l(E)}{dE} = -\frac{2\mu R^2}{(2l+1)\hbar^2} \frac{dT_l(E)}{dl} \qquad (2\text{-}3\text{-}31)$$

Inserting this in (2-3-24), we get

$$\frac{d(E\sigma)}{dE} = -\pi R^2 \int_{l=0}^{l=\infty} dT_l(E) \qquad (2\text{-}3\text{-}32)$$

since $T_\infty = 0$, we obtain

$$\frac{d(E\sigma)}{dE} = \pi R^2 T_0(E) \qquad (2\text{-}3\text{-}33)$$

Since this expression holds for any barrier, in a situation where a distribution of barriers is involved and the fusion radius changes with barrier, the gradient of the measured function $E\sigma$ determines the average transmission coefficient and the fusion radii, for $l = 0$, thus

$$\frac{d(E\sigma)}{dE} = \int_0^\infty \pi R^2(B)\, T_0(B,E)\, D(B)\, dB = \pi \overline{R^2 T_0}(E) \qquad (2\text{-}3\text{-}34)$$

If one assumes that the R does not change with the barrier, which is approximately true for spherical interacting nuclei, then

$$\frac{d(E\sigma)}{dE} = \pi R^2\, \overline{T}_0(E) \qquad (2\text{-}3\text{-}35)$$

Thus the average of $\overline{T}_0(E)$ can be determined from the measured fusion cross-section data.

For deformed nuclei, the assumption made above is incorrect because the barrier heights and the fusion radii change with the orientations of the interacting nuclei. For instance, in the reaction $^{154}Sm + ^{16}O$, the estimated changes of the fusion radii range from +1.5 fm and -0.5 fm compared with the average fusion radius of ~10.56 fm (details of these estimates are given in Chapter 5). The maximum error

estimated in the above case would be ~30% on $\overline{T}_0(E)$. However, this is only for the extreme case, and it only occurs when the energy is far lower than the Coulomb barrier, when only the lowest barrier, hence the largest fusion radius contributes to the fusion. In the region of energy well above the barriers the $T_0(E) \sim 1$ and expression (2-3-34) gives the average fusion radius $\overline{R^2}$.

Fig.2-3-10 shows the $\overline{T}_0(E)$ extracted from a recent measurement of the fusion excitation functions [Wei91a] for the reaction $^{154}Sm + ^{16}O$. The

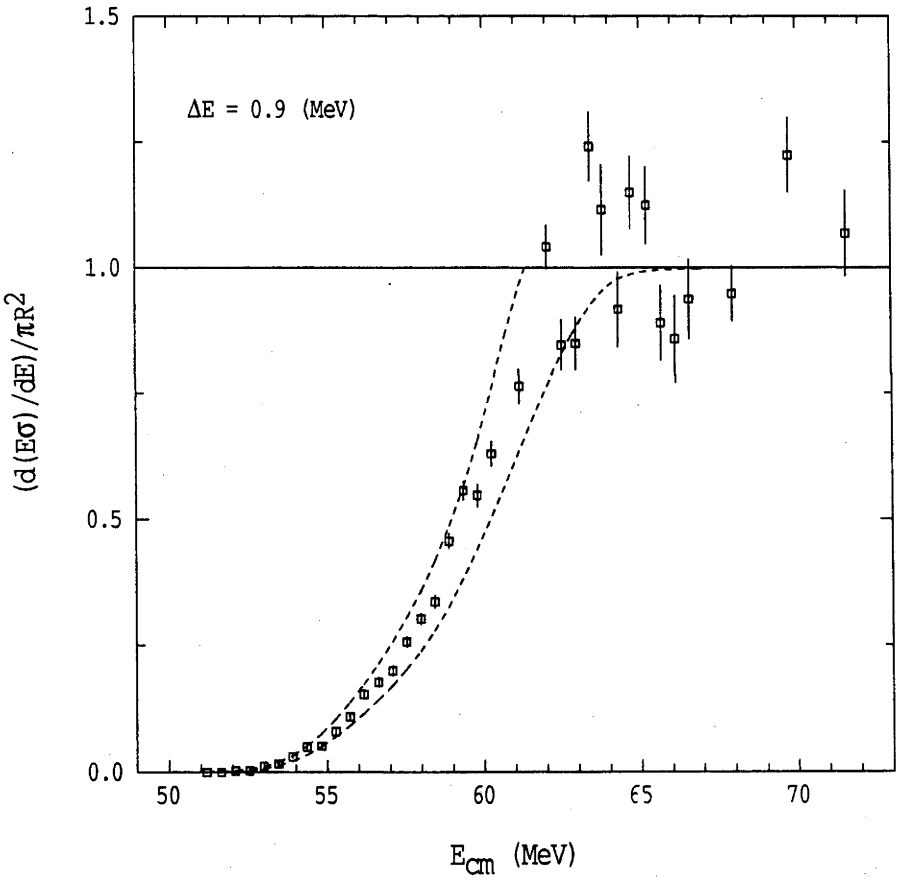

Fig. 2-3-10: Values of T_0 $(d(E\sigma)/dE/\pi R^2)$ extracted from newly measured fusion cross-sections in this work. The dashed curves indicated the maximum error of ±30% in the extracted T_0, reflected the maximum uncertainty of 15% in R used in the extraction.

uncertainty of ±30% for this case is also shown in this figure by the dashed lines in the barrier region.

An important aspect of this method is the ability to extract the full fusion l-distribution from the data. The l-dependence of the average transmission coefficients at fixed energy $\overline{T}_l(E)$ can be simply extracted making use of equation (2-3-26); thus

$$\overline{T}_l(E) \simeq \overline{T}_0\left(E - \frac{l(l+1)\hbar^2}{2\mu R^2}\right) \tag{2-3-36}$$

Therefore, the fusion l-distribution for any E can be determined if the excitation function, and hence $\overline{T}_0$, is measured over an appropriate range in

$$E' = E - \frac{l(l+1)\hbar^2}{2\mu R^2}. \tag{2-3-37}$$

Knowing the transmission coefficients $\overline{T}_l(E)$, the $\langle l \rangle$ and $\langle l(l+1) \rangle$ can be calculated, thus

$$\langle l \rangle = \frac{\hbar^2}{2\mu E\sigma} \int_0^\infty l\,(2l+1)\,T_l(E)\,dl \tag{2-3-38}$$

and

$$\langle l(l+1) \rangle = \frac{\hbar^2}{2\mu E\sigma} \int_0^\infty l(l+1)\,(2l+1)\,T_l(E)\,dl \tag{2-3-39}$$

It can be shown that simple analytical expressions can be obtained for $\langle l \rangle$ and $\langle l(l+1) \rangle$,

$$\langle l \rangle = \frac{\mu R^2}{\hbar^2 E\sigma} \int_0^E \frac{E'\sigma(E')}{\sqrt{\frac{2\mu R^2}{\hbar^2}(E - E') + \frac{1}{4}}}\,dE' \tag{2-3-40}$$

and

$$\langle l(l+1)\rangle = \frac{2\mu R^2}{\hbar^2 E\sigma}\int_0^E E'\sigma(E')\,dE' \qquad (2\text{-}3\text{-}41)$$

Details of the extraction of fusion angular momentum distributions from the fusion data and the uncertainty of this method will be discussed further in Chapter 5.

Chapter 3
Experimental Methods

The experiments in this work were performed at the ANU, Department of Nuclear Physics. Heavy ion beams of ^{16}O were accelerated by the 14 UD Pelletron tandem electrostatic accelerator, and were used to irradiate targets of ^{154}Sm and ^{186}W. The fusion of these reactions was studied with the energy range of the beam particles from 58 MeV up to 110 MeV in the lab system.

Measurement of the fusion reaction products involved the detection and identification of particles. The principles of the detector operation and the techniques of product identification and separation are described in the first three sections. The specific experimental apparatus and the experimental methods used in this work are described in §3.4 and §3.5 respectively.

3.1 THEORY OF DETECTOR OPERATION

It is common in nuclear physics to detect particles by the ionization produced in selected materials. To collect the resultant charge an electric field must be applied across these materials, which may be in a solid, liquid or a gaseous state. They require, however, the following two characteristics: 1. they must be free of charge carriers; 2. charges created by ionization should be capable of rapid and easy movement

toward the electrodes without recombination and trapping. Thus, solid metals or insulators cannot be used for this purpose because the two features do not simultaneously exist in either of them.

Semiconductors and gases are found to be amongst the best materials to use in detectors. Two common types are the Si surface barrier detector (SSB) and the gas ionization chamber, and both were used in this work. The basic theory of their operation together with the details of their construction, where appropriate, will be described.

3.1.1 Silicon Surface-Barrier Detectors

A Si surface-barrier (SSB) detector consists of a p-n junction (see for example Fig. 3-1-1). In this junction the charge carriers have been completely removed and a strong electric field established. The junction region is therefore a perfect charge-carrier-free region and is used to detect the energetic and ionising particles. When a reversed bias, V, is applied across the junction, this depleted region is extended. For a thin detector, the extended region could be across the whole depth of the detector. Electron-hole pairs, which are created by the passage of an ionising particle, are quickly swept out of this region, giving a rapidly rising output pulse from the detector, with excellent timing properties. The average energy needed to create an electron-hole pair is very small (about 3.6 eV). Good energy resolution (about 16 keV for 5.4 MeV α-particles [Eng74]) is obtained in this detector because of the high statistical accuracy of the collected charge, resulting from a large number of electron-hole pairs created by the incident charged particle. The height of the pulse is proportional to the energy loss of the particle in the depletion

region. Because of the high stopping power the detector can be made very thin. For instance, for a 5 MeV α-particle in Si the stopping power is ~0.6 MeV/(mg/cm^2) and the stopping range is ~6 mg/cm^2 [Nor70]. Typically detectors can be made varying from 20 μm to several mm in thickness. Energetic charged particles can pass through, or stop in, the detector depending on its thickness and the energy of the particles.

Si detectors are widely used owing to their excellent energy resolution, linear response to the charged particle's energy, compact size, wide range of thickness, the ability to produce very thin energy loss detectors and their ease of operation in vacuum of the scattering chamber.

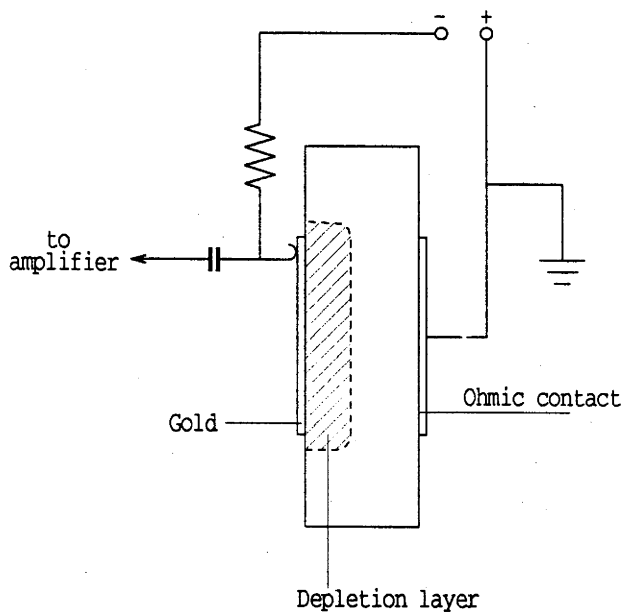

Fig. 3-1-1: Schematic representation of a surface barrier silicon detector (adapted from [Coc68]).

However, there are also some disadvantages with this type of detector. One of the disadvantages which affected the application in this work is the degradation of the detector performance after exposure to intense radiation. Typically exposure to ~10^7/cm^2 heavy ion particles [Mar78, Eng74]) results in the deterioration of the energy and time resolution accompanied by an increase in leakage current. For this reason the SSB detectors cannot be used effectively at angles close to the beam direction because of the intense elastic scattering.

All SSB detectors used in this work were manufactured at the ANU, following the prescription of England [Eng74]. The thickness of these detectors was 200 μm, which was sufficient to stop all the species of interest.

3.1.2 Gas Ionization Chamber

Fig. 3-1-2 is a representation of a simple parallel-plate ionization chamber. Electrons which have been produced by the passage of a charged particle through the sensitive gas volume are detected. The electric field, which separates the electrons and positive ion pairs, is normally either parallel or perpendicular to the particle's trajectory. The strength of the field is high enough to move the electrons before recombination with the positive ions can take place and low enough that an electron cannot gain sufficient energy to ionize the gas. Fig. 3-1-3 shows how the signal size varies with the applied voltage. Ionization chambers operate in the flat plateau of the voltage independent region. Because positive ions are much heavier than electrons, they drift much more slowly. It takes about a hundred times longer to collect the positive ions than the electrons. Ionization

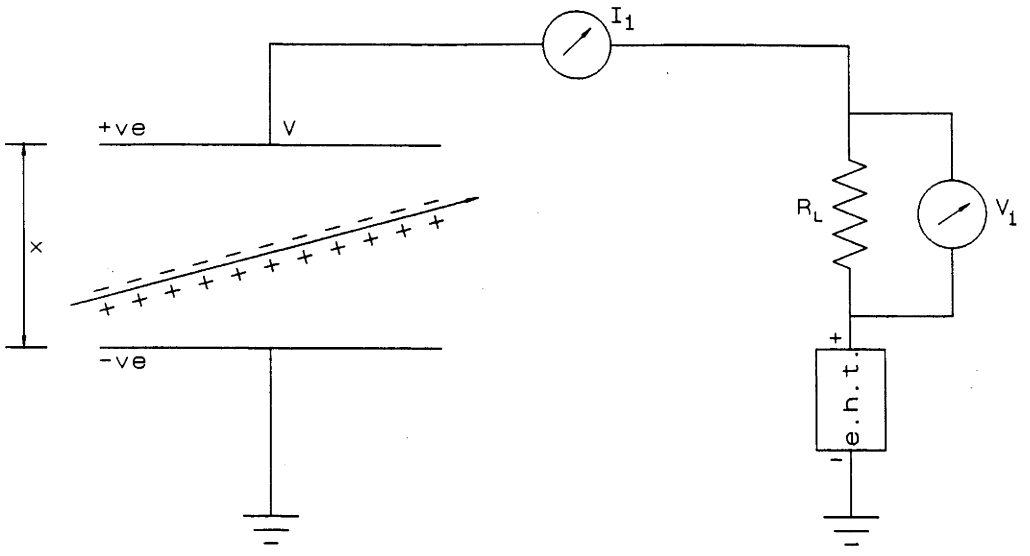

Fig. 3-1-2: Illustration of a simple parallel plate ionization chamber (adapted from [Eng74]).

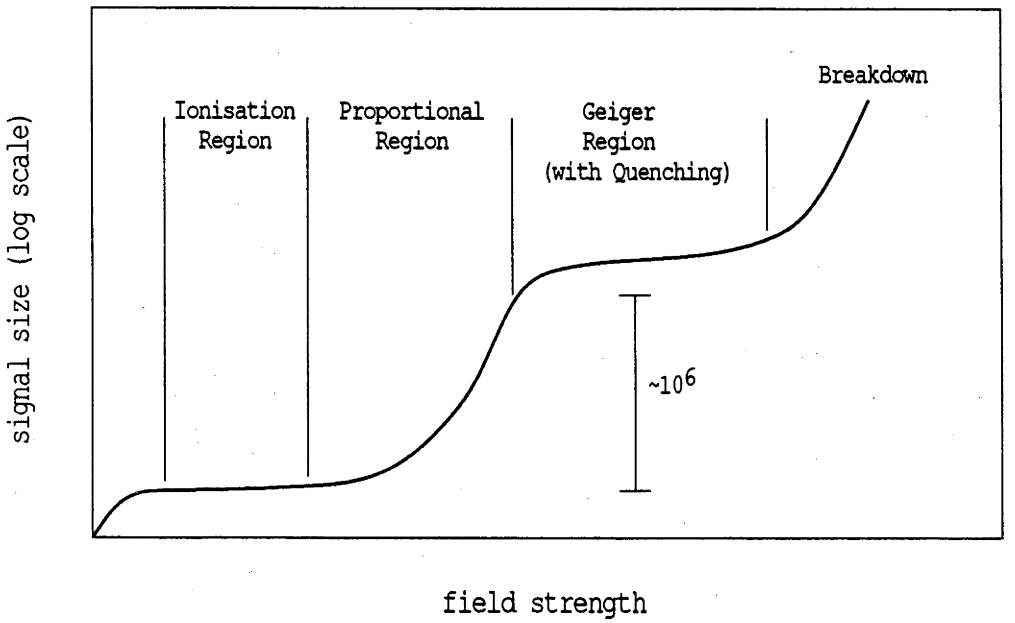

Fig. 3-1-3: Variation of signal size with applied voltage in a parallel plate ionization chamber (adapted from [Eng74]).

counters are, therefore, often operated in pulse mode. Only the fast component of the output current, due to the motion of the electrons, is utilized. However, the pulse height of the electron component of the induced signal, measured in the external circuit, is proportional to the drift distance of the electrons in the field, hence, the pulse height is dependent on the position of the particle track in the detector. This deteriorates the energy resolution. A solution to this problem was found by placing a Frisch grid [Bun49] across the detector which screens the anode from the area between grid and cathode. In this way the induced charge is due only to the motion of electrons between the grid and the anode. The pulse height is then independent of the particle track position.

The signal on the anode of an ionization chamber from a charged particle is dependent on the number of primary electrons produced. Charged particles not only lose kinetic energy from ionisation but also from excitation of gas molecules. Therefore the relationship between the output pulse height and the energy loss of the charged particle in the gas depends on the competition between the ionisation and excitation processes. However, it turns out that, to a high degree of accuracy, the number of electrons produced depends linearly on the energy loss of the particle in the gas, if the particle energy is higher than a few hundred keV [Ste83]. This linear response to the energy loss of a charged particle means that there is a fixed mean energy required to create one electron-ion pair. Therefore, the output pulse height is proportional to the energy deposited in the gas by the charged particles. On the average, the amount of energy needed to create an electron-ion pair in isobutane gas is about 30 eV. Energy resolutions

of 0.7% (FWHM) have been routinely achieved by using ionisation chambers [Ste83].

3.1.3 Gas Proportional Counter

As the electric field increases in an ionisation chamber the electrons gain more energy between collisions. Once this energy is sufficient to ionize the gas, electron multiplication takes place and a Townsend avalanche is created. The detector works in the avalanche manner in the proportional region, as shown on Fig. 3-1-3. The gas amplification is dependent on the field and can be substantial (up to 10^6). The output of the pulse is still proportional to the energy deposited in the gas by the particles but the charge collected is the product of the multiplication factor and the primary charge created by the particles. This type of detector is therefore called a gas proportional counter. Because of the multiplication, the minimum energy deposited into the gas, required to create a sufficiently large output pulse to be identified from the noise, is much reduced compared with that required in the ionisation detector. Since the energy loss of a particle in the chamber is related to the ionisation path and the gas pressure, the pressure and the path length in a proportional counter could be significantly reduced compared with that of ionisation counter. It turns out that in the proportional counter a few Torr of isobutane and a few mm of ionisation path is sufficient to detect energetic heavy ions (such as the ones of interest in this work). The counter, therefore, can be made very thin (low gas pressure and thin entrance window) so that the particles can easily pass though it. This feature has been frequently utilised in the timing measurements. Detail of this feature and the principle of the detector will be discussed below.

PARALLEL PLATE AVALANCHE COUNTER (PPAC)

One type of gas proportional chamber is the parallel plate avalanche counter consisting of two parallel plate electrodes just a few mm apart. These parallel plates are often made of thin metallized plastic foils. The particles enter the PPAC perpendicular to the plates. The rise time, corresponding to the collection time of the the electrons in the sensitive volume of the detector, is related to the drift velocity of the electrons. A high drift velocity is achieved in PPAC by using a high electric field, E, and a low gas pressure, p, in other words a high reduced electric field, E/p (values of E/p are typically a few hundred V/cm/Torr). These rapidly moving electrons form the fast component of the output pulse in an external circuit, rise times of a few ns being easily obtained. Because of the excellent time resolution, easy transmission of the particle, simple design and operation of this detector, it has been widely used as a start detector in time of flight measurements for particle identification.

MULTIWIRE PROPORTIONAL COUNTER (MWPC)

To further reduce the total thickness of a PPAC one of the electrodes or both of them could be replaced by one or two thin wire planes [Lei81]. This detector, which was first introduced by Charpak in 1968 [Cha68], is called a multiwire proportional counter.

The wire plane is normally made of wire 10 ~ 20 μm in diameter spaced by 1 ~ 2 mm. The typical distance between two electrodes is 3 mm. By applying a potential to the wire plane, the electric field across the gap in the vicinity of the wire varies approximately as the inverse of the distance, r, from the centre of the wire. The electric field

becomes essentially constant at a distance of a few tenths of a millimetre from the wire plane [Bre77a]. The field close to the surface of the wires can be about two orders of magnitude higher than that in the constant region. Different gas multiplication processes may occur in the vicinity of the anode compared to the constant field region.

At higher gas pressures, resulting in lower attainable reduced electric fields (E/p) in the constant region, the electrons released in the gap by ionizing particles slowly drift towards the anode wires, and start an amplification process only when the field strength allows them to undergo inelastic collisions with the gas molecules - therefore in the region of the wires. The collection time of the electrons depends on their initial positions and takes several tens of nanoseconds, depending on the drift velocity in the particular gas.

At low gas pressures (about 1 ~ 5 Torr) the reduced electric field strength in the constant field region reaches values of several hundreds of V/cm/Torr, which is very close to that reached in PPACs operating with the same gases and pressures [Bre77, Bre82]. Electrons released in the sensitive volume can gain enough energy to start an avalanche in the constant field region [Maz83, Bre79]; a second amplification step occurs when the electron swarm reaches the wires. Because the multiplication of the primary electrons varies exponentially with the distance from the anode to the position where the primary electrons were created, these primary electrons will be multiplied by different factors for differing initial positions. Taking this into account, Mazor and Ribrag did a calculation [Maz83] which shows that 90% of the signal observed on the anode comes from the primary electrons originating in the first 8% of the distance from the cathode to the anode. In most cases, the primary electrons released

on the track of a particle in the cathode region will experience a force toward a single wire. Therefore, most of the secondary electron swarm will be drifted toward and be collected on this single wire. In the rare cases when electrons are produced exactly mid way between the two wires each wire will produce a pulse with similar size.

This feature is of great use for position measurement. A very fast rise time (a few ns) and excellent timing resolution of the order of 100 ps (FWHM) [Bre82, Bre79] can be achieved with such a MWPC. Because of the rather poor ΔE resolution (40% FWHM), due to energy straggling of the charged particle in the gas resulting in a fluctuation in the number of electron-ion pairs produced, these detectors are mainly used to provide time signals and position information as will be discussed below. On the average only about 26 ion pairs for 5.4 MeV α-particles and about 260 ion pairs for 27 MeV ^{16}O are produced in 2 Torr isobutane with a gap of 3.2 mm [Bre82, Nor70, Bro59].

3.1.4 Position Sensitive Gas Counter

As discussed above most of the signal in a MWPC comes from a single wire of the wire plane. If one can identify from which wire the signal comes, the position where the particle enters the detector may be determined. Two alternative methods are commonly used for this purpose.

One method divides the charge along a resistive wire [Ful73, Ata70] and the ratio of the signals from the two ends of the wire is a measure of the wire position. The second method uses the finite propagation time of electromagnetic signals in an LC delay line [Gro70]. The propagation time difference between the ends of the delay line

represents a measure of the wire position. This method uses standard time-to-pulse-height (TAC) or time-to-digital converter (TDC) electronics.

If we simply identify the wire which collects most of the secondary electrons, the position resolution is equal to the separation between two wires. The space between two wires is typically 1 mm, hence the resolution is 1 mm. More accurate position resolution can be obtained by comparing the charge collected on neighbouring wires. A position resolution of 80 μm was obtained by using this method. The details of this technique can be found in Bre82, Bre83 and references therein.

3.2 PARTICLE IDENTIFICATION TECHNIQUES

Following a heavy ion reaction many different products can enter the detecting system. To detect and select the species of interest, a reliable particle identification technique is required. Parameters such as energy, energy loss, time of flight and position are used individually or in combination to identify the detected particles. Common identification techniques are discussed.

3.2.1 ΔE-E

In this identification method both the energy loss (ΔE) in a transmission detector and the total kinetic energy (E) in a stop detector are used. The rate of energy loss (-dE/dx) of a non-relativistic ion in a medium is given by the Bethe-Bloch equation.

$$-\frac{dE}{dx} \propto \frac{Z_{eff}^2}{v^2}\ln\left(\frac{m_e v^2}{I}\right) \qquad (3\text{-}2\text{-}1)$$

Where m_e is the electron rest mass, I is the average ionization potential of the material, v is the velocity of incident ion and Z_{eff} is the effective charge state of the incident ion.

The effective charge state Z_{eff} is used to account for the fact that heavy-ions constantly change charge-state while traversing the medium, and the Z_{eff} does not depend on the initial charge state of the ions after the ions have passed through a certain path of the material. For example 65 MeV Cu reaches it's equilibrium charge state (~18) after it has passed through a carbon foil of ~15 $\mu g/cm^2$ [Shi86, Zai84]. The Z_{eff} increases initially as the particle energy increases and reaches the atomic number of the ions Z when the energy of ions is sufficiently high. For instance the Z_{eff} of O beam particle becomes close to 8 at an energy larger than 80 MeV. Hence, for a particle with mass A and atomic number Z, -dE/dx initially increases with energy as Z_{eff} increases. However, this increase will be offset at some point due to the term of $(1/v^2)$. The -dE/dx will have a maximum at this point and decrease roughly as $1/v^2$ and thus as 1/E.

Showing on Fig. 3-2-1 is -dE/dx vs energy for various nuclear species in isobutane gas, taken from the tabulations of Northcliffe and Schilling [Nor70]. Fission fragments (Z~40, A~100), which are positioned near the maximum of the -dE/dx curve have the largest energy loss and hence are well separated from all other groups of interest in the ΔE-E plane. The electrons are almost fully stripped from the elastically scattered beam particles, due to their high energy (for instance the energies of ^{16}O beams are 58 to 110 MeV in this work) and relatively light mass. The scattered beam particles are positioned on the tail of -dE/dx, well after the peak, and only lose a small amount of energy, so they are separated from other particles in the ΔE-E plane.

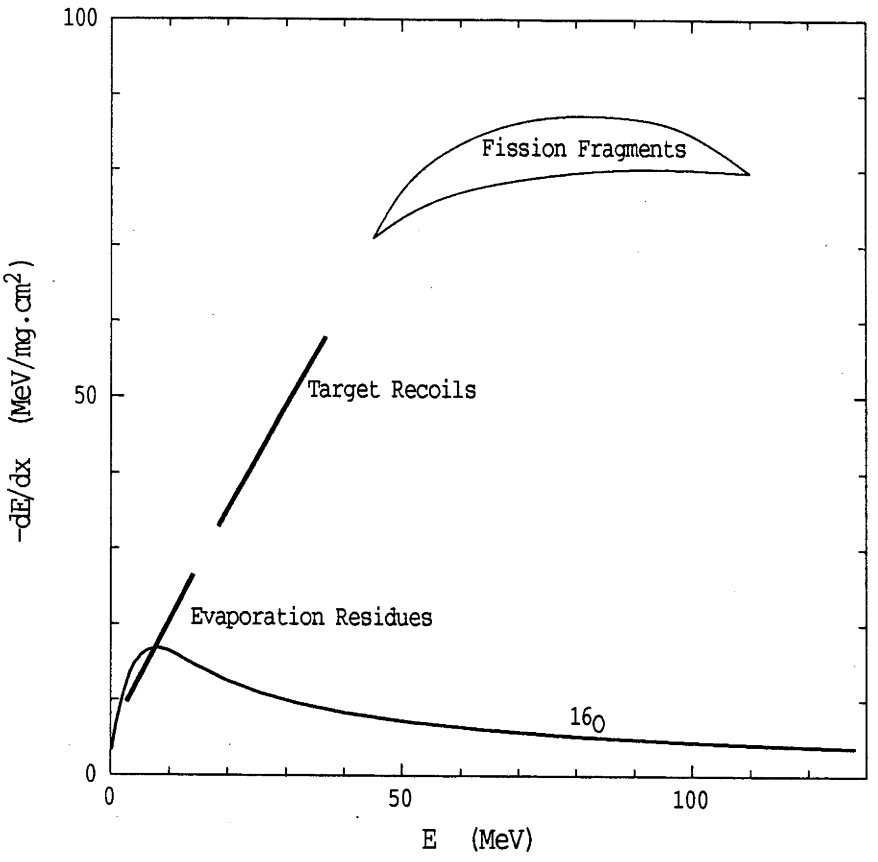

Fig. 3-2-1: Illustration of energy losses (dE/dx) of different ion species passing through in isobutane gas. Taken from the tables of [Nor70].

However the evaporation residues (ER) of mass (~180) produced by reactions with ^{16}O ions at bombarding energies accessible with the 14 UD accelerator have low energy (about a few MeV). Because of their low velocity, they are incompletely stripped, and thus have a low -dE/dx. Fig. 3-2-1 shows that beam particles with the same energy as typical evaporation residues have a similar -dE/dx. Such particles are produced by scattering at apertures in the beam lines and can be much more intense than ER at forward angles (a few degrees). Though it may be possible to reduce this flux of slit-scattered beam particles, it is often difficult to totally eliminate them. The ΔE-E

method alone is, therefore, not suitable for measuring ERs. The slit scattered particles have to be removed from the ERs and/or another method has to be combined with this ΔE-E method.

3.2.2 Time - Of - Flight

For non-relativistic particles with mass m and energy E, the time t for the particle to traverse a distance D is given by

$$t = \sqrt{\frac{m}{2E}}D \qquad (3\text{-}2\text{-}2)$$

Hence

$$m = \frac{2Et^2}{D^2} \qquad (3\text{-}2\text{-}3)$$

It follows that the mass of a particle can be identified if both the time of flight and the energy of the particle are measured. In this work, it is necessary to identify ERs. Particles with masses similar to those of ERs are recoiling target like nuclei (REC) which are directed to forward angles by the scattering of projectiles to backward angles. However their energy is higher than that of ERs because of the larger momentum transfer. The ratio of their energies at zero degrees to the beam direction can be easily shown to be:

$$\frac{E_{ER}}{E_{REC}} \sim \frac{m_T + m_P}{4m_T} \qquad (3\text{-}2\text{-}4)$$

and the ratio of flight times is:

$$\frac{t_{ER}}{t_{REC}} \sim 2 \qquad (3\text{-}2\text{-}5)$$

where m_T and m_P are the target and projectile masses respectively.

As the angle increases, the energy of recoils will be reduced. However, at the angles of interest (≤ 25°), there is less than a 20%

reduction of their energies compared to that of the recoils at 0°. This results in less than a 10% increase of their time of flight (TOF) and hence, it causes no problem in the identification of the ERs from the recoils by their TOFs.

At energies higher than the Coulomb barrier, fewer target recoils are emitted at the angles of interest because the projectiles can easily overcome the barrier and fusion reactions take place. At energies lower than the Coulomb barrier, the recoils are well grouped by their time of flight owing to their well defined energies.

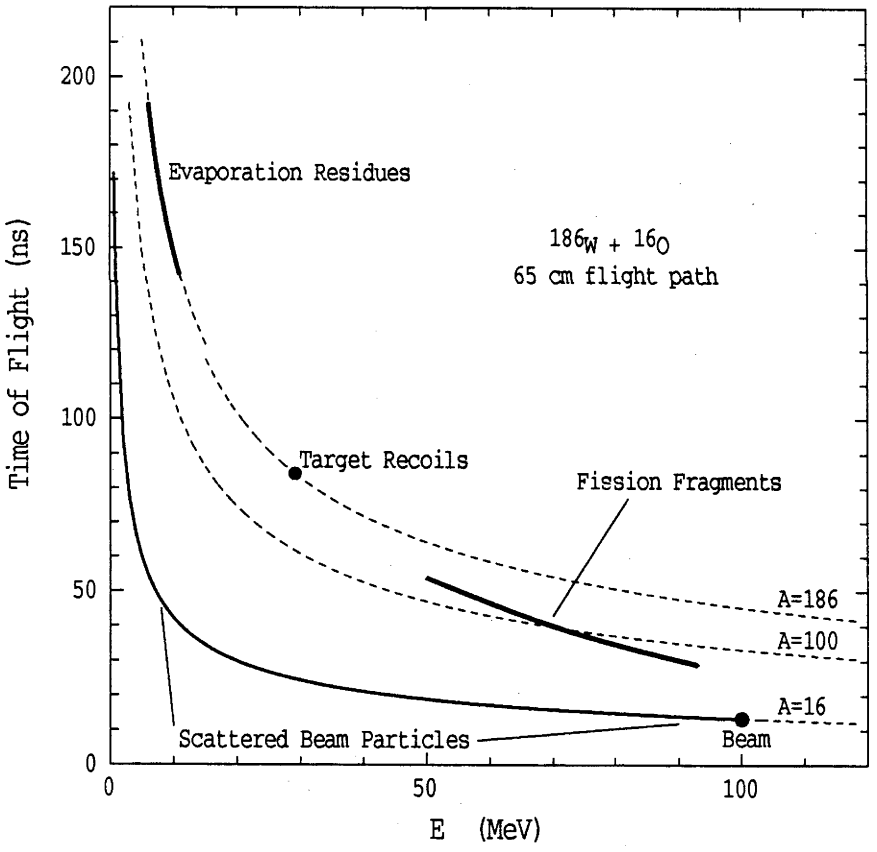

Fig. 3-2-2: The TOF vs energy for various nuclei. The beam and recoil particles with well defined energies are indicated by solid circles and the other typical particles of interest are indicated by heavy solid lines.

The recoils can also be multiply-scattered when passing through the target and their energy can be significantly reduced after this process if the target is thick. Calculations show that multiple scattering, with the thin targets (~40 $\mu m/cm^2$) used in this work, plays an insignificant role, and the smearing of the energy and angular distribution of the recoils can be ignored [Sig74, Hin82].

Thus in principle ERs can be identified uniquely by measuring the energy and time of flight as shown in Fig. 3-2-2. In practice, a direct measurement of ERs by this method is precluded at the necessary forward angles, because of the very intense elastically scattered beam particles. Possible solutions to measuring the ERs at the very forward angles are discussed in the following sections.

3.3 PARTICLE SEPARATION TECHNIQUES

The initial momentum of a compound nucleus formed following fusion is the same as that of the projectile. The final momentum of an evaporation residue is changed due to the emission of light particles from the compound nucleus during the de-excitation process. However, the momentum of the light particles is relatively small compared with that of the projectile, so that the deflection of the evaporation residue is small. Hence evaporation residues concentrate at very small angles to the beam direction. For example, experimental measurement shows that the full width at half maximum (FWHM) of the ERs for the reaction $^{16}O + ^{154}Sm$ to be about 3 degrees in the laboratory system. It, therefore, becomes essential to measure the ERs very close to the beam direction if high precision experimental data are desired. The problem is then raised that any type of detector

cannot be directly placed at such small angles because the intensity of the elastic scattering ($\propto 1/\sin^4\theta/2$) is too strong. Si detectors can be damaged immediately if they have been placed close to 0°. For example, in the work of [Hin82], the Si detector, which was used to measure the ERs, had to be changed after measuring for only few hours and the measurements were restricted to angles larger than 2°. Gas counters may not be damaged but the counting rate may greatly exceed their counting capabilities. Alternatively, very low beam intensity may be used resulting in very long collection times. This causes a major difficulty which has to be overcome in order to increase the precision of the measurement of ERs.

To solve this problem it is necessary to separate the elastic scattered beam particles (EL) from the ERs. This should be done in such a way that the separation does not result in a loss of ERs. The common separation techniques are described as below.

3.3.1 Magnetic Deflection

When a charged particle passes through a magnetic field perpendicularly, a force is experienced by the particle and it is deflected from its initial direction as shown in Fig. 3-3-1a. The charged particle travels along a circular orbit perpendicular to the magnetic field. The force, F, applied to the particle and the radius, R, of the orbit are related by

$$F = Bqv \qquad (3\text{-}3\text{-}1)$$

$$R = \frac{mv}{Bq}, \qquad (3\text{-}3\text{-}2)$$

where B is the magnetic field, m, q, v are the mass, charge, velocity of

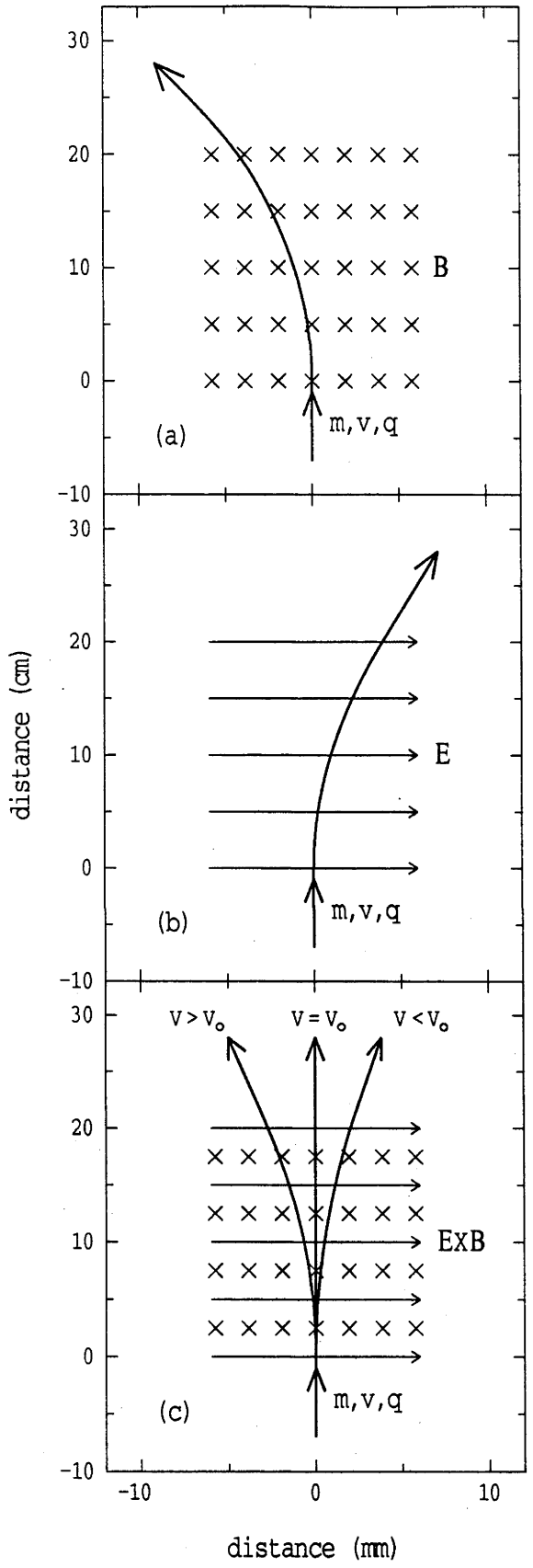

Fig. 3-3-1 Principle of a positively charged particle separation technique by using magnetic and electric fields. (a) The charged particle travels in a magnetic field which is perpendicular to the paper and enters the paper from above. The particle is deflected to the left. (b) The charged particle travels in an electric field which is parallel to the paper and from left to the right. The particle is deflected to the right. (c) Positive charged particles passing through **EXB** fields. Those particles with velocity v_0 are not deflected and those particles with different velocities will be deflected to the left or right depending on whether their velocity is bigger or smaller than v_0.

the particle. However the momenta of the ERs and elastically scattered particles are similar and their charge distributions overlap, making this method unattractive in this work.

3.3.2 Electric Deflection

Fig. 3-3-1b shows a charged particle passing through an electric field, E. The forces, F, and the deflection, Δs, are:

$$F = Eq \tag{3-3-3}$$

$$\Delta s = \frac{1}{2}\frac{Eq}{m}\frac{L^2}{v^2} = \frac{EL^2}{2(mv)^2}mq \tag{3-3-4}$$

Where L is the length of the electric field region.

Hence the deflection is proportional to $1/(mv)^2$ and mq. Since the ERs have similar momentum to elastically scattered particles, the separation of ERs from elastic scattering is proportional to mq. Then:

$$\frac{\Delta s_{ER}}{\Delta s_{EL}} \simeq \frac{m_{ER}q_{ER}}{m_{EL}q_{EL}}$$

Thus, in the case of projectile relatively lighter than the target, the ERs will be separated from elastic scattering by applying an electric field because the mq of ERs is larger than that of elastically scattered particles.

This method has been used to separate ERs from elastically scattered particles [Fre83, Fre83a, Beg85, Sch88, Cha88] but the efficiency of transmission and detection are not easily determined and varies from reaction to reaction. This is because ERs have a wide range of charge states, as well as a range of velocities. They are thus deflected

differently and are dispersed over a wide area frequently larger than that covered by the detector. The cross-sections measured in ref [Fre83, Fre83a] have a quoted error of 20% because of such problems.

3.3.3 The **EXB** Velocity Filter

The large dispersion associated with electrostatic deflectors can be reduced dramatically if the plates are located inside a magnetic field, with the magnetic field direction perpendicular to the electric field. The use of such devices, first suggested by Wien [Wie1898, Wie02], is not uncommon in polarised ion sources as a means of rotating the direction of polarisation [Bai60] and in sources of heavy ions as a mass selector [Wah64, Sal77].

When a charged particle passes through crossed electric and magnetic fields, as shown in Fig. 3-3-1c, and if the length of the crossed field region is much smaller than the radius of the particle orbit in the magnetic field, $L << R = mv/Bq$, the force experienced by the particle is:

$$F = Bqv - Eq \qquad (3\text{-}3\text{-}5)$$

For given magnetic and electric fields, B and E, there is a particular velocity v_0, for which the net force experienced by the charged particle vanishes, and hence the particle is not deflected. That is:

$$Bqv_0 - Eq = 0$$

thus:

$$v_0 = \frac{E}{B} \qquad (3\text{-}3\text{-}6)$$

and this is charge independent.

In principle, therefore, if one chooses the ratio of E/B, those particles with velocity of v_0 may be selected out by detecting them in their original direction. The other particles are deflected from their original direction either to the left side or to the right side, depending on whether the velocities of the particles are larger or smaller than v_0.

If we choose the E/B to let v_0 be equal to the initial velocity of the compound nucleus formed by a fusion reaction, that is

$$\frac{E}{B} = v_0 = \frac{m_P v_P}{m_P + m_T} \qquad (3\text{-}3\text{-}7)$$

where m_P, m_T are the masses of the beam particle and target, the v_P is the velocity of beam particle, then the ERs will peak on the central axis of the filter and all elastic scattering will be deflected to the left side.

Inserting (3-3-6) in (3-3-5) one may rewrite (3-3-5) as:

$$F = Eq\left(\frac{v}{v_0} - 1\right) \qquad (3\text{-}3\text{-}8)$$

or:

$$F = Bq(v - v_0) \qquad (3\text{-}3\text{-}9)$$

If we compare Eq. (3-3-8) with (3-3-3) and note that the velocity of ERs is not too far from the initial velocity of the compound nucleus, we will see that the force applied to the ER can be considered as an electric force only, but be reduced by a factor of $(v/v_0 - 1)$. For those ERs with the velocity of v_0 the net force is reduced to zero, hence no deflection at all, even though they have a wide range of charge distribution. Due to the emission of light particles during the de-excitation process, the velocity of ERs spreads in a range of $v_0 \pm \Delta v_0$, and it has been shown that the $\Delta v_0/v_0$ is less than 30% [Hin82]. For those ERs with a velocity not equal to v_0, even though the net force is not reduced to zero, it is reduced to less than 30% of that in a simple electrostatic deflector.

Therefore the dispersion of ERs after passing through a Wien filter will be much less than that after passing through an electrostatic deflector. In other words, the ER will be peaked around their original direction with a small dispersion in angle.

If we compare equation (3-3-9) with (3-3-1) and note that in this work the velocity of elastic scattered beam particles, v_{EL}, is about 10 times bigger than v_0 ($v_{EL}/v_0 = (m_P + m_T)/m_P$), we see that the electric force experienced by the elastically scattered particles is only about 1/10 of the magnetic one. Thus, the net force applied to these particles is like a purely magnetic one but the strength of the force is reduced by about 10%, depending on the masses of projectile and target. If one increases the magnetic and electric field to maintain the same ratio of $E/B = v_0$, the ERs will be still peaked in the original direction of particle momentum, but the deflection of the elastically scattered particles will be increased, and their separation from ERs increases.

To conclude this section, the velocity filter is a very suitable device to separate the ERs from the elastically scattered particles for high precision ER cross section measurements.

A velocity filter [Wei91] has, therefore, been designed and constructed for this purpose.

3.4 EXPERIMENTAL APPARATUS

All experimental measurements have been carried out within a 2 m diameter scattering chamber. Movable arms inside the chamber allowed the velocity filter and associated detectors to be moved over a wide range of angles. The movement of the arms could be controlled

from outside of the chamber, and the angle could be reproduced to an accuracy of ~0.01°. The apparatus used is described in the following sections.

3.4.1 Velocity Filter

As has been discussed in the last section, to measure ER cross-sections with high precision it is essential to separate ERs from ELs and this can be achieved by using a velocity filter. To build the velocity filter the following factors were taken into account:

1. To achieve a sufficient strength of magnetic and electric fields in a relatively big space to allow all the particles to be transmitted by the velocity filter.

2. A small volume so that it can operate in the 2 m chamber.

3. Sufficiently light weight so that the movable arm will operate, and be easy to move over a wide range of angles in the forward direction.

It was found that requirement 1 conflicted with 2 and 3 to some degree, since meeting with requirement 1 requires more space and increasing the weight. Therefore it becomes necessary to achieve the strongest electric and magnetic fields possible whilst also minimizing the volume and weight. Fig. 3-4-1 shows the plan and section drawing of the velocity filter. Details of this filter are given as follows.

MAGNETIC DESIGN

As discussed in §3.3.3, if we keep E/B = v_0, the elastically scattered beam particles are mainly deflected by the magnetic field and ERs

peak at the central axis of the filter. The strength and the length of the magnetic field determined the basic character of the separation function of the filter. Calculations showed that if a magnetic field of ~ 0.15 Tesla or stronger and an electric field up to 15 kV/cm or stronger could be established within a length of 200 mm, it would be sufficient to separate the ERs from the elastically scattered beam particles within the available energy and particle ranges which could be provided by the 14 UD accelerator in this laboratory.

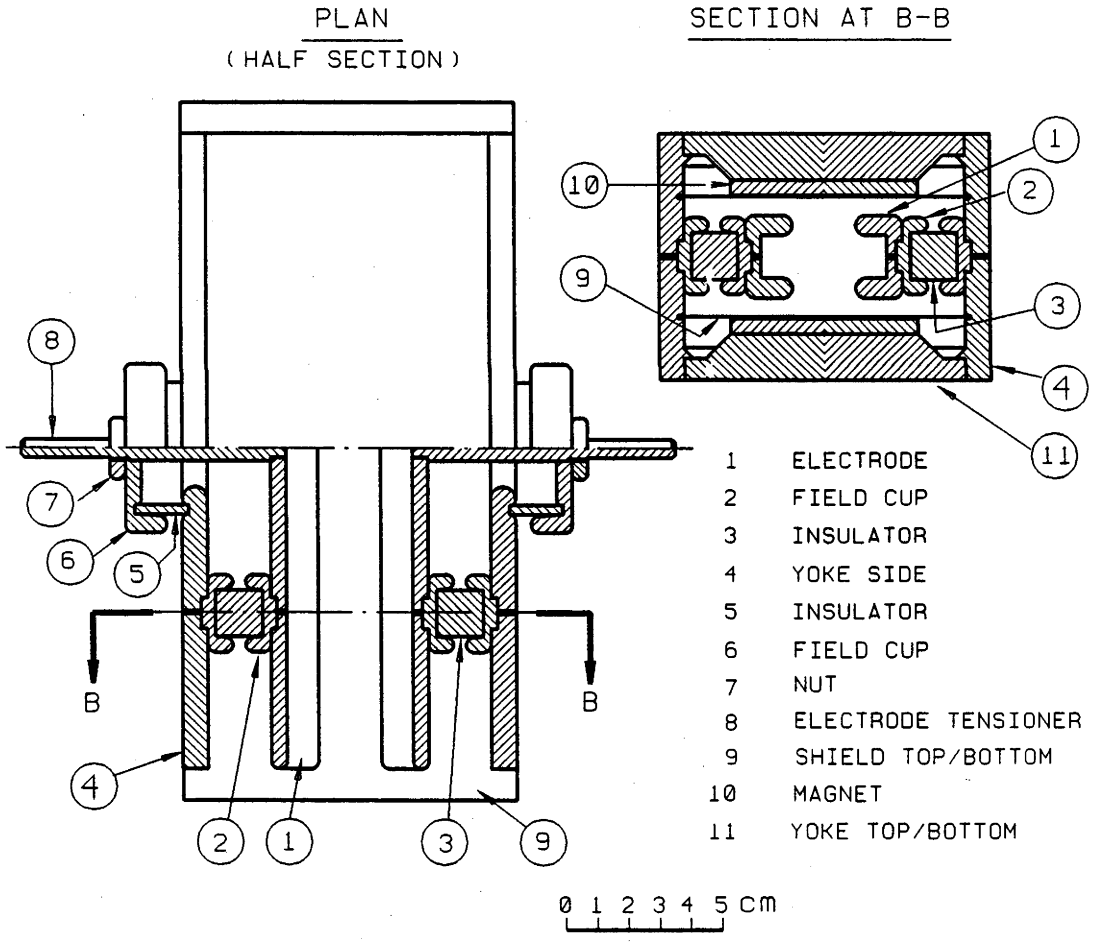

Fig. 3-4-1: View of the velocity filter showing the positions of the magnets and electrostatic deflector plates. The high voltage feedthroughs and the field cups used to support the deflector plates are illustrated.

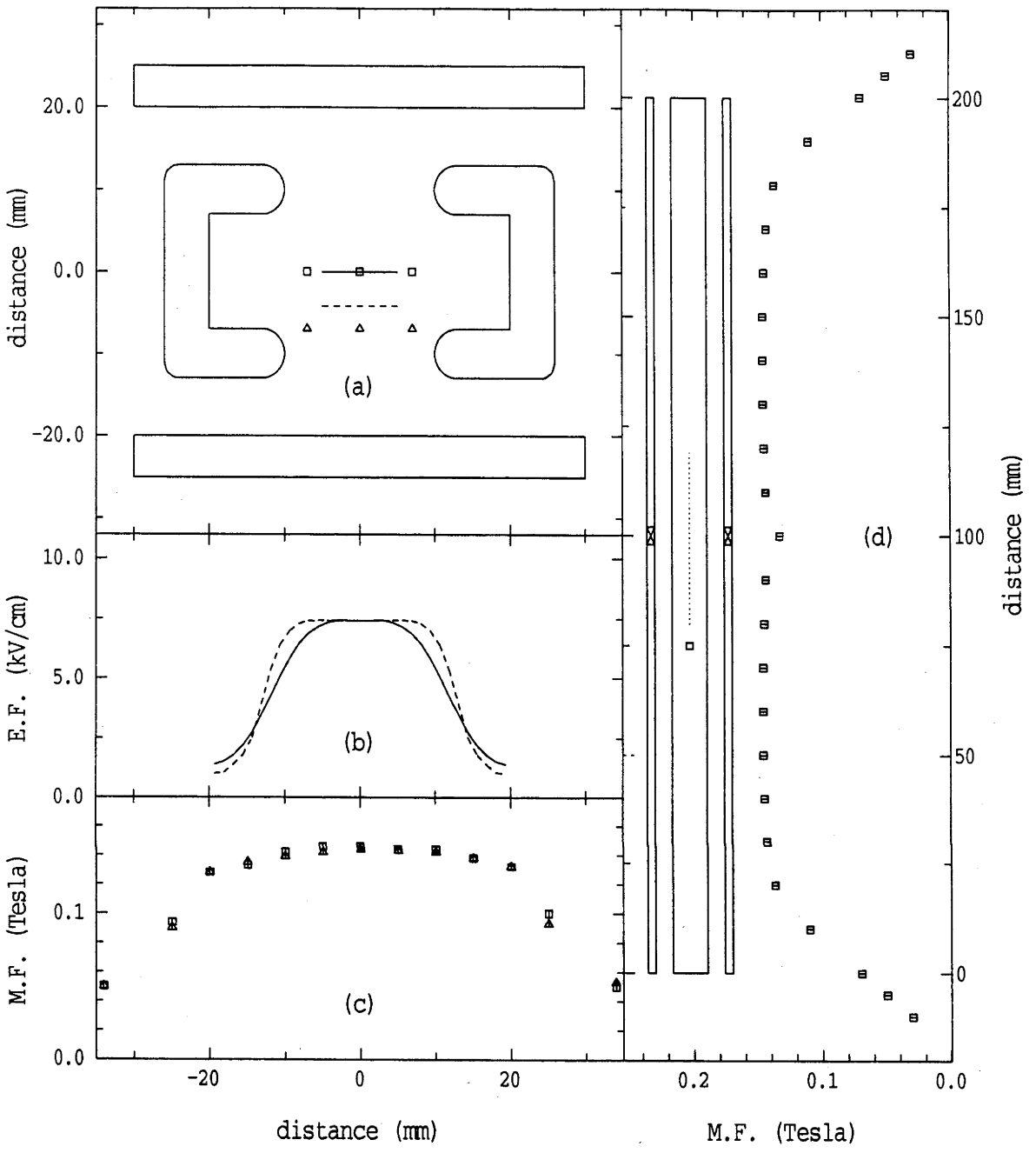

Fig. 3-4-2: Measured magnetic field and calculated electric field inside the velocity filter. (a) The cross-section of the filter, the lines and symbols indicated the regions where the electric fields in (b) have been calculated and the magnetic fields in (c) were measured. (b) Calculated electric field, the solid line represented the field across the middle of the electrodes, the dashed line is 5 mm from the middle as indicated in (a). (c) Measured magnetic fields across the filter at the position shown in (a). (d) Measured magnetic fields on the central axis of the filter.

Permanent samarium-cobalt magnets* were chosen to build the velocity filter. These commercial magnets are 100 mm long, 60 mm wide and 5 mm thick and they are magnetised along the 5 mm dimension. A soft iron yoke was designed to maximize the magnetic field. Four of these magnets are then attached in pairs to the faces of the soft iron yoke to give an overall length of 200 mm. Thin soft iron spacers are needed to join the ends of each pair of magnets; this results in only a small reduction in field strength in the vicinity of the joint. A relatively large distance between the two magnets is needed to place the electrodes inside the magnetic field, but increasing the separation results in a weaker magnetic field. A preliminary test showed that when the distance between the two magnets was 20 mm and placed inside a proper yoke, a magnetic field of 0.22 Tesla could be achieved. This field would be reduced to 0.14 Tesla if the distance was increased to 40 mm. Considering the space needed to house the electrodes, the 40 mm distance between the magnets has been used. The measured magnetic fields are shown in Fig. 3-4-2 (c) and (d). A uniform field, to within a few percent is achieved over 20 mm on either side of the filter central axis. Along the filter the magnetic field starts to fall at about 10 mm from the ends. The field in the vicinity of the joints of the pairs of the magnets is reduced by ~10%, but only over a distance of ~5 mm.

THE ELECTRIC FIELD DESIGN

The ideal electric field should be uniform both in the horizontal and vertical directions (refer to figure 3-4-2 (a)). In order to achieve this uniformity the dimensions of the electrodes must be much greater

---

* Rare-earth cobalt magnets, HICOREX-B, made by Hitachi Magnets Corp.

than their separation, if a pair of flat plates are used. However, inside the velocity filter the space is limited. The width of electrodes which could be accommodated is about 20 mm but the space needed between the two electrodes is about 20 mm as well. The electric field generated by such flat electrodes is non-uniform in the horizontal as well as the vertical direction. The calculated electric field shows that it changes very quickly, even at locations very close to the central axis. The non-uniformity of electric field is caused by edge effects in which electric flux escapes from the inside of the electrodes. If one could restore the electric flux by reducing the distance between the two electrodes at the edge, the electric field would be more uniform in the middle.

Further studies showed that a much more uniform electric field could be achieved by using a pair of Π shaped electrodes. The calculated electric field for this geometry is shown in Fig. 3-4-2b. The electric field produced in the middle of the electrodes is only slightly lower than that for flat plates which are only 20 mm apart, but now the field is uniform over a wide range. Field variations of up to 10% occur at displacements of 10 mm in either direction. Therefore, for the region of interest of the filter both the electric field and magnetic field are sufficiently uniform; the typical elastically scattered particles and ERs are deflected horizontally within the filter by about 5 mm from the central axis and constrained geometrically to ~3 mm vertical displacement.

As well as providing good electric field uniformity in the region of interest, the electrode shape produces a reduced field inside the legs of the Π. Thus ERs of very low velocity which enter into this weak field region experience a net force back towards the central axis because the magnetic field is still uniform. Therefore, the weak and sharply

reduced electric field inside the leg of ∏ may play a role in grouping the position of very low energy ERs. The electrodes are made of stainless steel and all the edges of the electrodes are properly rounded to avoid electrical breakdown.

THE HIGH VOLTAGE PERFORMANCE

A high potential difference up to 40 kV is required between the electrodes. This can be achieved by supplying +20 kV to one electrode and -20 kV to another. It is not an easy task to produce this high voltage within the limited space of the filter and to prevent sparking during long running periods; a single spark can create thousands of "noise signals" in the electronics measuring position, ΔE and timing in the MWPC.

Quite often, under a good vacuum of ~10^{-6} Torr, high voltage breakdown occurs on the surfaces of insulators, in other words, the vacuum itself is a much better "material" than all other kinds of insulators. Hence the best high voltage performance is achieved by minimising the use of insulator material. In the filter it is only used in the electrode supports and in the high voltage connectors which pass through the wall of the magnet yoke. Field cups (see Fig. 3-4-1) with 5 mm gaps are placed around the insulators to ensure that there are no regions of high field strength at the insulator-conductor boundaries. With the exception of these field cups, the minimum voltage-to-earth distance is 6.5 mm, between the electrodes and the magnets. Breakdown in this region is prevented by covering the rough surfaces of the magnets, manufactured by sintering, with smooth stainless steel sheets, which are recessed into the walls of the yoke. All other edges are appropriately rounded to make sure that the strength

of electric field everywhere in the filter is less than that across the field cups. Hence, the breakdown, if there is any, should occur across the field cups which were designed to hold more than 20 kV.

Because the filter is designed to mount on the movable arm inside the 2 m diameter scattering chamber and is required to move over a wide angular range, $-15° < \theta < 30°$, the high voltage connection from the chamber walls to the filter must be able to accommodate this movement. It is equally important to ensure that the connections, especially the flexible parts, do not break down when the high voltage is applied to them. This has been done by using two rigid metal rods (6 mm in diameter) to link to the filter and to pass through the wall of the 2 m chamber; these rods are then linked by a flexible conducting loop of braid (3 mm in diameter) for each connection. All the joints, between the rods and the flexible loops or between the rods, are covered by appropriately rounded aluminium cylinders, 15 mm in diameter. As the filter is rotated, the loops tighten or droop depending on the direction of motion. The photographs show the velocity filter assembled inside the 2 m diameter scattering chamber. On the bottom of each conducting loop is a stainless steel weight which prevents the loops from touching each other due to the attractive electric force and the tension in the loops themselves.

High voltage testing of the velocity filter was carried out in the 2 m diameter chamber; the vacuum inside was about 10^{-6} Torr, and up to ±20 kV was supplied to the electrodes of the velocity filter. Voltage breakdowns were recorded on a chart recorder. Initially, a few breakdowns were recorded with ±20 kV applied, but no breakdowns were recorded after the system had been "conditioned", by keeping voltage on the filter for about 24 hours.

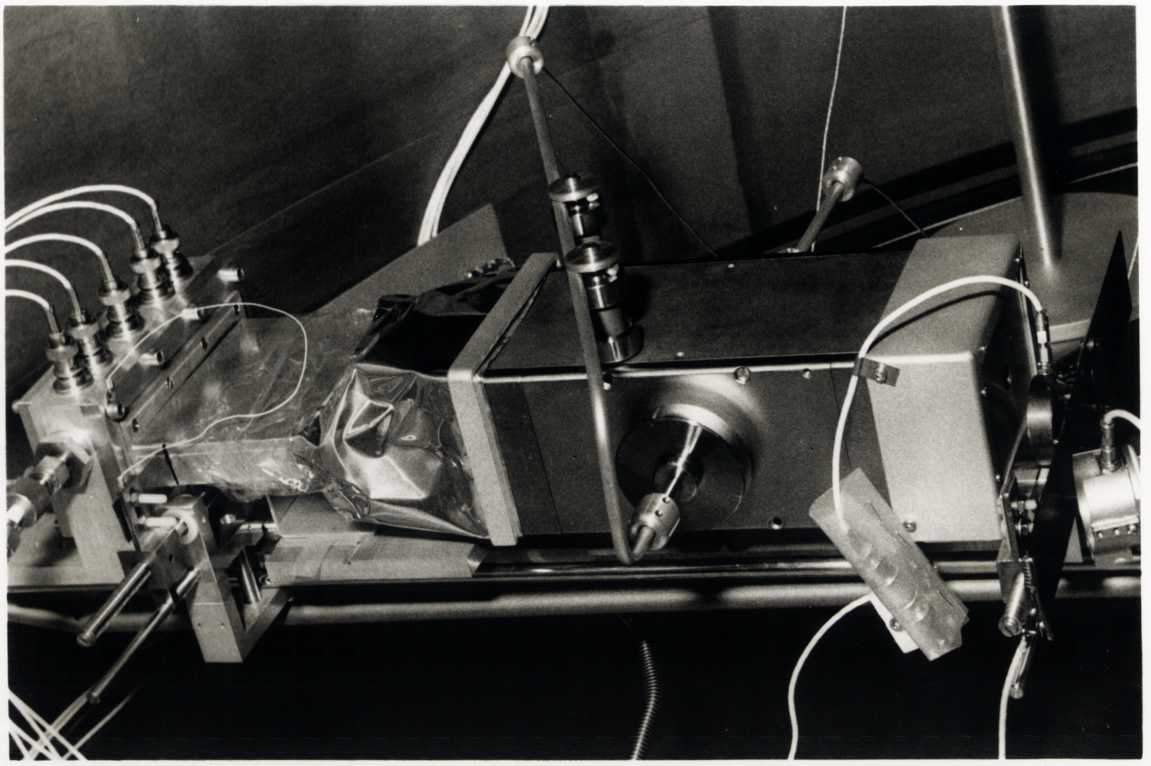

A view of the Velocity Filter and MWPC (above)
and a wider view of the experimental set-up (below).

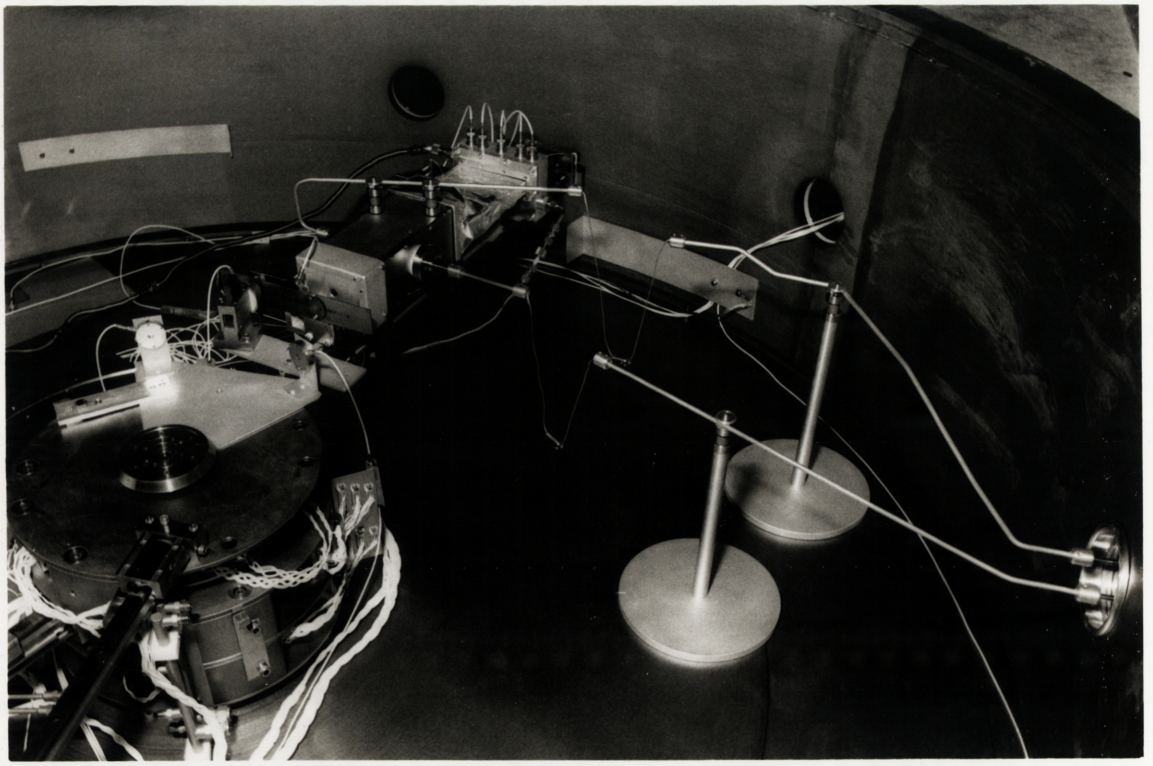

3.4.2 The Position Sensitive MWPC

A position sensitive multiwire proportional counter (MWPC) was located 20 cm behind the velocity filter to detect the ERs after they had been separated from the intense elastic scattering by the filter. The target was firstly irradiated by a low intensity pulsed beam with 1 ns wide bursts every 533 ns. The ERs were identified by their energy loss ΔE(s), position and time of flight (TOF). The TOF was measured by using the MWPC to give the start signal and a radio frequency (RF) signal, related to the beam pulse, to give the stop signal. After the position of the ELs had been determined in the MPWC, the ELs could be physically blocked by a "finger" just in front of the entrance window of the MWPC and then the beam was increased to the required level without exceeding the allowable counting rate of the detector. A detailed description of this detector and the blocking of the ELs is given in this section.

The following are the basic requirements for this detector.

1. A large area to accept all particles transmitted by the filter. To do this an active area of the detector of about 100 mm X 20 mm is required.

2. Reasonable time resolution to enable identification of all incoming particles by their TOF.

3. Position sensitivity and good position resolution over the 100 mm length to localise the ERs and ELs.

4. Reasonable ΔE(s) resolution, to identify the ERs in the presence of low energy beam particles scattered from the

slits and the collimator, which cause a continuous background in TOF and position.

5. In order to achieve requirements 2 and 3 the detector must work with a very low gas pressure (around 2 Torr).

These requirements would not be too difficult to meet in the detection of high energy heavy ions, like fission fragments with energy of hundreds of MeV, but this is not the case for ERs. Actually, the requirements are rather difficult to meet due to the very small energy loss of the heavy (A ~ 170) and "slow" (caused by their low energies, a few MeV) ERs in the gas at the pressure of about 2 Torr.

For example, the technique which has been used to obtain the position is to measure the finite propagation time of electromagnetic signals in an LC delay line. Having a good fast rise time signal (a few ns) from the wires is, therefore, essential to get good position resolution. However, since the primary ionization of ERs is very low, up to 10 times smaller than that of fission fragments, a much higher gain, thus, a much stronger reduced electric field E/P, should be achieved for this detector than for a fission fragment detector [Maz83]. To reach this strong field requires very careful work at every stage of designing and constructing the detector.

Another difficulty is in meeting the requirement 4. Because scattered beam particles have a continuous energy distribution some of these particles, with very low energy, could have similar velocities to those of ERs and be transmitted to the same position as ERs. Although the energy of these particles is very small their energy loss (ΔE) is not so small, so they are not well separated from the ERs since the ΔE resolution of the MWPC is rather poor.

Slit scattering has been minimised by not having collimators in the scattering chamber. However, a small amount of slit scattering still arises from other, more distant, components of the beam line. At the level of a few mb of ER cross-section, the intensity of this slit scattering is low compared with the ERs and is not troublesome. When the ER cross-section is below the 1 mb level, this small amount of slit scattering will have a comparable intensity with the ERs.

It is, therefore, necessary to find a way to measure more parameters of the ERs for those measured at sub-barrier energies. This has been solved, in this work, by coupling another detector cell behind the MWPC to obtain an additional, better ΔE resolution signal without disturbing the MWPC itself. With this improved ΔE measurement the detector, which now provides TOF, position and two ΔE signals, is capable of measuring the cross-section of ERs down to the 0.1 mb level.

It should also be mentioned that the foil at the entrance window of the detector or other foils inside the detector, should all be thin enough to allow the "heavy" and "slow" ERs to pass through them. Calculation shows the maximum thickness which will allow all ERs to pass through is about 150 $\mu g/cm^2$ of polypropylene.

DESIGN OF THE DETECTOR AND PRINCIPLE OF OPERATION

After considering all the effects mentioned above and a number of different designs the final version of the detector is shown in Fig. 3-4-3. It consists of two elementary cells with a common cathode which is located between a wire plane and a metal mesh plane. The wire plane, in front of the cathode serves as an anode and provides the position measurement. The mesh metal plane, at the back of the

cathode, is grounded and serves as a grid. Further separated from the mesh plane is a metal plane serving as another anode.

The wire plane and the common cathode, 3.2 mm apart from each other, constitute one of the elementary cells. The strongest electric field in this detector is supplied in this region to let this cell work as a multiwire avalanche counter. The wires in the wire planewere linked with a delay line. Identification of the wires is a measure of the position.

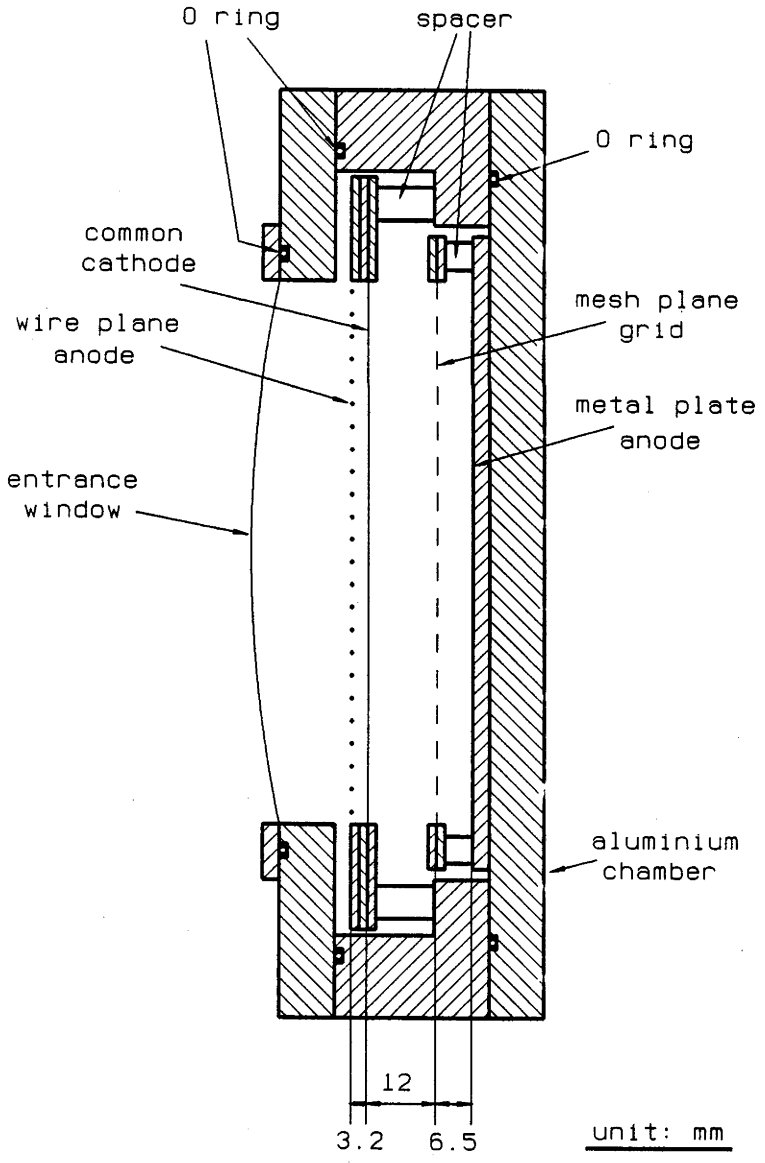

Fig. 3-4-3: A cross-section view of the position sensitive MWPC.

The metal plane, grid plane and the common cathode constitute another cell giving better ΔE signals. This cell is divided into two regions by the grid, and the strength of electric fields applied to the two regions are different. The first region is from the cathode to the grid and has a longer distance of 12 mm. A weak electric field was supplied across this region to let it operate as an ionisation collection area. The second region is from the grid to the metal plate anode and it has a shorter distance of 6.5 mm. The stronger electric field supplied in this region is of sufficient strength to cause an avalanche. This region is therefore working as an amplification region. The potential on each electrode has been chosen to ensure both elementary cells of the detector operate without interfering with each other through the common cathode.

When a heavy ion enters the detector it passes through the common cathode and stops at the anode of the solid metal plate. A track of primary electrons is created in the two elementary cells on both sides of the common cathode. These electrons drift away from the common cathode in opposite directions on each side of the cathode, towards the wire plane in front of the cathode and towards the grid at the back of the cathode.

These primary electrons created in the front cell will be multiplied as they move towards the wire plane creating secondary electrons, and most of these primary and secondary electrons will be collected on a single wire which is closest to the intercept of particle track and cathode (see §3.1.3 for details). This produces a negative pulse on this wire and the pulse propagates through the delay line. The time difference of the arrival of the pulse at each end allows the exact

identification of the wire which has collected most of the electrons. In the cases when the intercept has the same distance to two wires there will be two pulses with similar sizes on the two wires. This will result in a uncertainty of 1 mm on the extracted position but the chance of such cases is very rare. As discussed in §3.1.3 only the first 8% distance (about 0.3 mm) close to the cathode constitutes the effective ionisation path of the front cell. Hence, the statistical fluctuation of the primary electrons at such a short distance is large, which results in a poor ΔE resolution of the front cell.

Those electrons drifting toward the grid in the back cell experience a weak electric field in which no multiplication of electrons occurs. Since the grid is 98% transparent, most primary electrons created by the heavy ion along the 12 mm path pass through the grid. As soon as these electrons pass through the grid they experience a much stronger electric field in the same direction, and the number of electrons is multiplied until the solid metal plate anode is reached. As all the primary electrons swept through the grid gain an equally large multiplication, a bigger ΔE signal with better resolution is observed from this anode than that from the first one. However because in the ionisation region the drift distance varies from zero to 12 mm depending on the electron's initial position and a weak, reduced field is supplied, the drift time for the electron is long and varies for different electrons. This results in a longer rise time of the signals and therefore in a poorer time resolution than in the front cell. Therefore only the ΔE signals from the back cell were used.

By electrostatic induction a positive signal is generated on the cathode. Since the cathode is common the signal consists of two pulses coming from the two cells on each side of the cathode. Due to the long drift

time of electrons behind the cathode, the pulse coming from the back cell has a rather long rise time and appears on the cathode later than that coming from the front cell. If this delayed and slowly rising pulse had a size comparable with that of the pulse coming from the front cell this pulse would produce a deterioration of the rise time of the cathode signal and hence the time resolution. However, because the slow pulse is generated by the primary electrons without multiplication its size is small enough to cause no significant deterioration of the pulse coming from the front cell of this detector. A timing signal and a ΔE signal are obtained from this cathode, but the resolution of this ΔE is rather poor due to the short effective primary ionisation path in the front cell as discussed before.

CONSTRUCTION AND ASSEMBLY

The cathode is a polypropylene foil (40 ~ 50 $\mu g/cm^2$) stretched and glued on to an epoxy frame. A layer of gold (~70$\mu g/cm^2$) is evaporated on each side of the cathode. The electrical contacts on each side are made with great care outside the active area. Both sides of the cathode are held at the same negative potential.

The grid is a stainless steel mesh (98% transmission) stretched and clamped by two 1.6 mm thick resin bonded fibre-glass frames and is held at ground potential.

The metal plate anode consists of a printed circuit board with a layer of copper, 104 mm X 24 mm, covering all the active area.

The wire plane consists of one hundred parallel 20 μm, gold plated tungsten wires spaced by 1 mm over all of the detector active area. The wires are connected in pairs and attached to a delay line

(ESC 2P50). Neighbouring pairs have nominal 5 ns delay between them. The position resolution is therefore 2 mm over the 100 mm length. To match the impedance of the delay line, each end of the delay line of the wire plane is connected through a 200 Ω resistor to a charge sensitive pre-amplifier.

The potential difference is 550 V between the wire plane and the cathode plane. The reduced electric field reaches 860 V/cm/Torr in the constant field region. To make the detector work stably under this strong electric field, it is essential to have a high quality wire plane with uniform tension on all the wires and no sharp points.

The major problem initially encountered in making this detector was the thermal expansion of the wires when they were being soldered into position directly to the circuit board as is commonly done for this type of detector. This results in non-uniform tension of these short (2 cm long) wires; some being visibly loose. A loose wire could be deflected toward the cathode by the electric field, and cause breakdown at low voltages. This problem was overcome by gluing the wires to the frame then soldering them to the electrical contacts. Before the wires were glued to the frame the tension and the spacing of the wires could be easily adjusted. After the wires had been firmly glued the soldering of the wires to the circuit board no longer caused problems. A high quality wire plane, with extremely uniform tension and spacing for all the 100 wires, has been made by using this technique.

It is equally important to choose very homogeneous wires to avoid sharp edges which will cause discharge in the chamber. Also dust particles, small drops of glue or solder on the wires lead to similar problems and must be avoided. Before assembling the detector, the

chamber, wire plane and window frames were washed in ethyl-alcohol and cleaned in an ultrasonic bath.

The whole detector is assembled inside an aluminium chamber. The charged particles enter the detector through a front window made of stretched polypropylene 40-50 $\mu g/cm^2$ thick. Viton O-rings are used to seal the window to the front plate and this plate to the chamber. A check for gas leaks of the window and the O-ring seals was carried out by immersing the whole chamber in alcohol and applying an internal pressure of up to 10 Torr above the external pressure. Any major leakage of the window or of the O-ring seals would cause bubbles in the alcohol. Those found to be gas tight by this method were generally found to be leak-proof in the high vacuum 2 m scattering chamber where extremely small leaks can be observed.

The aluminium chamber is connected to an external gas handling system by two stainless steel bellows, which allow free angular travel from -15° to +30° relative to the beam direction inside the 2 m scattering chamber. The gas handling system allows isobutane gas to flow through the detector and maintains a steady gas pressure inside the detector of ~2 Torr.

The particles will not enter the active area of the detector if they hit the tungsten wires on the wire plane. Since the wires block an area equivalent to their diameter, 20 μm, in every 1 mm space, the detector efficiency should be 98%.

Although the grid plane made by a mesh is also 98% transparent it will not affect the detection efficiency. Because even if the particle is stopped by the grid the electrons produced by the particle before it hit the grid will drift towards and pass through the grid. As discussed

before, these electrons will be multiplied and form the output signal on the anode on the back of the grid.

ELECTRONICS SET-UP

The electronics set-up associated with this detector is shown in Fig. 3-4-4. Each of the signals is transmitted by 50 Ω cables and is amplified by a charge sensitive pre-amplifier (PA) just outside the 2 m scattering chamber. The signal from the "energy" output of each PA is fed into a main amplifier giving the ΔE signal. The fast signal from the "time" output of the each PA is fed into a fast amplifier and then into a constant fraction timing discriminator to obtain a timing signal. The position is given by the time difference between the signals arriving at each end of the delay line. This time difference is measured by means of a time to amplitude converter (TAC).

PERFORMANCE AND RESULTS

Figures 3-4-5 and 3-4-6 show respectively the time vs ΔE and a part of the position distribution obtained by measuring the reaction of ^{16}O + ^{154}Sm at a beam energy of 70.5 MeV. The detector was set behind the velocity filter at 1.5° to the beam direction. The finger was used to cover part of the detector to prevent the scattered beam particles from entering into the detector directly. Only those beam particles scattered from the edge of the finger or the entrance collimater, resulting in a wide range of positions, can get into the detector. The flight path from the target to the detector was 650 mm. The pressure was 2 Torr of isobutane and the voltages applied to the wire plane, cathode, grid and metal plate anode were +250V, -300V, 0V and +450V respectively.

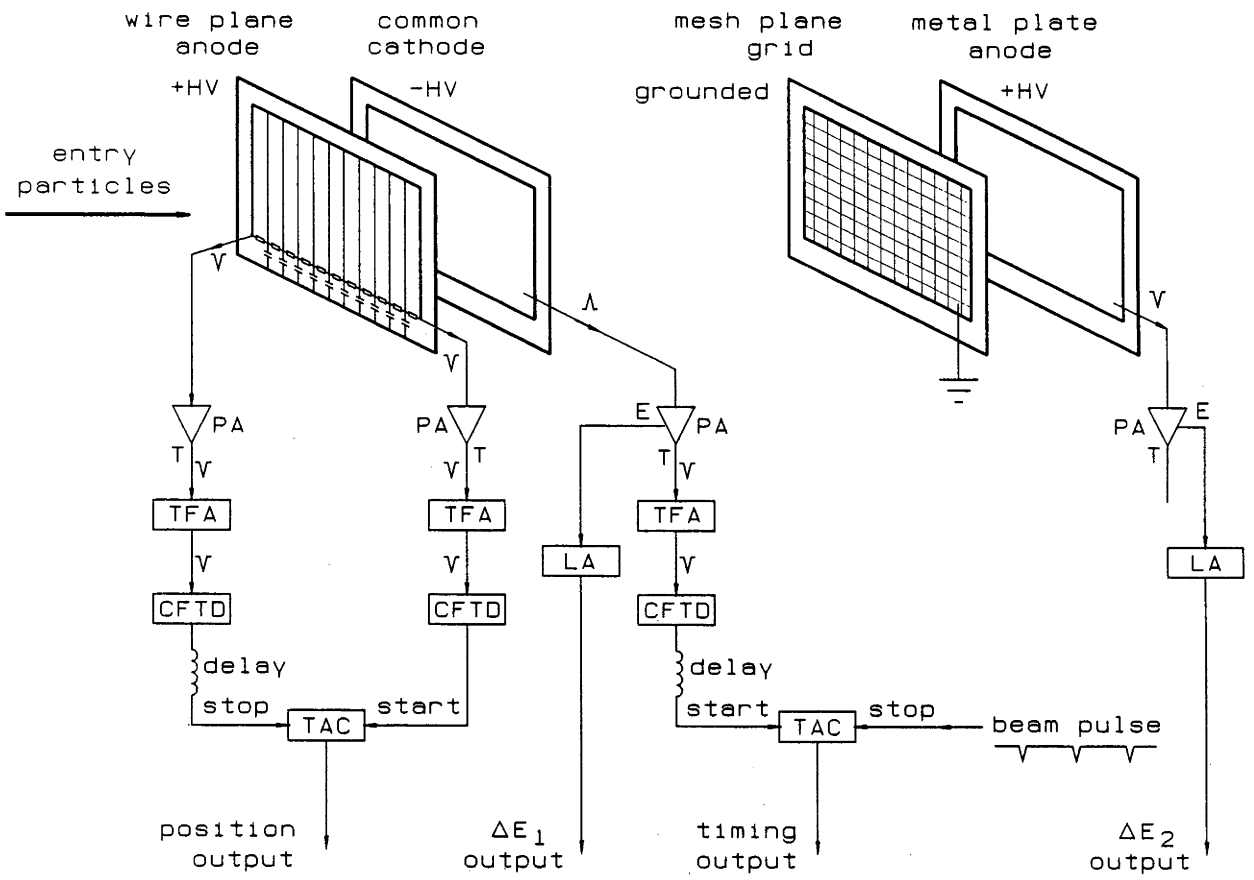

Fig. 3-4-4: Details of the electronic set-up for position, timing and ΔEs measurements.

Table 3-4-1.

PA	Ortec 142B Pre-amplifier.
TFA	Ortec 454 Timing Filter Amplifier.
CFTD	Ortec 473 Constant Fraction Discriminator.
TAC	Canberra 1443 Time Analyser.
LA	Tennelec 203 BLR Linear Amplifier.

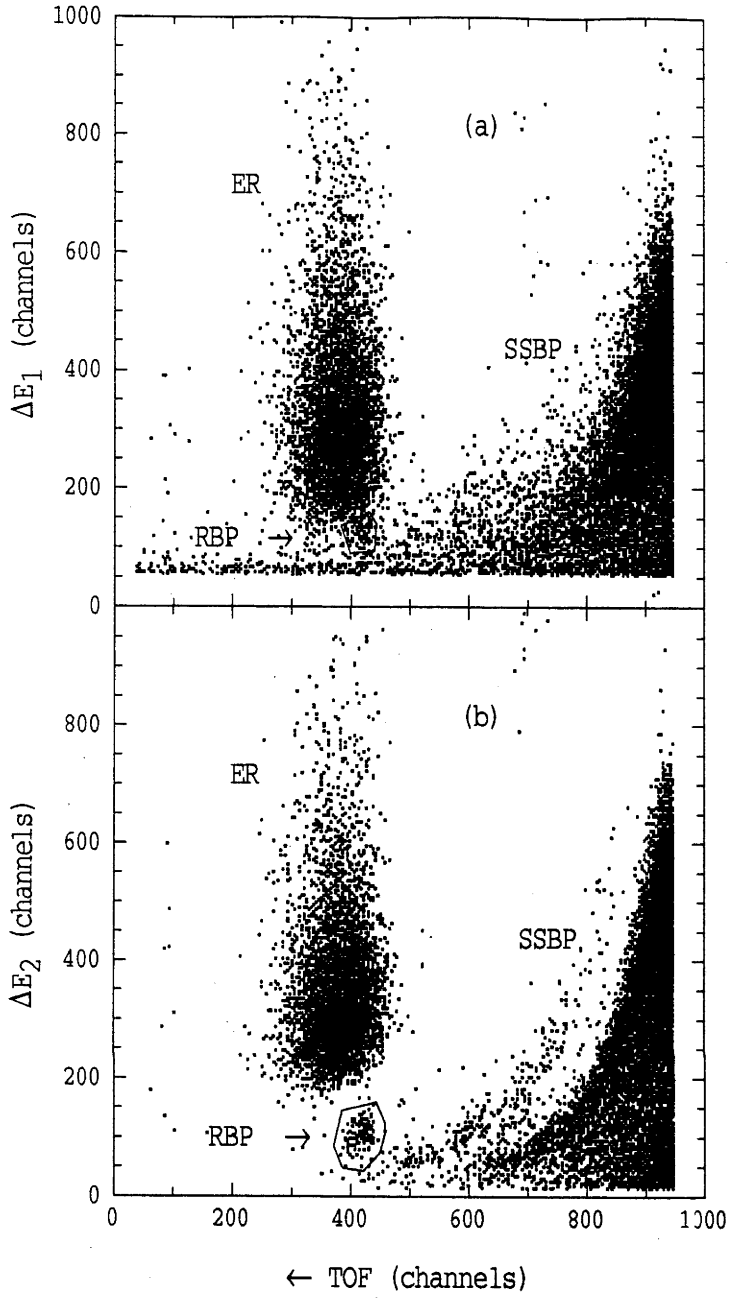

Fig. 3-4-5: Energy loss in the position sensitive MWPC plotted against the time of flight. (b) The ΔE_2 signal from the metal plate in the back of the detector shows significantly improved energy resolution compared with that of (a) The ΔE_1 output from the cathode in the middle of the detector. Low energy "recoiled" beam particles and slit scattered beam particles are not able to be distinguished from the ERs in (a), but they are well separated in (b).

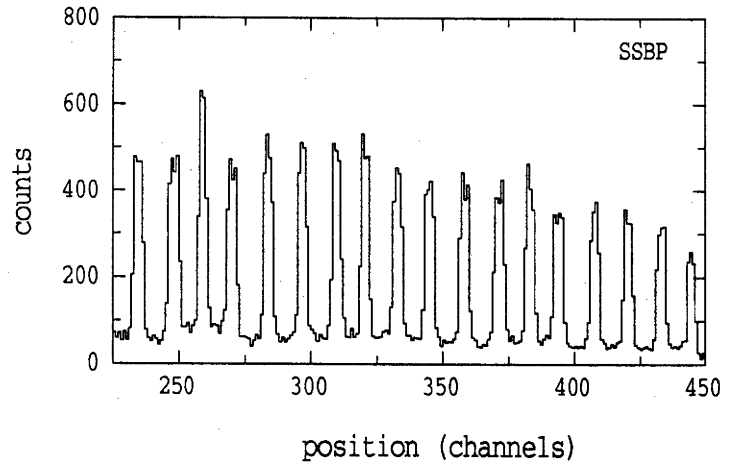

Fig. 3-4-6: Part of the position distribution of slit scattered beam particles on the wire plane anode.

The ER events are grouped on the plots of TOF vs ΔE_1 and ΔE_2, shown in Fig. 3-4-5 (a) and (b), where the ΔE_1 and ΔE_2 are the signals from the cathode and the metal plate anode respectively. A long tail through out the range of the TOF of these plots is a result of low energy, slit scattered beam particles (SSBP). Because of the poor ΔE resolution of ΔE_1 (~30% FWHM) there is no clear gap between the ERs and the slit scattered beam particles at the bottom of Fig. 3-4-5 (a). A significant improvement of ΔE resolution in ΔE_2 (~15% FWHM) can be seen in Fig. 3-4-5 (b) with an obvious gap between ERs and low energy slit scattering. Fig. 3-4-5 shows that there are other well grouped particles with similar TOF to the ERs and with the ΔE between the ERs and the low energy SSBPs. They are beam particles scattered from the carbon backing of the target, near 180° in the centre of mass system. However, these "recoiled" beam particles (RBP) continue to move in the forward direction in the laboratory system. Calculation shows RBPs have a very low energy (~1 MeV) and similar velocity to ERs, hence they are transmitted by the velocity filter to the same position of ERs in the MWPC. Even though RBPs have a much smaller energy than that of ERs, their energy loss, ΔE, is only slightly smaller than that of ERs. Clearly, RBPs can not be separated from the ERs in the plane of TOF-ΔE_1 (Fig. 3-4-5 (a)) but they are well separated in the plane of TOF-ΔE_2 (Fig. 3-4-5 (b)) because of the much better resolution of ΔE_2.

The rise time of the fast component output from the PA is about a few ns for the signals coming from the wires and the cathode. The time resolution of this detector was measured on line by detecting the target recoils resulting from the elastic scattering of a pulsed ^{16}O beam at 20° to the beam direction. The resolution was found to be 1.5 ns (FWHM)

but it should be noticed that this also included the 1 ns width of the pulsed beam.

A part of the one dimensional projection of the position distribution of slit scattered beam particles is shown in Fig. 3-4-6. Each peak shows the signals from a pair of the wires and they are well separated from each other. The peaks in Fig. 3-4-6 are not equally spaced because each delay is slightly different. This was not however a drawback in our case since we were still able to separate the signals from each pair of wires. Similar results were obtained by irradiating the detector with 5.5 MeV α-particles and ^{252}Cf fission fragments under the same conditions. Even though the ionization produced by α-particles and fission fragments differs by about a factor of 40, all types of particles were detected simultaneously.

The ionization produced by α-particles and RBPs is smaller than that of ERs. The feature of these particles being efficiently detected is important in this work, as it guaranteed that the ERs can be efficiently detected.

3.5 EXPERIMENTAL MEASUREMENTS

3.5.1 Experiment Arrangement

All experimental measurements were performed in the 2 m diameter scattering chamber. The velocity filter and the MWPC, described in the last section, were mounted on a movable arm inside the 2 m chamber so as to measure the ERs at forward angles. Particles entering the filter were confined to the central axis by a 1.5 mm

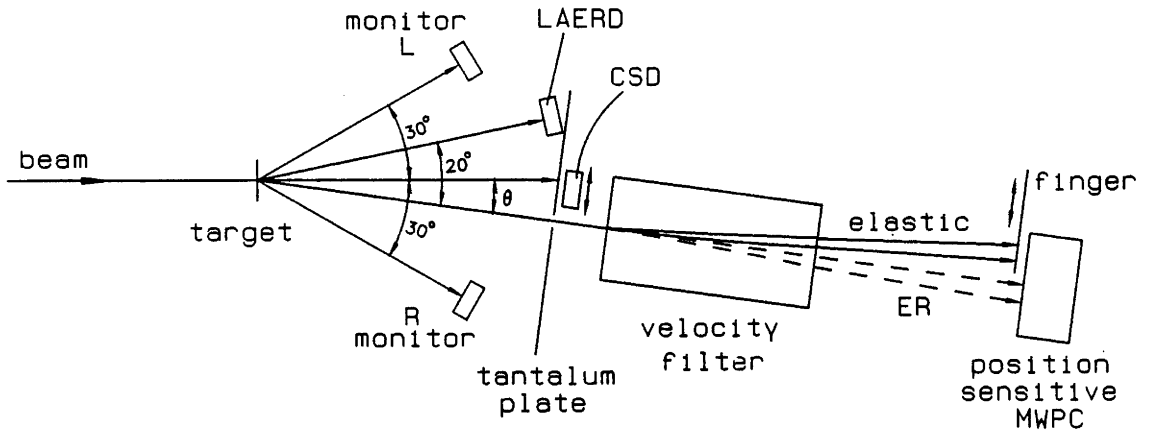

Fig. 3-5-1 The overall arrangement of the ER measuring system. Except for the monitors, all detectors and the velocity filter are mounted on a movable arm which can be rotated from -15° to 30° to beam direction. The calibration silicon-surface-barrier detector (CSD) and the tantalum finger can be moved to intercept scattered particles. The beam is stopped by the tantalum plate.

diameter collimator 250 mm from the target. The solid angle of the entrance aperture was ~2.83×10^{-5} sr. Transmitted particles were detected in the position sensitive MWPC. The collimator was attached to the front surface of the tantalum plate which stopped the beam. The distance from the collimator to the entrance of the filter is ~50 mm and the filter is 200 mm long. A further 200 mm behind the back of the filter, a tantalum finger was located just in front of the MWPC; it could be moved at right angles to the velocity filter axis and could block up to half of the detector length. During the measurements this finger was positioned so that it totally blocked the elastically scattered particles and allowed all of the ERs which had passed through the filter to be detected. This arrangement is illustrated in Fig. 3-5-1.

The targets used were ~40 $\mu g/cm^2$ thick and 2 mm wide stripes, supported by carbon backings of thickness ~10 $\mu g/cm^2$. They were mounted on a wheel which holds six targets; the locations of these can be easily changed from one to another by rotating the wheel. The target of interest was located at the centre of the 2 m diameter chamber and perpendicular to the beam axis.

To minimise slit scattering the collimators inside the two meter chamber were removed. The beam was then focused in the following manner. One of the targets on the wheel was replaced by a tantalum frame with a 2 mm wide and 3 mm high rectangular hole in the centre. The tantalum frame was first located in the target position and the beam was then focused through the hole of the frame by minimising the counting rate of beam particles, slit scattered from the edge of the frame, at the MWPC at angle ~5°. The size of the focused beam spot is about 1 mm diameter. After the beam had been focused, the frame was replaced by the target by rotating the wheel. The beam spot may shift slightly during the measurement, but the 2 mm strip target ensured this shift is less than ±1 mm horizontally. The average shift of the beam spot was monitored by the two monitors as discussed below.

Two SSB detectors, with collimaters of ~16 mm in diameter, were mounted on a fixed table inside the chamber at about ±30° to the beam axis and 195 mm from the target. These detectors, with approximately the same solid angles (~5.3×10^{-3} sr), were used to monitor Rutherford scattering. Yields of these elastic events were used to normalise the beam and to extract the differential cross sections of ERs measured in the MWPC. The ratio of the yields in the two monitors was also used to indicate, and correct for, small changes

in the beam spot position due to the movement of the beam spot and/or the minor changes in the angle of entry of the beam. Details of the extraction of the differential cross section of ER, and the determinations of the angle and the solid angle of the filter will be described in the following subsections.

As the angle increases the differential cross-section of the ERs decreases very quickly. The angle, at which the differential cross section of ERs falls to 10% of that at 0°, is ~10° for the ^{16}O induced reactions. The small solid angle of the filter is not appropriate for measurements at large angles ($|\theta| > 10°$); nor is its ability to remove elastically scattered particles necessary at such angles. A silicon surface barrier detector, with a solid angle larger by a factor of 10 than that of the velocity filter, was mounted on the same arm as the filter but displaced 20° from it. As ERs were measured at the angles $\theta < +10°$ by the filter, the ERs were simultaneously measured at the angle $\theta < -10°$ by this Si detector. The ERs in this detector were identified by their energy and TOF. This detector is also shown on the Fig. 3-5-1 and assigned as the large angle ER detector (LAERD). The angle and the solid angle of this detector were determined in the same manner as that of the velocity filter, as described below.

3.5.2 The Determination of the Angles of the ER Detectors

Rutherford scattering varies rapidly at the forward angles and can be used to determine the angles and the solid angles of the ER detectors. If the Rutherford scattering cross-section is measured (relative to the fixed monitor detectors) at two angles with a well defined separation angle φ then these two angles can be determined. For instance,

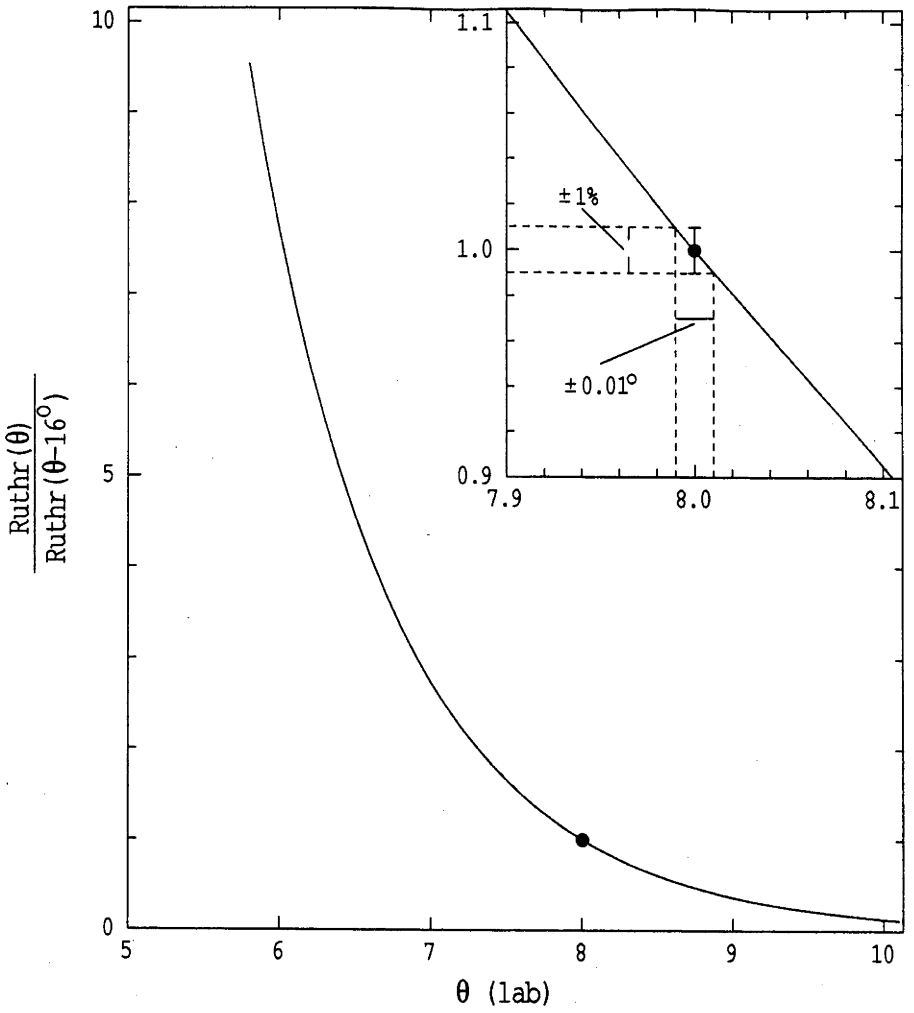

Fig. 3-5-2: Illustrations of the determination of the angle of the ER detector by measuring the Rutherford scattering at forward angles of ±θ. See text for details.

Fig 3-5-2 shows the calculated ratios of the Rutherford cross-sections at angles θ and θ - 16° for θ-value near 8°. If measurements are made at nominal angles of +8° and -8° then, as seen with the inset, an offset of 0.1° in angle θ results in a ratio different from unity by 10%. If the beam is offset from the centre of the rotation arm, there is an offset of the solid angle Ω of the detector as well. Taking this effect into account the accuracy of the true angle of the ER detectors can be defined to about ±0.02° if the ratio is measured to 1% and the measurements are made at the nominal angle θ ~ 10° (see the

Appendix for details). This technique becomes less precise as the nominal angle increases. For example, a ±1% measurement of the ratio of the cross-sections at ±30° defines the angle to about ±0.03°.

In order to use the above method, the Rutherford scattering from the target material must be resolved from other reaction products such as particles elastically scattered from the carbon backing of the target and other light impurities (like oxygen and so on). At forward angles the energy of these scattered particles is only slightly smaller than of those scattered from the target material. For instance, at 6° the energy of particles scattered from ^{16}O is only about ~500 keV less than those scattered from a ^{154}Sm target. This small energy difference can not be resolved by a MWPC but can be using a SSB detector. Another movable SSB detector was, therefore, mounted in front of the filter and just behind the entrance aperture, which is also shown on the Fig. 3-5-1. This SSB detector is assigned as the calibration Si detector (CSD). Using this detector, when it is immediately behind the aperture, the Rutherford scattering from the target (at angles $\theta \geq 6°$) can be measured hence the true angle of the filter and its solid angle can be determined by the following procedures.

The sequence of measurements made is shown schematically in Fig. 3-5-3 and the changes of the angle θ due to the shift of beam spot is illustrated in Fig. 3-5-4. For simplicity, the velocity filter and the MWPC, which are set behind the CSD and not being used for the calibration purposes, have been omitted on this figure. The entrance collimator, just in front of CSD, is approximately aligned on the centre axis of the movable arm. A measurement of elastic scattering was first made by positioning the arm at a nominal angle θ. Another measurement was then made without changing any conditions of the

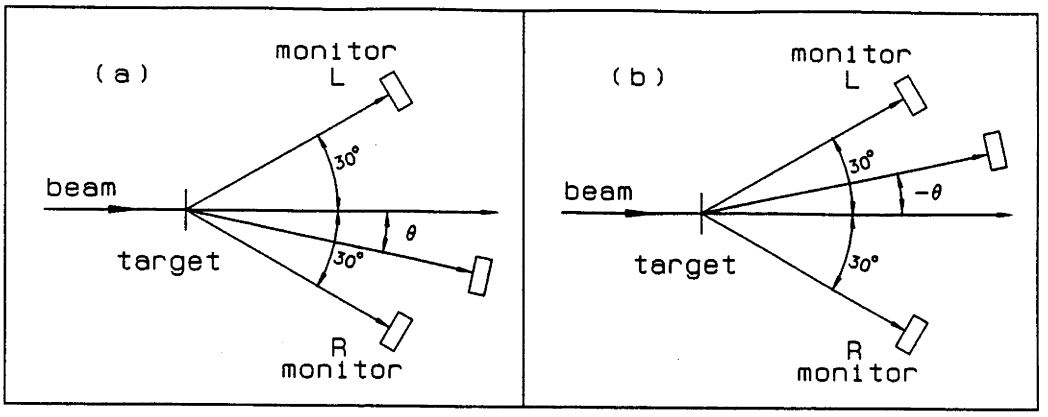

Fig. 3-5-3: Sequence of measurements made in calibrating the angle and solid angle of the ER detectors. The measurements had been made at the nominal angles ±6°, ±8°, ±10° and ±12°.

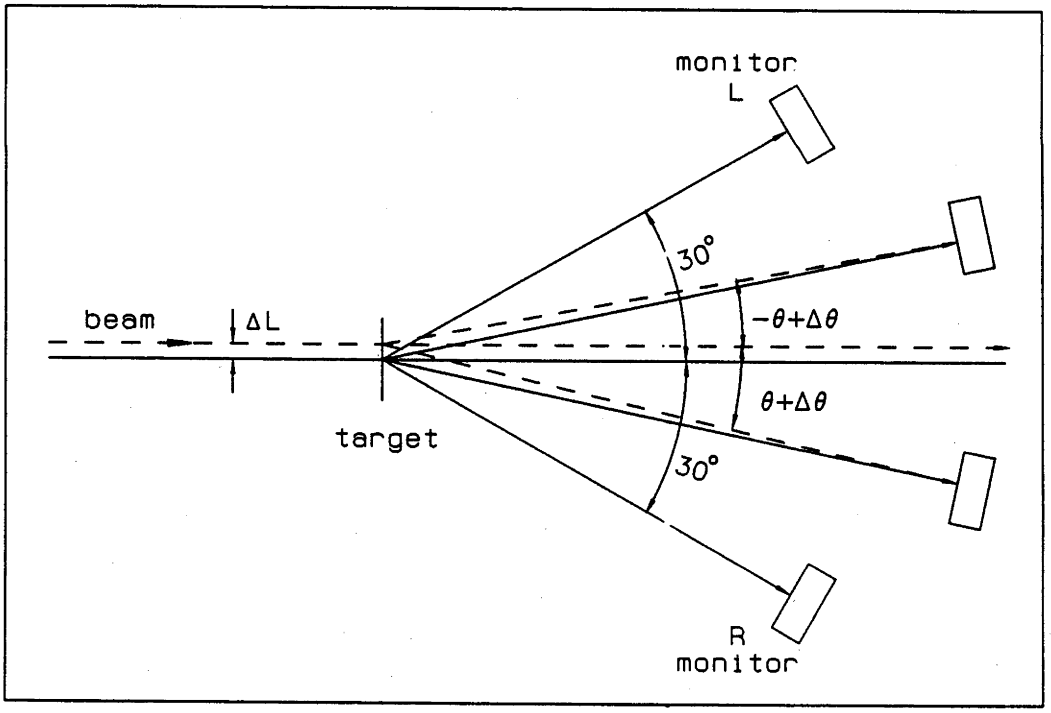

Fig. 3-5-4: Illustration of the angle θ changes due to the parallel shift of the beam spot position horizontally from the symmetry axis of the experimental set up.

set-up but the arm was moved through an angle $\varphi = 2\theta$ to be located nominally at $-\theta$ (Fig. 3-5-3b). As it will be discussed in §5.5.7, the accuracy of the rotation angle φ was estimated to be ~0.01°. Elastic scattering was measured with sufficient statistics in all counters to give <1% accuracy in the ratio of the Rutherford cross-sections at angles $\pm\theta$. This sequence of measurements has been followed for a nominal angle θ equal to 6°, 8°, 10°, 12° and a consistent value for $\Delta\theta$ obtained within the statistical errors (<0.02°). After the angle had been determined the CSD was withdrawn and the ERs can be measured by the position sensitive MWPC.

The re-tuning of the beam, during the changes of beam energy, may shift the beam spot position. However, this will result in a change of the ratio of the elastic scattering of the two monitors (at ±30° to the beam). This change of the ratio of two monitors was used to extract the changes of beam spot at each measurement. Since the two monitors were located approximately ±30° to the beam axis, only ~0.03° accuracy of the angle change $\Delta\theta$ could be determined, as previously discussed. Considering all factors the angle of the filter was determined to an accuracy of ~±0.05° (see the Appendix for details).

The same procedure is applied to the large angle ER detector (LAERD). A ±0.05° accuracy of the true angle of this detector is then also achieved.

As well as a horizontal shift in beam spot, there could be a vertical shift of it. Calculations show, to the first approximation, the change of the angle and the solid angle of ERs are about one to two orders of magnitude smaller than that of the beam moving horizontally; hence vertical movements have been ignored.

3.5.3 Determination of Absolute Cross-Sections of ERs

The sequence of measurements discussed above were used also for the purpose of determining the absolute cross-sections of ERs. Adding the ratio of the elastic scattering measured in the monitors and CSD at angles $\pm\theta$, one gets (see Appendix for detail, for instance the Eqs. (A-3), (A-6) and (A-13))

$$\frac{N(\theta)_+}{(N_{ML}+N_{MR})_+}+\frac{N(\theta)_-}{(N_{ML}+N_{MR})_-} = \frac{2\frac{d\sigma(\theta)}{d\Omega}\Omega}{\frac{d\sigma}{d\Omega_{ML}}\Omega_{ML}+\frac{d\sigma}{d\Omega_{MR}}\Omega_{MR}}$$

$$= 2\frac{d\sigma(\theta)}{d\Omega}\frac{1}{T} \qquad (3\text{-}5\text{-}1)$$

where $N(\theta)$, N_{ML} and N_{MR} are the detected elastic events in the CSD, the left and right monitors.

The value

$$T = \frac{\frac{d\sigma}{d\Omega_{ML}}\Omega_{ML}+\frac{d\sigma}{d\Omega_{MR}}\Omega_{MR}}{\Omega} = \frac{2\frac{d\sigma(\theta)}{d\Omega}}{\left[\frac{N(\theta)_+}{(N_{ML}+N_{MR})_+}+\frac{N(\theta)_-}{(N_{ML}+N_{MR})_-}\right]}$$

(3-5-2)

is constant for a given energy.

Since to first order, as it has been shown in the Appendix, the errors resulting from the offset angle $\Delta\theta$ vanish in the equation (3-5-1) then the angle θ is known, the value of T can be determined accurately.

Using all the ratios measured at ±6°, ±8°, ±10° and ±12°, and noting that the ratios were measured to ~1%, the T was determined to ~1% by a least square fit.

For evaporation residue measurements, the ratio of the number of ER measured, N_{ER}, to the summed numbers of elastic scattering events measured in monitor L and R , $N_{ML} + N_{MR}$ is:

$$\frac{N_{ER}}{N_{ML} + N_{MR}} = \frac{\left(\frac{d\sigma}{d\Omega}\right)_{ER} \Omega}{\frac{d\sigma}{d\Omega_{ML}} \Omega_{ML} + \frac{d\sigma}{d\Omega_{MR}} \Omega_{MR}} \qquad (3\text{-}5\text{-}3)$$

this gives:

$$\left(\frac{d\sigma}{d\Omega}\right)_{ER} = \frac{N_{ER}}{N_{ML} + N_{MR}} \left[\frac{\frac{d\sigma}{d\Omega_{ML}} \Omega_{ML} + \frac{d\sigma}{d\Omega_{MR}} \Omega_{MR}}{\Omega} \right] \qquad (3\text{-}5\text{-}4)$$

The factor in the square brackets is simply equal to T, hence the differential cross-section of ER is known:

$$\left(\frac{d\sigma}{d\Omega}\right)_{ER} = \frac{N_{ER}}{N_{ML} + N_{MR}} T \qquad (3\text{-}5\text{-}5)$$

As shown in the above equation, elastic scatterings measured in two monitors were summed together for the normalization. There is an advantage to extracting ER differential cross-sections accurately by placing the two monitors at both sides of beam direction. Because even though the measured elastic events in both monitors are affected by the movement of the beam spot, the sum of them is not affected by the changes of the effective beam spot at each measurement (see the Appendix for details).

3.5.4 Targets

Targets of ^{154}Sm and ^{186}W were made by evaporating or sputtering the isotopically enriched (~98.69%, ~97.06% respectively) target materials onto ~10μg/cm^2 carbon backings. By placing a suitable mask in front of the carbon backing, target material was deposited in a 2 mm vertical strip so that only if the beam spot shifts less than 1 mm horizontally from the centre can it hit the target during the measurements. The thicknesses of the targets were approximately estimated by weighing reference foils, placed with the targets in the evaporator. Since multiple scattering smears out the angular distributions and it is dependent on the thickness of the target, this was minimised by making thin (~40μg/cm^2) targets. Calculation shows that with this thickness of targets, the smearing of the angular distribution is negligible [Sig74, Hin82]. Average energy loss of beam particles is ~50 keV for passing through the carbon backing and ~100 keV for passing through the target [Nor70]. The average beam energy was therefore ~100 keV lower than the nominal value of beam energy.

3.5.5 Electronics

The electronics arrangement used for the measurements is shown in Fig. 3-5-5 and a list of the units and their designations not given in Table 3-4-1 is given in Table 3-5-1. It consists of "fast" and "slow" electronic units. The fast units, located near the 2 m scattering chamber, produced the TOF and position signals, and the slow electronic units, located in the accelerator control room, produced the ΔE, energy and logical signals. All the TOF signals obtained from MWPC, LAERD, and monitors were derived from Time to Amplitude

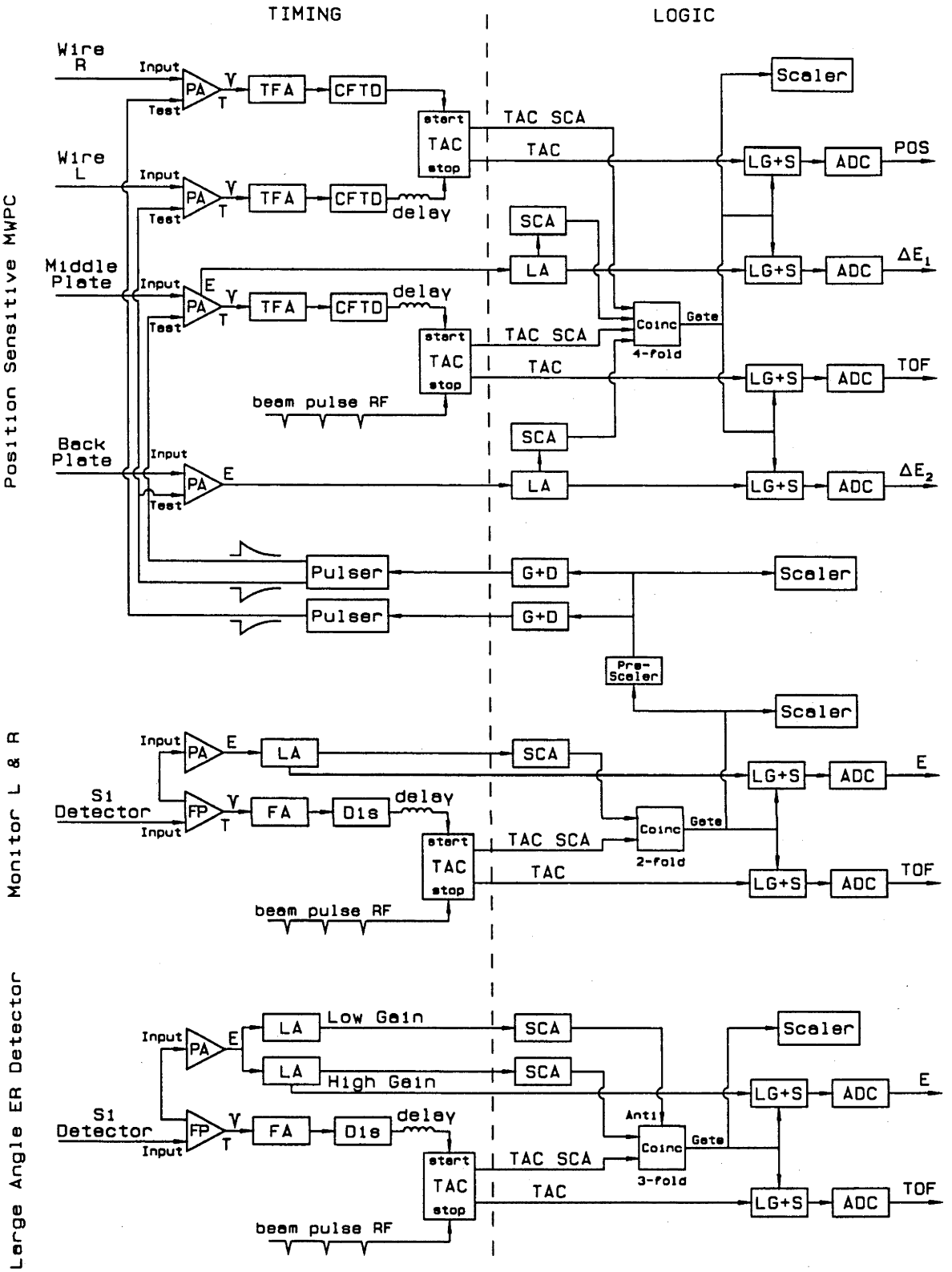

Fig. 3-5-5 Electronics scheme for ER measurements.

Table 3-5-1

FP	ANU Fast Preamplifier.
FA	LeCroy 612A 12 Channel PM Amplifier.
Dis	LeCroy 821 Quad Discriminator
SCA	Canberra 1437 Time Single Channel Analyser.
LG+S	Canberra 1454 Linear Gate and Stretcher.
Coinc	Canberra 1446 Coincidence Unit.
G+D	Ortec 416A Gate & Delay Generator.
Anti	Anticoincidence input.
ADC	Canberra 7432 UHS Analog to Digital Converter.
Pre-scaler	ANU Pre-scaler.
Scaler	ANU Scaler.
Pulser	BNC BL-2 Pulse Generator.

Converters started by the signals from the detectors and stopped by the RF signal from which the beam pulsing was derived.

The position signals from the MWPC were obtained, as discussed in §3.4.2, by measuring the finite propagation time of electromagnetic signals in the delay line linked to each wire of the MWPC. The time difference at each end of the delay line was also converted to amplitude by a TAC.

The logic electronics selected only those events coincident with ΔE_1 ΔE_2, TOF and position signals for the MWPC, and those events coincident with TOF and energy for the LAERD and the monitors.

All the signals were recorded event by event on a magnetic tape through a VAX 750 computer. All the logic signals, used for gate signals in the (LG+S), were counted by scalars. These counted numbers were compared with the number of the events recorded by the computer to extract the dead time of the computer and the LG+S units.

Since the position sensitive MWPC was used to measure the ERs at very forward angles (as close as 0.5° to the beam). The counting rate of the MWPC could be very high at angles less than 2° resulting from slit scattering of beam particles from the entrance collimator of the MWPC. In this situation the beam was reduced to keep the counting rate of the MWPC less than 5000 Hz . In order to monitor the dead time of the whole system, electronic pulses were injected into the detecting system. Two pulsers were used and both were triggered by one of the monitors. The pulses were sent to the MWPC through the test input of the pre-amplifiers and were sent also through an ADC to be recorded on the magnetic tape. A comparison was made between the numbers of the injected pulses and the numbers of the coincident events of ΔE_1, ΔE_2, TOF and position of the MWPC, which were generated by the pulses. The dead time of the whole system of the MWPC was, therefore, extracted. The use of the monitor signals to trigger the pulsers is because the number of pulses sent to the MWPC per-second reflects the intensity of the beam which changes the counting rate of the system, hence the dead time of the system.

Since the MWPC had four output signals to input to the computer, it would cause a considerable dead time to the computer when the counting rate is high. In order to reduce this dead time the TOF range was restricted so that particles with "short" flight times were

rejected. Thus, the events of "elastic-like" particles which could contribute high counting rates were suppressed and were not sent to the computer.

In each measurement the dead time of the whole system of the MWPC was checked, and was found to be less than 1%. The data were then corrected by these extracted dead times.

Since the counting rates on the monitors and the LAERD were low (~100 Hz), the dead time of these detectors was negligible and hence, was not monitored.

There were two linear signals from the energy output of the large angle ER detector, one with a low gain and the other with a high gain. This was because the energy output of ERs in the Si detector was much smaller than that of ELs, therefore a rather high gain of the linear amplifier was required in order to obtain the ER's energy signal. Under this high gain the energy signals of EL were saturated. The saturated pulses (about 10 V) could not be cut completely by setting an SCA window. The output of an additional low gain amplifier was sent to another SCA unit with a window on the elastic signals only. The logic pulses from this SCA were than used in anticoincidence to ensure total rejection of the elastic events.

3.5.6 Efficiency of The Experimental Apparatus

The efficiency for transmission of ER through the filter was determined in the following manner [Wei91].

The velocity filter is designed for the measurements of ER cross-sections after fusion induced by a range of projectiles with a mass

range of A~10 to A~40, such as ^{16}O and ^{28}Si, which are available from the 14 UD at the ANU. Calculation shows that the separation between the ERs and the elastics increases as the mass of the projectile is decreased. For example, in the ^{16}O induced reactions the separation is about one and half times larger than that for the ^{28}Si induced reactions. In order to provide the most stringent test, measurements were made for the heavier projectile ^{28}Si on a target of ^{130}Te. The target (~40 $\mu g/cm^2$) was 2 mm wide vertical strip on a carbon backing (~10 $\mu g/cm^2$). For all the measurements performed in here, the beam was pulsed to provide a 1 ns wide burst every 533 ns. The beam energy was 160 MeV and the energy of ERs was expected to peak at ~28.4 MeV. The high voltages supplied to the electrodes of the filter were ±13.5 kV.

The transmission efficiency of the velocity filter was firstly studied. The filter was set at 5° to the beam direction, where elastic scattering was not too intense. The differential cross-section for the ERs was then measured using the SSB detector, just behind the entrance collimator. The energy and time of flight (TOF) of the detected particles were used to identify the ERs. With all other conditions unchanged the SSB detector was withdrawn and the cross-section was re-measured with the MWPC, now after passage through the filter. The ER were identified by their energy loss, ΔE, position and TOF. The ratio of the cross-sections measured behind and in front of the filter was 1.03 ± 0.04; consistent with an efficiency close to 98%.

Before making the test measurements of blocking the elastics, calculations for the deflections of the particles had been made. Shown in Fig. 3-5-6 are the calculated deflections of the ERs, the elastics and the target recoils, at the MWPC position, for the reaction of $^{130}Te + ^{28}Si$.

The magnetic and electric fields of the filter are 0.14 Tesla and 10 kV/cm respectively. For ^{28}Si and ^{130}Te the solid line is for the equilibrium charge state whilst the dashed lines show the effect of the FWHM of the charge state distribution (from ref. [Bet72]). For the highly excited ER, represented by ^{154}Dy, the average charge state is expected to be higher than the equilibrium value (~15±5) and the FWHM of the distribution wider [Fre83a, Cor83]. A higher average charge state value of 20 is used in the calculation for the ERs of ^{154}Dy

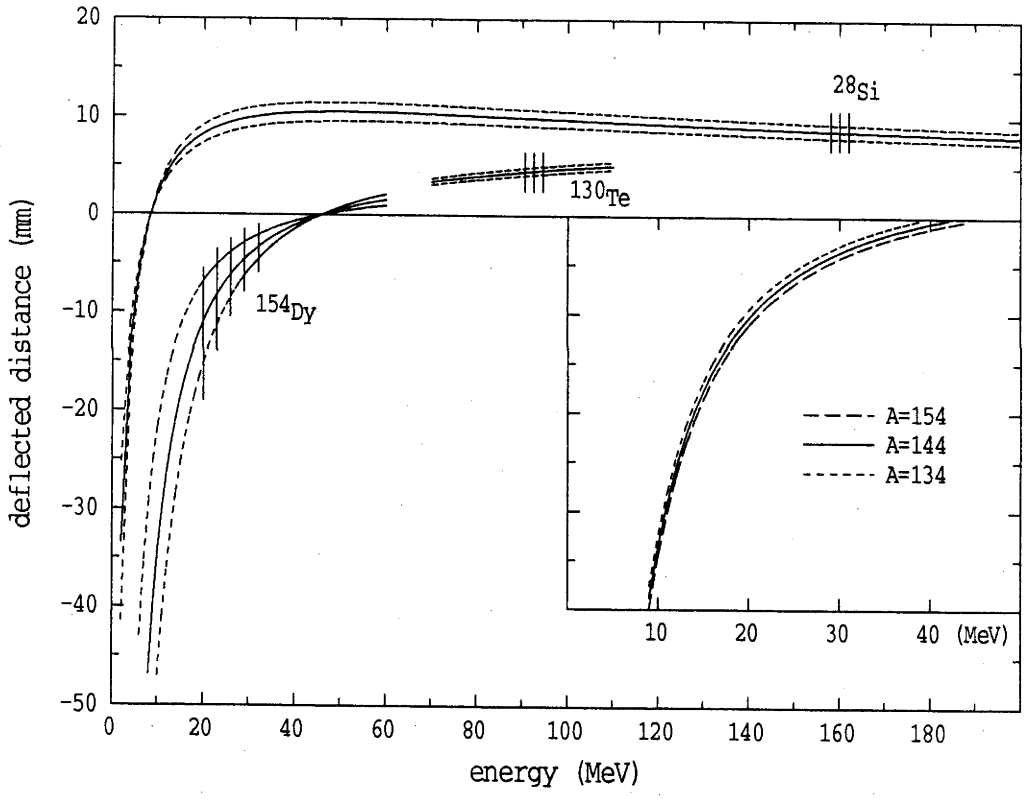

Fig. 3-5-6: Calculated deflections of elastic events, recoiling target nuclei and ERs for the reaction ^{130}Te + ^{28}Si. The vertical hatched areas indicated the expected energy distributions of these products for 160 MeV ^{28}Si. The dashed lines indicate the spread in deflection due to the charge state distributions. The inset shows the deflection for ERs of different mass.

(after four neutrons are emitted from the compound nuclei). This is shown on the figure by solid line and indicated by "^{154}Dy". The dashed lines for ^{154}Dy represent the charge states of 12 and 27 respectively.

The vertical hatched areas indicate the energies expected for the ERs, the recoiling target ^{130}Te and 160 MeV ^{28}Si ions. The ^{28}Si and ^{130}Te are well localised in both position and energy. The ERs have a larger spread in position due mainly to their wide energy range, estimated using the Monte Carlo evaporation code PACE2 [Gav80]; the charge state distribution plays a significant but secondary role. The range of masses comprising the ER is relatively unimportant, as indicated in the inset in Fig. 3-5-6, for a fixed charge state of 20. Thus all ERs, with their wide energy, charge and mass distributions, are expected to be transmitted through the filter to form a peak of width ~10 mm in our detector.

At this energy and at the forward angle of a few degrees, the intensity of the targets recoils is negligible, however, if there are any, they will be identified and separated from the ERs by their TOF (as discussed in §3.1.2) and/or their energies (as showing in Fig. 3-5-6).

The measurements to determine the effectiveness of blocking elastic scattering were carried out at 4°. Initially the beam intensity was very low and the finger was withdrawn. All the ERs and the elastic events entered the position sensitive MWPC and were identified by their time of flight and energy loss (ΔE). After about one hour there were a few thousand ER events detected and the ERs and elastics could be well located, the finger (a thin tantalum plate ~200 μm thick) was then moved in to stop the elastically scattered beam and the ERs were re-measured.

The results of these measurements are illustrated in Fig. 3-5-7. The lower half of the figure shows TOF vs ΔE, with elastically scattered particles impinging on the MWPC. On the right are the position spectra corresponding to the indicated windows for the ER and elastic

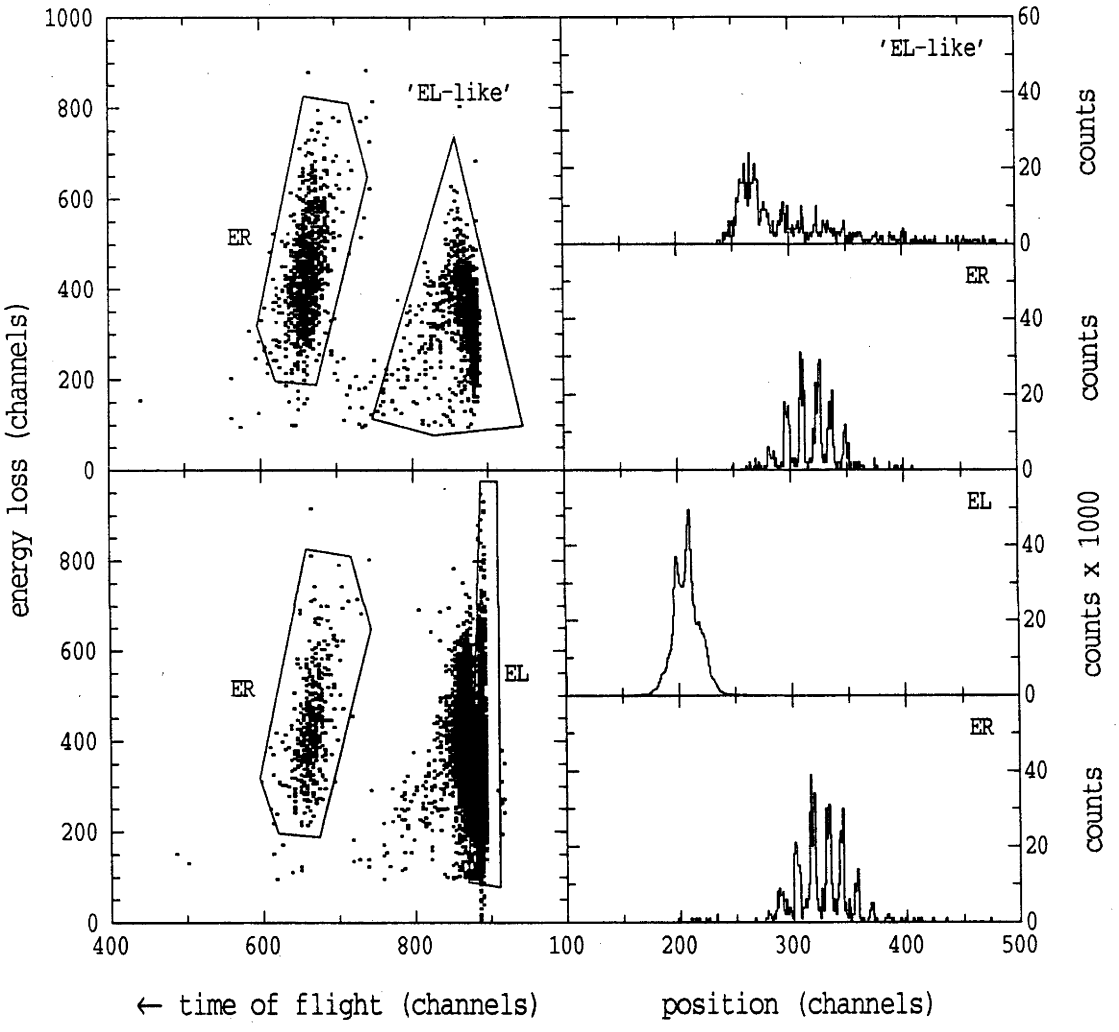

Fig. 3-5-7: Energy loss in the MWPC plotted against time of flight. The lower spectrum contains elastically scattered particles which, as seen in the projections of the two dimensional gates on the right, are well separated from ERs in position. Note the change in scale for the elastic peak. The top half of the figure shows the effects of blocking the elastic scattering with a tantalum stopper.

scattering. The ER position spectrum is well grouped in the MWPC, covering only ~20 mm of the 100 mm length and the elastic peak is only ~3 mm wide. The positions and widths are in good agreement with those expected from Fig. 3-5-6. The spikes in the spectrum show individual position wires. The position and ΔE distributions show no evidence of loss of the ERs, consistent with the measured efficiency.

More importantly, the ER group is well separated in position from the elastic peak. Therefore the elastic peak can be physically blocked without effecting the detection of the ERs. The upper half of Fig. 3-5-7 shows the effect of blocking the elastic peak. In this case the tantalum stopper reduced the count rate in the MWPC by a factor 2000, totally suppressing the elastic scattering.

A group of particles, now of only minor intensity, with TOF and ΔE consistent with elastic-like particles, remains but their positions are spread throughout the detector. These are almost certainly the result of scattering from the aperture at the entrance to the filter. Elastic scattering from the target is deflected by only ~1.5° in the filter, thus a deflection of this order at the entrance to the filter can result in particles being transmitted and detected. Even so the ERs constitute almost half of the total count rate in the MWPC.

3.5.7 Procedures

The experiments in this work were designed to measure the evaporation residue cross-section to a high precision (up to ~1%) at energies around the Coulomb barrier. To achieve this high precision attention had to be paid to define the beam energy, detector angle and target.

In order to set up the beam energy correctly the energy defining the magnet field was recycled slowly three times from zero to its maximum value and to zero again. Then the magnet field was increased slowly to reach the field required for the lowest beam energy taking care not to exceed the required field. When a higher field setting was required the magnet was slowly increased but when a lower value was required the recycling procedure was again used. This procedure was adopted in order to avoid differential hysteresis effects. The magnetic field was measured at one point using a NMR probe. The hysteresis effect may be slightly different between the measured point and along the trajectory of the particles. The recycling method has been shown to accurately reproduce the field at the NMR location [Spe77]. More than twenty magnet calibration measurements over the last 15 years have a standard deviation of ±0.04%. The most recent measurements, using the $^{12}C(p,\alpha)^{9}Be$ resonance at 14.23 MeV, were performed during these fusion experiments. Thus, the absolute energies of the beam can be defined better than ±50 keV at a bombarding energy of 50 MeV and better than ±100 keV at bombarding energy of 100 MeV, and the relative beam energies in a 0.5 MeV interval were defined with an accuracy of ±5 keV.

In order to reproduce the angle of the ER detector accurately the rotating arm on which the ER detectors are mounted was always moved in the same direction when setting angles. The digital read-out of the angle is limited to a precision of 0.1°, but it takes a few seconds for the arm, when rotating slowly to travel through this angle. The read-out will not change while the arm is rotating until it reaches the next 0.1° higher (or lower) value. In order to set up the angle accurately the arm was always rotated slowly and was de-clutched as

soon as the setting value appears on the control panel. This procedure may introduce some "human" error, but it was shown that the error is less the 0.01° after measuring the ERs at the same energy and the same angle but re-setting the angle many times.

Since, due to multiple scattering, the angular distribution of the evaporation residues may change if the target thickness changes, for each reaction all the measurements were carried out with one target. At the end of each reaction measurement, the ER differential cross-sections which were measured at the beginning of the measurement were re-measured. The results consistently agreed with each other within experimental error; indicating that there was no significant change in the thickness of the target.

A number of ER angular distributions at different beam energies were measured for each reaction. These spanned a range from a few MeV below the Coulomb barrier to an energy of 110 MeV. It would be too time consuming to measure full angular distributions for each beam energy. Therefore most measurements were carried out only at ±2° for each half MeV interval and these were then converted to the total cross-sections.

3.5.8 Accuracy of the Measurements

As previously discussed in this chapter the efficiency of the velocity filter and the position sensitive counter are consistent with the expected value of 98%. The angles of the ER detectors were determined to be better than ±0.05°, the relative energies of the beam were determined to better than ±5 keV and the absolute energies of the

beam were determined better than 100 keV. The smallest angle to the beam direction at which the ERs were measured was 0.5°.

The measurements carried out using this system are reasonably efficient. An excitation function can be completed within 72 hours of machine time, involving 40 to 50 different energies spanning the Coulomb barrier region.

The statistical errors of the ER cross-sections were generally < 30% for cross-sections up to 1 mb and ~±1% for cross-sections higher than 100 mb and < 5% in between. In principle, a lower statistical error for the higher cross-sections (≥ 100 mb) can be obtained by measuring more ER events and this can be done very easily and quickly in a short time by using this system (for example it took only about 20 minutes to achieve a precision of ±1% (~10,000 events) at higher energy). However, other random errors, involved in, for example, defining the energy steps and setting the ER detector angles at ±2° have to be taken into account. Though, as described before, extreme care had been taken to reduce these errors, we have chosen arbitrarily to restrict the quoted errors to 1%, even though some of the total cross-sections had statistical errors less than this value.

Systematic errors, such as the defining of the absolute beam energy, (even though they are expected to be very small), may occur and result in a systematic shift of the measured ER excitation function, for example a few tens of keV shift of the excitation function by the uncertainty in the absolute beam energy. However, because the major aim in this work is to extract the barrier distribution from the fusion excitation function, these systematic errors are relatively unimportant. It results only in a minor scaling or a minor shift of the

extracted barrier distribution without affecting its overall shape; the most interesting features of the relative weighting of barriers can be still observed in the distribution.

A systematic error in the beam energy may result from the recycling procedure of the magnet. This results in a shift of the excitation functions measured before and after the recycling procedure. However, as discussed before and the details given in §4.2.1, this has been found to be small and no error larger than the statistical uncertainty was found after the magnet recycle procedure.

To extract the fusion cross-sections one needs to know both the ER and the fission cross-sections. In the $^{154}Sm + ^{16}O$ reaction the fission cross-sections are very small compared with the ER cross-sections in the energy ranges studied in this work. Even at the highest energy of 110 MeV the fission constitutes less than 1% [Sik64, Cha84]. The fusion cross-sections were simply taken as the ER cross-sections for the reaction of $^{154}Sm + ^{16}O$. The precision of the fusion cross-section is therefore equal to that of ER cross-section.

There is a small but non-negligible fission possibility for the heavier target ^{186}W in the energy region we studied. The fission cross-sections were taken from the measurements of Bemis et al [Bem87]. Though the fission-cross-sections were not measured to ±1%, they will not affect the precision of our fusion cross-sections because the fission cross-sections are less than 2% of the ERs at the energies of most interest (~67 to ~80 MeV in lab energy). For example, at the worst case of 80 MeV, the fission cross-section is only ~4 mb while the ER cross-section is ~230 mb Even if the uncertainty in the fission cross-section is

10%, the total error of the fusion cross-section maintains the same error of 1% of the ERs.

There may also be some systematic errors introduced by using these fission cross-sections. The energy scale used in the fission measurements may be shifted slightly with respect to the scale used in this work and hence result in a systematic shift for the total fusion cross-section. For instance the ER excitation function measured by Bemis et al has a relative shift of ~0.5 MeV. Thus it is possible there is a similar relative shift in their fission measurement even though the fission cross-sections were measured at a machine different with the one used for their ER measurement. Taking the worst case as an example again, ~±0.5 MeV shift of the absolute value at this lab energy results in an error of ~±1.1 mb in the fission cross-section of ~4 mb. Added this to fusion, the total error of the fusion cross-section is ~1.5% instead of ~1% of the statistical error only. However, since the 0.5% error is the systematic error it will only cause a minor error in the extracted barrier distribution at the higher energies (close to 80 MeV) and will not affect the shape of the extracted barrier distribution.

For the highest energies of 90 and 100 MeV, the fission cross-sections are ~12% and ~30% to the ER cross-section. Half MeV shift in these energies will result in extra ~±6 mb and ~±10 mb errors to the fusion cross-sections at 90 and 100 MeV respectively. These will add a considerable error to the fusion cross-sections (the total error in fusion will be ~±3%), but since the energies are well above the barrier region, they will not affect the extracted barrier distribution.

Chapter 4
Experimental Results and Analysis

4.1 EVAPORATION RESIDUES

4.1.1 Spectra

Typical spectra from the reaction induced by 74 MeV ^{16}O on ^{154}Sm in the MWPC are shown in Fig 4-1-1; (a) and (b) of this figure show the position vs ΔE_1 and TOF respectively. The left side of the MWPC, up to the vertical dashed line, has been covered by the tantalum finger to stop the elastically scattered particles that are deflected to, and peaked at, the left side of this line. However, this did not affect the detection of ERs that deflected to the right side, as is clearly shown in Fig. 4-1-1 (b); there was no cutoff on their position by the finger. The "elastic-like" beam particles, slit scattered from the aperture at the entrance to the filter or the edge of the finger, spread over the whole range of position in the MWPC and some of them had similar times of flight to the elastic events. On closer inspection of Fig. 4-1-1 (a) and (b) one may see structure in the position, which shows the individual wire pairs. Fig. 4-1-1 (c) and (d) shows the TOF vs the ΔE_1 and ΔE_2. ΔE_1 which comes from the front cell of the MWPC has been used to check whether all the ERs detected in the front cell have passed through the plastic foil (~50 $\mu g/cm^2$) of the cathode and given a ΔE_2 signal in the back cell. This has been checked for all the energies and all the angles. There is no evidence that there is a loss of ΔE_2 signals of ERs in the back cell of

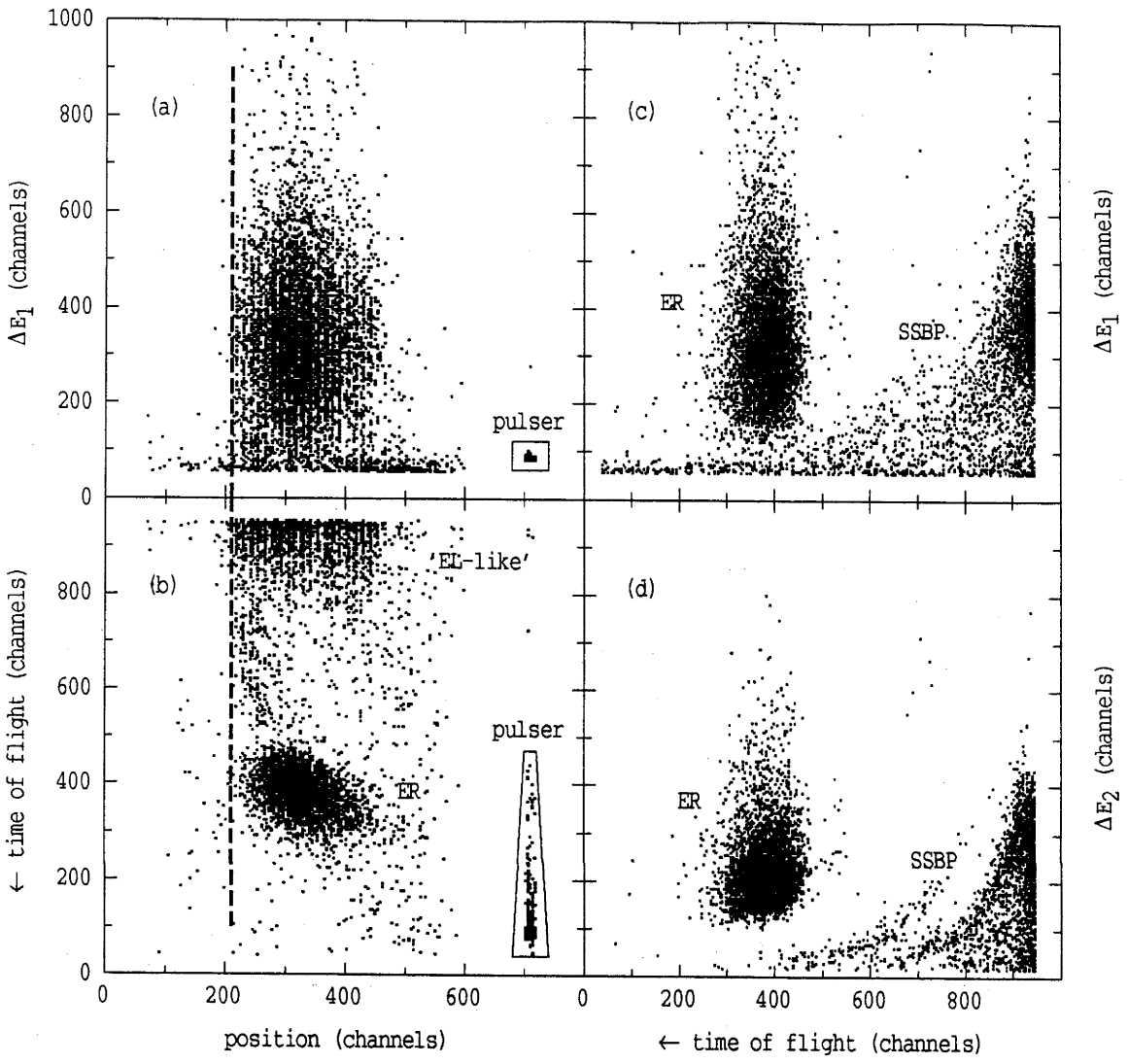

Fig. 4-1-1: Spectra for the reaction of ^{154}Sm + ^{16}O in MWPC at an angle of 4°. (a) and (b) show the position vs the ΔE_1 and TOF respectively. Evaporation residues are located at the right side of the dashed line. Up to that line the MWPC had been covered by a tantalum finger from the left. Intense elastic scattering, deflected to the left, had been stopped by the finger. (c) and (d) show the TOF vs ΔE_1 and ΔE_2. Better ΔE resolution on the ΔE_2, achieved by increasing the ionisation path, allowed a good separation of ERs.

the MWPC. Since there is better ΔE resolution (~15% FWHM) from the back cell, a very clear separation of ERs from other particles can be seen in the spectrum TOF vs ΔE_2 in the Fig. 4-1-1 (d). This was true for all the angles and all the energies in the reactions studied in this work. This spectrum, TOF vs ΔE_2 was therefore used in the extraction of the cross-sections measured using the MWPC.

When the MWPC measured the ERs at an angle of 4° to the beam axis the LAERD measured ERs at -16° simultaneously. Fig. 4-1-2 shows the spectrum of TOF vs energy of the LAERD. Although there are some low energy particles spread over a large range of TOF their intensity is relatively low and the ERs can still be reasonably identified. The statistical error at this angle is still a few percent, and this gives a rather reliable determination of the shape of the angular distribution of the ERs as discussed in §4-1-3.

The background formed by these low energy particles in the spectra of LAERD has been found to be almost independent of energy and only increasing slightly with increasing angle. These particles are quite possibly multiply-scattered target nuclei recoiling initially at large angles. For examply, when 74 MeV beam particles elastically scatter to 30°, the target particles recoil to ~73° with energy ~2 MeV. With the recoiling angle of ~73° to the beam direction the effective thickness of the target is about three times greater than that if they recoil to 0° to the beam direction, hence it increases the chances of multiple scattering. Though the intensity of these low energy multiply-scattered recoils is very low, when the differential cross-section decreases as the angle increases or as beam energy decreases, these low energy target recoils will still form a noticeable background in the

spectra of the ER detector, like the one shown in Fig. 4-1-2, but not in Fig. 4-1-1. Because the differential cross-section at 16° is two and half orders of magnitude smaller than at 4°, the uncertainty in the differential cross-section for ERs has only a minor effect on the extracted total ER cross-sections.

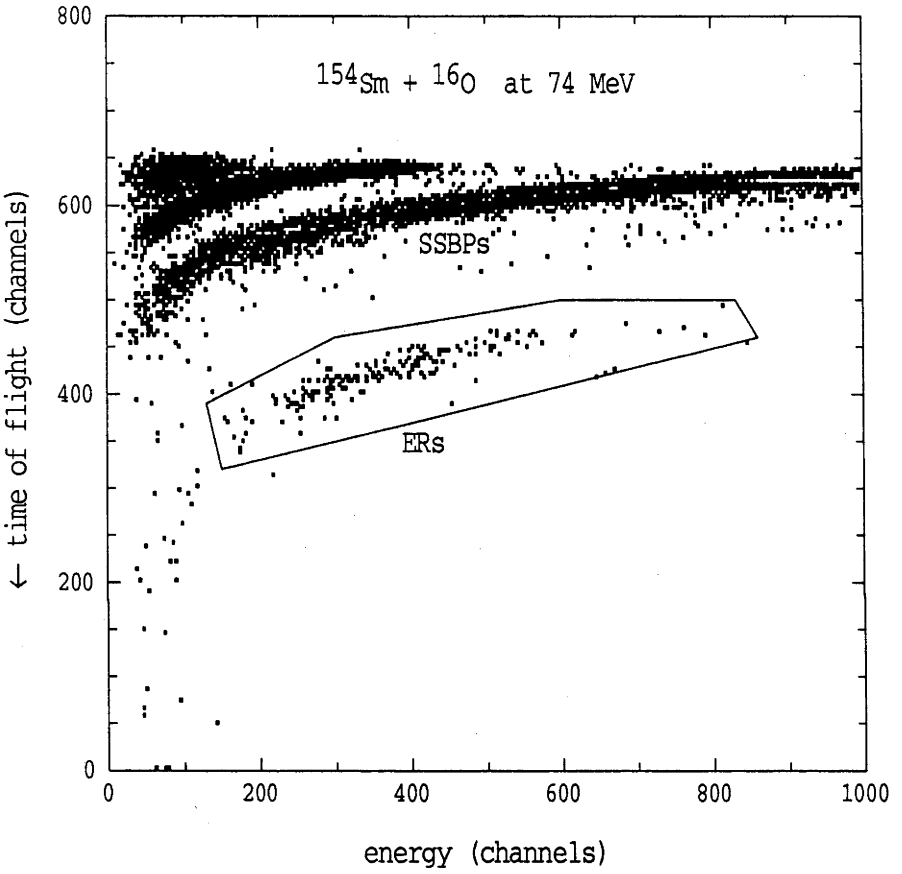

Fig. 4-1-2: Energy vs time-of-flight spectrum for reaction of ^{154}Sm + ^{16}O at -16° measured by a Si detector (LAERD).

4.1.2 Differential Cross-Sections

The differential cross-sections for ER were normalised and extracted by the methods discussed in §3.5.3, and the formula (3-5-5) is used. The values of T for the MWPC and the LAERD were found in the

elastic scattering measurements at the energy of 90 MeV. Table 4-1-1 is the list of the measured values of T_{MWPC} and T_{LAERD}.

Table 4-1-1: T values for the reactions listed

Reactions	E_{lab} (MeV)	T_{MWPC} (mb/sr)	T_{LAERD} (mb/sr)
$^{154}Sm + ^{16}O$	90	1.76×10^6	1.78×10^7
$^{186}W + ^{16}O$	90	2.53×10^6	2.56×10^7

The different values of T for different reactions reflect the variation of the Rutherford scattering cross-section with the product of reaction atomic numbers $(Z_1Z_2)^2$ at the same bombarding energy. At other energies, the values of T were readily extracted from the measured values at 90 MeV because Rutherford scattering cross-sections are $\propto \frac{1}{E^2}$. Thus:

$$T(E) = \frac{90^2}{E^2} T(90) \qquad (4\text{-}1\text{-}1)$$

4.1.3 Angular Distributions of Evaporation Residues

Typical angular distributions of the ERs are shown in Fig. 4-1-3. The common features of the angular distributions are the relatively strong and narrow Gaussian-like distribution and a less intense tail extending to larger angles. The explanation is based on the evaporation of neutrons, protons, and α-particles; the neutrons and protons have relatively small momentum and hence produce only a small deflection to the ER; this results in the narrow Gaussian-like distribution of ERs. The higher momentum of the α-particles

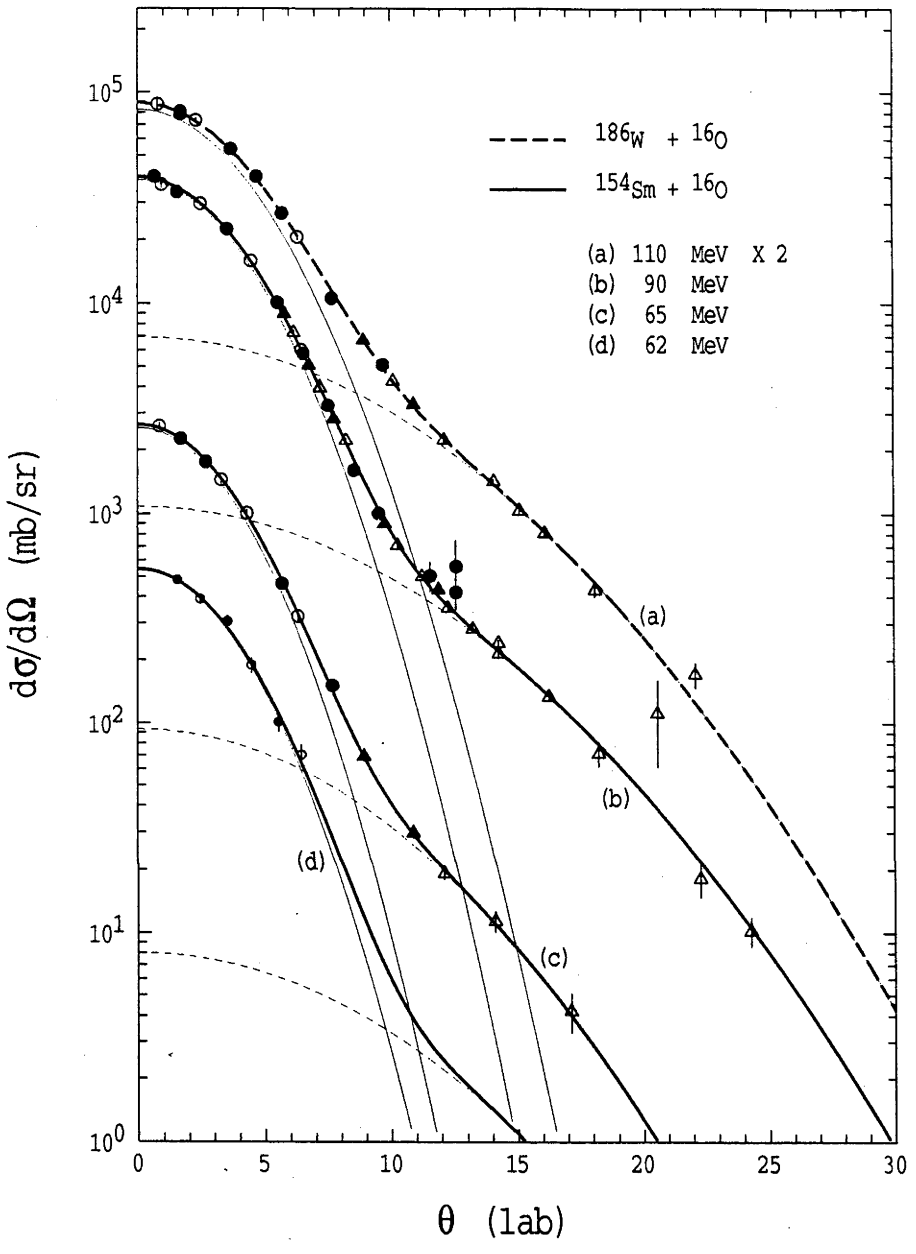

Fig. 4-1-3: Typical ER angular distributions for $^{154}Sm + ^{16}O$ and $^{186}W + ^{16}O$. The circles were measured with the MWPC and the triangles were measured with the LAERD. The solid symbols indicate positive angles, whilst hollow ones show measurements made at negative angles. The heavy lines are fits to the data, each comprising the sum of two Gaussian distributions (fine and short dashed lines).

produces much larger deflections to the ER, resulting in the tail extending to the larger angles.

A program has been used to fit these angular distributions by adjusting the free parameters of various functions in order to minimize the χ^2 of the fit. A number of functions have been used for this purpose. The number of free parameters used in those functions varies from 5 for two Gaussians (two heights, two widths, and a small offset of zero angle of the two Gaussian functions) to 10 for a complex function which combined a Gaussian, exponential tail and Fermi function. It was found that the more complex distributions gave only a marginal improvement in the quality of fitting when compared with the two-Gaussian method.

Thus, because of the simplicity and fewer parameters the two-Gaussian distribution was chosen to fit all the ER angular distributions measured in this work. The typical normalised χ^2/N of the fits are between 1 and 4, and vary from reaction to reaction. The heavy solid lines shown in Fig. 4-1-3 are the two-Gaussian fits to the measurements.

Even though both positive and negative angles were measured, and the true zero angle was determined to $\pm 0.05^\circ$ from elastic scattering as in section §3.5, a small additional offset of zero angle was allowed in the fitting procedure. Typical offsets of $\sim 0.01^\circ$ were found indicating that the measured angles were indeed appropriate.

The total cross-section was extracted from the two Gaussian functions fitted to the data (details will be given in §4.1.4). However, at a level of a few percent the two Gaussian distributions did not represent the ER angular distribution. To ensure that this did not affect the extracted

cross-sections, the Monte Carlo code PACE2 [Gav80] was used to calculate the ER distribution for known cross-sections. The

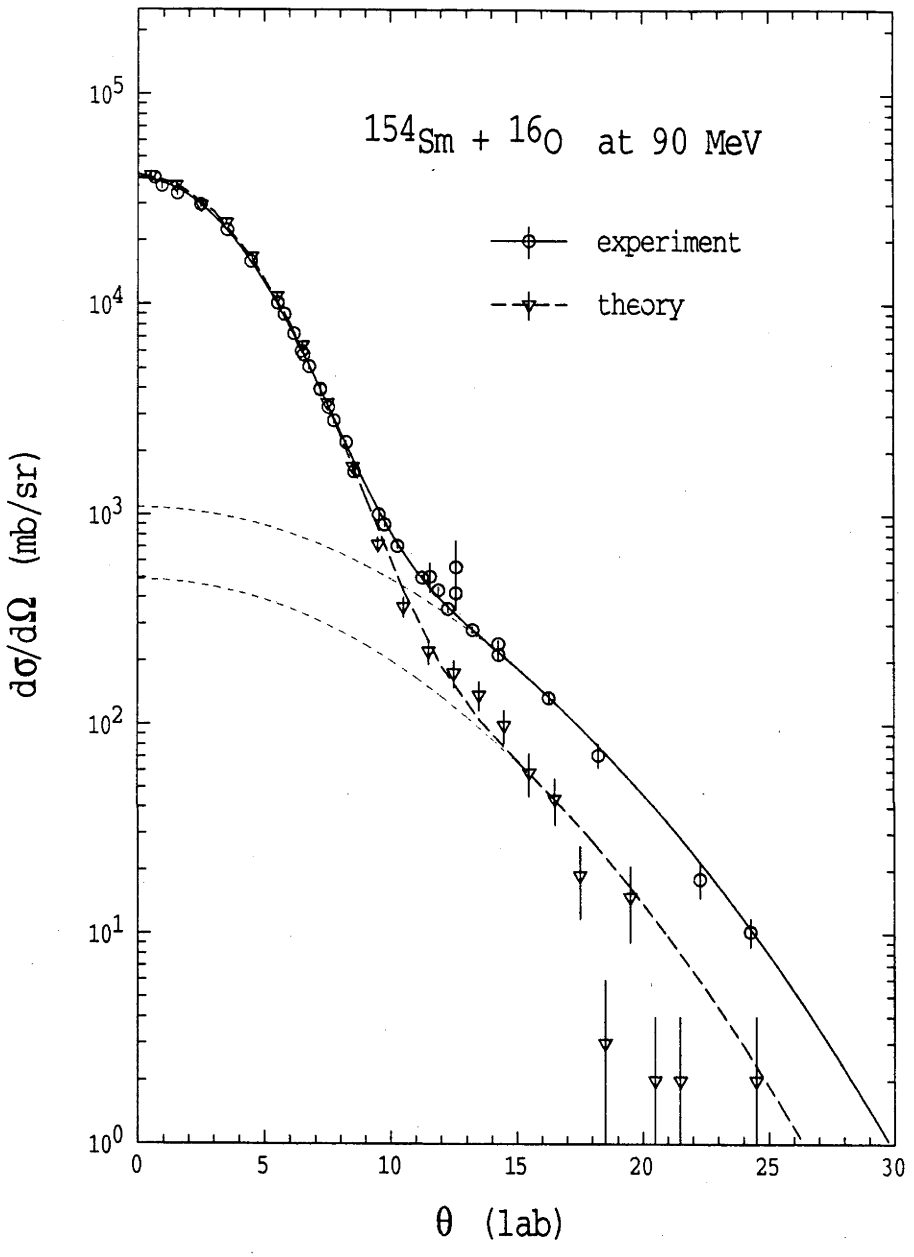

Fig. 4-1-4: The measured and calculated (by PACE2) ER angular distributions for ^{154}Sm + ^{16}O at 90 MeV. The theoretical calculation is systematically lower than the experimental one for angles ≥ 10°. The curves are two Gaussian distributions fitted to the data. The short dashed lines show the fit of the broader Gaussian only.

calculated ER angular distributions were then fitted with a two-Gaussian function. The χ^2/N for fitting these theoretical data were also between 1 and 4, however the extracted cross-sections were consistently within 1% of the input value to the PACE program. Also the broader Gaussian fit to the PACE data gave a cross-section close to that calculated for α emission. Fig. 4-1-4 shows the two-Gaussian fits to the PACE data and the measured experimental data. At the large angles (>10°) the calculated "data" are systematically smaller, by about a factor 2, than the experiment. Presumably, the PACE calculation underestimates the α emission cross-sections, though the reasons for this are not clear.

Full ER angular distributions for the reactions $^{154}Sm + ^{16}O$ and $^{186}W + ^{16}O$ are shown in Fig. 4-1-5. Typical widths of the two-Gaussian fit to the measured data were ~3° and ~7.5° for the both reactions. Since the ERs have been measured up to 20° by the LAERD, the shape of the angular distributions are well defined at most of the measured energies. At a few energies there were not enough measured data at large angles to define the width of the broader Gaussian distribution. Hence the extracted width from the neighbouring energies have then been used.

At 100 MeV bombarding energy in the reaction of $^{154}Sm + ^{16}O$, the fitted angular distribution crosses that for 90 MeV at about 25°. This is caused by a smaller width (6.84°) found by the fitting program for the broader Gaussian distribution compared with those (~7.5°) found for the neighbouring energies of 90 and 110 MeV. However, this only results in a small change in the extracted total cross-section because the contributions to the total cross-section from the large angles are very small (see §4.1.4). For instance, there is only ~0.5% change in the

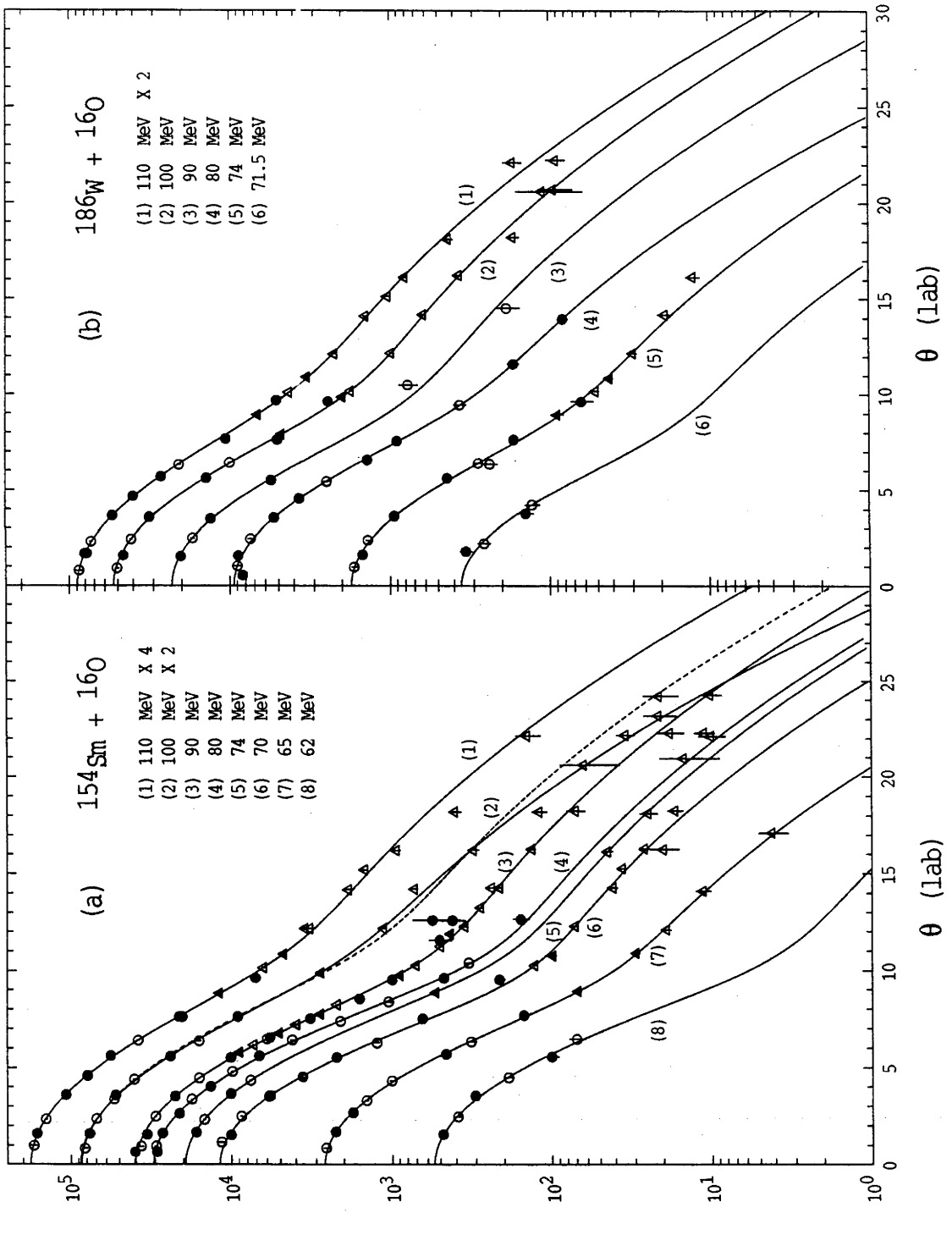

Fig. 4-1-5: Full ER angular distributions for the ^{16}O projectile induced reactions. The symbols are the same as in Fig. 4-1-3. The curves are the fits of two Gaussian distributions. The dashed line (2) in (a) indicates that if a value of 7.5° were taken as the width of the broader Gaussian distribution instead of the value of 6.84° (solid line). See text for details.

total cross-section if a larger value of 7.5°, instead of the 6.85°, was used for the width of the broader Gaussian distribution.

4.1.4 The Cross-Section of Evaporation Residues

For the reactions studied in this work, the full angular distributions of ERs have been measured from close to the Coulomb barrier up to 110 MeV for the ^{16}O projectile at intervals of 5 or 10 MeV. For the purpose of the barrier distribution measurement, at energies below and around the Coulomb barrier, the differential cross-sections were measured at ±2° in energy steps of ~0.5 MeV. The ER cross-sections have been extracted by two different methods for the different measurements.

When full angular distributions were measured, the ER cross-sections were extracted by using the areas of the two Gaussian distributions. Thus:

$$\sigma_{ER}(\theta) = \int_0^{\pi} \frac{d\sigma}{d\theta} d\theta = \int_0^{\pi} 2\pi \sin\theta \frac{d\sigma}{d\Omega}(\theta)\, d\theta \qquad (4\text{-}1\text{-}2)$$

where:

$$\frac{d\sigma}{d\Omega}(\theta) = A_1 \exp\left(\frac{-\theta^2}{2\sigma_1^2}\right) + A_2 \exp\left(\frac{-\theta^2}{2\sigma_2^2}\right) \qquad (4\text{-}1\text{-}3)$$

is the fitted two-Gaussian distribution and A_1, A_2, σ_1, σ_2 were extracted from the measured experimental data. Typical examples of $d\sigma/d\theta$ as function of angle are shown in Fig. 4-1-6 for the reaction of $^{154}Sm + ^{16}O$ at 100 MeV. The fine lines show the contributions from the narrower and broader Gaussian distributions. The error introduced by changing the broader width by ±10% (from 6.84° to 7.5°) is also

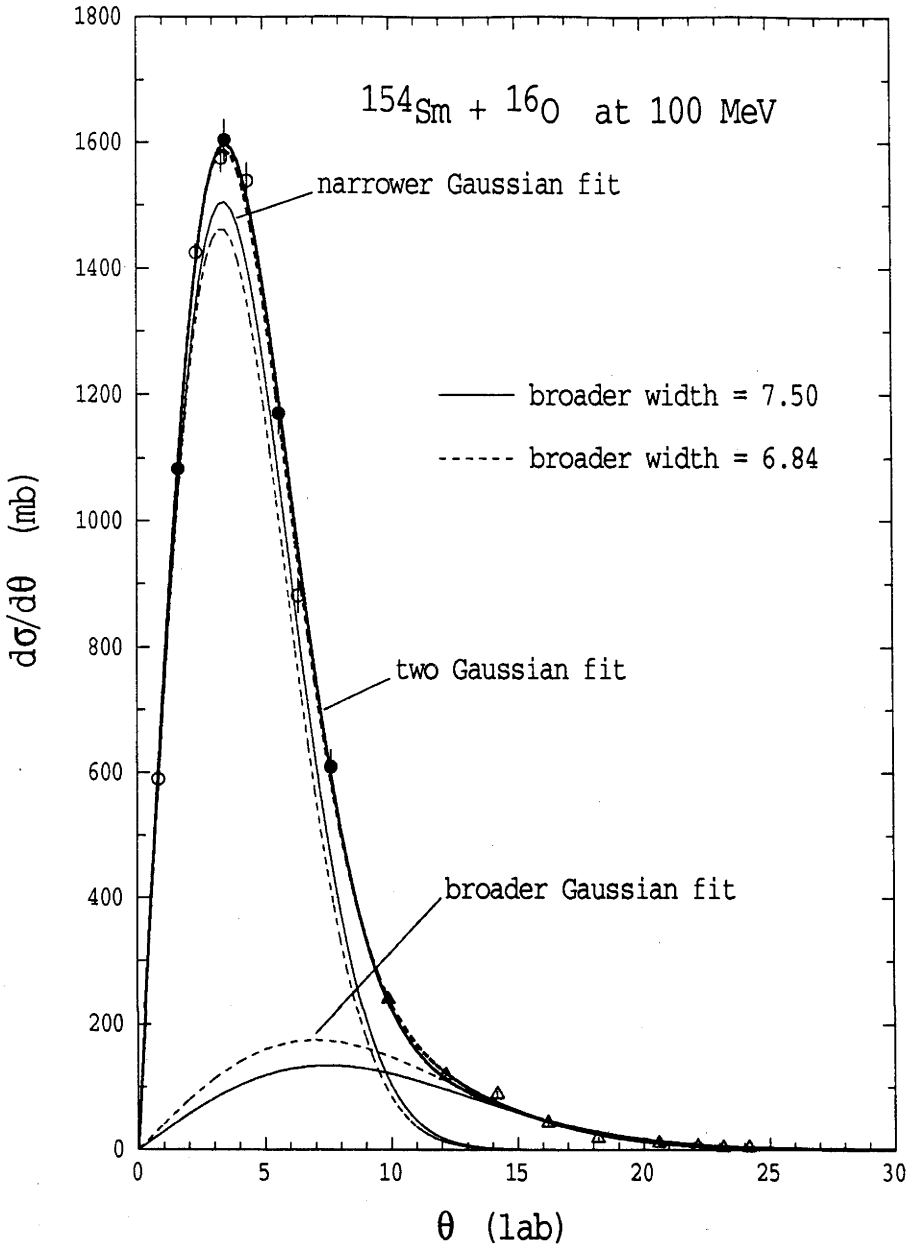

Fig. 4-1-6: ER angular distribution multiplied by $2\pi\sin\theta$ to give $d\sigma/d\theta$. Total cross-sections were extracted through the two Gaussian distributions.

indicated in Fig. 4-1-6. The χ^2 of the fitting increases from ~3 to ~4 and the extracted total cross-section increases from 1112 mb to 1117 mb which is less than ±0.5% to the total cross-section. Therefore an error of ±0.5% was assigned to the extracted cross-sections for this energy. An extra error of ±0.5% was also assigned to total cross-sections for

those energies where only a few points of the angular distribution were measured, since the neighbouring shapes were employed to fit the data.

The ratios (R) of the total ER cross-section to $d\sigma/d\Omega$ at 2° are shown in Fig. 4-1-7 for the reaction $^{154}Sm + ^{16}O$. Theoretical calculations with PACE are also shown in this figure. Both the experimental and theoretical data vary linearly with the energy at energies of 5 MeV above the Coulomb barrier. At the lower energies the experimental ones were scattered by few percent from the line. The theoretical ratios were systematically lower than the experimental ones. The solid and dashed lines are the least square linear fits to the experimental and theoretical data respectively. The gradient, K, is indicated in the figure. It is understood, as discussed in the last section, that the PACE calculation underestimated the α emission cross-section resulting in a higher differential cross-section at smaller angles, hence a smaller ratio of the total cross-section to differential cross-section at 2°. Nevertheless, the gradient of the theoretical fit is consistent with the experiment one. The differential cross-sections at 2°, therefore, can confidently be converted to total cross-sections using the fitted line. Details of the converting procedures will be given in the next subsection. Similar features for the ratios of differential cross-section at 2° to the total cross-section were obtained from the reaction of $^{186}W + ^{16}O$, but their K value is close to zero.

The typical uncertainty in K values is ~15% and the resultant error in R is then energy dependent [Lyo86]. However, since the K is small, R does not change much with energy; the error in R is less than 1% for energies above the barrier and up to 1.5% at the lowest energies where the statistical errors are much larger. Though the changes of absolute

value of R will result in a systematic shift in the total cross-sections, it has a minor effect on the curvature of the excitation function. Calculations show that at an energy interval 2 MeV, which is used as the energy steps, as discussed in §4.2.2, in the extraction of barrier and angular momentum distributions, the relative error of total cross-sections caused by the uncertainties of the K and R is only ~±0.15%.

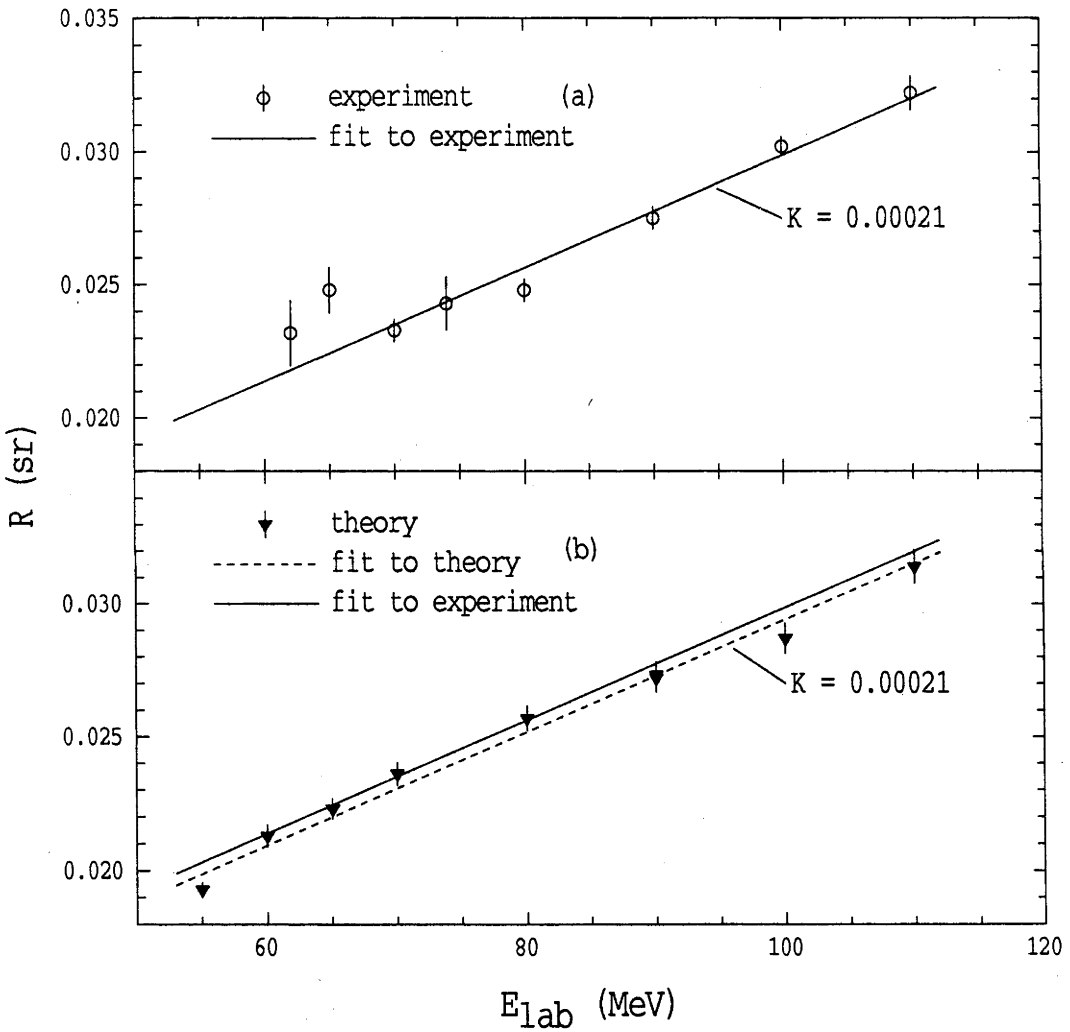

Fig. 4-1-7: The ratios of ER total cross-section to ER differential cross-section at 2° at the energies where the full angular distributions have been measured. The theoretical ones were calculated using PACE2. The solid and dashed lines are the least square fits for the experimental and theoretical data respectively. The K is the slope of these lines.

This will not affect the shape, but will result in a minor scaling of the extracted barrier and angular momentum distributions which are related to the curvature of the excitation function, as will be discussed.

At bombarding energies below the Coulomb barrier, the cross-section of the ERs becomes very small (less than a few mb). The measurement of the full angular distributions of ERs becomes impracticable. At these energies the differential cross-sections are too small to measure at angles larger than a few degrees because the counting rate of background events becomes important compared with that of the ERs. Thus the measurements of the ERs at these energies were only carried out at ±2° to the beam direction. When the energy is further reduced and the total cross-sections is below the 0.1 mb level the measurement of ERs become difficult even at the angles of ±2°. The lowest cross-sections measured in this work is, therefore, ~0.1 mb.

Because the real angles of the Velocity Filter were not precisely at ±2° the differential cross-section at 2° was interpolated using an exponential function to link the two measured points. The use of the exponential rather than a Gaussian function only introduces a minor error in the extracted differential cross-sections at 2° because the offset of the angles were very small.

The extraction was done by solving the two equations:

$$\frac{d\sigma}{d\Omega}(+2°) = A\, e^{a(2+\Delta\theta_+)} \qquad (4\text{-}1\text{-}4)$$

$$\frac{d\sigma}{d\Omega}(-2°) = A\, e^{a(2+\Delta\theta_-)} \qquad (4\text{-}1\text{-}5)$$

The offset angles $\Delta\theta_+$ and $\Delta\theta_-$ were extracted from the ratio of the elastic scattering in the monitors at ±30° as discussed in Chapter 3.

Then

$$\frac{d\sigma}{d\Omega}(2°) = A\, e^{2a} \quad . \qquad (4\text{-}1\text{-}6)$$

The ER cross section was obtained by using the $\frac{d\sigma}{d\Omega}(2°)$ multiplied by the converting factor, R, that is

$$\sigma = R\frac{d\sigma}{d\Omega}(2°) \qquad (4\text{-}1\text{-}7)$$

The excitation functions of the ERs are shown in Fig 4-1-8. The triangles represent the measurements at $\pm 2^{0}$ and the circles represent the full angular distributions.

§4.2 FUSION AND ITS EXCITATION FUNCTION

§4.2.1 Fusion Excitation Functions

As discussed in §3.5.7 the fusion cross-sections for the reaction of $^{154}Sm + ^{16}O$ are simply taken as the ER cross-sections because of negligible fission decay at the energies studied in this work. For the reaction of $^{186}W + ^{16}O$ the fission cross-sections, as shown in the Fig. 4-1-8, were taken from the reference [Bem87]. For those energies where the measured fission cross-section is not available an interpolated value has been used from the curve of fission in Fig. 4-1-8. The measured ER differential cross-sections at ±2° and the fusion excitation functions of the reaction of $^{16}O + ^{154}Sm$ and ^{186}W are shown in Table 4-2-1, 4-2-2, 4-2-3 and 4-2-4 respectively. The cross-sections, from the full angular distribution measurements are listed separately. As it is expected, those total ER cross-sections extracted from full angular distribution measurements agree, within their

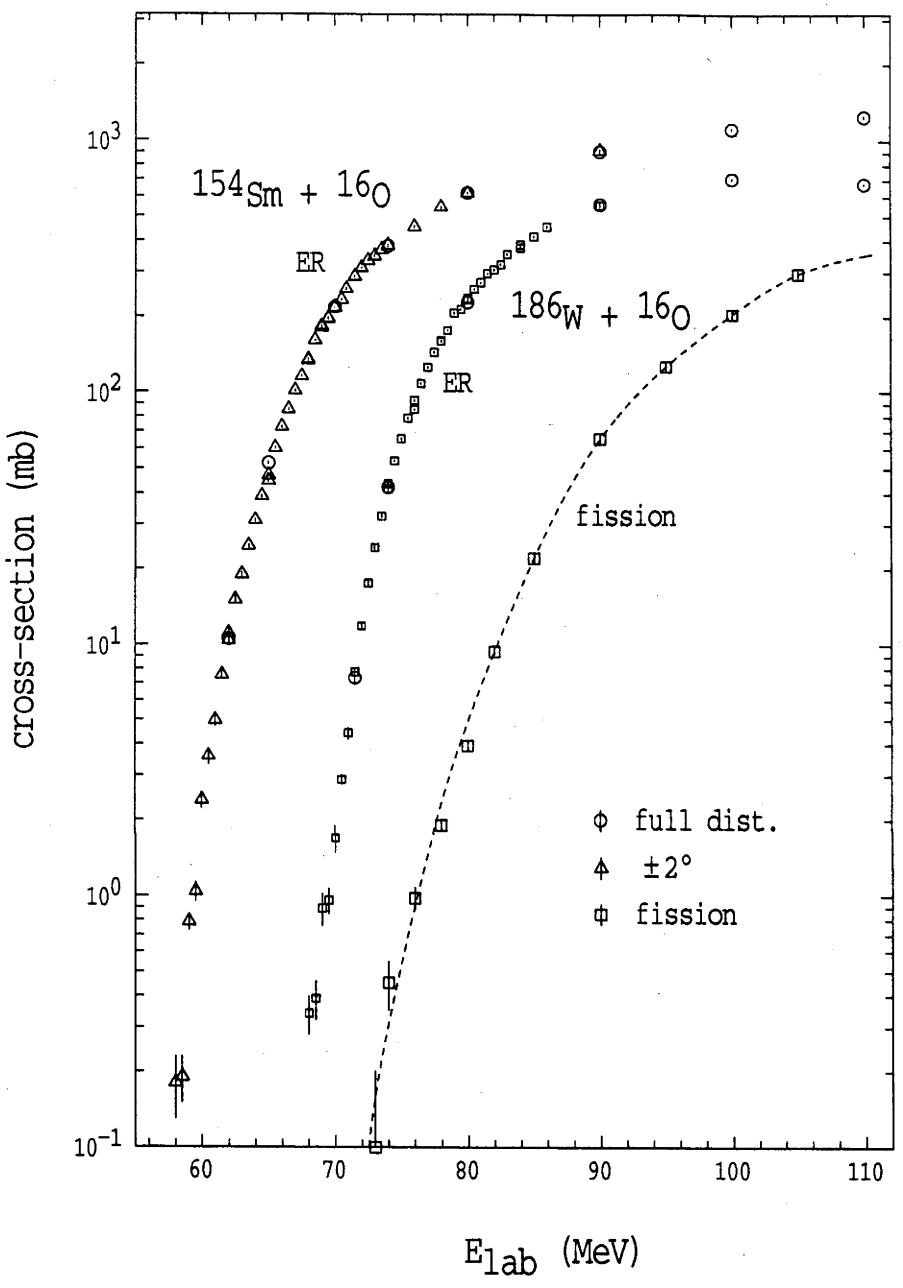

Fig.4-1-8: The evaporation residue excitation functions for the reactions of $^{154}Sm + ^{16}O$, $^{186}W + ^{16}O$. Fission cross-sections for $^{186}W + ^{16}O$, taken from [Bem87], are also shown. The dashed line guides the eye.

error, to the ones extracted from ±2° measurements. However the errors of the total cross-sections from the full angular distribution measurements were generally not measured to the precision of 1% and the energies of these measurements were not so precisely set as they were done in the ±2° measurement. Hence these data are not suitable and are not used in the applications of the extractions of the barrier and angular momentum distributions.

Only the statistical errors are shown in these tables. No correction was made to the cross-sections resulting from systematic errors. For instance, no correction was made for the cross-sections resulting from only 98% transparency of the MWPC, as discussed in §3.4.2 and the 100 keV energy less than the nominal values resulting from the energy loss of beam passing the carbon backing and the target, as discussed in §3.5.4.

Non-statistical random errors were estimated from the reproducibility of the cross-sections at several different energies for each reaction and by six measurements at one energy for reaction $^{154}Sm + ^{16}O$ after re-cycling the magnet, re-focusing the beam and re-setting the velocity filter angles. The distribution of cross-sections was generally randomly scattered within a range of ~±1%, even though statistical errors were significantly smaller. Thus the minimum random error was taken to be 1%. In one case, at lab beam energy of 70.5 MeV in reaction $^{154}Sm + ^{16}O$, a difference in differential cross-section of 7% was obtained and this was probably due to "human" error. As it will be shown in Fig. 4-2-2 (c) for the extracted $d^2(E\sigma)/dE^2$, this re-measured cross-section results in the additional solid circles at the ~62 and ~64 MeV, displaced significantly from the other data, illustrating the care required in making these measurements.

Table 4-2-1: Measured $d\sigma/d\Omega$ of ^{154}Sm + ^{16}O at nominal angles ±2°, and the extracted $d\sigma/d\Omega$ at 2°. Only the statistical errors, Δ, are indicated.

E_{lab} (MeV)	$\frac{d\sigma(+2°)}{d\Omega} \pm \Delta$ (mb/sr)		$\frac{d\sigma(-2°)}{d\Omega} \pm \Delta$ (mb/sr)		$\frac{d\sigma(2°)}{d\Omega} \pm \Delta$ (mb/sr)	
58.0	10	4	7.4	3	8.7	3
58.5	10	3	7.7	2	8.9	2
59.0	45	4	30	3	37	3
59.5	49	6	49	6	49	4
60.0	120	15	100	9	110	8
60.5	180	20	150	16	170	12
61.0	260	20	210	16	230	13
61.5	360	20	340	21	350	14
62.0	490	20	460	20	480	15
62.0	580	30	450	20	510	20
62.5	770	30	610	20	690	20
63.0	930	30	800	20	860	20
63.5	1200	20	1040	20	1120	20
64.0	1500	20	1310	30	1400	20
64.5	1950	30	1570	30	1740	20
65.0	2270	40	1910	30	2090	20
65.0	2120	30	1870	30	1990	20
65.5	2900	40	2450	30	2670	30
66.0	3510	50	2930	50	3210	30
66.5	4120	60	3390	50	3740	40
67.0	4840	70	3990	50	4430	40
67.5	5500	70	4620	60	5030	50
68.0	6330	80	5400	80	5860	60
68.0	6370	80	5300	60	5810	50
68.5	7670	100	6220	80	6960	60
69.0	8570	110	7040	80	7770	70
69.0	8460	110	7410	80	7900	70
69.5	9020	110	7940	100	8450	80
69.5	9120	100	7750	80	8390	70
70.0	9950	120	8570	100	9240	80
70.0	10300	120	8330	100	9290	80
70.5	11500	170	9670	130	10600	110
70.5	10800	130	9030	110	9910	80
70.9	11800	190	10100	160	10900	130
71.5	13200	140	11100	120	12100	90
72.0	14200	140	11900	120	13000	90
72.5	14800	140	13000	160	13900	110
73.0	15400	140	13400	140	14400	100
73.5	16100	180	14200	140	15100	110
74.0	16600	150	14800	130	15700	100
76.0	19900	250	17000	210	18300	160
78.0	23100	280	20500	250	21600	190
80.0	26000	330	22300	220	24100	200
90.0	35100	410	31300	310	33000	260

E_{lab} (MeV)	$\sigma \pm \Delta\sigma$ (mb)	
58.0	0.18	0.05
58.5	0.19	0.04
59.0	0.79	0.06
59.5	1.0	0.1
60.0	2.4	0.2
60.5	3.6	0.3
61.0	5.0	0.3
61.5	7.6	0.3
62.0	10.4	0.3
62.0	11.1	0.4
62.5	15.1	0.4
63.0	19.0	0.4
63.5	24.7	0.4
64.0	31.3	0.4
64.5	39.0	0.5
65.0	47.0	0.5
65.0	44.8	0.5
65.5	60.3	0.6
66.0	72.8	0.7
66.5	85.3	0.9
67.0	101	1
67.5	116	1
68.0	135	1
68.0	134	1
68.5	162	2
69.0	181	2
69.0	184	2
69.5	198	2
69.5	196	2
70.0	217	2
70.0	219	2
70.5	251	3
70.5	234	2
70.9	258	3
71.5	289	3
72.0	312	3
72.5	334	3
73.0	347	4
73.5	367	4
74.0	383	4
76.0	454	5
78.0	544	5
80.0	617	6
90.0	914	9

Table 4-2-2: Fusion cross-sections for $^{154}Sm + ^{16}O$. The decay of fission is negligible in this reaction and the fusion cross-section is equal to the ER cross-section. Errors shown in this table are statistical errors only. When the statistic error less than 1%, a error of 1% is assigned. The cross-sections, where the angular distributions of ER had been measured, are listed in the table below.

E_{lab} (MeV)	$\sigma \pm \Delta\sigma$ (mb)	
62.0	10.5	0.3
65.0	52	7
70.0	219	2
74.0	380	4
80.0	619	6
90.0	904	9
100.0	1112	11
110.0	1256	13

Table 4-2-3: Measured $d\sigma/d\Omega$ of $^{186}W + ^{16}O$ at nominal angles ±2°, and the extracted $d\sigma/d\Omega$ at 2°. Only the statistical errors, Δ, are indicated.

E_{lab} (MeV)	$\frac{d\sigma(+2°)}{d\Omega} \pm \Delta$ (mb/sr)		$\frac{d\sigma(-2°)}{d\Omega} \pm \Delta$ (mb/sr)		$\frac{d\sigma(2°)}{d\Omega} \pm \Delta$ (mb/sr)	
68.0	10	3	12	3	12	2
68.5	12	3	15	3	13	3
69.0	38	7	24	6	31	5
69.5	34	6	31	5	33	4
70.0	46	10	72	10	58	7
70.5	90	5	110	7	98	4
71.0	150	10	160	10	150	8
71.5	270	10	260	10	270	9
72.0	440	20	380	20	400	10
72.5	560	20	620	20	600	20
73.0	860	20	800	20	830	10
73.5	1160	20	1100	20	1110	10
74.0	1490	30	1480	30	1480	20
74.0	1490	20	1350	20	1420	20
74.5	1870	20	1790	20	1830	20
75.0	2280	30	2170	30	2230	20
75.5	2730	30	2640	30	2680	20
76.0	3230	40	3140	40	3160	30
76.5	3830	50	3520	40	3700	30
77.0	4640	60	3970	50	4290	40
77.5	5020	60	4800	60	4920	40
78.0	5690	60	5160	60	5460	40
78.0	5690	60	5340	50	5490	40
78.5	6040	60	6020	60	6030	40
79.0	7360	90	6800	70	7070	60
79.5	7480	70	7200	60	7320	40
80.0	8500	90	7520	100	7970	70
80.0	8040	70	8070	60	8060	50
80.5	9020	80	8670	80	8780	60
81.0	10190	90	8580	100	9310	70
81.5	10200	90	9910	120	10100	70
82.0	11000	140	9960	110	10500	90
82.5	11100	130	10800	110	11000	80
83.0	12600	170	11500	100	12000	100
84.0	13400	120	12900	110	13100	80
84.0	13800	160	11800	120	12800	100
85.0	14800	170	13500	160	14200	120
86.0	16300	180	14600	190	15400	130
90.0	20000	240	17600	200	18800	160

Table 4-2-4: Fusion cross-sections σ for $^{186}W + ^{16}O$. The ER cross-sections σ_{ER} are converted from $d\sigma/d\Omega$ measured at nominal angles ±2°. Fission cross-sections σ_{fi} are taken from [Bem87] and indicated by *. At the energies when fission was not measured interpolated values from the measured ones at the neighbouring energies are used. Errors shown in this table are statistical errors only. When the statistical error is less than 1%, an error of 1% is assigned.

E_{lab} (MeV)	$\sigma_{ER} \pm \Delta\sigma_{ER}$ (mb)		$\sigma_{fi} \pm \Delta\sigma_{fi}$ (mb)		$\sigma \pm \Delta\sigma$ (mb)	
68.0	0.34	0.06		<0.05	0.34	0.08
68.5	0.39	0.07		<0.05	0.39	0.09
69.0	0.9	0.1		<0.05	0.9	0.2
69.5	1.0	0.1		<0.05	1.0	0.1
70.0	1.7	0.2		<0.05	1.7	0.2
70.5	2.9	0.2		<0.1	2.9	0.2
71.0	4.4	0.3		<0.1	4.4	0.3
71.5	7.8	0.3		<0.1	7.8	0.3
72.0	11.9	0.4		<0.1	11.9	0.4
72.5	17.5	0.5		<0.1	17.5	0.5
73.0	24.3	0.4	* 0.1	0.1	24.4	0.4
73.5	32.4	0.4	0.3	0.1	32.7	0.4
74.0	43.5	0.7	* 0.5	0.1	44.0	0.7
74.0	41.5	0.5	* 0.5	0.1	42.0	0.5
74.5	53.5	0.5	0.6	0.1	54.1	0.5
75.0	65.3	0.7	0.7	0.1	66.0	0.7
75.5	78.6	0.7	0.8	0.1	79.4	0.7
76.0	92.7	0.8	* 1.0	0.1	93.7	0.8
76.5	108	1	1.1	0.1	109	1
77.0	126	1	1.3	0.1	127	1
77.5	144	2	1.5	0.1	146	2
78.0	161	2	* 1.9	0.1	163	2
78.0	160	2	* 1.9	0.1	162	2
78.5	177	2	2.3	0.2	179	2
79.0	207	2	2.8	0.2	210	2
79.5	215	2	3.4	0.2	218	2
80.0	234	2	* 4.0	0.2	238	3
80.0	236	2	* 4.0	0.2	240	3
80.5	257	2	5.1	0.3	262	3
81.0	273	2	6.5	0.3	280	3
81.5	296	3	7.7	0.3	304	3
82.0	307	3	* 9.4	0.3	316	3
82.5	322	3	11	1	333	3
83.0	353	3	13	1	366	4
84.0	385	3	17	1	402	4
84.0	375	3	17	1	392	4
85.0	415	4	* 22	1	437	4
86.0	452	4	29	3	481	5
90.0	550	5	* 65	3	615	6

Table 4-2-5: Fusion cross-sections for $^{186}W + ^{16}O$. ER cross-sections are converted from the measurements of full angular distribution of $d\sigma/d\Omega$. Fission cross-sections are taken from [Bem87] and indicated by *. Errors shown in this table are statistical errors only.

E_{lab} (MeV)	$\sigma_{ER} \pm \Delta\sigma_{ER}$ (mb)		$\sigma_{fi} \pm \Delta\sigma_{fi}$ (mb)		$\sigma \pm \Delta\sigma$ (mb)	
71.5	7.4	0.5		<0.10	7.4	0.5
74.0	42	1	* 0.45	0.1	43	1
80.0	229	4	* 3.95	0.2	233	4
90.0	556	13	* 65.4	3.1	621	13
100.0	704	5	* 205.	8	909	10
110.0	675	5				

§4.2.2. Curvature of The Fusion Excitation Functions

It is common to plot the fusion cross-section against 1/E or plot $E\sigma$ against E to extract the average fusion barrier, B_0, and fusion radius, R [Gut73, Eis77, Jah82, Bec83, Mos84]. The plots of $E\sigma$ vs E for the two systems of $^{16}O + ^{154}Sm$ and ^{186}W are shown in Fig. 4-2-1. The fusion barrier B_0 and πR^2 can be obtained by fitting the data by a straight line with the least squares method. The measured cross-sections used in the fitting are those above 100 mb.

The intercept on the E axis is B_0, and the slope of the straight line is πR^2. Results are shown in Table 4-2-6 and indicated in Fig. 4-2-1. Those data used in the fitting are indicated by solid symbols.

Table 4-2-6: The extracted B_0, πR^2 and the fusion radius R.

Reactions	B_0(MeV)	πR^2 (mb)	R (fm)
$^{154}Sm + ^{16}O$	59.2	3300	10.25
$^{186}W + ^{16}O$	68.6	3520	10.59

Below the linear region, around and below B_0, the plot is curved. Recent studies have shown that the curvature and slope of the fusion excitation function in this region carry much more information about the fusion process. It has been shown [Bal83, Rei85, Bal86, Das86] that d(Eσ)/dE carries information on the angular momentum brought into

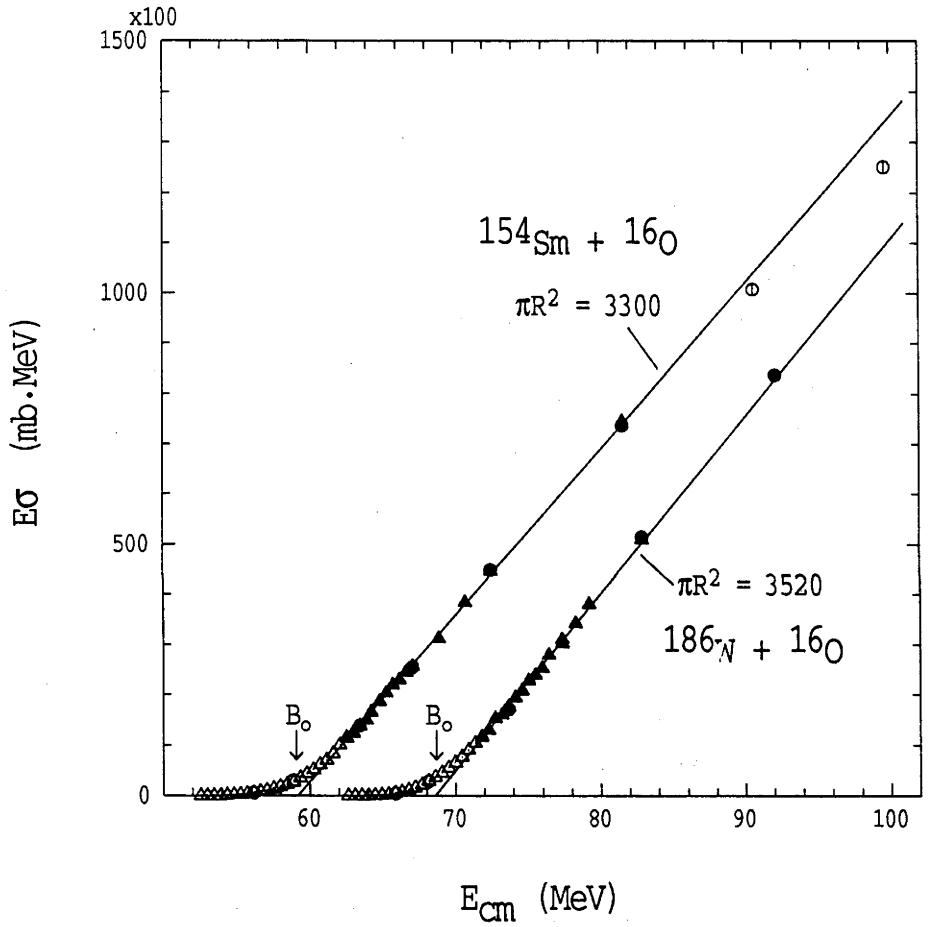

Fig. 4-2-1: Plots of the Eσ vs E in centre of mass system for the reactions of ^{16}O + ^{154}Sm and ^{186}W. The straight lines show the least squares fit to the data. The data used in the fitting are indicated by solid symbols. Average fusion barriers, B_0, values of πR^2 (see text) are indicated. The circles represent measurements where the ER angular distributions were measured and the triangles where they were only measured at ±2°.

the fused system and that $d^2(E\sigma)/dE^2$ gives information on the distribution of barrier heights [Row91, Row91a]. These can be extracted from the data using cross-sections σ_-, σ and σ_+ at centre of mass energies E-ΔE, E and E+ΔE respectively if the fusion cross-sections have been measured to a high precision and in fine energy steps [Wei91a]. Thus

$$\frac{d(E\sigma)}{dE} \simeq \frac{(E + \Delta E)\sigma_+ - E\sigma}{\Delta E} \qquad (4\text{-}2\text{-}1)$$

and

$$\frac{d^2(E\sigma)}{dE^2} \simeq \frac{(E + \Delta E)\sigma_+ - 2E\sigma + (E - \Delta E)\,\sigma_-}{\Delta E^2} \qquad (4\text{-}2\text{-}2)$$

where $d(E\sigma)/dE$ gives the value of the gradient at the energy E+ΔE/2, and the $d^2(E\sigma)/dE^2$ gives the value at energy E.

Experimentally, only a finite ΔE can be used in the above equations, the extracted $d(E\sigma)/dE$ and $d^2(E\sigma)/dE^2$ are therefore not the true values in strict mathematical terms. However, it can be shown that there is only a minor difference when ΔE values up to ~1.8 MeV are used (see §5.1.3 and Fig. 5-1-5 for details).

The statistical uncertainty associated with $d(E\sigma)/dE$ and $d^2(E\sigma)/dE^2$ are given approximately by

$$\delta_g \simeq \frac{E}{\Delta E}\sqrt{(\delta\sigma_+)^2 + (\delta\sigma)^2} \qquad (4\text{-}2\text{-}3)$$

and

$$\delta_c \simeq \frac{E}{\Delta E^2}\sqrt{(\delta\sigma_+)^2 + 4(\delta\sigma)^2 + (\delta\sigma_-)^2} \qquad (4\text{-}2\text{-}4)$$

respectively,

where the $\delta\sigma$'s are statistical errors in the cross-sections in mb. The values of δ_g and δ_c in Eqs. 4-2-3 and 4-2-4 increase with the value of $\delta\sigma$. It is also evident from these two Eqs. that δ_g and δ_c are proportional to ΔE^{-1} and ΔE^{-2} respectively. Fig. 4-2-2 illustrates the dependence of error in $d^2(E\sigma)/dE^2$ on the step length of ΔE. In the Fig. 4-2-2 (a), the energy interval is ~0.45 MeV (0.5 MeV in lab energy); it is difficult to see any structure in the distribution. However, the structure becomes clear when the energy interval is ~1.8 MeV (2 MeV in beam energy), as shown in Fig. 4-2-2- (c).

To maintain a constant value of δ_c over the energy range of interest requires much higher statistical accuracy in percentage terms at higher energies. For instance, to achieve an error $\delta\sigma$ = 1 mb requires measurements of only 10% precision at beam energy ~ 66 MeV but 0.2% at 71 MeV. We ensured, as discussed in §3.5.8, that statistical errors were ≤ 1 mb for cross-sections up to 100 mb (at about the energy of the Coulomb barrier) and ≤ 1% for higher values.

The extracted values of $d(E\sigma)/dE$ and $d^2(E\sigma),dE^2$ for the reaction of $^{154}Sm + ^{16}O$ and $^{186}W + ^{16}O$ are shown in Fig. 4-2-3 and Fig. 4-2-4. Figures 4-2-3 (b) and 4-2-4 (b) show results for the subset of the data, mentioned above, for which the analysing magnet was increased monotonically; (a) and (c) in figures 4-2-3 and 4-2-4 display all the data, including the repeated points. Energy steps used in the extraction are indicated in these figures.

Details of the features of the extracted $d(E\sigma)/dE$ and $d^2(E\sigma)/dE^2$ will be discussed in Chapter 5.

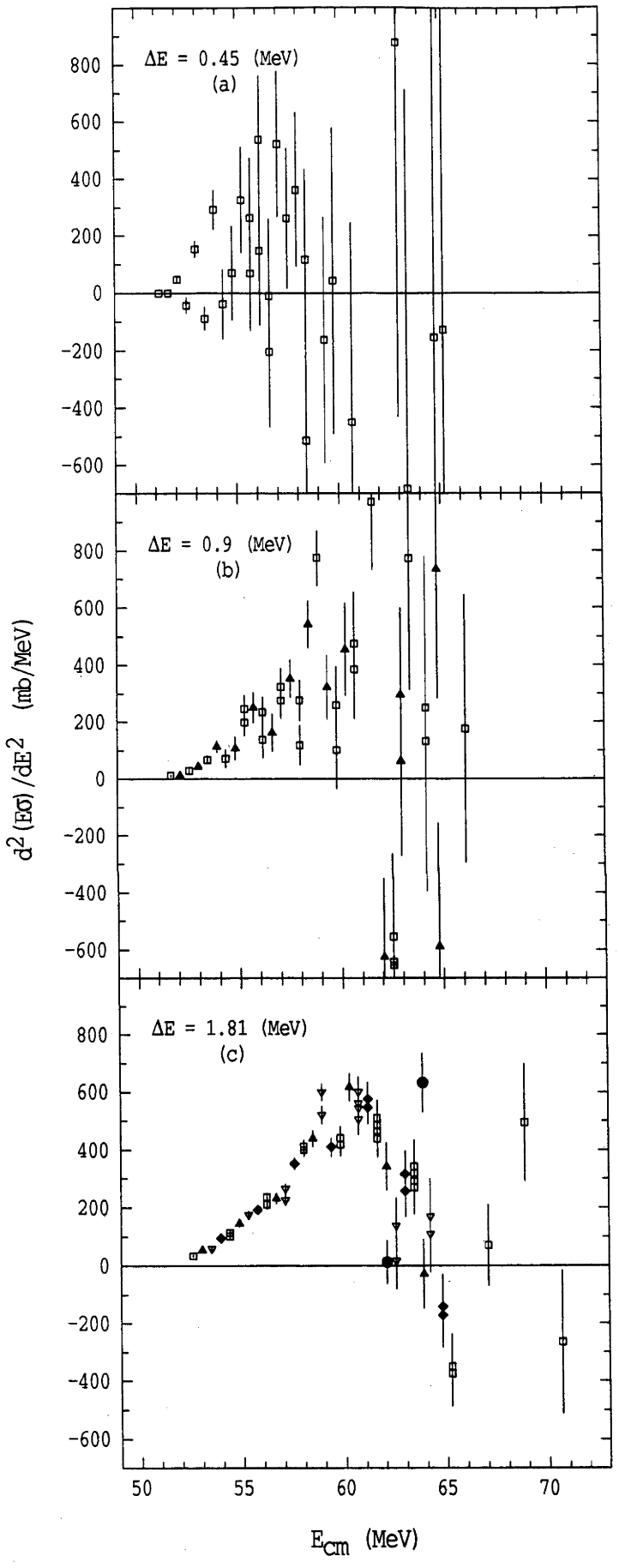

Fig. 4-2-2: Illustrations of the variation of errors of $d^2(E\sigma)/dE^2$ with the energy interval ΔE. The errors are correlated to some degree. The correlated ones are indicated by the same symbols. Each point is correlated with both neighbouring points with the same symbol. In the extremely case of (a) they are all correlated with their nearest neighbouring points.

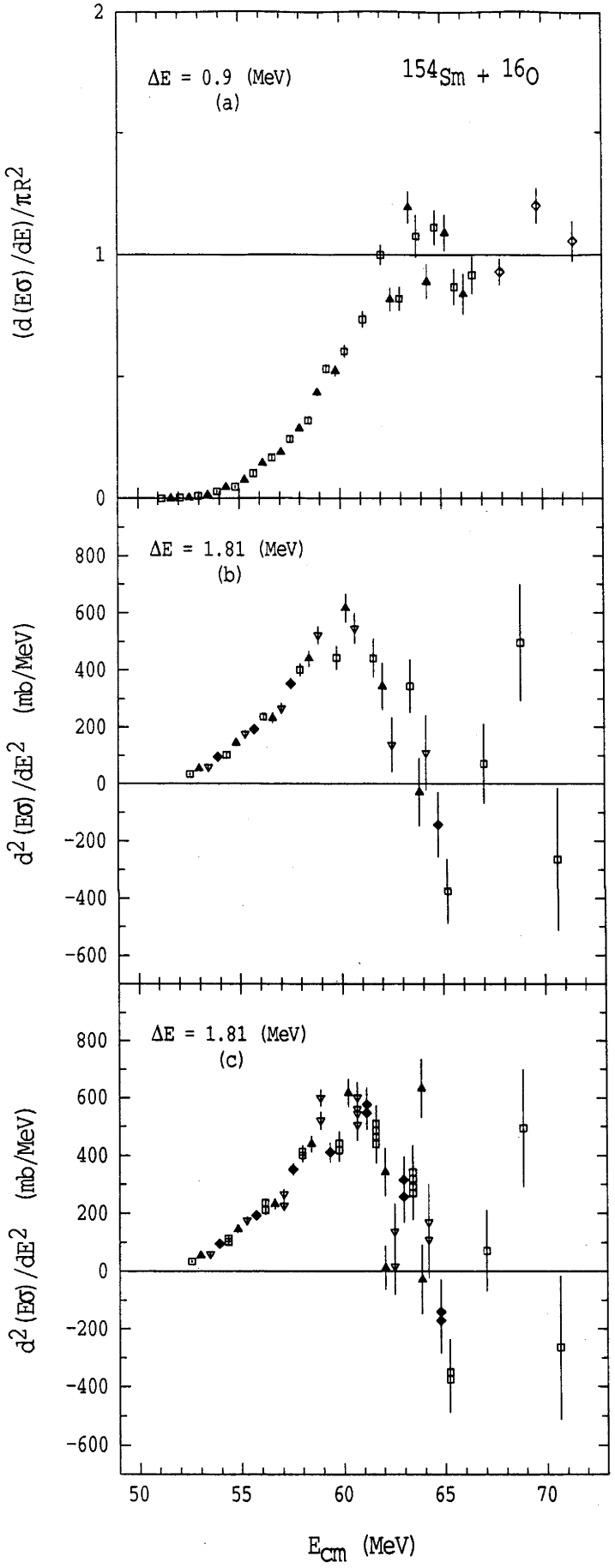

Fig. 4-2-3: Extracted $d(E\sigma)/dE$ and $d^2(E\sigma)/dE^2$ for reaction $^{154}Sm + ^{16}O$. The data points in (a) have been normalised by $\pi R^2 = 3300$. The energy steps in (a) are 0.9 MeV (1 MeV in Lab system) excepting the diamond ones at the high energies where the energy steps are 1.81 MeV (2 MeV in Lab system). Curvature $d^2(E\sigma)/dE^2$ from (b) data measured with monotonically increasing energy and (c) all data. Each point is evaluated using two or three cross-sections; neighbouring points with the *same* symbol have at least one of these cross-sections in common and are therefore correlated.

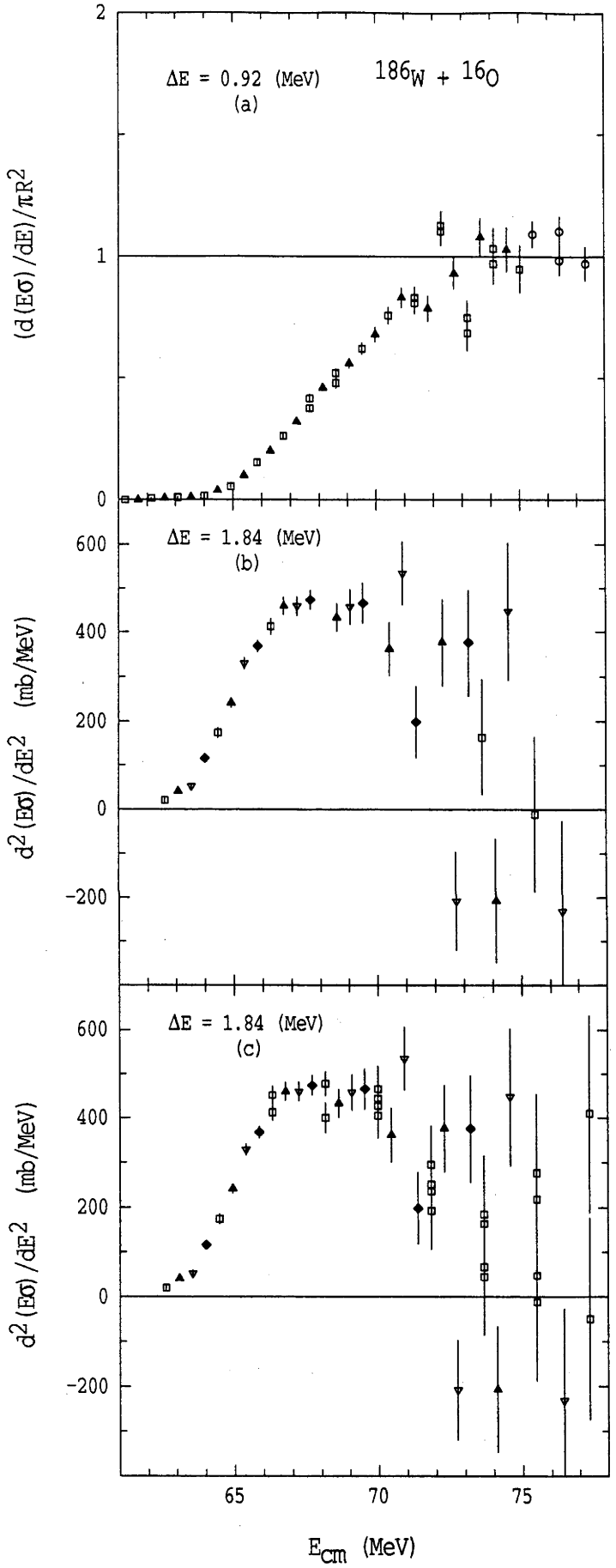

Fig. 4-2-4: Extracted $d(E\sigma)/dE$ and $d^2(E\sigma)/dE^2$ for reaction $^{186}W + ^{16}O$. The data points in (a) have been normalised by $\pi R^2 = 3520$. The energy steps in (a) are 0.92 MeV (1 MeV in Lab system) excepting the diamond ones at the high energies where the energy steps are 1.84 MeV (2 MeV in Lab system). Curvature $d^2(E\sigma)/dE^2$ from (b) data measured with monotonically increasing energy and (c) all data. Each point is evaluated using two or three cross-sections; neighbouring points with the *same* symbol have at least one of these cross-sections in common and are therefore correlated.

Chapter 5
Discussions and Conclusions

5.1 COMPARISONS OF CALCULATIONS TO EXPERIMENTAL FUSION DATA

In this chapter the fusion cross-sections of ^{154}Sm and $^{186}W + ^{16}O$ are fitted by different models. Theoretical barrier distributions from the models are compared with the distributions extracted from the experimental data. Deformation parameters of the targets are extracted from different models and angular momentum distributions are presented.

5.1.1 Average Fusion Barrier Height

As discussed in §2.1.2, in the case of a single barrier involved in fusion, the barrier height B_0 can be determined by plotting the $E\sigma$ vs E for the fusion data at the energies well above the barrier. However, in the case of a set of barriers (for example a continuous classical barrier distribution resulting from a deformed target) involved in fusion, this method determines the average barrier height $\bar{B}$, as shown below.

At bombarding energies well above all the fusion barriers, the classical expression for fusion Eq. (2-1-14) can be applied to each individual barrier. Then the total fusion cross-section is obtained by integration, giving

$$\sigma = \pi R^2 \int_{B_{min}}^{B_{max}} (1 - \frac{B}{E}) \, D(B) \, dB \qquad (5\text{-}1\text{-}1)$$

Since $\int D(B)\, dB = 1$, the above expression can be written as

$$\sigma = \pi R^2 \left[1 - \frac{1}{E} \int_{B_{min}}^{B_{max}} B \, D(B) \, dB \right] \qquad (5\text{-}1\text{-}2)$$

Now the integration is just the average barrier $\bar{B}$, thus

$$\sigma = \pi R^2 (1 - \frac{\bar{B}}{E}) \qquad (E \gg B_{max}) \qquad (5\text{-}1\text{-}3)$$

This expression is the same as that for single barrier of Eq. (2-1-14), except that $\bar{B}$ replaces B_0. Hence the expression (5-1-3) holds for different fusion barrier distributions and the excitation function behaves as if the average barrier was a single barrier. For this reason, in the following the average $\bar{B}$ will be designated by B_0 which is extracted from high energy fusion data (as showing in Fig. 4-2-1 and listed on Table 4-2-6).

5.1.2 Flat Barrier Height Distributions

The fusion excitation functions were fitted with the flat barrier distribution model using the recipe of Stelson [Ste90]. As discussed in Chapter 2, the barrier distribution width is defined by $2(B_0 - T)$ and the T can be found from the intercept of a straight line extended from the linear region of the plotted data $\sqrt{E\sigma}$, to the E axis. The parameter Ω, which characterises the modulation of the edge of the flat distribution, in Eq. (2-3-7) was varied to minimise the χ^2 of the theoretical fit to the experimental fusion excitation function. The parameters extracted for the reactions $^{154}Sm + ^{16}O$ and $^{186}W + ^{16}O$ are listed on Table 5-1-1.

Table 5-1-1: The extracted B_0, T (centre of mass system) from the experimental data; the Ω, with the best fit to the fusion excitation function, and associated χ^2 per point for the fits.

Reactions	B_0(MeV)	T_0(MeV)	Ω (MeV)	χ^2
$^{154}Sm + ^{16}O$	59.2	55.0	1.8	17
$^{186}W + ^{16}O$	68.6	64.4	1.1	3.3

The spectrum $\sqrt{E\sigma}$ vs E for the reaction of $^{186}W + ^{16}O$ is shown in Fig. 5-1-1 (a). The solid symbols were used to extract the straight line by the least squares method. As required by Stelson's recipe, these solid symbols are the fusion cross-sections between 10 mb and 200 mb. It appears that they represent the straight line very nicely and the χ^2 per point of the least square fitting is very close to one (~1.25). Since, in the suggested linear region of $\sqrt{E\sigma}$, $E\sigma \propto E^2$ then the curvature of $E\sigma$, $d^2(E\sigma)/dE^2$, should be a constant. Indeed, in (b) of this figure, there is a plateau appearing in the extracted $d^2(E\sigma)/dE^2$ from the data in the so called "linear" region of $\sqrt{E\sigma}$.

The value of T extracted from (a) of the figure is 4.2 MeV less than B_0. The dashed line in Fig. 5-1-1 (b) shows the flat barrier distribution whose width is $2(B_0 - T) = 8.4$ MeV. The solid line shows the modulated barrier distribution with $\Omega = 1.1$ MeV with which the calculation yields a best fit to the fusion excitation function. The theoretical fit to the fusion excitation function and the ratio of the theoretical calculation to the experiment for each measured point, by using this modulated barrier distribution model, are shown in Fig. 5-1-2 (a) and (b). The χ^2 per point for this fit is ~3.3.

One can see, from Fig. 5-1-1 (b) that the modulated flat barrier distribution fits the extracted barrier distribution very well. This may not be surprising, because the experimental barrier distribution for

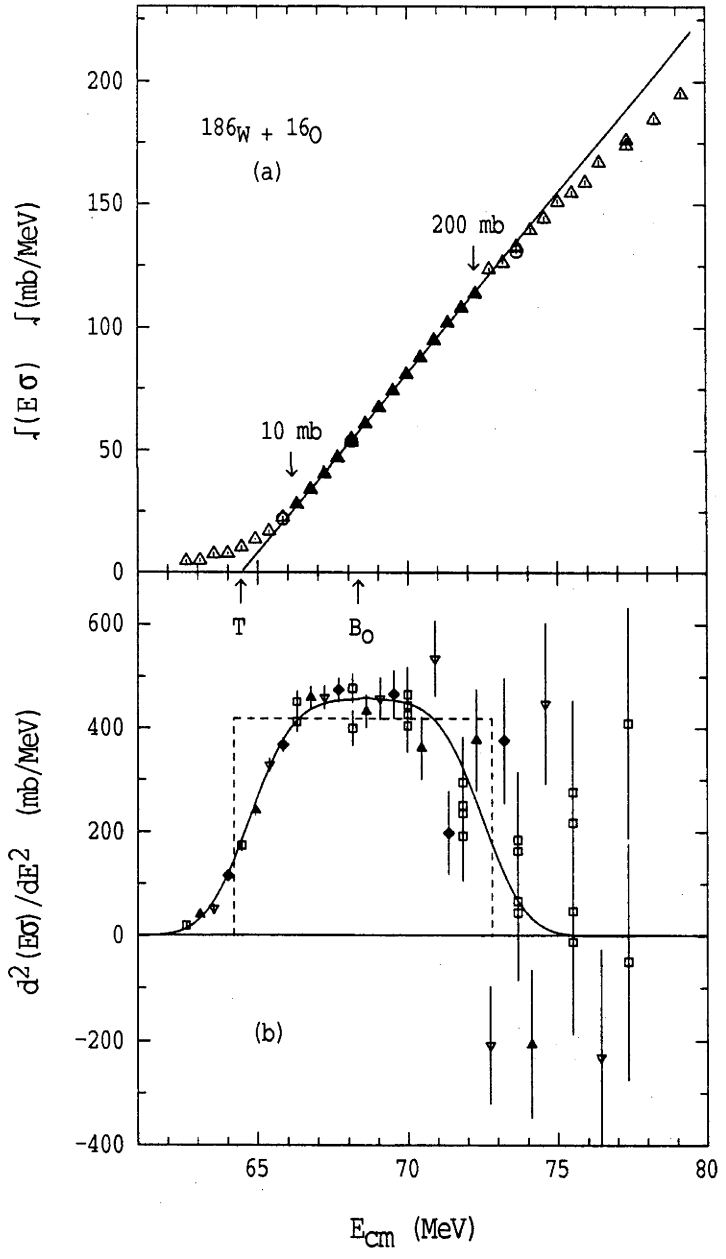

Fig. 5-1-1: (a) Square root of $E\sigma$ vs the energy E_{cm} for the reaction $^{186}W + ^{16}O$. The solid symbols in (a) were used to determine the straight line, by the least squares method. The intercept of this line on the energy axis gives the value of T. The average barrier B_0 is indicated.
(b) Calculated barrier distribution, $\frac{d^2(E\sigma)}{dE^2}$. The dashed line shows the flat barrier distribution which has a width of $2(B_0 - T)$, and the solid line shows the modulated distribution with $\Omega = 1.1$ MeV.

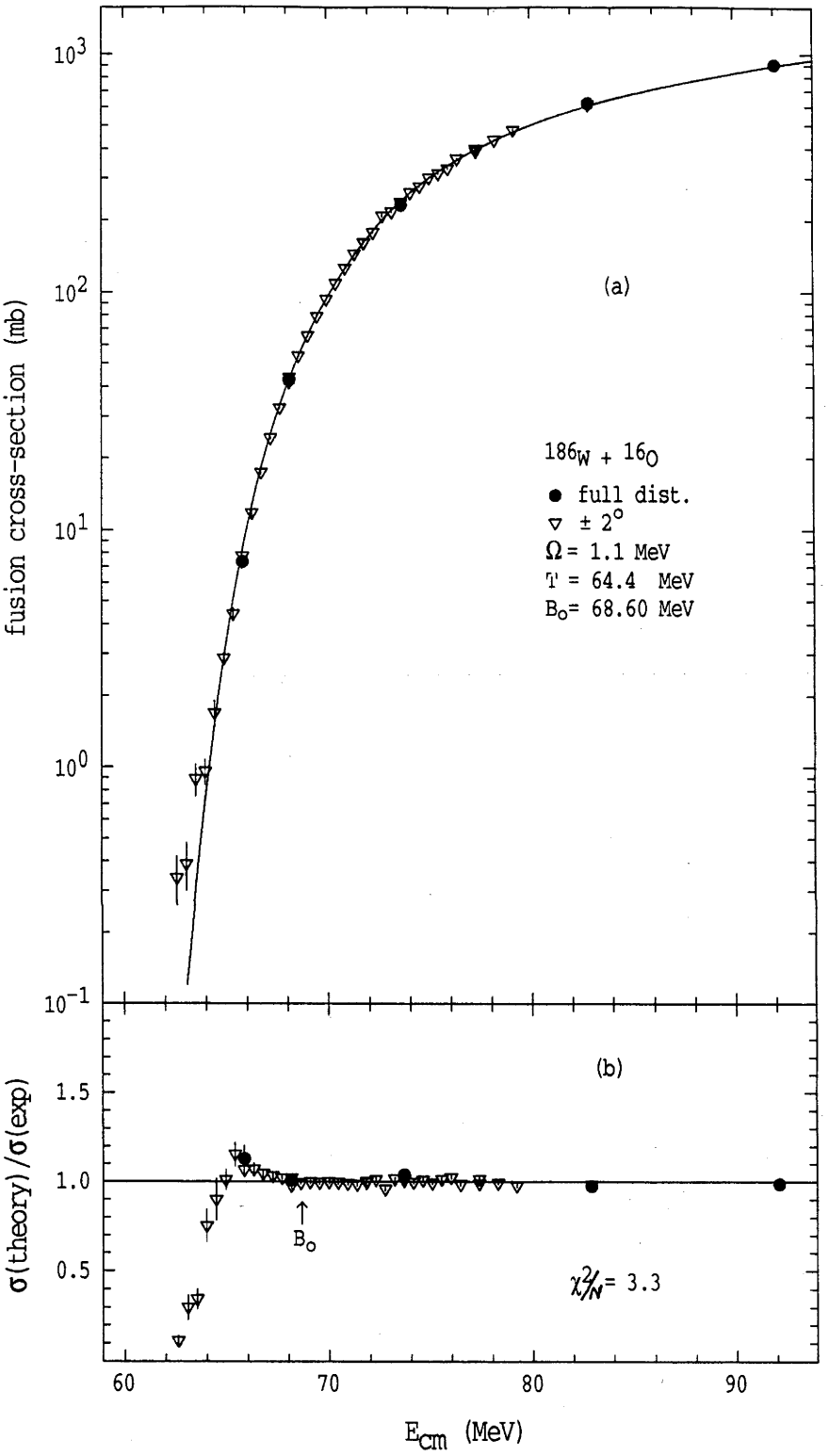

Fig. 5-1-2: (a) The fusion excitation function of $^{186}W + ^{16}O$. The curve is the result of the calculation using the modulated flat barrier distribution of Fig. 5-1-1 (b). (b) The ratio of calculation to experiment.

this reaction is symmetrical about the B_0, and the recipe of Stelson applies specifically to such cases. However, the symmetric barrier distribution is not applicable for the reaction $^{154}Sm + ^{16}O$, since its distribution is asymmetric.

Fig. 5-1-3 (a) shows $\sqrt{E\sigma}$ vs E for the reaction $^{154}Sm + ^{16}O$. As in the $^{186}W + ^{16}O$ case, the solid symbols in (a) were fitted by a straight line. However, this straight line does not fit the symbols related to the fusion cross-sections from 10 to 200 mb, as suggested by Stelson [Ste90]. The $\sqrt{E\sigma}$ appears linear at the range related to the fusion cross-sections from 33 mb to 340 mb, which are much larger than Stelson suggested and much larger than that in the case of $^{186}W + ^{16}O$ as well. The χ^2 per point of the least square fitting is ~12.6; about 10 times larger than that of ^{186}W case. The poor fit of the straight line to the plot $\sqrt{E\sigma}$ is clearly shown in (b) of this figure; in contrast to the ^{186}W case there is no plateau appearing in the extracted curvature, $d^2(E\sigma)/dE^2$, from data in the region where the $\sqrt{E\sigma}$ is "linear".

As in the ^{186}W case, the extracted T-value is 4.2 MeV less than B_0. The dashed line in (b) shows the flat barrier distribution with width $2(B_0 - T) = 8.4$ MeV. The solid line shows the modulated barrier distribution giving the optimum fit to the data. A large value of $\Omega = 1.8$ MeV is required, so as to fit all the cross-sections below 33 mb. The symmetry of this modulated barrier distribution still remains, but the shape of the barrier distribution is far from flat. The modulated distribution fits the barriers well at energies lower than B_0, but, it cannot reproduce the barriers higher than B_0; since the experimental barrier distribution is clearly not symmetrical. The fit to the fusion excitation function is shown in Fig. 5-1-4 (a) and the ratio of the

theoretical calculation to the experimental cross-section is illustrated in (b) of this figure. An average χ^2 of 17 per point is obtained.

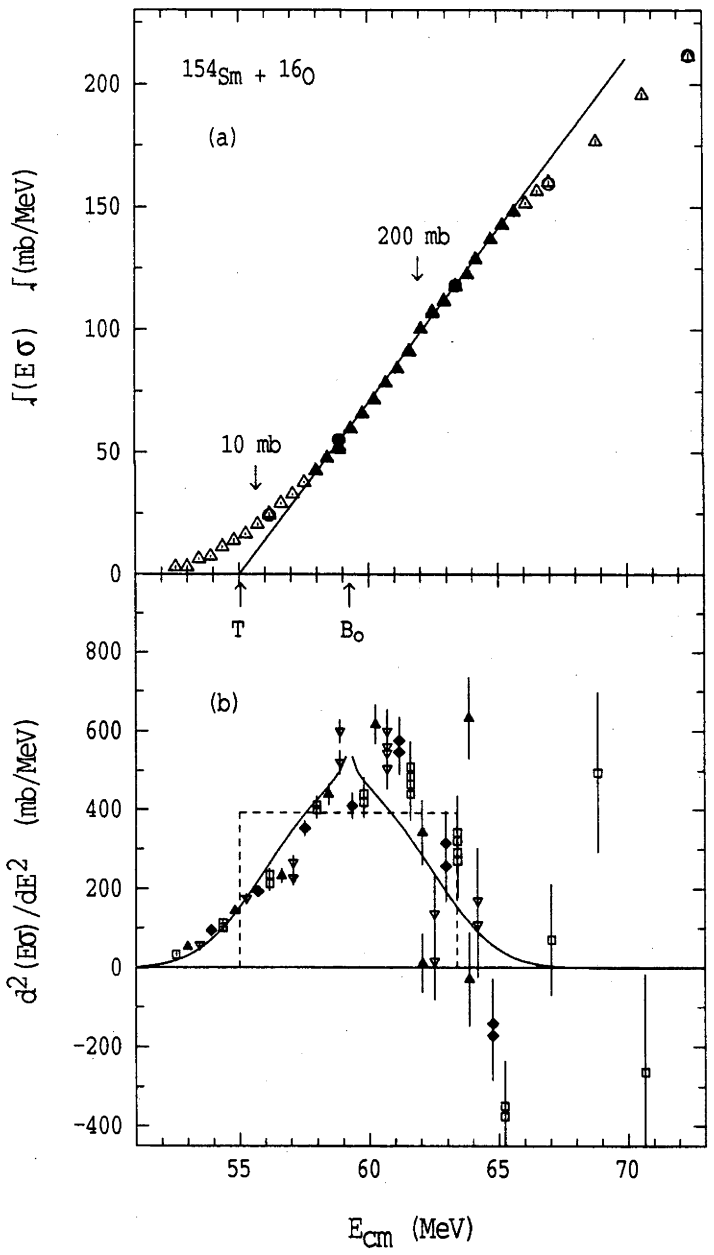

Fig. 5-1-3: (a) Square root of Eσ vs the energy E_{cm} for the reaction $^{154}Sm + ^{16}O$. The solid symbols in (a) were used to determine the straight line, by the least squares method. The intercept of this line on the energy axis gives the value of T. The average barrier B_0 is indicated.
(b) Calculated barrier distribution, $\frac{d^2(E\sigma)}{dE^2}$. The dashed line shows the flat barrier distribution which has the width of $2(B_0 - T)$, and the solid line shows the modulated distribution with $\Omega = 1.8$ MeV.

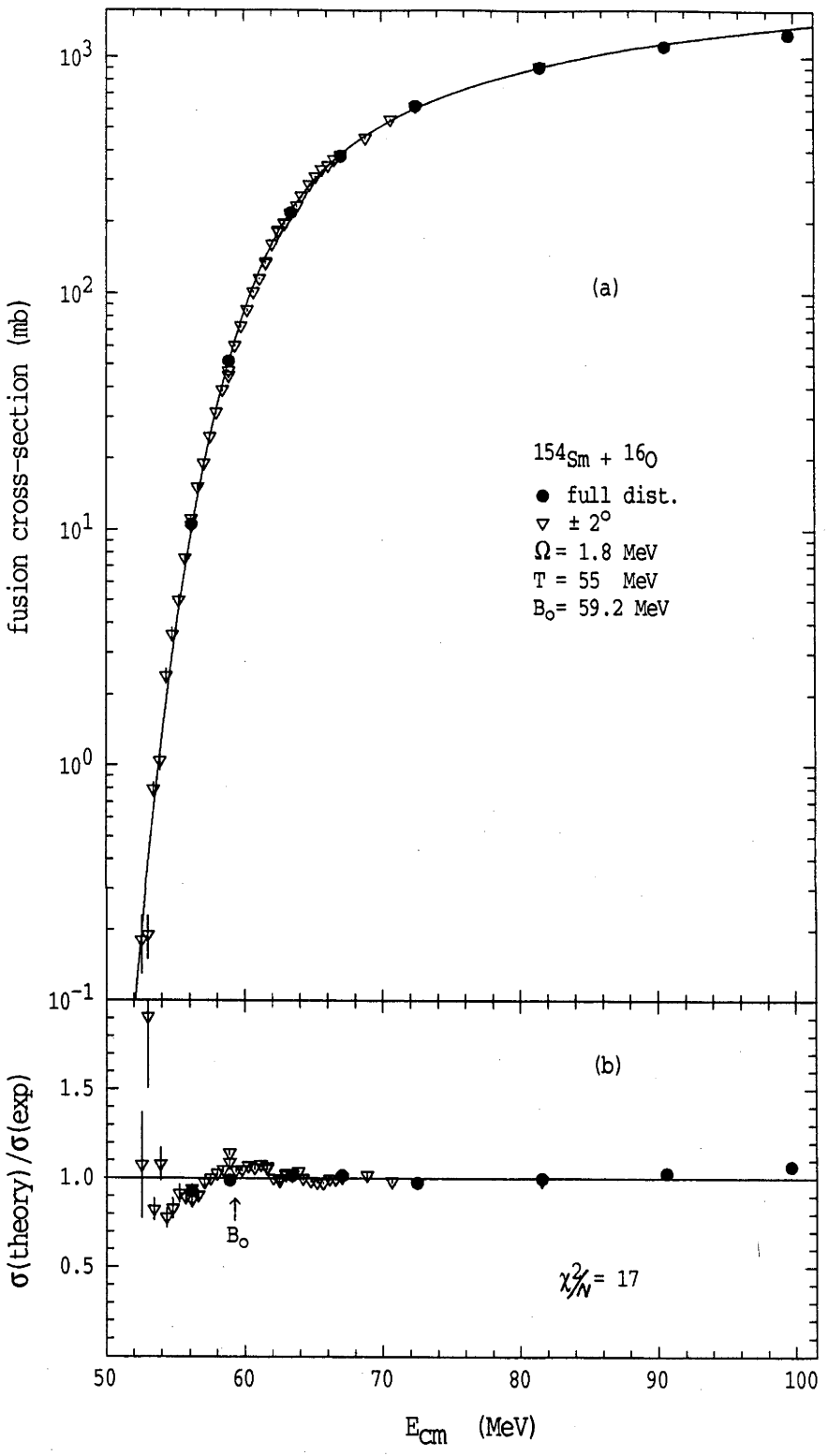

Fig. 5-1-4: (a) Fusion excitation function of ^{154}Sm + ^{16}O. The curve is the result of the calculation using the modulated flat barrier distribution of Fig. 5-1-3 (b). (b) The ratio of calculation to experiment.

5.1.3 Barrier Distribution Associated With Static Deformation

The recipe in Stelson et al is an empirical one, based on a flat and symmetric distribution of barriers. It makes no attempt to take the properties of the interacting nuclei into account. As discussed in Chapter 2, the static deformation of the projectile and/or target results in a distribution of fusion barriers, and the targets, studied in this work, are well deformed.

To illustrate the effects of the deformation I have used a simple model which includes quadrupole deformation, to first order, in the nuclear potential, whilst still using a monopole (spherical) Coulomb potential. Then the shape of a nucleus with a quadrupole deformation parameter β_2, can be represented by (see Chapter 2)

$$R_t(\theta) = R_t[1 + \beta_2 Y_{20}(\theta)] \qquad (5\text{-}1\text{-}4)$$

The barrier height of a deformed target interacting with a spherical projectile, can be approximately written as [Row91]

$$B(\theta) = B_0[1 - \frac{\beta_2 R_t}{R_c} Y_{20}(\theta)] \qquad (5\text{-}1\text{-}5)$$

where

$$R_t \sim 1.2\, A_t^{1/3}(\text{fm})$$

and $$R_c = \frac{Z_1 Z_2\, e^2}{B_0}$$

It has been show that the barrier height $B(\theta)$ in equation (5-1-5) varies monotonically with incident angle θ of the projectile, and the distribution of barrier heights can be found [Bac85, Row91] by

$$D(\theta)d\theta = \sin\theta d\theta = D(B)dB = \frac{1}{\sqrt{6\alpha(B_0 + 0.5\alpha - B)}} dB$$

thus

$$D(B) = \frac{1}{\sqrt{6\alpha(B_0 + 0.5\alpha - B)}} \tag{5-1-6}$$

where

$$\alpha = \sqrt{\frac{5}{4\pi}}\frac{\beta_2 B_0 R_t}{R_c} \tag{5-1-7}$$

Ignoring the changes of the barrier position R and curvature $\hbar\omega$ with angular momentum $l\hbar$, the fusion cross-section for each barrier can be written as [Won73]

$$\sigma(E, B) = \frac{\hbar\omega R^2}{2E}\ln[1 + \exp(\frac{2\pi\,(E - B)}{\hbar\omega})] \tag{5-1-8}$$

The total fusion cross-section for the full distribution of barriers D(B) can be calculated analytically

$$\sigma(E) = \int_{B_0 - \alpha}^{B_0 + 0.5\alpha} \frac{\hbar\omega R^2}{2E}\ln[1 + \exp(\frac{2\pi\,(E - B)}{\hbar\omega})]\frac{1}{\sqrt{6\alpha(B_0 + 0.5\alpha - B)}}dB \tag{5-1-9}$$

From this expression the smoothed distribution $\bar{D}(E)$ can be also obtained

$$\bar{D}(E) = \frac{d^2(E\sigma)}{dE^2} = \int_{B_0 - \alpha}^{B_0 + 0.5\alpha} \frac{2\pi}{\hbar\omega}\frac{e^x}{(1 + e^x)^2}\frac{1}{\sqrt{6\alpha(B_0 + 0.5\alpha - B)}}dB \tag{5-1-10}$$

where $x = \frac{2\pi}{\hbar\omega}(E - B)$ as it is defined by Eq. (2-3-19).

The best fit to the fusion excitation function can then be found by adjusting the deformation parameter β_2, hence the parameter α, in the expressions (5-1-9) and (5-1-10).

Fig. 5-1-5 illustrates the barrier distribution for this classical, static deformation model for the reaction of $^{154}Sm + ^{16}O$. The fine line in (a) is the classical barrier distribution D(B) for a target with a quadrupole deformation parameter $\beta_2 = 0.23$. This distribution is smoothed by barrier penetration, and the heavy line shows the smoothed barrier distribution $\bar{D}(E)$ of the expression (5-1-10). These distributions were obtained with the average barrier $B_0 = 59.2$ MeV and $\pi R^2 = 3300$ mb, both obtained from the high energy fusion data (as discussed in §4.2.2 and §5.1.1), and the barrier curvature $\hbar\omega = 4.3$ MeV was taken from Ref. [Row91a]. As discussed in §4.2.2, instead of the energy steps $dE \rightarrow 0$ in $d^2(E\sigma)/dE^2$, energy steps of $\Delta E = 1.81$ MeV in the centre of mass system have been used to extract the experimental barrier distribution $\Delta^2(E\sigma)/\Delta E^2$. This finite energy step introduces a further smoothing of the barrier distribution. This is illustrated by the dashed line in Fig. 5-1-5 (a) which shows the $\bar{D}(B)$ extracted from the theoretical cross-sections; treating them in the same manner as the experimental data, using energy steps $\Delta E = 1.81$ MeV. Only minor differences were found in the regions where the curvature of the barrier distribution $d^2(E\sigma)/dE^2$ is changing very quickly.

The target deformation parameter β_2 was adjusted and the best fit was obtained with $\beta_2 = 0.23$, consistent with that from previous fusion analyses [Sto78, Sto80], but significantly lower than the value of $\beta_2 \sim 0.3$ extracted from the Coulomb excitation measurements (see the later discussion and references [Fis77, Har79] for detail). The larger

β_2-value results in the much wider distribution in this simple model, as shown in Fig. 5-1-5 (b).

Fusion cross-sections calculated with this model are compared with experiment in Fig. 5-1-6. The agreement is good for all but the lowest energies, where the smoothed theoretical barrier distribution is

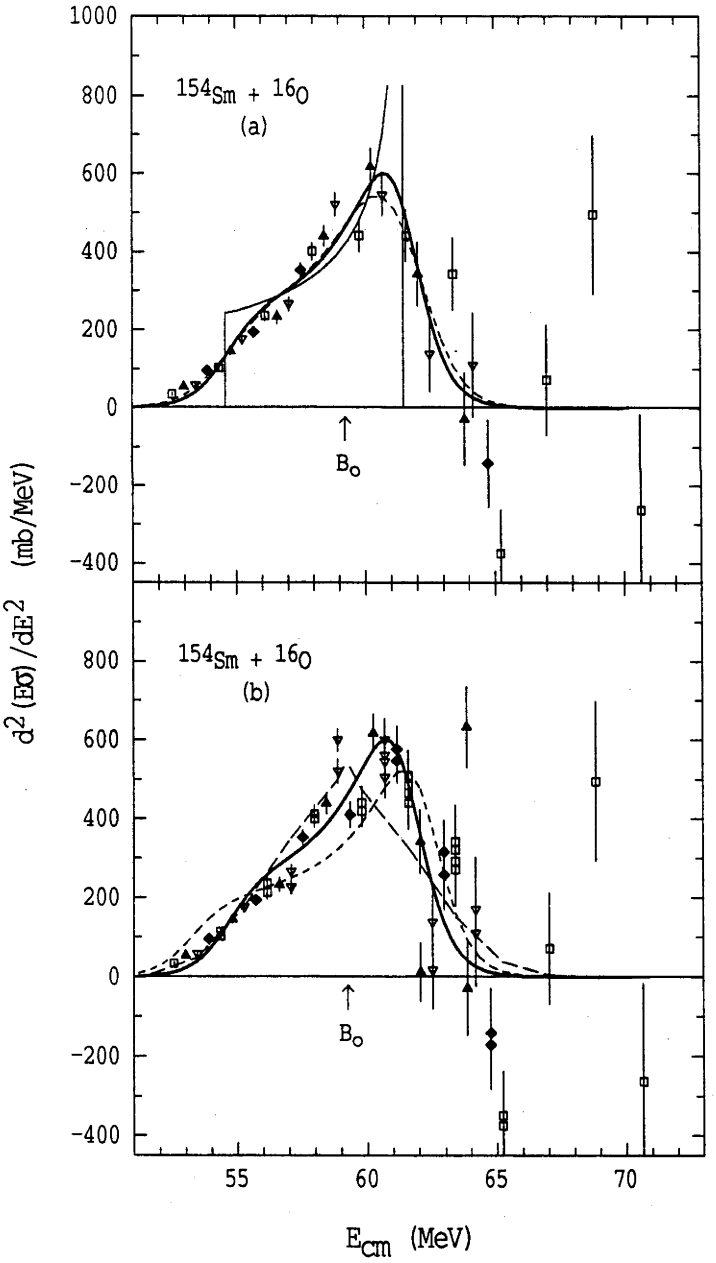

Fig. 5-1-5:
Curvature $d^2(E\sigma)/dE^2$ from (a) data measured with monotonically increasing energy and (b) all data. The curves in (a) are the classical barrier distributions for a target with a quadrupole deformation parameter $\beta_2 = 0.23$ (fine line), smoothed by barrier penetration (heavy line) and the effect of analysis with $\Delta E = 1.81$ MeV (dashed line). The curves in (b) correspond to the smoothed distribution (heavy line) from (a), the distribution for $\beta_2 = 0.3$ (short dash) and the modulated flat barrier distribution (long dash).

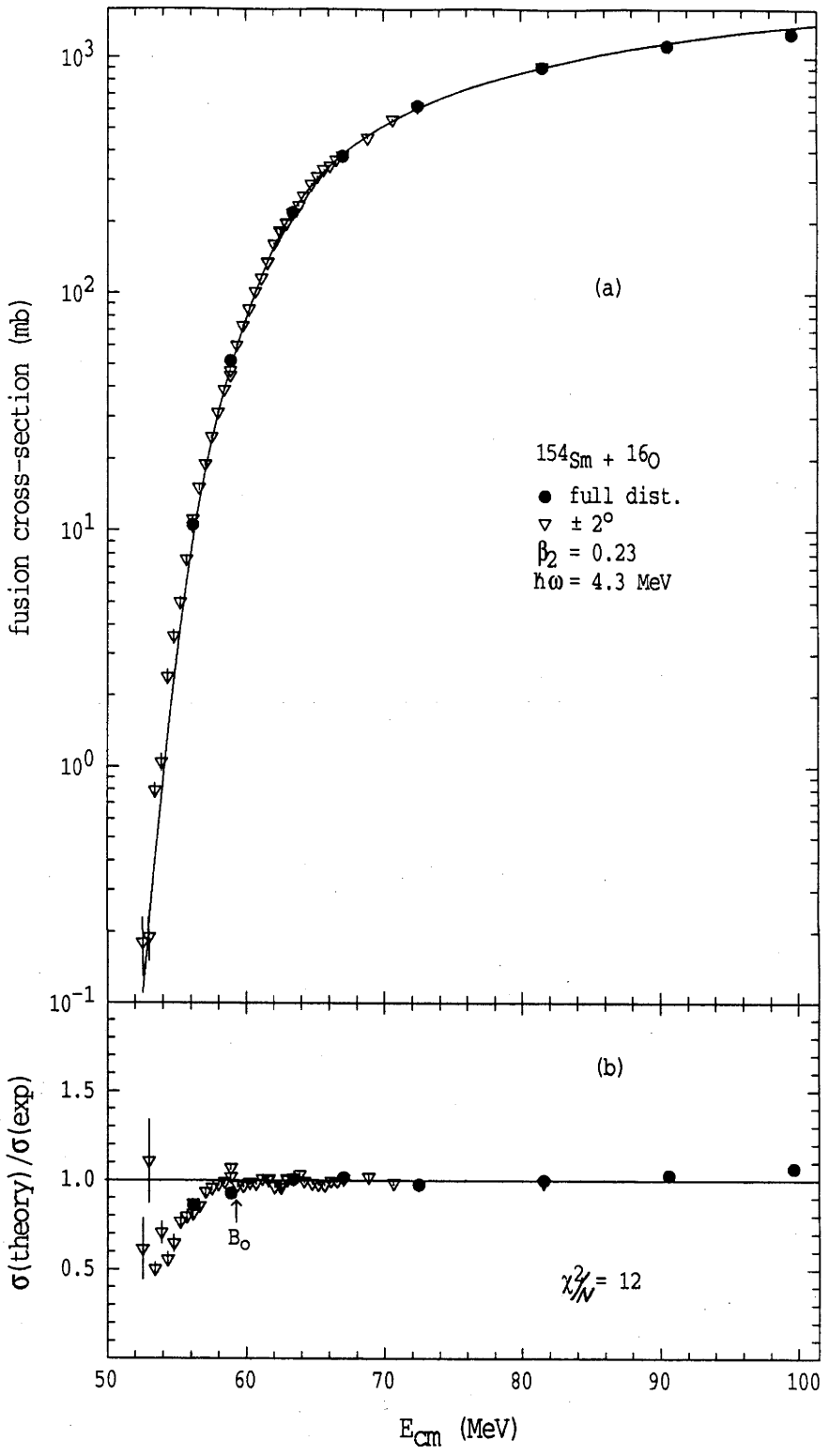

Fig. 5-1-6: (a) Fusion excitation function of ^{154}Sm + ^{16}O. The curve is the result of the calculation using the classical barrier distribution of Fig. 5-1-5 (b). Only the quadrupole deformation of the target was taken into account in the calculation. (b) The ratio of calculation to experiment.

slightly lower than experiment (Fig. 5-1-5 (a)) resulting in this deviation. The average χ^2 per point is ~12. Even though the χ^2 is still far from ideal ($\chi^2 \sim 1$), it is satisfying that such a simple model with only one adjustable parameter β_2, can fit the experiment fusion cross-sections over a range spanning four orders of magnitude. If one notices that the experimental statistical error is only about 1%, this classical static deformation model fits the experiment within an average error of only 3~4%.

As well as the quadrupole deformation, there is a hexadecapole deformation of the target. To include the hexadecapole deformation, an extra term β_4 should be included in the expressions (5-1-4) and (5-1-5) .

$$R_t(\theta) = R_t[1 + \beta_2 Y_{20}(\theta) + \beta_4 Y_{40}(\theta)] \qquad (5\text{-}1\text{-}11)$$

and

$$B(\theta) = B_o[1 - \frac{\beta_2 R_t}{R_c} Y_{20}(\theta) - \frac{\beta_4 R_t}{R_c} Y_{40}(\theta)] \qquad (5\text{-}1\text{-}11a)$$

However, one cannot get an analytical expression for D(B) similar to the expression of equation 5-1-6. Numerical methods have been used to convert the $D(\theta)d\theta$ to the D(B)dB. The fusion cross section can then be calculated numerically by using this barrier distribution. Thus

$$\sigma(E) = \int_{B_{min}}^{B_{max}} \frac{\hbar\omega R^2}{2E} \ln[1 + \exp(\frac{2\pi (E - B)}{\hbar\omega})] D(B)\, dB \qquad (5\text{-}1\text{-}12)$$

All parameters are the same as those used in the calculations in expression (5-1-9) when only a quadrupole deformation was considered. Now two parameters, β_2 and β_4, are allowed to vary to fit the fusion excitation function. For a given value of β_2 and β_4, the B_{min} and B_{max} are found numerically.

For the reaction of $^{154}Sm + ^{16}O$, the best fit was found when β_2 and β_4 had the values of 0.24 and 0.030 respectively; again they are significant smaller than those extracted from Coulomb excitation measurements [Fis77, Har79]. Fischer et al extracted the nucleus charge deformation parameters β_2, β_4 from their measured electric moments E2 and E4, by assuming a deformed Fermi distribution with diffuse nuclear surface. The radius parameter r_0 and the diffuseness a which they used ranged from r_0 = 1.10 fm, a = 0.6 to r_0 = 1.16 fm, a = 0.66, which yielded values of β_2 from 0.309±0.005 to 0.277±0.005 and β_4 from 0.122±0.020 to 0.096±0.019 respectively. The reasons for the disagreement of the extracted deformation parameters β_2, β_4 from fusion and from Coulomb excitation measurements [Fis77, Sto80] have remained unknown for a long time. This will be discussed in more details in §5.1.4 when a more realistic model is used in the analysis of our high precision data.

Fig. 5-1-7 (a) shows the best fit to the fusion excitation function. The ratios of the theoretical calculations to the experimental cross-sections are illustrated in Fig. 5-1-7 (b). This calculation gives a better fit to the fusion excitation function. The average χ^2 per point obtained from this fit is reduced to 7.4 from 12 obtained without β_4 as discussed before.

Fig. 5-1-8 shows that the comparison of the barrier distributions from the calculations with and without the β_4 deformation. There is a small but a significant change in the shape of the distribution when the β_4 deformation is included.

Fig. 5-1-9 shows the calculated barrier distributions of $^{186}W + ^{16}O$ obtained from the classical model with the quadrupole deformation of target, $\beta_2 = 0.195$, without (a) and with (b) the hexadecapole deformation.

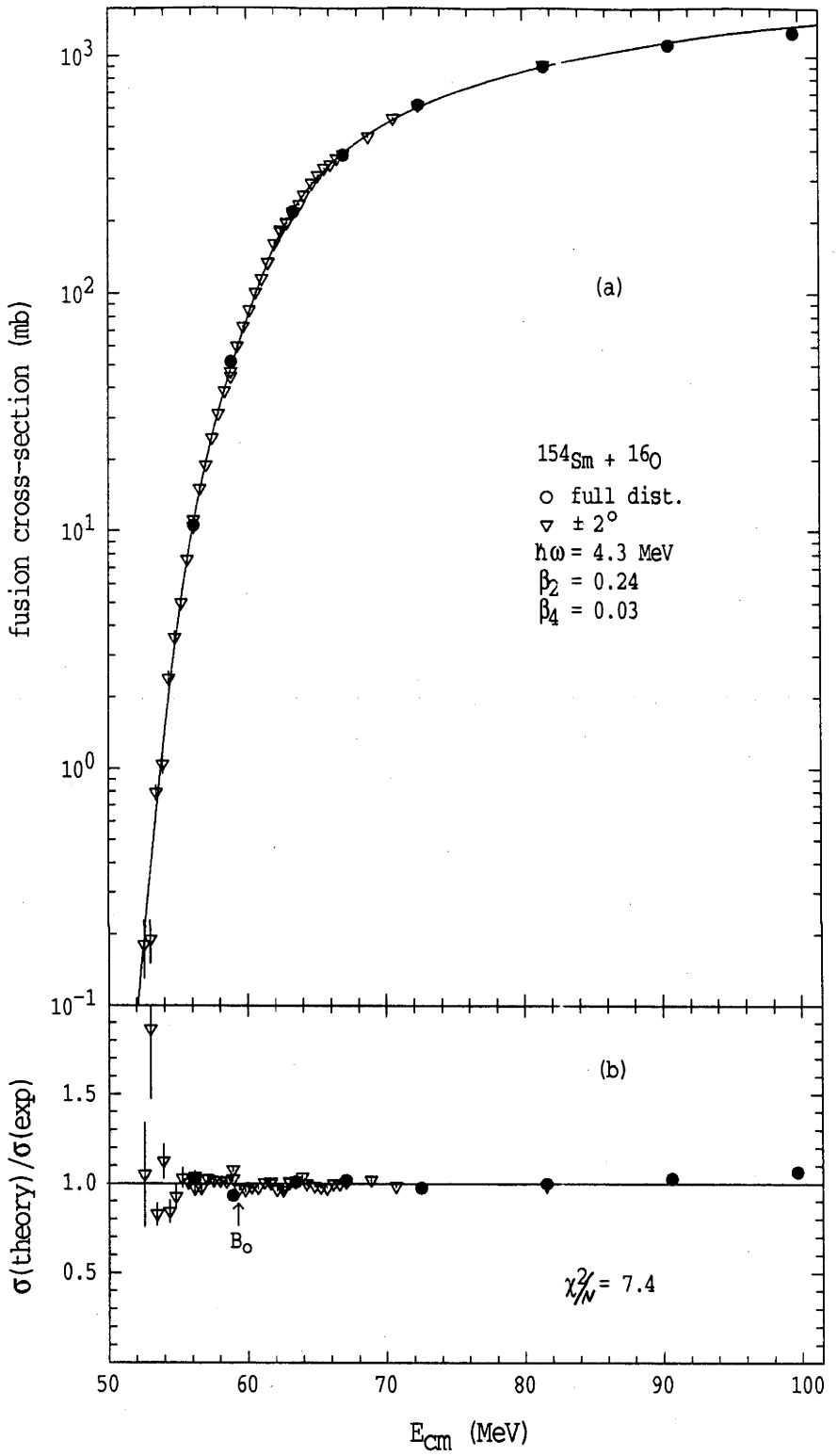

Fig. 5-1-7: (a) Fusion excitation function of ^{154}Sm + ^{16}O. The curve is the result of the calculation using the classical barrier distribution of Fig. 5-1-5 (b). Both the quadrupole and hexadecapole deformations of target were taken into account in the calculation. (b) The ratio of calculation to experiment.

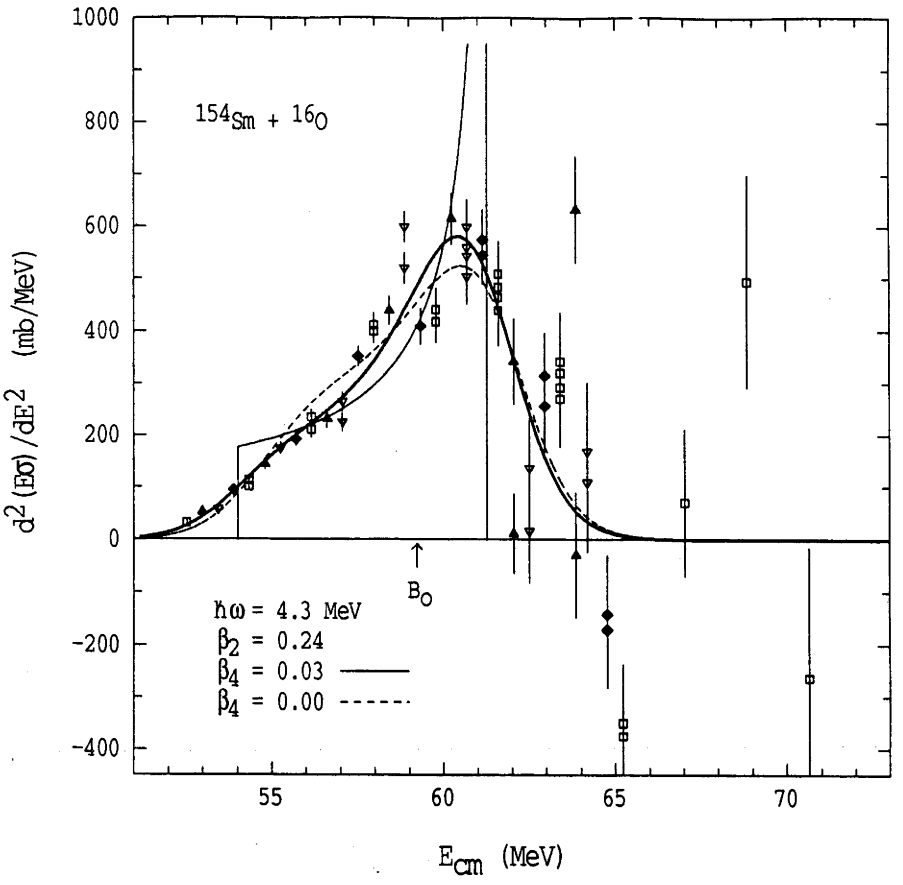

Fig. 5-1-8: Calculated classical barrier distribution D(B) with the target deformation parameter $\beta_2 = 0.24$ and $\beta_4 = 0.030$ (solid fine line), and the associated smoothed distribution $d^2(E\sigma)/dE^2$ obtained with energy steps of $\Delta E = 1.81$ MeV (solid line). The dashed line shows the curvature $d^2(E\sigma)/dE^2$ with the same quadrupole deformation, but without a hexadecapole deformation ($\beta_4 = 0$).

The shape of the barrier distribution for this reaction is changed significantly by the *negative hexadecapole* deformation ($\beta_4 = -0.035$) which is necessary to fit the data. Without the hexadecapole deformation, for the solid curve in (a) a large discrepancy occurs around the average barrier B_0 (68.6 MeV). The calculation overestimates the barrier distribution at the energies just above the B_0

and underestimates them at the energies just below the B_0. A negative hexadecapole deformation dramatically improves the fit as shown in Fig. 5-1-9 (b). As in the Sm case, the extracted $\beta_2 = 0.195$ and $\beta_4 = -0.035$ are systematically smaller than those extracted from Coulomb excitation measurements ($\beta_2 = 0.224 \sim 0.244$ and $\beta_4 = -0.088 \sim -0.178$).

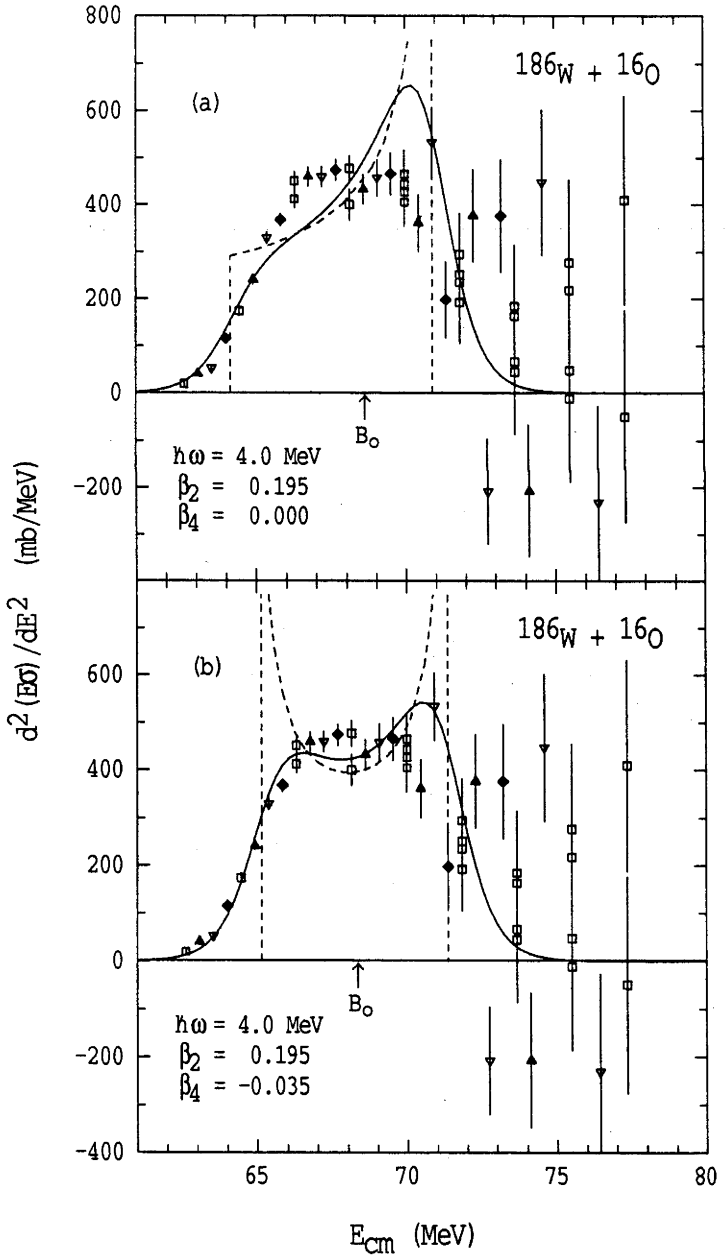

Fig. 5-1-9: Calculated curvature $d^2(E\sigma)/dE^2$ obtained with the energy steps of ΔE = 1.84 MeV for the permanently deformed target ^{186}W. (a) For the target with quadrupole deformation only ($\beta_2 = 0.195$), (b) with the same quadrupole deformation in (a), but with a hexadecapole deformation as well ($\beta_4 = -0.035$). The dash curves correspond to the classical barrier distributions resulting from the deformation of target and the solid curves correspond to the smoothed barrier distributions.

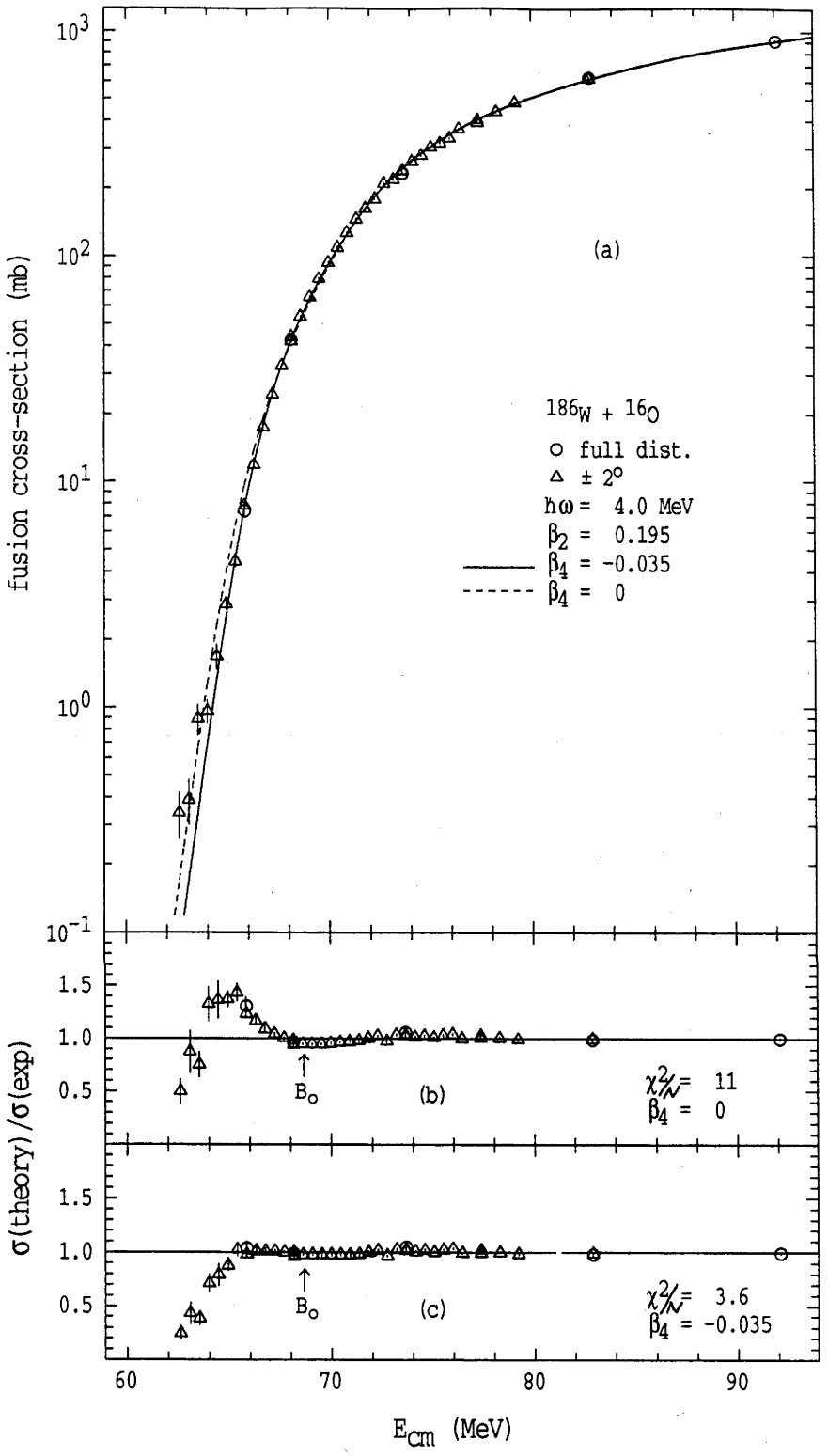

Fig. 5-1-10: (a) Fusion excitation function of $^{186}W + ^{16}O$. The curves are the results of the calculations using the classical barrier distributions of Fig. 5-1-9. The dashed line corresponds to a quadrupole deformation of target only. The solid line corresponds to quadrupole and hexadecapole deformations of target. (b) and (c) the ratios of these calculations to the experiment.

Fig. 5-1-10 shows the calculated fusion excitation functions, with (solid line) and without (dashed line) the hexadecapole deformation, compared with the measured data; the average χ^2 per point for these two calculations are ~3.6 and ~11 respectively. For energies higher than B_0 the calculations are almost identical and fit the fusion cross sections well. However, at lower energies the $\beta_4 = 0$ calculation overestimates the fusion.

The parameters of the best fit, used in the classical model, are listed in Table 5-1-2.

Table 5-1-2: The parameters used in the classical model, with which the calculations have the best fit to the fusion excitation function, and associated χ^2 per point for the fits. The energy indicated is in the centre of mass system.

Reactions	B_0(MeV)	πR^2	β_2	β_4	χ^2
$^{154}Sm + ^{16}O$	59.2	3300	0.24	0.030	7.4
$^{186}W + ^{16}O$	68.6	3520	0.195	-0.035	3.6

Concluding this section, various calculations using simple models appear to fit the fusion excitation function almost equally well (2~4%). However, they do not equally well reproduce the barrier distribution of the reaction system. For instance, without the negative hexadecapole deformation the barrier distribution of $^{186}W + ^{16}O$ can not be reproduced. The deformation parameters β_2, and β_4 deduced from fusion in the simple classical deformation model are not quantitatively consistent with those deduced from Coulomb excitation. This may not be surprising because the simple models do not consider the

internuclear potential properly; for instance, the effects of the multipole Coulomb potential resulting from the deformed charge distribution of the nucleus are not taken into account. These effects and the possible reasons for the above discrepancy in the extracted deformation parameters are discussed below.

5.1.4 Deformation Parameters Determined From Fusion Excitation Function

In the above analysis, with the simple static deformation model, only the monopole term of the Coulomb interaction was used. However, the monopole interaction is not adequate for large deformations. For more accurate calculations, the Coulomb potential for a deformed charged distribution should have been used. This is derived from the general formulae of reference [Ald75] and, to first order in β_2, is given by

$$V_c = \frac{Z_1 Z_2}{r}\left[1 + \frac{3}{5}\frac{\beta_2 R_t^2}{r^2} Y_{20}(\theta)\right] \qquad (5\text{-}1\text{-}13)$$

where Z_1 and Z_2 are the atomic numbers of target and projectile and R_t is the mean radius of the target, as defined earlier.

It can be easily shown that expanding the above at $R_c = Z_1 Z_2 e^2/B_0$ and ignoring the higher order β_2 terms one gets

$$B(\theta) = B_0\left[1 - \frac{\beta_2 R_t}{R_c} Y_{20}(\theta) + \frac{3}{5}\frac{\beta_2 R_t^2}{R_c^2} Y_{20}(\theta)\right]$$

$$= B_0\left[1 - \left(1 - \frac{3}{5}\frac{R_t}{R_c}\right)\frac{\beta_2 R_t}{R_c} Y_{20}(\theta)\right] \qquad (5\text{-}1\text{-}14)$$

Comparing this with Eq. 5-1-5 for the barrier height of the monopole Coulomb potential, one can see that it gives essentially the same

distribution of barrier heights if $\beta_2(1 - 3R_t/5R_c)$ is equal to the β_2-value obtained using the spherical Coulomb potential. For $^{154}Sm + ^{16}O$, $R_t/R_c \sim 0.6$, implying that the β_2, extracted in the last section (§5.1.3) for ^{154}Sm, was about 64% of the value expected using a more realistic deformed Coulomb potential.

It has been shown, in the course of this work [Lei93], that in the earlier analyses of the fusion data for ^{16}O induced reactions on isotopes of Sm performed by other authors [Sto78,81, DiG86, DiG89], the quadrupole deformation parameter, β_2, had also been underestimated for various reasons. This may explain why the β_2 extracted in the last section is consistent with their result of $\beta_2 = 0.2 \sim 0.23$.

In order to investigate the above effect in more details, calculations of the orientation dependent barriers, without the previous approximations, and including the effects of angular momentum l have been performed.

The nuclear potential, $V_N(r,\theta)$, is essentially taken to have an exponential tail and may therefore be simply parameterised by its surface diffuseness a and potential strength at some radius. The advantage of using the exponential form is that the potential can also be parameterised in terms of the resulting barrier height B_0 for the spherical case. Since at the barrier position R

$$\frac{dV_N(r)}{dr} = -\frac{dV_c}{dr}$$

we can parameterise $V_N(r)$ as

$$V_N(r) = -\frac{a}{R}\frac{Z_1Z_2e^2}{R}\exp(-\frac{r - R}{a}) \qquad (5\text{-}1\text{-}15)$$

and

$$B_0 = V_N(R) + V_c(R) = \frac{Z_1 Z_2 e^2}{R}(1 - \frac{a}{R}) \qquad (5\text{-}1\text{-}16)$$

To account for the angular dependence of the radius of the deformed target, the exponent in $V_N(r,\theta)$ can be written as [Gut73, Row89]

$$V_N(r,\theta) = -\frac{a}{R}\frac{Z_1 Z_2 e^2}{R} \exp(-\frac{r - R(\theta)}{a}) \qquad (5\text{-}1\text{-}17)$$

where

$$R(\theta) = R + R_t[\beta_2 Y_{20}(\theta) + \beta_4 Y_{40}(\theta)] \qquad (5\text{-}1\text{-}18)$$

where the target radius R_t can be obtained from its atomic number A_t, thus

$$R_t = r_0 A_t^{1/3} \qquad (5\text{-}1\text{-}19)$$

and 1.06 fm was used for the radius parameter r_0.

The Coulomb potential, $V_c(r,\theta)$, now including the quadrupole and hexadecapole terms and expanded to order β_2^2 and β_4, becomes

$$V_c(r,\theta) = B_0[1 + \frac{3}{5}\frac{R_t^2}{r^2}(\beta_2 + \sqrt{\frac{5}{\pi}}\beta_2^2)Y_{20}(\theta) + \frac{1}{3}\frac{R_t^4}{r^4}(\beta_4 + \frac{9}{7\sqrt{\pi}}\beta_2^2)Y_{40}(\theta)] \qquad (5\text{-}1\text{-}20)$$

Knowing the V_N and V_c, and including the usual angular momentum barrier, $\hbar^2 l(l+1)/2\mu r^2$, the θ dependent internuclear potential $V_l(r,\theta)$ is obtained.

The barrier height, $B_l(\theta)$, position $R_l(\theta)$ and curvature $\hbar\omega_l$ are calculated numerically for each l and target orientation angle. The

barrier is then approximated by an inverted parabolic potential for which the partial fusion cross-sections are calculated, thus

$$\sigma_l(\theta) = \pi\lambda\!\!\!^{-2}\frac{2l+1}{1+\exp[\frac{2\pi}{\hbar\omega_l(\theta)}(B_0(\theta)+\frac{l(l+1)\hbar^2}{2\mu R_l^2(\theta)}-E)]} \qquad (5\text{-}1\text{-}22)$$

The total fusion cross-section may then be calculated using

$$\sigma = \sum_l \int_0^{\pi/2} \sigma_l(\theta)\,\sin\theta d\theta \qquad (5\text{-}1\text{-}23)$$

In practice the integration above was performed using the eigenchannel formalism of references [Lin84, Nag86]. The results converge for any number of eigenchannels greater than six, corresponding to a standard coupled-channels calculation, including states up to 10^+ in the rotational band of ^{154}Sm and ^{186}W; twenty eigenchannels were used in this calculation.

The ^{154}Sm case is discussed first. The experimental data were fitted using this model. Approximate values of the nuclear potential parameters, a and B_0, were obtained by fitting only the cross-sections for bombarding energies above 70 MeV, where the calculated cross-sections are not expected to be sensitive to the deformation parameters. Subsequently these parameters were readjusted in conjunction with the deformation parameters β_2 and β_4 to optimise the fit to the complete excitation function.

The optimum fits are obtained with β_2 and β_4 - values of 0.304 and 0.052 compared with 0.24 and 0.035 in the above simple static deformation model when only a monopole Coulomb potential used. The nuclear potential which gives the optimum fit has a value of -8.53 MeV at 10.5 fm and a diffuseness of a = 1.27 fm. This gives B_0 = 59.50

MeV and the resulting $\hbar\omega$ of the spherical barrier at l = 0 is 3.4 MeV. The value of a = 1.27 fm is higher than that obtained from elastic scattering data [Chr76]. However, a double-folded potential for heavy ions [Sat79] does produce a rather deep potential with an effective surface diffuseness of the same order as that obtained in this analysis.

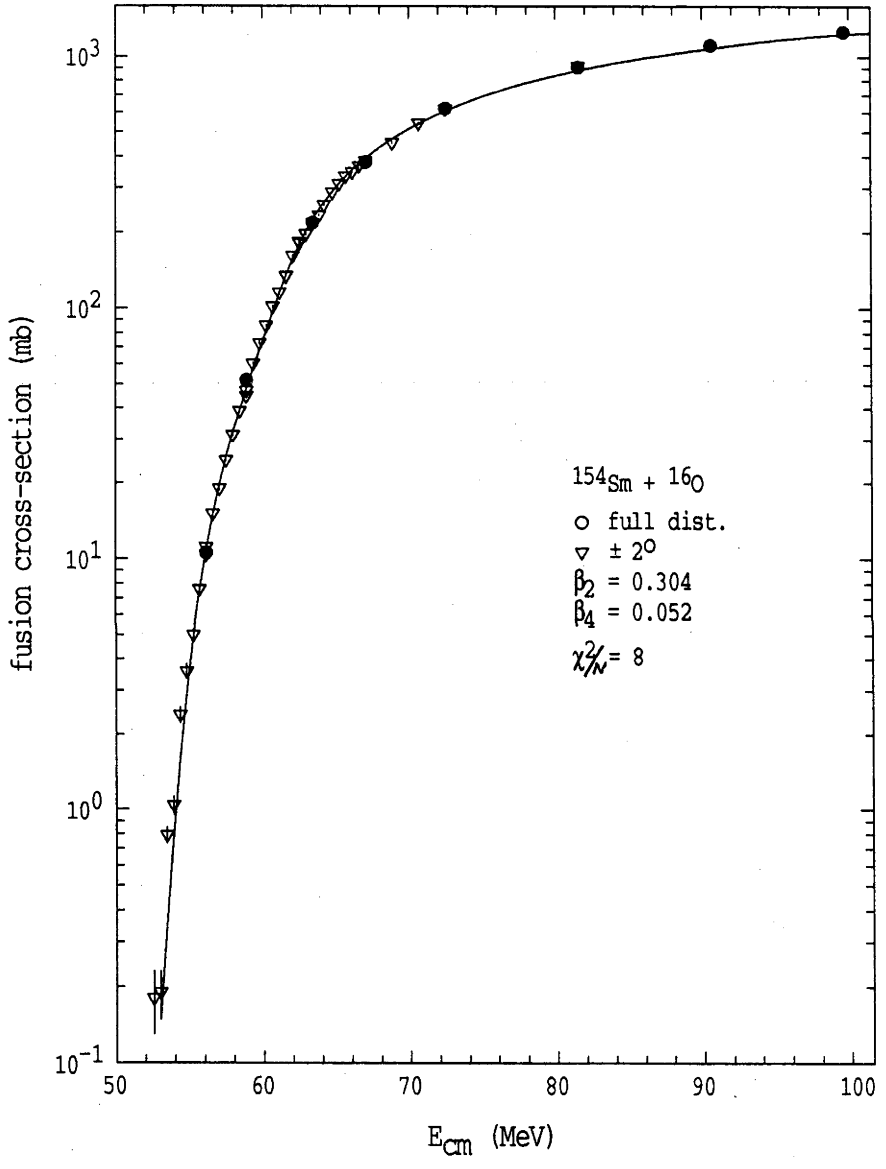

Fig. 5-1-11: Fusion excitation function of $^{154}Sm + ^{16}O$. The curve is the result of the calculation using the classical barrier distribution (see text for details and see Fig. 5-1-12 for the smoothed barrier distribution). The deformation parameters of the target are listed on the figure.

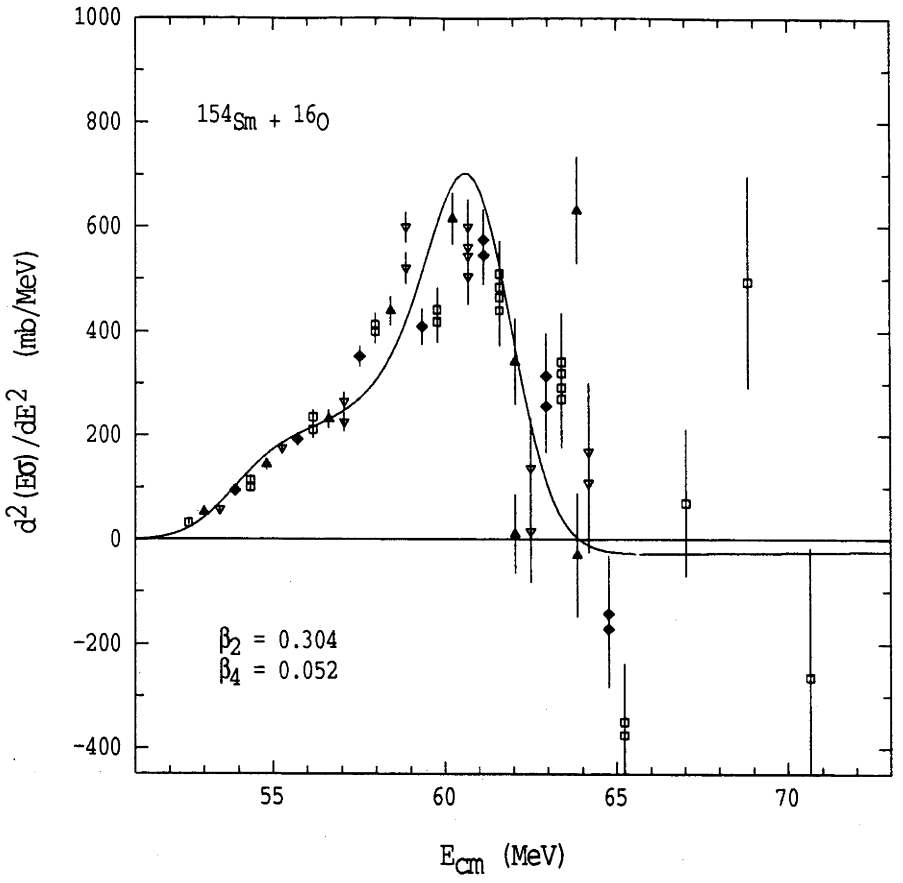

Fig. 5-1-12: The curvature of Eσ vs E extracted from the measured fusion excitation function for ^{154}Sm + ^{16}O, compared with the theoretical values (1.81 MeV steps were used in the extraction of both distributions). The monopole, quadrupole and hexadecapole Coulomb potentials were used in the calculation of the internuclear barrier. The deformation parameters of the target are listed on the figure.

Fig. 5-1-11 shows the calculated fusion excitation function, and Fig. 5-1-12 illustrates the smoothed fusion barrier distribution (solid line) used in the calculation. The χ^2 per point, in fitting the cross-sections, is about 8. The remaining discrepancies evident in Fig. 5-1-11 still appear to be systematic and this may reflect the inadequacy of the model at this ~3% level. There are several effects resulting from transfer reactions and projectile excitation, for example, which may

affect the theoretical distribution but are more difficult to be taken into account.

Though the quality of fit to the experimental data over the whole range of the excitation function is almost the same as the simple classical model, the value of β_2 is now, however, consistent with other non-fusion estimates which vary from 0.26 to 0.34 [Ste71, Fis77, Ram86]. The value β_4 is also within the range of previously published values, 0.044 to 0.13 [Ste71, Bru74, Fis77]. These ranges of deformation parameters result, in large degree, from the choice of the Coulomb radius parameter; analyses of Coulomb excitation data [Sha74, Lee74, Lee75, Fis77] which use a radius parameter of ~1.10, close to our value of 1.06, all yield values of β_2 close to 0.30 and β_4's near 0.11. The inelastic scattering data of reference [Hen68, Hen73] gives $\beta_2 = 0.29$ and $\beta_4 = 0.06$, when adjusted to this same radius parameter. The agreement between these results and the new fusion analysis is remarkable for this case though there is uncertainty in the choice of the nucleus radius r_0. However, the sensitivity of the deformation parameters to the choice of radius is small in this model; a 10% increase in radius gives ~5% decrease in the beta's. Thus it is clear that the interpretation of fusion for this reaction does require much larger deformation parameters than those previously published. It is also evident that the fusion excitation function is not only sensitive to the β_2 deformation but also to the higher orders of the deformation such as the β_4 deformation.

Fig. 5-1-13 (a) shows the typical shapes of calculated barrier distributions associated with a spherical projectile incident on a target with a positive quadrupole deformation (prolate shape, $\beta_2 > 0$). The solid line in (a) shows the barrier distribution associated to the target

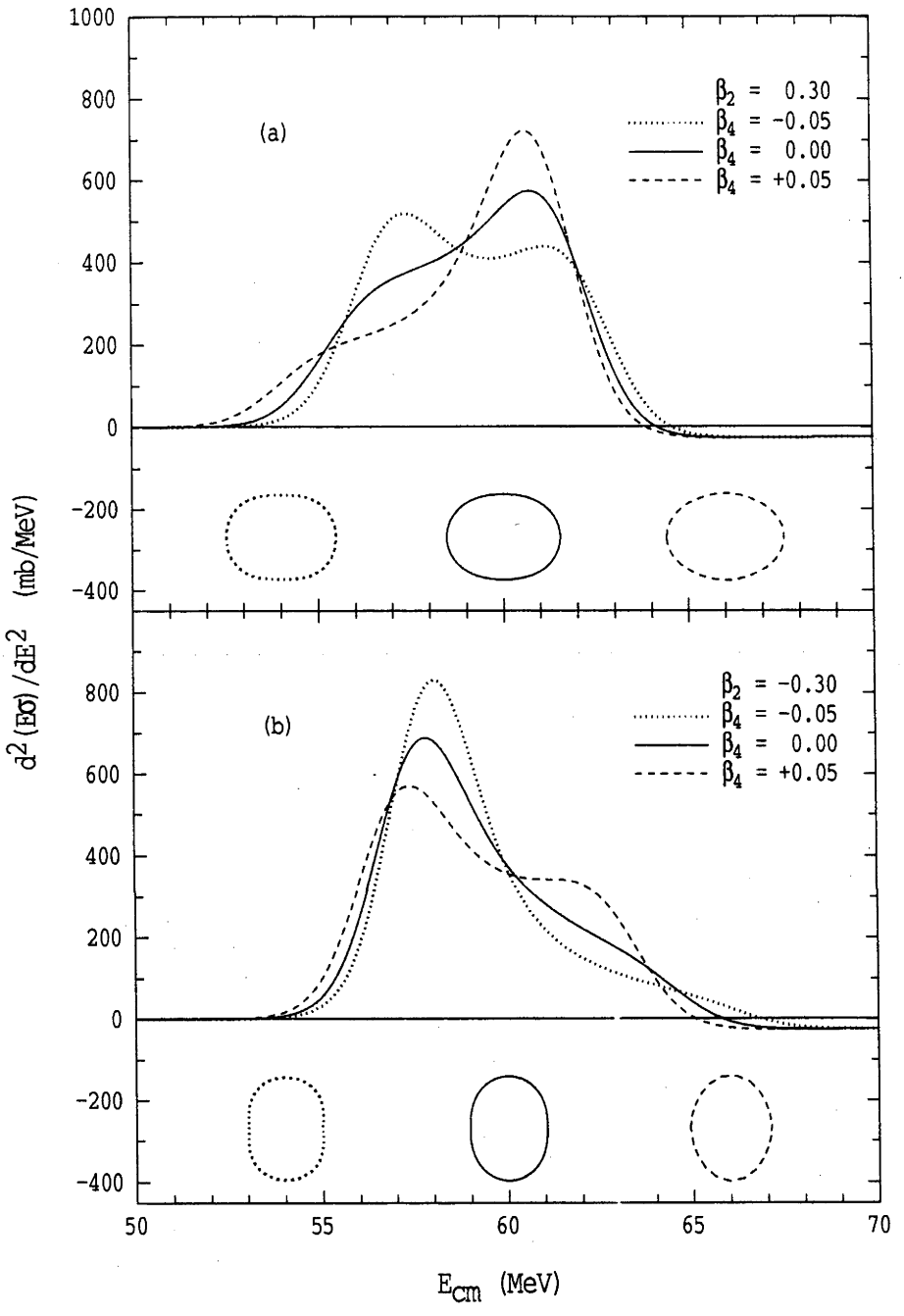

Fig. 5-1-13: The curvature of Eσ calculated for fixed quadrupole deformation, β_2 = 0.3 in (a) and β_2 = -0.3 in (b), with various hexadecapole deformations β_4 = +0.05 (dashed line), β_4 = 0.0 (solid) and β_4 = -0.05 (dotted). The shapes of these nuclei are also indicated in the lower part of each figure. Clearly, the value of β_4 has a significant effect on the distribution although the changes in nuclear shapes are not so dramatic.

with a positive quadrupole deformation only, while the dot and dashed lines are associated with the same quadrupole deformation but with a negative and a positive hexadecapole deformation respectively. Clearly, the dashed line, with the positive hexadecapole deformation, represents best the experimental barrier distribution of ^{154}Sm + ^{16}O. Fig. 5-1-13 (b) shows the other typical shapes of barrier distributions associated with reactions induced by a spherical projectile incident on a target with negative quadrupole deformation (oblate shape, $\beta_2 < 0$). The shapes are significantly different with those of (a), though there may be some confusion at some stage between a prolate target with negative β_4 deformation and an oblate target with positive β_4 deformation. However, since there are few oblate deformed nuclei, this will not result in confusion for the determination of the signs of deformation parameters for most nuclei. Qualitatively, without looking at the details of the distribution, the signs of the deformations parameters, β_2, β_4, can be easily determined.

Fig. 5-1-14 shows the calculated fusion excitation function which has the best fit to the data for reaction ^{186}W + ^{16}O. The smoothed barrier distribution used in the calculations is shown in Fig. 5-1-15. The nuclear potential which gives the optimum fit has a value of -9.1 MeV at 10.9 fm and a diffuseness of a = 1.27 fm. This gives B_0 = 69.03 MeV and the resulting $\hbar\omega$ of the spherical barrier at l = 0 is 3.5 MeV. Again the value of a = 1.27 fm is higher than that obtained from elastic scattering data [Chr76]. The parameters β_2 and β_4 for the optimum fits are 0.295 and -0.023 respectively. This, however, overestimates the β_2-value by 20 ~ 30%, and underestimates the β_4-value compared with other non-fusion estimates of β_2 and β_4 which vary from 0.224 [Ram86] to 0.244 [Bru74], and from -0.088 [Lee75] to -0.178 [Bru74] respectively.

The reason for these discrepancies is unknown at the moment. It is possible that the excellent agreement in the extracted deformation parameters in ^{154}Sm case is just fortuitous; alternatively there may be other effects in the ^{186}W case which are not included in this model. For instance, coupling to additional channels, such as vibration or

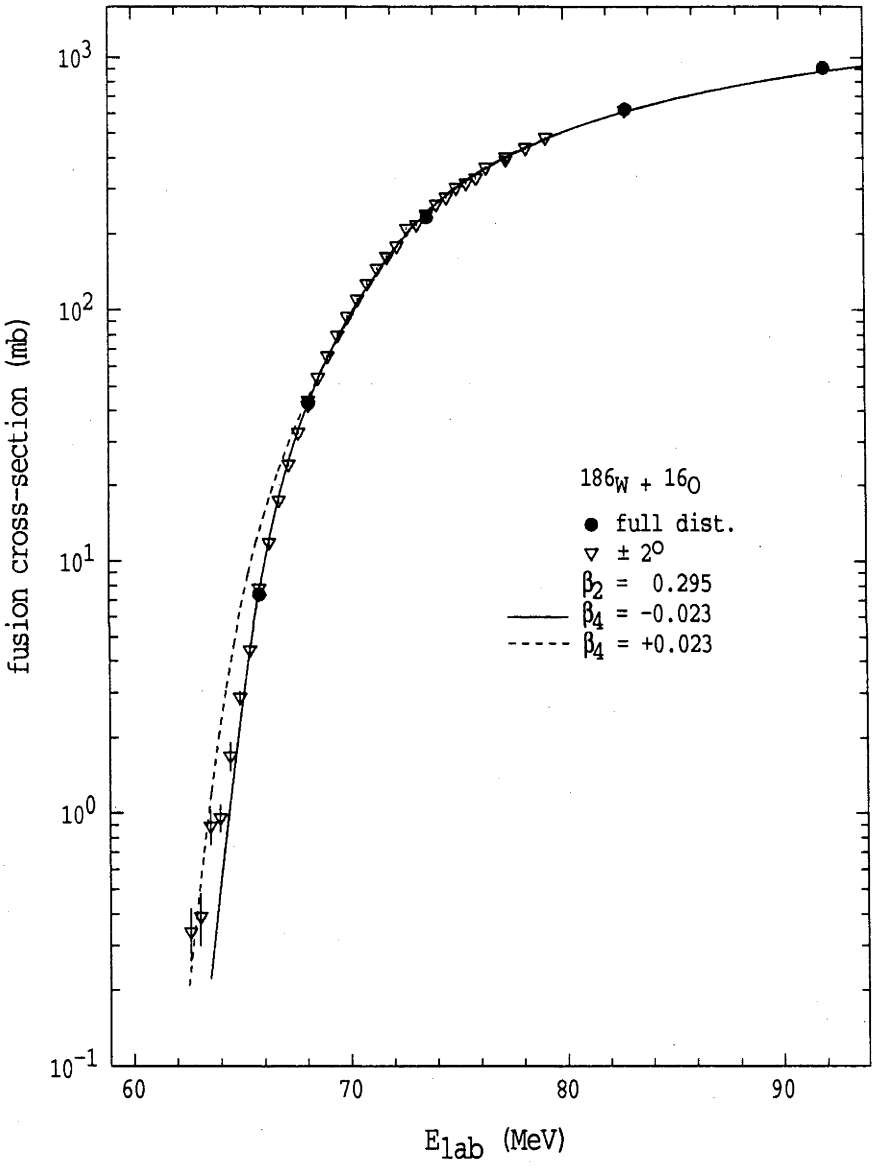

Fig. 5-1-14: Fusion excitation function of $^{186}W + ^{16}O$. The curve is the result of the calculation using the classical barrier distribution (see text for details and see Fig. 5-1-14 for the smoothed barrier distribution). The deformation parameters of the target are listed on the figure.

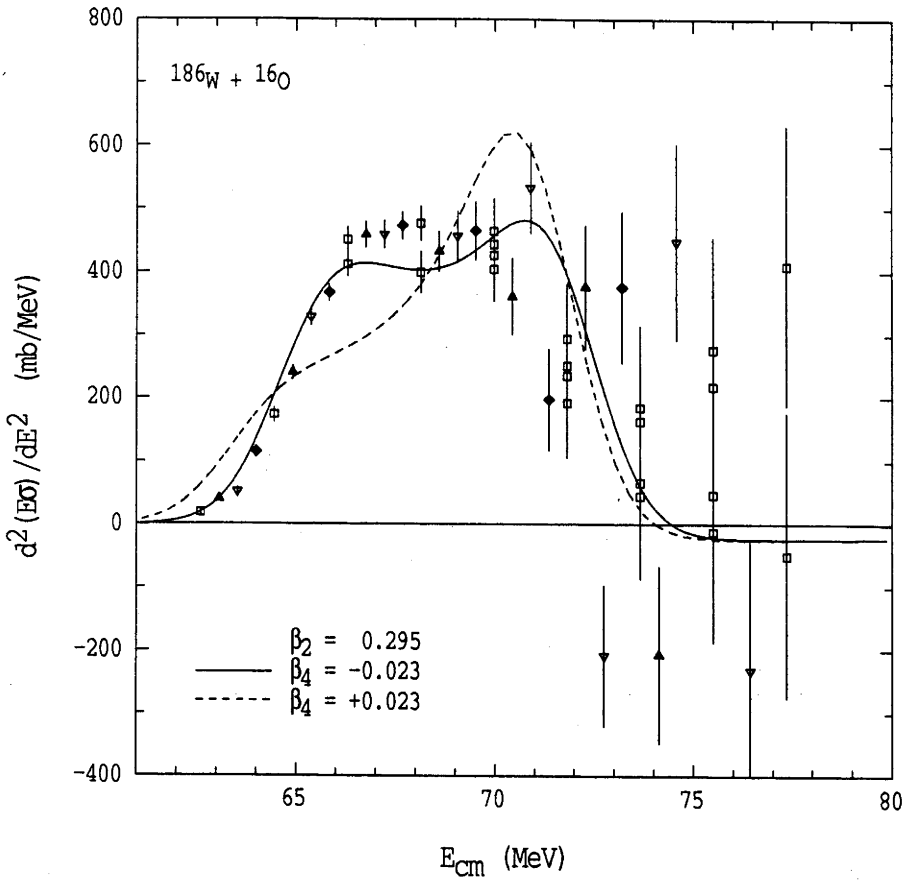

Fig. 5-1-15: The curvature Eσ vs E extracted from the measured fusion excitation function for $^{186}W + ^{16}O$, comparing with the theoretical values. The monopole, quadrupole and hexadecapole Coulomb potential are used in the calculations of internuclear barrier. The deformation parameters of the target are listed on the figure.

transfer channels, will result in additional barriers, producing a smearing of the barrier distribution. Since, in this model, we only considered the classical deformation (or coupling to the ground state rotational band), any additional coupling would require a larger value of β_2 and/or a smaller absolute value of the negative β_4 to compensate the broader barrier distribution [Lem93]. Systematic measurements

using a range of projectiles on the various targets may be helpful in clarifying this problem.

Nonetheless, the classical deformation parameters of the target ^{186}W have been qualitatively determined and the barrier distribution has been well reproduced. There is no doubt that a negative value of β_4 is necessary to fit the excitation function and to reproduce the barrier distribution; as shown in Fig. 5-1-14 and Fig. 5-1-15 a positive, or even a zero value of β_4 cannot fit the fusion excitation function and reproduce the barrier distribution. The χ^2 per point of the calculated fit to the cross-sections is about 5.6. This makes the quality of the average fitting to the level of 2 ~ 3%.

The parameters of the best fit, used in this model, are listed in Table 5-1-3.

Table 5-1-3: The parameters used in this model, with which the calculations have the best fit to the fusion excitation function, and associated χ^2 per point for the fits. The energy indicated is in the centre of mass system.

Reactions	B_0(MeV)	a (fm)	β_2	β_4	χ^2
$^{154}Sm + ^{16}O$	59.50	1.27	0.304	0.052	8.0
$^{186}W + ^{16}O$	69.03	1.27	0.295	-0.023	5.6

To conclude this section, distributions of barriers have been effectively extracted from the high precision measurements of fusion cross-sections for the reactions of $^{154}Sm + ^{16}O$ and $^{186}W + ^{16}O$. There are pronounced differences between the two distributions. Comparing qualitatively the shapes of the barrier distributions extracted from the

data to the calculated ones in Fig. 5-1-13, shows that these two cases are typical of prolate deformed targets with either positive (^{154}Sm) or negative (^{186}W) hexadecapole deformations. Though the values of β_2 and β_4 extracted from these fusion measurements do not always quantitatively agree with those extracted from Coulomb excitation measurements, these deformation parameters are qualitatively determined, in particularly the signs of the hexadecapole deformation can be unambiguously determined. This is an important and model independent feature. With this feature, the negative sign of the β_4 deformation of ^{186}W can be undoubtedly determined.

5.2 FUSION ANGULAR MOMENTUM DISTRIBUTIONS

As discussed in Chapter 2, it may be possible to extract the angular momentum distribution in fusion from an excitation function if it has been measured to high precision and if certain approximations are made. Those approximations are:

1. that the shape of the internuclear potential and the position R of the barrier are independent of l, and

2. that the l-dependent barriers have the same form as the $l = 0$ barrier, but the heights are increased in energy by $l(l + 1)\hbar^2/2\mu R^2$.

The high precision measurements of fusion cross-sections for ^{154}Sm and ^{186}W + ^{16}O reactions in this work offer the opportunity to extract the angular momentum distribution directly from the excitation functions quantitatively. Details of the extraction and the uncertainties of this method are discussed in the following sections.

5.2.1 Angular Momentum Distributions Extracted From Fusion Excitation Functions

Figures 5-2-1 and 5-2-2 show the extracted $d(E\sigma)/dE$, using the expression (4-2-1), from the experimental data of reactions ^{154}Sm and $^{186}W + ^{16}O$. The data points in this figure have been normalised by the πR^2 values shown in Table 4-2-6. As discussed in Chapter 2, if one assumes further that the fusion radius R does not change with the barriers (this is approximately true when both projectile and target are spherical), then the normalised value of $d(E\sigma)/dE$ gives the average $l = 0$ transmission coefficient $\overline{T}_0(E)$. Thus

$$\overline{T}_0(E) = \frac{1}{\pi R^2}\frac{d(E\sigma)}{dE} \qquad (5\text{-}2\text{-}1)$$

In the reactions studied here, this approximation of R not changing with the barriers introduces an error in the extracted $\overline{T}_0$ and angular momentum distributions due to the deformations of the targets. However, we shall initially ignore this and will discuss it later.

The figures show that the $\overline{T}_0$ increase smoothly from zero to unity over the energy range 52 to 63 MeV and 61 to 73 MeV for the reactions $^{154}Sm + ^{16}O$ and $^{186}W + ^{16}O$ respectively. At the average fusion barriers of 59.2 and 68.6 MeV respectively, the values of $\overline{T}_0$ are ~0.5, as expected.

The $\overline{T}_0(E)$ are also calculated theoretically using the Wong expression (2-2-6) averaged over the distribution of barriers, thus

$$\overline{T}_0(E) = \int_0^\infty T_0(E,B)\, D(B)\, dB \qquad (5\text{-}2\text{-}2)$$

As indicated by dashed lines in Fig. 5-2-1 and Fig. 5-2-2, the $\overline{T}_0$ are well fitted by the above calculations using the classical barrier distributions (see Eq. 5-1-12) with the target deformation parameters indicated in Table 5-1-2. The excellent agreement, in these and subsequent figures, is not particularly surprising since the model parameters were chosen to fit the experimental cross-sections and the assumptions made in this analysis are also implicit in the Wong expression (2-2-6), which applies to deformed nuclei. Therefore the calculations mainly serve to guide the eye, although such good agreement may not be expected in general.

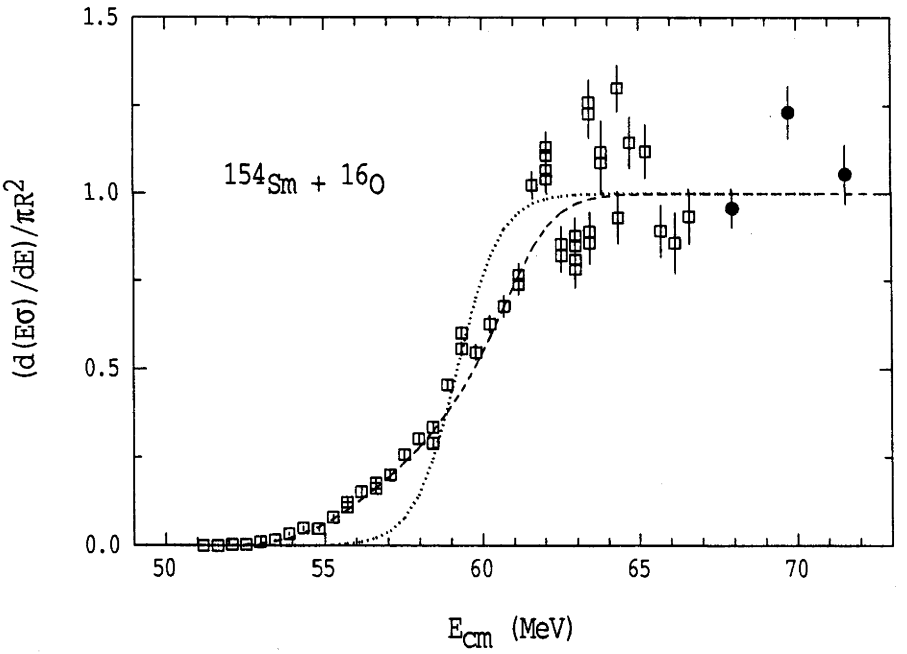

Fig. 5-2-1: Values of $\overline{T}_0$, extracted from measured fusion cross-sections, calculated at energy intervals of 0.91 MeV (squares) and 1.81 MeV (circles) at the highest energies. The curves are calculated using the Wong expression of (2-2-6) averaged by the distribution of barriers (dashed line) and by a single barrier B_0 (dotted line) respectively.

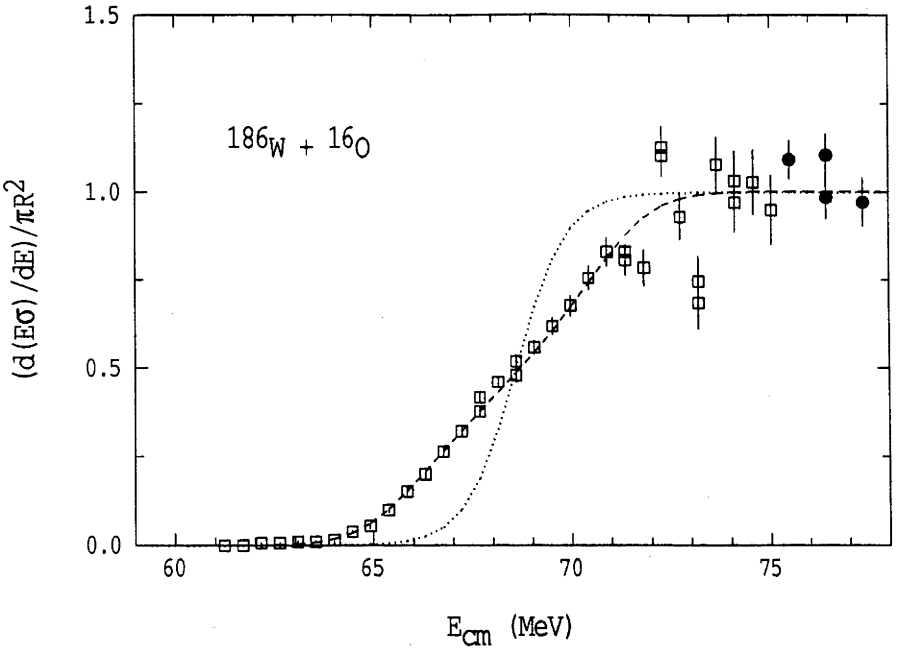

Fig. 5-2-2: Values of $\overline{T}_0$, extracted from measured fusion cross-sections, calculated at energy intervals of 0.92 MeV (squares) and 1.84 MeV (circles) at the highest energies. The curves are calculated using the Wong expression of (2-2-6) averaged by the distribution of barriers (dashed line) and by a single barrier B_0 (dotted line) respectively.

For comparison, the T_0 values calculated by using a single barrier B_0 are also indicated in these figures by the dotted line. The transition from 0 to 1 is much sharper than the experimental one which reflects the deformation, hence the barrier distribution of the targets. For instance, the long tail of the dashed lines indicate that the barriers extend to energies much lower than B_0.

A useful aspect of this analysis is the ability to extract the full fusion l-distributions from the data. The l-dependence of the average transmission coefficients at a fixed energy $\overline{T}_l(E)$ can be extracted making use of equation (2-3-36); thus $\overline{T}_l(E) = \overline{T}_0(E')$ for any l-value, where $E' = E - l(l+1)\hbar^2/2\mu R^2$.

Full $\overline{T}_l(E)$ distributions for a series of energies are shown in Fig. 5-2-3 (a) and Fig. 5-2-4 (a) for reactions ^{154}Sm and $^{186}W + ^{16}O$ respectively. They were obtained using each of the extracted values of the $\overline{T}_0$ at 0.5 MeV beam energy intervals, for energies equal to or below the incident energy and calculating the l-value (non-integer) giving the appropriate value of Δl. Thus the same transmission coefficients are used repeatedly but appear at different l-values for each energy. The diffuseness of the extracted distributions increases as the barrier region is approached as expected; again the model calculations guide the eye. The more familiar shapes of the reduced partial cross-sections, $\sigma_l/\pi\lambda\!\!\!^{-2}$ for the experimental data are shown in Fig. 5-2-3 (b) and Fig. 5-2-4 (b).

5.2.2 The Validity of This Method In The Extraction of Angular Momentum Distributions

The validity of the approximations 1 and 2, as stated at the beginning of §5.2, that the fusion barrier radius and shape are essentially independent of l, have been checked in the following manner. Calculations have been performed for a fusion potential comprising Coulomb, nuclear and centrifugal terms; the radius and curvature of the barrier for each l-value were then determined. A classical distribution of barrier heights, for a target nucleus with a permanent quadrupole deformation, was then imposed on each l-dependent barrier. Transmission coefficients and cross-sections were then calculated using the parabolic barrier, Hill-Wheeler, approximation. The calculated $\overline{T}_l$ are shown by the curves in Fig. 5-2-5 (a). The calculated cross-sections were then treated as data and subjected to the analysis described above, assuming a constant value of πR^2 taken

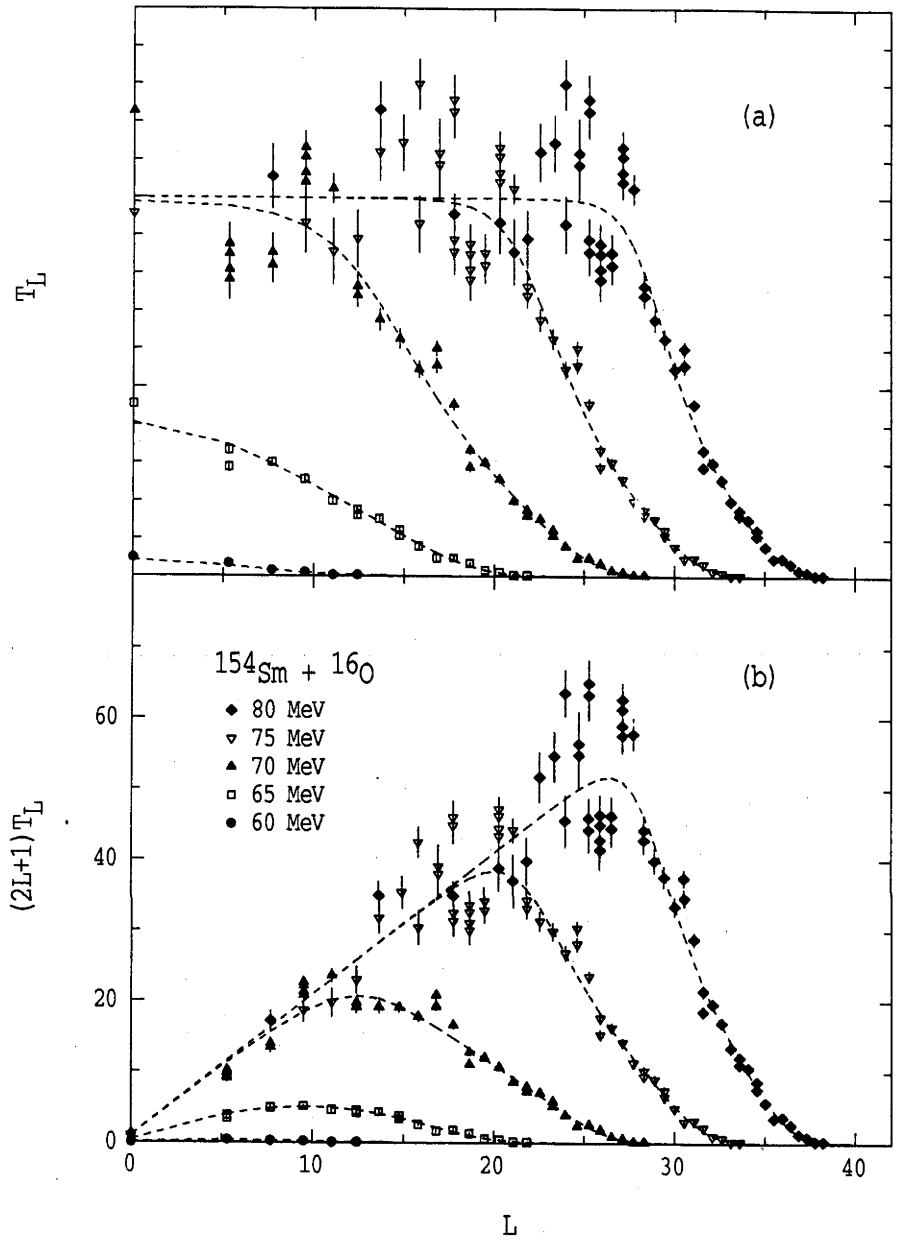

Fig. 5-2-3: (a) Angular momentum dependent, average transmission coefficients for reaction $^{154}Sm + ^{16}O$ at bombarding energies of 60, 65, 70, 75 and 80 MeV in lab. (b) Reduced partial cross-sections, $\sigma_l/\pi\lambda\!\!\!^{-2}$, for the same energies. The dashed curves are calculations with the Wong expression of (2-2-6) averaged by the distribution of barriers. The parameters used in the calculations are indicated in Table 5-1-2.

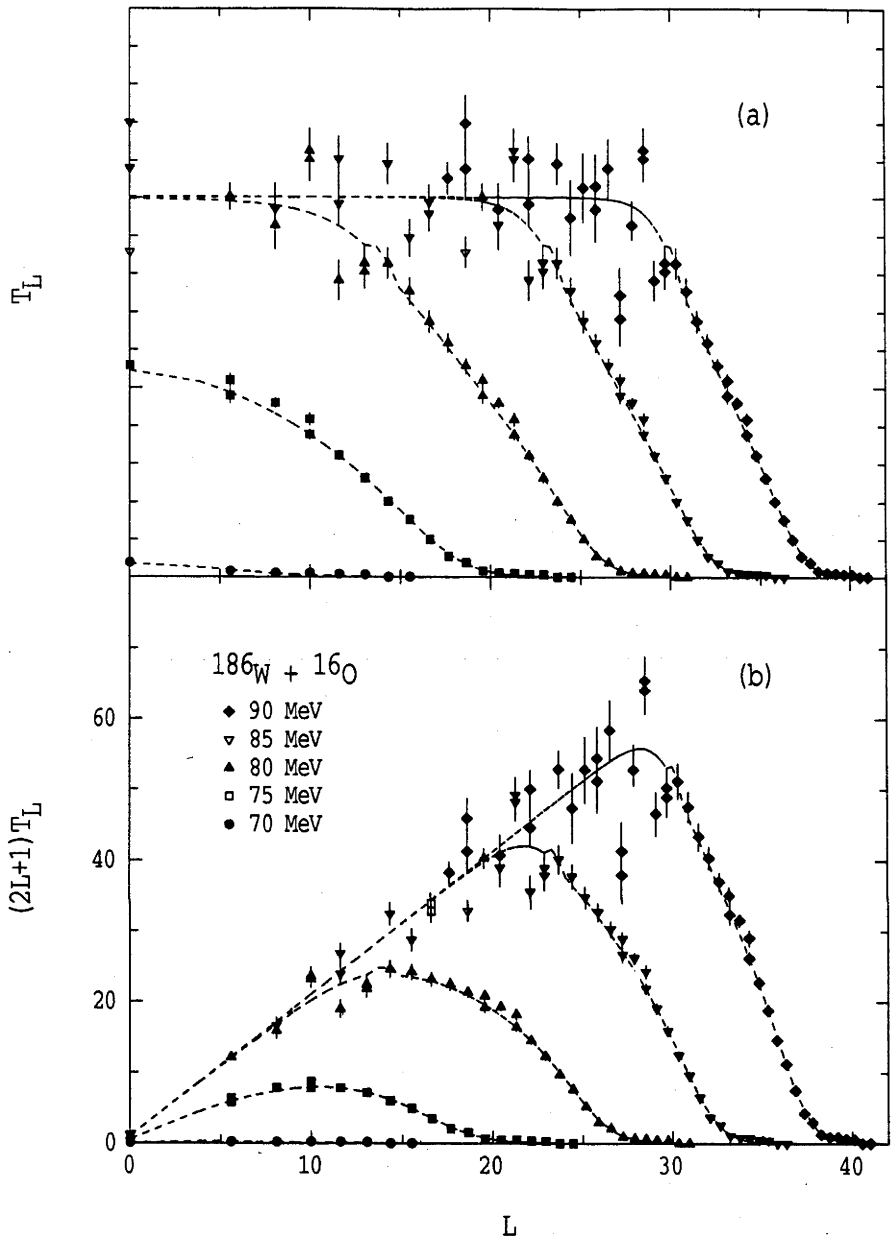

Fig. 5-2-4: (a) Angular momentum dependent, average transmission coefficients for reaction $^{186}W + ^{16}O$ at bombarding energies of 70, 75, 80, 85 and 90 MeV in lab. (b) Reduced partial cross-sections, $\sigma_l/\pi\lambda\!\!\!^{-2}$, for the same energies. The dashed curves are calculations with the Wong expression of (2-2-6) averaged by the distribution of barriers. The parameters used in the calculations are indicated in Table 5-1-2.

as the gradient of Eσ at 75 MeV. The extracted $\bar{T}_l$ are shown by the various symbols in the Fig. 5-2-5 (a). The extracted distributions are good approximations to the calculated ones at the higher l-values when the $\bar{T}_l$ are less than one. However, there is a small but systematic discrepancy occurring in the region when $\bar{T}_l \sim 1$. As the l decreases and when the $\bar{T}_l$ approach unity, they over-predict the transmission coefficient, then decline as l further decreases; they underpredict the transmission coefficient when l approaches zero. This effect is more obvious at the higher energies. This has been studied.

Since we have taken $\bar{T}_l(E) = \bar{T}_0(E')$

when $$E - \frac{l(l+1)\hbar^2}{2\mu R^2} = E' \gg B_0$$

we have $$\bar{T}_0(E') \sim 1 \qquad (5\text{-}2\text{-}3)$$

Then from Eq. (5-2-1) we have

$$\frac{d(E'\sigma(E'))}{dE'} \sim \pi R^2 \qquad E' \gg B_0 \qquad (5\text{-}2\text{-}4)$$

Now the decrease in the extracted T_l's in Fig. 5-2-5 (a) reflects the decrease in the average R-value as the energy increases and the barrier radius for higher l-values decreases. In other words, the effects are caused by the changes of the potential shape and barrier position with l, and appear as an energy dependence of $R^2(E)$.

It can be shown that, without making the two approximations 1 and 2 mentioned at the beginning of 5.2, in an inverse parabolic model, the $R^2(E)$ can be approximately written as:

$$R^2(E) \sim \left[R_0^2 - \frac{2|B_0 - E|}{\mu \omega_0^2}\right] \sqrt{1 - \frac{2|B_0 - E|}{\mu \omega_0^2 R_0^2}} \qquad (5\text{-}2\text{-}5)$$

where μ is the reduce mass, R_0 and $\hbar\omega_0$ are the barrier radius and internuclear potential curvature at $l = 0$.

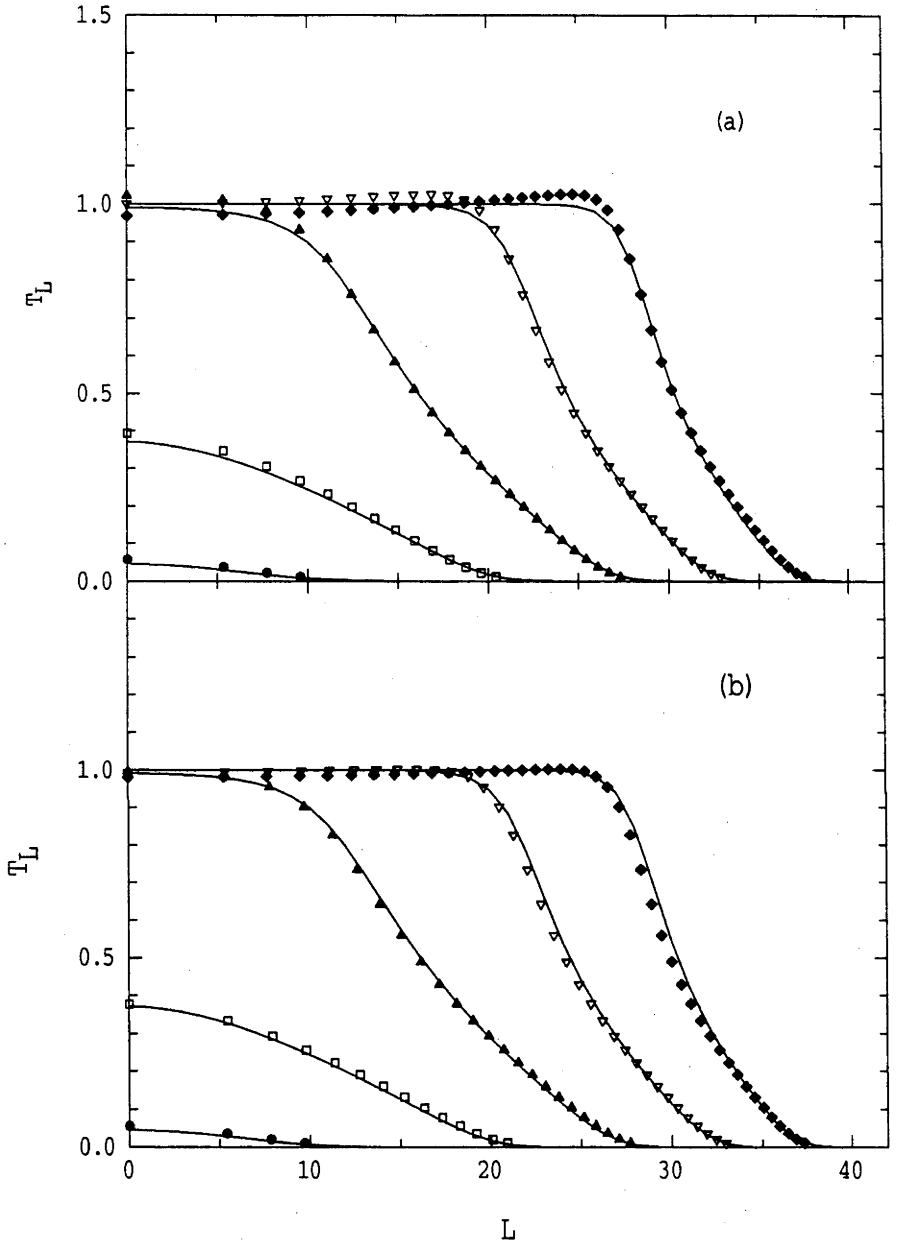

Fig. 5-2-5: (a) Transmission coefficients, at the energies indicated in Fig. 5-2-3, calculated using a parabolic barrier approximation (solid lines) and those using our analysis method on the cross-sections from that calculation (symbols). (b) After corrections have been made to the energy dependent of $R^2(E)$ (See the text for details).

Fig. 5-2-5 (b) shows the extracted $\bar{T}_l(E)$ from the calculated cross-sections using the same model used in (a), but using the $R^2(E)$ instead of a constant R^2, in the extraction of $\bar{T}_0(E)$. One can see an improvement in the agreement between the extracted $\bar{T}_l$ and those from this method, though some discrepancies remain at high energies and low l.

To conclude this section, the angular momentum distribution extracted from the fusion excitation functions are based on the WKB approximation for the transmission coefficient of a projectile travelling through the fusion barrier. Two basic approximations (1 and 2) have to be made in order to extract the transmission coefficient $\bar{T}_0$. These have been tested above, showing that the extracted $\bar{T}_l(E)$ agree with the theoretical ones within a few percent. Hence the approximations 1 and 2 are good approximations.

However, in the above test the fusion radii do not change with barriers, which is approximately true only for the spherical case. For deformed nuclei, instead of a single fusion radius, there is a distribution of fusion radii, dependent on the orientation of the interacting nuclei, which produce a distribution of fusion barriers. Calculations show, that changes in up to 15% of the average fusion radius can occur for well deformed nuclei (for example in the ^{154}Sm case). Then the assumption that fusion radii do not change with the fusion barrier is not valid. Since the l and R always appear together in the potential, $l(l+1)\hbar^2/2\mu R^2$, the variation in R results in a variation in the extracted l distributions. This effect will be discussed in the following, together with the discussions of the extracted mean value of fusion angular momentum.

5.2.3 The Mean Angular Momentum

The <*l*> -values for the extracted angular momentum distributions in Fig. 5-2-3 (b) are shown in Fig. 5-2-6 (b) for the reaction $^{154}Sm + ^{16}O$. The statistical errors on the extracted values of <*l*>, generally smaller than the data points, are correlated since they are based on the same values of $\overline{T}_0$, although the number of values contributing increases as the energy increases. The solid line in this figure shows the calculated <*l*> using the Wong expression (2-2-6) averaged over the barrier distribution. An average fusion radius was used in these calculations. The dashed lines in these figures show the same calculation but with the fusion radius increased by 15%.

For a comparison, the <*l*> values from the measurement of γ-ray multiplicities for the reaction of $^{154}Sm + ^{16}O$, in the energy region of barriers [Bie93, Van92, Cha88], are shown in Fig. 5-2-6 (a). It appears that there is some variation in their results depending on the type of measurement and the form of analysis. Comparing the latest results of reference [Bie93] (solid diamond) to the ones extracted from our fusion data by using a constant average fusion radius R (the open and solid triangles in Fig. 5-2-6 (b)), there is a small but consistent difference; the ones extracted from fusion are about 1.5~2 units smaller than those of the γ-ray measurements. The reasons for these discrepancies are given below.

Since the ^{154}Sm target is highly deformed, the fusion radius varies with the orientation of the deformed nucleus. This effect is not included in the method used above where only an average fusion radius is used. At energies above the barriers, this will not introduce

a significant error in the extracted <*l*> because all of the fusion barriers have contributed to the fusion, hence all of the fusion radii.

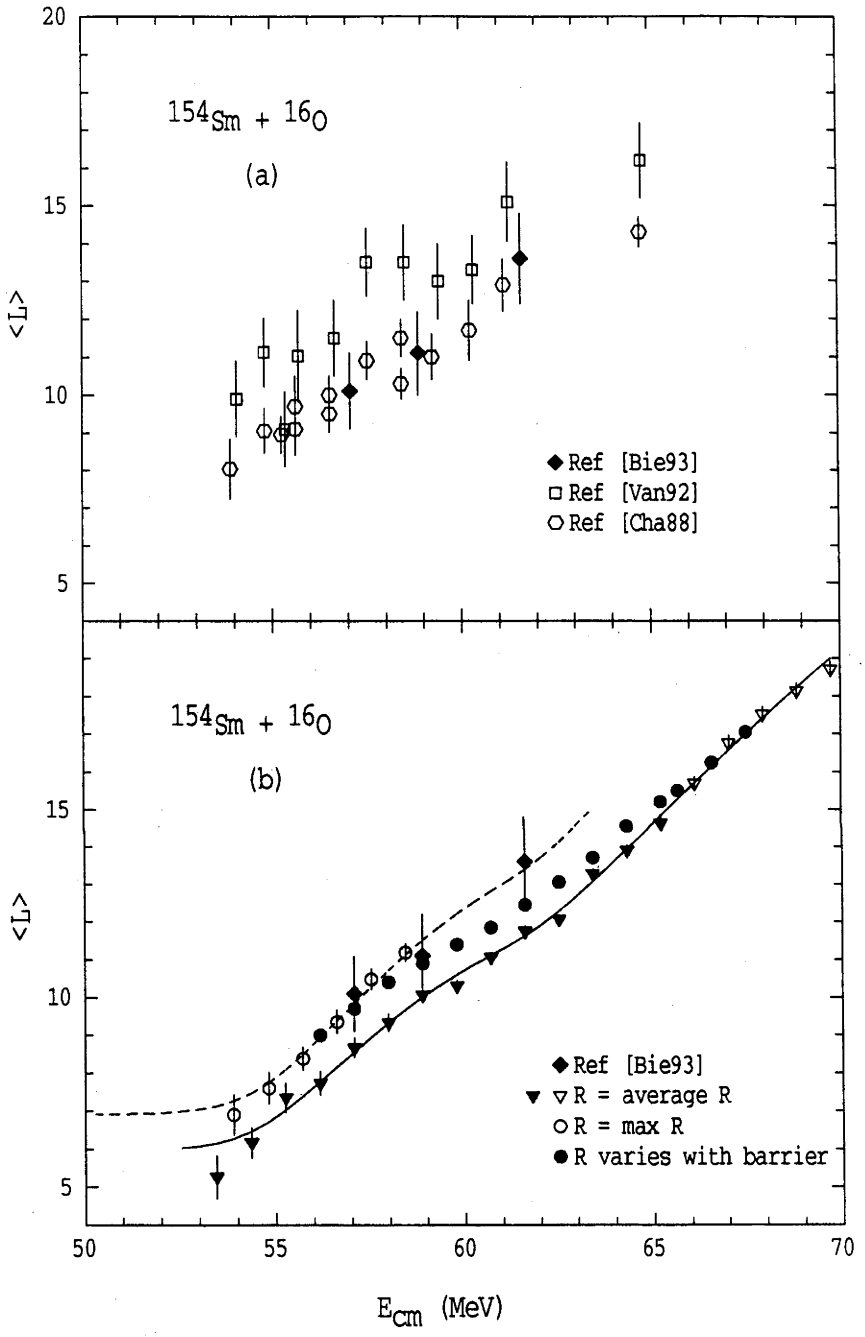

Fig. 5-2-6: (a) Mean l values determined from γ-ray multiplicities. The latest results (solid diamond) are also shown in (b) to compare with those extracted from fusion data (see text for details). The curves are calculations of expression (5-2-2) using the average fusion radius (solid line) and the largest fusion radius (dashed line).

Therefore, using an average fusion radius in the extraction should be a good approximation. However, at energies in the barrier region, only the barriers that are lower than the bombarding energies give a significant contribution to fusion, so that these fusion radii are, in general, larger than the average fusion radius obtained at the high energies. At the lowest energies studied in this work, the fusion occurs only when the projecticle encounters the tip of the deformed target. Hence using the largest fusion radius in the extraction should be a good approximation at these low energies.

The variation of the fusion radius and its effect on the extracted angular momentum can be estimated assuming the deformed target has radii

$$R_t(\theta) = R_t [1 + \beta_2 Y_{20}(\theta) + \beta_4 Y_{40}(\theta)]$$

The maximum and minimum radii are R(0°) and R(90°) respectively. Hence the maximum variations in the radius are

$$\Delta R_+ = \frac{1}{2}\sqrt{\frac{5}{\pi}}\,\beta_2 R_t + \frac{3}{2}\frac{1}{\sqrt{\pi}}\,\beta_4 R_t \qquad (5\text{-}2\text{-}6)$$

and

$$\Delta R_- = -\frac{1}{4}\sqrt{\frac{5}{\pi}}\,\beta_2 R_t + \frac{9}{16}\frac{1}{\sqrt{\pi}}\,\beta_4 R_t \qquad (5\text{-}2\text{-}7)$$

In the reaction of $^{154}Sm + ^{16}O$, $\beta_2 \sim 0.3$ and $\beta_4 \sim 0.05$ which gives $\Delta R_+ \sim$ 1.5 fm and $\Delta R_- \sim 0.5$ fm respectively. If the fusion radius changes the same amount as the target radius, and the average fusion radius determined at the high energies is ~10.56 fm, the actual fusion radius can be up to 15% larger or 5% lower than R for the two extremely cases. Because the $\langle l \rangle$ is proportional to R, as seen in expression of

(2-3-40), using the largest fusion radius results in a 15% increase in the extracted <l> value. This has been illustrated by open circles in Fig. 5-2-6 (b) in which the largest fusion radius was used in the extraction. The dashed line follows these data points very well; this is not particularly surprising because in the calculations of the dashed line the largest fusion radius (15% larger than the average radius R) was also used.

The effect of the changes of the fusion radius on the extracted $\overline{T}_l$ is demonstrated in Fig. 5-2-7. It shows the variation of $(2l + 1)\overline{T}_l$ when the fusion radius is taken as the average one (solid line) and increased

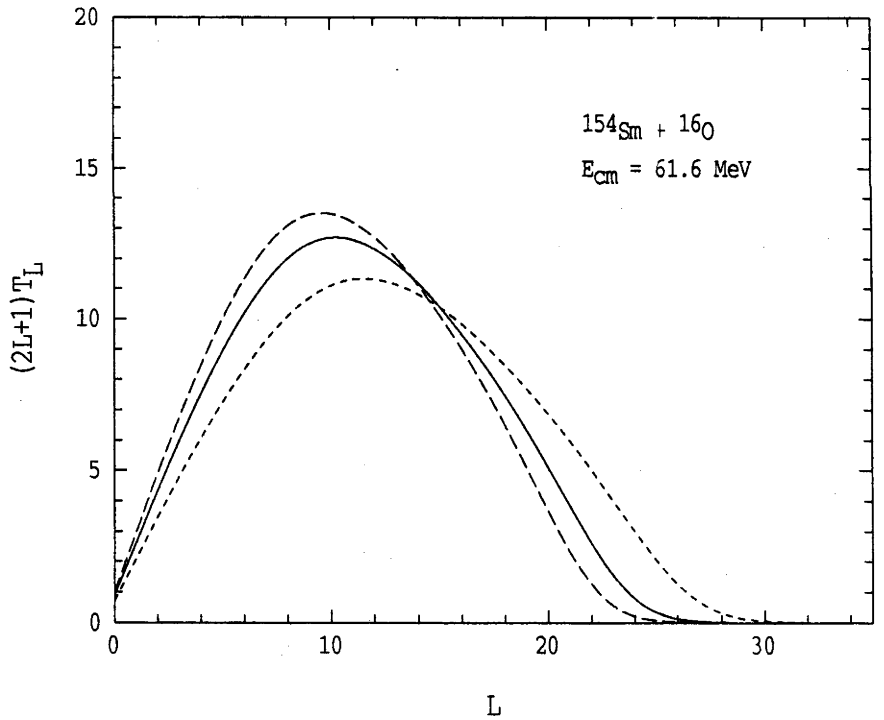

Fig. 5-2-7: Calculated transmission co-efficient varies with the fusion radius; average R (solid line), and the radius increased by +15% (dashed line) or decreased by 5% (long dashed line) from the average.

by 15% (dashed line) or decreased by -5% (long dashed line) from the average. The "true" values of the $\overline{T}_l$, as discussed above, should lie between the dashed and solid lines. The value of $<l>$ is 11.8 when a average R is used and is 13.6 when the largest fusion radius is used. As is expected the mean angular momentum changes by the same percentage as the fusion radius.

Now, we have good reason to believe that using the average fusion radius and the largest fusion radius are good approximations for energies above and well below the fusion barriers respectively. While in the energy region around the barriers, R should lie between these two approximations. A recent development, in the course of this work [Row93], shows the mean radius, and hence the $<l>$, can be estimated in the intermediate energy range.

Equation (5-1-16) shows, to first order for a known fusion barrier, that the fusion radius can be written as

$$B = \frac{Z_1 Z_2 e^2}{R(B)}\left(1 - \frac{a}{R(B)}\right) \qquad (5\text{-}2\text{-}8)$$

This gives

$$R(B) = \frac{R_c}{2}\left(1 + \sqrt{1\text{-}4a/R_c}\right) \qquad (5\text{-}2\text{-}9)$$

where $R_c = Z_1 Z_2 e^2/B$ is the distance of closest approach at which the Coulomb potential equals the fusion barrier.

Knowing the fusion radius associated with barrier B, we can rewrite equation (2-2-3) as

$$T_l(E, B) = \frac{1}{1 + \exp\left[\frac{2\pi}{\hbar\omega}\left(B + \frac{l(l+1)\hbar^2}{2\mu R^2(B)} - E\right)\right]} \qquad (5\text{-}2\text{-}10)$$

Now if we know the weights associated with each barrier B, we can use the above formula to evaluate $<l>$.

Since the smoothed barrier distribution, as discussed in the last section, has been extracted from the experimental fusion data, we may now use it to obtain those weights approximately. Thus for a given energy bin between E_n and E_{n+1} the weights are

$$W_n = \int_{E_n}^{E_{n+1}} \bar{D}(B)\, dB = \frac{1}{\pi R^2(E_{n+1/2})} \Delta\left(\frac{dE\sigma}{dE}\right) \qquad (5\text{-}2\text{-}11)$$

Where the average energy $E_{n+1/2} = (E_n + E_{n+1})/2$.

Using these weights, the $<l>$ values can be calculated, thus

$$<l> = \sum_{n\, l} l(2l+1) W_n T_l(E, E_{n+1/2}) \qquad (5\text{-}2\text{-}12)$$

The solid circles in Fig. 5-2-6 (b) show the results of this calculation. As expected, the solid circles provide a nice bridge between the open triangles extracted directly from data using the average fusion radius at energies above the barriers and the open circles extracted directly from data using the largest fusion radius R at energies below the barriers.

Now, over all the energy range around the Coulomb barrier, for the reaction $^{154}Sm + ^{16}O$, the open circles, the solid circles and the open triangles give a clear and smoothly changing picture of the extracted mean fusion angular momentum from fusion around the barriers. Comparing these extracted $<l>$ from fusion with the latest results obtained by γ-ray multiplicity measurements they agree very well as demonstrated in Fig. 5-2-6 (b).

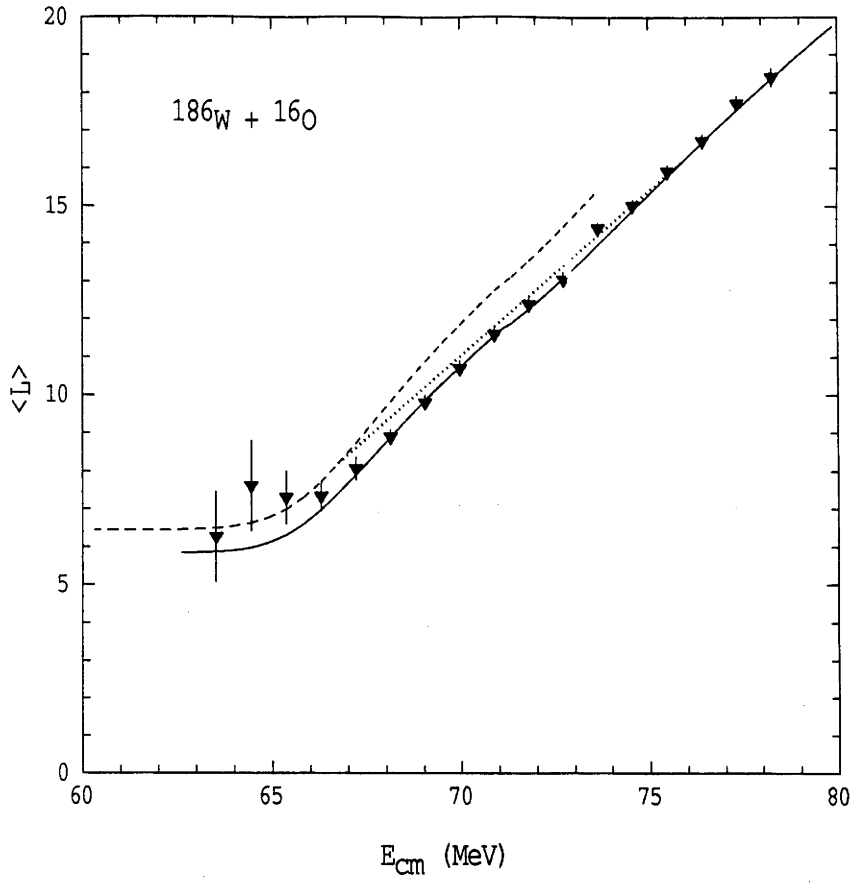

Fig. 5-2-8: Mean l values determined from fusion data (triangles). The solid curve is a calculation using the Wong expression of (2-2-6) averaged by the distribution of barriers. The dashed curve is the same calculation as the solid one but with an increase of 10% in the fusion radius R.

Fig. 5-2-8 shows the extracted $<l>$ by using the average fusion radius. The solid and dashed lines in this figure shows the calculated $<l>$ using the average and the largest fusion radius respectively. The largest fusion radius is estimated by Eq. 5-2-14 and is ~10% (~15% in ^{154}Sm case, as above) larger than the average one. The error of $<l>$ introduced by using the average fusion radius is, therefore, ≤10% and less than that in ^{154}Sm case. This reflects the fact that ^{186}W is less elongated than the ^{154}Sm. Since there is only about 1 $\hbar$ difference between the two approximations in the barrier region, a line, even a

straight line (the dotted line as shown in this figure) across the barrier region, should serve as a good guide to link the two curvatures (solid and dashed) at the energies above and below the barriers.

5.3 CONCLUSIONS

The fusion cross-sections of ^{16}O induced reactions on the targets of ^{154}Sm and ^{186}W have been measured to unprecedented precision. This was done by measuring the ER cross-sections using new experimental apparatus consisting of a velocity filter and a position sensitive multiwire proportional counter. This apparatus was developed in the course of this work and it has been shown to work very effectively.

With the high precision data, well defined barrier distributions have been obtained for the first time. These distributions are in good agreement with those expected from the static deformations of the target nuclei. It has been shown that small differences in fusion excitation functions appear as large effects in the barrier distribution. Thus the barrier distribution is very sensitive way of displaying excitation function. For example, the large difference in shapes of the barrier distributions for the reactions studied reflects the small difference in shapes of the target nuclei resulting from their different hexadecapole deformations.

It can be concluded that plotting the excitation function in term of barrier distribution provides a powerful tool for testing fusion models at the energies near the Coulomb barrier. Any model which can reproduce the cross-sections (within the experimental error) must of

course reproduce the behaviour of $d^2(E\sigma)/dE^2$ and hence must reproduce the barrier distribution.

This conclusion has challenged the common view that the excitation function itself contains little information about the details of fusion. However, this common view would be still valid if the fusion excitation functions had not been measured to such high precision, as presented in this thesis.

The chosen fusion reactions studied in this work, involve classically deformed targets, ^{154}Sm, ^{186}W, and the doubly-closed-shell spherical projectile, ^{16}O. The initial aim of choosing these reactions was to test the validity of the novel analysis method proposed by Rowley et al in 1990. With the excellent results obtained we are now confident of expanding this method to cases where static deformation is not the only effect responsible for the enhancement of the sub-barrier fusion. This will give insight into other couplings which may be dominant.

The fusion angular momentum distributions for these two reactions have been quantitatively extracted for the first time directly from the fusion excitation functions. The uncertainty resulting from using an the average fusion radius in the extraction varies from reaction to reaction, depending on the static deformation of the interacting nuclei. This uncertainty is larger for ^{154}Sm than that for ^{186}W, because the former is some more "elongated" than the latter.

Nonetheless, after correcting the fusion radii in the barrier region the extracted $<l>$ is in a good agreement with that from the γ-ray multiplicity measurements for the reaction of ^{154}Sm + ^{16}O [Bie93]. There is no such data available for comparison in the ^{186}W case.

A simple way of correcting for the distribution of fusion radii in the extraction of T_l has not yet been found. However, the maximum error is not difficult to estimate. There is no significant error at energies smaller than the lowest barrier if the largest fusion radius is used. Since the $<l^2>$ saturates and is proportional to the R^2 [Das86] at energies lower than the barriers, the largest fusion radius can, in principal, be deduced from the extracted angular momentum distribution. To do so, however, we need to measure fusion cross-sections at lower energies than those measured here. Such measurements of cross-sections less than 0.1 mb, though interesting, are beyond the scope of this thesis.

However, it may be emphasized that even including all the aforesaid uncertainties, the angular momentum distribution and $<l>$ derived from the fusion excitation function are of comparable accuracy to those from other methods such as the γ-ray multiplicities and isomer ratios which involve other uncertainties.

Appendix

If the sequence of measurements, as shown schematically in Fig. 3-5-3, are made, for a misalignment of the beam axis to the symmetry axis of the experimental setting, as shown in Fig. 3-5-4, there is an off set $\Delta\theta$ of the angle. The true angles change from $\pm\theta$ to $\pm\theta+\Delta\theta$, and the solid angle of the detector changes from Ω to $\Omega\pm\Delta\Omega$. The changes in the angle θ and the solid angle Ω can be written:

$$\Delta\theta = -\frac{\Delta L}{L}\cos\theta \qquad \text{(A-1)}$$

$$\Delta\Omega = \frac{2\Delta L\sin\theta}{L}\Omega \qquad \text{(A-2)}$$

where ΔL is the off set of the effective beam axis from the symmetry axis of the experimental setting and the L is the distance from the target, at the centre of the 2 m chamber, to the entrance collimater of the detector.

The numbers of elastic events, detected at angles $(\pm\theta + \Delta\theta)$, $N(\theta)_{\pm}$, relative to the numbers detected in both monitors, $(N_{ML} + N_{MR})_{\pm}$, are given by

$$R_{\pm} = \frac{N(\theta)_{\pm}}{(N_{ML} + N_{MR})_{\pm}} = \frac{\frac{d\sigma(\pm\theta + \Delta\theta)}{d\Omega}(\Omega \pm \Delta\Omega)}{\frac{d\sigma}{d\Omega_{ML}}\Omega_{ML} + \frac{d\sigma}{d\Omega_{MR}}\Omega_{MR}} \qquad \text{(A-3)}$$

The ratio $\frac{R_-}{R_+}$, which is measured, is given by:

$$\frac{R_-}{R_+} = \frac{\frac{d\sigma(-\theta + \Delta\theta)}{d\Omega}(\Omega - \Delta\Omega)}{\frac{d\sigma(+\theta + \Delta\theta)}{d\Omega}(\Omega + \Delta\Omega)} \qquad \text{(A-4)}$$

where the $\frac{d\sigma(\theta)}{d\Omega}$ is the differential cross-section in the laboratory system. To transfer $\frac{d\sigma(\theta)}{d\Omega}$ to the centre of mass system we denote subscript cm for the centre of mass system and have:

$$\tan\theta = \frac{\sin\theta_{cm}}{\gamma + \cos\theta_{cm}} \tag{A-5}$$

and

$$\frac{d\sigma(\theta)}{d\Omega} = F(\theta_{cm})\frac{d\sigma(\theta_{cm})}{d\Omega_{cm}} \tag{A-6}$$

Where $\frac{d\sigma(\theta_{cm})}{d\Omega_{cm}}$ is the Rutherford scattering differential cross-section in the centre of mass system and is giving by

$$\frac{d\sigma(\theta_{cm})}{d\Omega_{cm}} \propto \frac{1}{\sin^4\frac{\theta_{cm}}{2}} \tag{A-7}$$

$F(\theta_{cm})$ is the transformation function of the differential cross-section from the centre of mass system to the laboratory system, and

$$F(\theta_{cm}) = \frac{(\gamma^2 + 2\gamma\cos\theta_{cm} + 1)^{3/2}}{1 + \gamma\cos\theta_{cm}} \tag{A-8}$$

where

$$\gamma = \frac{m_P}{m_T}$$

Considering a small change in angle, from θ to $\theta + \Delta\theta$, then (A-6) can be, at the first approximation, expanded as:

$$\frac{d\sigma(\theta + \Delta\theta)}{d\Omega} = F(\theta_{cm})\frac{d\sigma(\theta_{cm})}{d\Omega_{cm}} + \left[F(\theta_{cm})\left(\frac{d\sigma(\theta_{cm})}{d\Omega_{cm}}\right)' + F'(\theta_{cm})\frac{d\sigma(\theta_{cm})}{d\Omega_{cm}}\right]\frac{d\theta_{cm}}{d\theta}\Delta\theta \tag{A-9}$$

here

$$f'(\theta_{cm}) = \frac{d}{d\theta_{cm}} f(\theta_{cm})$$

From (A-5) and (A-7), it can be found that:

$$\frac{d\theta_{cm}}{d\theta} = \frac{(\gamma^2 + 2\gamma\cos\theta_{cm} + 1)}{1 + \gamma\cos\theta_{cm}} \qquad \text{(A-10)}$$

and

$$\left(\frac{d\sigma(\theta_{cm})}{d\Omega_{cm}}\right)' = -2\frac{d\sigma(\theta_{cm})}{d\Omega_{cm}}\cot\left(\frac{\theta_{cm}}{2}\right) \qquad \text{(A-11)}$$

Insert (A-11) into (A-9) we get:

$$\frac{d\sigma(\theta + \Delta\theta)}{d\Omega} = F(\theta_{cm})\frac{d\sigma(\theta_{cm})}{d\Omega_{cm}}\left\{1 - \left[2\cot\left(\frac{\theta_{cm}}{2}\right) - \frac{F'(\theta_{cm})}{F(\theta_{cm})}\right]\frac{d\theta_{cm}}{d\theta}\Delta\theta\right\}$$

(A-12)

Since

$$\frac{F'(\theta_{cm})}{F(\theta_{cm})} = \frac{\gamma\sin\theta_{cm}}{1 + \gamma\cos\theta_{cm}}\,\frac{\gamma^2 - \gamma\cos\theta_{cm} - 2}{\gamma^2 + 2\gamma\cos\theta_{cm} + 1}$$

and in this work, $\gamma \sim \frac{1}{10}$

$$\left|\frac{F'(\theta_{cm})}{F(\theta_{cm})}\right| < \left|2\gamma\sin\theta_{cm}\right|$$

and at forward angles

$$\sin\theta \sim \theta, \qquad \cot\theta \sim \frac{1}{\theta}$$

Hence the term of $\frac{F'(\theta_{cm})}{F(\theta_{cm})}$ can be ignored comparing to $2\cot\left(\frac{\theta_{cm}}{2}\right)$

and then

$$\frac{d\sigma(\theta + \Delta\theta)}{d\Omega} = F(\theta_{cm})\frac{d\sigma(\theta_{cm})}{d\Omega_{cm}}\left\{1 - 2\cot\left(\frac{\theta_{cm}}{2}\right)\frac{d\theta_{cm}}{d\theta}\Delta\theta\right\} \qquad \text{(A-13)}$$

Insert (A-13) into (A-4) and consider that from (A-7) and (A-8) we have:

$$\frac{d\sigma(-\theta_{cm})}{d\Omega_{cm}} = \frac{d\sigma(\theta_{cm})}{d\Omega_{cm}}$$

$$F(-\theta_{cm}) = F(\theta_{cm})$$

and

$$\cot(-\theta_{cm}) = \cot(\theta_{cm})$$

we get:

$$\frac{R_-}{R_+} = \frac{1 + 2\cot(\frac{\theta_{cm}}{2})\frac{d\theta_{cm}}{d\theta}\Delta\theta}{1 - 2\cot(\frac{\theta_{cm}}{2})\frac{d\theta_{cm}}{d\theta}\Delta\theta}\frac{(\Omega - \Delta\Omega)}{(\Omega + \Delta\Omega)} \qquad \text{(A-14)}$$

Up to first approximation it becomes:

$$\frac{R_-}{R_+} = 1 + 4\cot(\frac{\theta_{cm}}{2})\frac{d\theta_{cm}}{d\theta}\Delta\theta - \frac{2\Delta\Omega}{\Omega} \qquad \text{(A-15)}$$

insert (A-1) and (A-2) we get:

$$\frac{R_-}{R_+} = 1 - 4\left\{\cot(\frac{\theta_{cm}}{2})\frac{d\theta_{cm}}{d\theta} + \tan\theta\right\}\frac{\Delta L}{L}\cos\theta \qquad \text{(A-16)}$$

or

$$\frac{R_-}{R_+} = 1 + 4\left\{\cot(\frac{\theta_{cm}}{2})\frac{d\theta_{cm}}{d\theta} + \tan\theta\right\}\Delta\theta \qquad \text{(A-16a)}$$

Thus the offset of the beam on the target ΔL can be found, hence the true angle of the detector can be known.

Since the two monitors are located approximately symmetrically to the beam axis the same procedure can be applied to the monitors. The offset angle of monitor $\Delta\theta_M$ can be found by the ratio of $\frac{N_{ML}}{N_{MR}}$ which can be written as:

$$\frac{N_{ML}}{N_{MR}} = 1 - 4\left\{\cot\left(\frac{\theta_{cm}}{2}\right)\frac{d\theta_{cm}}{d\theta} + \tan\theta\right\}_M \frac{\Delta L_M}{L_M}\cos\theta_M \frac{\Omega_{ML}}{\Omega_{MR}} \quad \text{(A-17)}$$

or

$$\frac{N_{ML}}{N_{MR}} = 1 + 4\left\{\cot\left(\frac{\theta_{cm}}{2}\right)\frac{d\theta_{cm}}{d\theta} + \tan\theta\right\}_M \Delta\theta_M \frac{\Omega_{ML}}{\Omega_{MR}} \quad \text{(A-17a)}$$

Above, there is a new term, $\frac{\Omega_{ML}}{\Omega_{MR}}$, with the value of 1±0.02. However, the uncertainty of the ratio of monitors' solid angle only introduced a systematic error of $\Delta\theta_M$ and it could not affect the relative error of $\delta(\Delta\theta_M)$ which was used to monitor the beam spot position movement as described below.

Knowing the $\Delta\theta_0$, ΔL_0, the $\Delta\theta_{M0}$ ΔL_{M0} and the ratio of monitor yields $(\frac{N_{ML}}{N_{MR}})_0$, at the initial, any changes of ΔL_M due to the beam position movement during subsequent ER measurements can be found from the changes in the ratio of the two monitor's yields $\frac{N_{ML}}{N_{MR}}$ at that measurement.

The difference of $\frac{N_{ML}}{N_{MR}}$ to $(\frac{N_{ML}}{N_{MR}})_0$ is:

$$\frac{N_{ML}}{N_{MR}} - \left(\frac{N_{ML}}{N_{MR}}\right)_0 = -4\left\{\cot\left(\frac{\theta_{cm}}{2}\right)\frac{d\theta_{cm}}{d\theta} + \tan\theta\right\}_M \frac{\Delta L_M - \Delta L_{M0}}{L_M}\cos\theta_M \frac{\Omega_{MR}}{\Omega_{ML}}$$

thus

$$\delta(\Delta L_M) = \Delta L_M - \Delta L_{M0} = \frac{\left(\frac{N_{ML}}{N_{MR}}\right)_0 - \frac{N_{ML}}{N_{MR}}}{4\left\{\cot\left(\frac{\theta_{cm}}{2}\right)\frac{d\theta_{cm}}{d\theta} + \tan\theta\right\}_M \frac{\Omega_{ML}}{\Omega_{MR}}} \frac{L_M}{\cos\theta_M}$$

(A-18)

From (A-1)

$$\delta(\Delta\theta_M) = \Delta\theta_M - \Delta\theta_{MO} = -\frac{\delta(\Delta L_M)}{L_M}\cos\theta_M \qquad \text{(A-18a)}$$

Hence since $\delta(\Delta L_M) = \delta(\Delta L)$ and

$$\delta(\Delta\theta) = -\frac{\delta(\Delta L)}{L}\cos\theta\,, \qquad \text{(A-19)}$$

we get

$$\delta(\Delta\theta) = \frac{L_M}{L}\frac{\cos\theta}{\cos\theta_M}(\Delta\theta_M - \Delta\theta_{MO}) \qquad \text{(A-19a)}$$

Therefore, the true angle θ_{ER} of the ER detector at each measurement is known:

$$\theta_{ER} = \theta + \Delta\theta_O + \delta(\Delta\theta) \qquad \text{(A-20)}$$

or

$$\theta_{ER} = \theta + \Delta\theta_O + \frac{L_M}{L}\frac{\cos\theta}{\cos\theta_M}(\Delta\theta_M - \Delta\theta_{MO}) \qquad \text{(A-20a)}$$

where θ is the reading angle of the turnable arm on which the ER detector is mounted. The $\Delta\theta_O$, as defined before, is the initial offset of the angle θ.

As discussed in §3.5.2, the arm can be set at an accuracy to ±0.01°, the accuracy for $\Delta\theta_O$ is ±0.02° and for $\Delta\theta_M$ and $\Delta\theta_{MO}$ is ±0.3°. The accuracy for θ_{ER} can then be written as:

$$(\Delta\theta_{ER})^2 = (0.01)^2 + (0.02)^2 + 2\left(\frac{L_M}{L}\frac{\cos\theta}{\cos\theta_M}\,0.03°\right)^2 \qquad \text{(A-21)}$$

Since in this work the ratio

$$\frac{L_M}{L}\frac{\cos\theta}{\cos\theta_M} \sim 1$$

then

$$\Delta\theta_{ER} = 0.05°$$

Thus the true angle of the velocity filter can be determined to an accuracy of ±0.05°.

The same procedure can be applied to the large angle ER detector. An accuracy of ±0.05° can then also be achieved.

References

[Ald75] K. Alder and A. Winther, in *Electromagnetic Excitation* (North Holland Publishing Co, Amsterdam, 1975), p. 17.

[Alj84] H. Aljuwair, R.J. Ledoux, M. Beckermam, S.B. Gazes, J. Wiggins, E.R. Cosman, R.R. Betts, S. Saini and Ole Hansen, Phys. Rev. C30 (1984) 1223.

[Ata70] M. Atac and J. Lack, Nucl. Instr. and Meth. **86** (1970) 173.

[Bac85] B.B. Back, R.R. Betts, J.E. Gindler, B.D. Wilkins, S. Saaini, M.B. Tsang, C.K. Gelble, W.G. Lynch, M.A. McMahan and P.A. Baisden, Phys. Rev . **C32** (1985) 195.

[Bai60] L.E. Bailey, Rev. Sci. Inst. **31** (1960) 1147.

[Bal83] A.B. Balantekin, S.E. Koonin, J.W. Neggele, Phys. Rev. **C28** (1983) 1565.

[Bal86] A.B. Balantekin and P.E. Reimer, Phys. Rev. **C33** (1986) 379.

[Bec80] M. Beckerman, M. Salomaa, A. Sperduto, H. Enge, J. Ball, A. DiRienzo, S. Gazes, Yan Chen, J.D. Molitoris and Mao Nai-feng, Phys. Rev. Lett. **45** (1980) 1472.

[Bec81] M. Beckerman, J. Ball, H.A. Enge, M. Salomaa, A. Sperduto, S. Gazes, A. DiRienzo and J.D. Molitoris, Phys. Rev. **C23** (1981) 1581.

[Bec82] M. Beckerman, M. Salomaa, A. Sperduto, J.D. Molitoris and A. DiRienzo Phys. Rev. **C25** (1982) 837.

[Bec83] M. Beckerman, M. Salomaa, J. Wiggins and R. Rohe, Phys. Rev. **C28** (1983) 1963.

[Bec85] M. Beckerman, Phys. Rep. **51** (1985) 145.

[Bec88] M. Beckerman, Rep. prog. Phys. **51** (1988) 1047.

[Beg85] S. Beghini, C. Signorini, S. Lunardi, M. Morando, G. Fortuna, A.M. Stefanini, W. Mexzynski and R. Pengo, Nucl. Instr. and Meth. **A239** (1985) 585.

[Bem87] C.E. Bemis, F.E. Obenshain, T.C. Awes, F. Plasil, J.R. Beene, P. Jacobs, R.L. Ferguson, Z. Frankel, H.J. Kim, U. Smilansky, F.K. McGowan, I. Tserruya, ORNLProgress Report for Period Ending September 30, 1986, p. 110.

[Bet72] H.D. Betz, Rev. Mod. Phys. **44** (1972) 465.

[Bie92] J.D. Bierman, A.W. Charlop, D.J. Prindle and R. Vandenbosch, Annual Report, University of Washington, (1992) p. 22.

[Bie93] J.D. Bierman, A.W. Charlop, D.J. Prindle, R. Vandenbosch and DYe, University of Washington, Seattle; preprint, March (1993).

[Boh75] A. Bohr and B. Mottelson, Nuclear Structure, Vol. II (Benjamin, NY, 1975).

[Bor86] A.M. Borges, et al, *Proceedings of Symposium, ANL Report*, NoPHY-86-1, (1986) p. 441.

[Bre77] A. Breskin and N. Zwang, Nucl. Instr. and Meth. **144** (1977) 609.

[Bre77a] A. Breskin, Nucl. Instr. and Meth. **141** (1977) 505.

[Bre79] A Breskin, R. Chechik and N. Zwang, Nucl. Instr. and Meth. **165** (1979) 125.

[Bre82] A. Breskin, Nucl. Instr. and Meth. 196 (1982) 11.

[Bre83] A. Breskin R. Chechik, I. Levin and N. Zwang, Nucl. Instr. and Meth. **217** (1983) 107.

[Bre84] A.Breskin, R. Chechik, Z. Fraenkel, P. Jacobs, I. Tserruya and N. Zwang, Nucl. Instr. and Meth. **A221** (1984) 363.

[Bro59] S.C. Brown, *Basic Data of Plasma Physics*, (MIT Press., Cambridge, Mass., 1959).

[Bro76] R.A. Broglia, C.H. Dasso and A. Winther, Phys. Lett. **61B** (1976) 113.

[Bro79] R.A. Broglia, C.H. Dasso, H. Esbensen, G. Pollarolo, A. Vitturi and A. Winther, Phys. Lett. **87B** (1979) 15.

[Bro79a] R.A. Broglia, C.H. Dasso, H. Esbensen, G. Pollarolo, A. Vitturi and A. Winther, Phys. Lett. **89B** (1979) 22.

[Bro83] R.A. Broglia, C.H. Dasso, S. Landowne and A. Winther, Phys. Rev. **C27** (1983) 2433.

[Bro83a] R.A. Broglia, C.H. Dasso, S. Landowne and A. Winther, Phys. Lett. **133B** (1983) 34.

[Bru74] W. Bruckner, D. Husar, D. Pelte, K. Traxel, M. Samuel and V. Smilansky, Nucl. Phys. **A231** (1974) 159.

[Bun49] O. Bunemann, T.E. Cranshaw and J.A. Harvey, Can. J. Res **A27** (1949) 191.

[Cha68] G. Charpak, R. Bouclier, T. Bressani, J. Favier and C. Zupancic, Nucl. Instr. and Meth. **62** (1968) 262.

[Cha84] R.J. Charity, Ph.D Thesis, Australian National University 1984 (unpublished).

[Cha86] R.J. Charity, J.R. Leigh, J.J.M. Bokhorst, A. Chatterjee, G.S. Foote, D.J. Hinde, J.O. Newton, S. Ogaza and D. Ward, Nucl. Phys. **A457** (1986) 441.

[Cha88] A. Charlop, A. Garcia, S. Gil, S.J. Luke and R. Vandenbosch, in Proceedings of a Symposium on *Heavy Ion Reactions around the Coulomb Barrier* (Legnaro, Italy, 1988), Lecture Notes in Physics, **317** edited by C. Signorini et al. (Springer-Verlag, Berlin, Heidelberg, New York, London Paris and Tokyo, 1988) p. 157.

[Chr76] P.R. Christensen and A. Winther, Phys. Lett. **65B** (1976) 19.

[Coc68] A. Coche and P. Siffert, *Semiconductor Detectors*, edited by G. Bertolini and A. Coche, (North-Holland Publishing Company - Amsterdam, 1968) p.132.

[Cor83] T.M. Cormier, P.M. Cormier, M. Herman, N.G. Nicolis and P.M. Stwertka, Phys. Rev. Lett. **51** (1983) 542.

[Cor90] L. Corradi, S.J. Skorka, U. Lenz, K.E.G. Löbner, P.R. Pascholai, U. Quade, K. Rudolph, W. Schomburg, M. Steinmary, H.G. Thies, G. Montagnoli, D.R. Napoli, A.M. Stefanini, A. Tivelli, S. Beghini, F. Scarlassara, C. Signorini and F. Soramel, Z. Phys. **A** (1990) 55.

[Das83] C.H. Dasso, S. Landowne and A. Winther, Nucl. Phys. **A405** (1983) 381.

[Das83a] C.H. Dasso, S. Landowne and A. Winther, Nucl. Phys. **A407** (1983) 221.

[Das86] C.H. Dasso, H. Esbensen and S. Landowne, Phys. Rev. Lett. **57** (1986) 1498.

[Das91] M. Dasgupta, A. Navin, Y.K. Agarwal, C.V.K. Bada, H.C. Jain, M.L. Jhingan and A. Roy, Phys. Rev. Lett. **66** (1991) 1414.

[DiG86] D.E. Digregorio, J.O. Fernandez Niello, A.J. Pacheco, D. Abriola, S. Gil, A.O. Macchiavelli, J.E. Testoni, P.R. Pascholati, V.R. Vanin, R.L iguori Neto, N. Carlin Filho, M.M. Coimbra, P.R. Silveira Gomes and R.G. Stokstad, Phys. Lett. **176B** (1986) 322.

[DiG89] D.E. Digregorio, M. diTada, D. Abriola, M. Elgue, A. Etchegoyen, M.C. Etchegoyen, J.O. Fernandez Niello, A.M.J. Ferrero, S. Gil, A.O. Macchiavelli, A.J. Pacheco, J.E. Testoni, P.R. Silveira Gomes, V.R. Vanin, R. Liguori Neto, E. Crema and R.G. Stokstad, Phys. Rev. **C39** (1989) 516.

[DiG90] D.E. DiGregorio, K.T. Lesko, B.A. Harmon, E.B. Norman, J. Pouliot, B. Sur, Y. Chen and R.G. Stokstad, Phys. Rev. **C42** (1990) 2108.

[Dol88] P. Doll, F.P. Brady, T.D. Ford, R. Garrett, H. Krupp and H.O. Klages, Nucl. Instr. and Meth. **A270** (1988) 437.

[Eis77] Y. Eisen, I. Tserruya, Y. Eyal, Z. Fraenkel and M. Hillman, Nucl. Phys. **A291** (1977) 459.

[Eng74] J.B.A. England, *Techniques in Nuclear Structure Physics*, Vol. 1 (Macmillan Press, London and Basingstoke, 1974).

[Eng77] H. Enge and D. Horn, Nucl. Instr. and Meth. **145** (1977) 271.

[Esb78] H.Esbensen, A. Winther, R.A. Broglia and C.H. Dasso, Phys. Rev. Lett. **41** (1978) 296.

[Esb81] H. Esbensen, Nucl. Phys. **A352** (1981) 147.

[Eve81] D. Evers, K. Rudolf, I. Weidl. P. Konrad, U. Quade, K.E.G. Löbner and S.J. Skorka, in *Proceedings of XIXWinter Meeting on Nuclear Physics,* Bormio, 1981, p. 500.

[Ewa76] H. Ewald, K. Guttner, G. Münzenberg, P. Armbruster, W. Faust, S. Hoffman, K.H. Schmidt, W. Schneider and K. Valli, Nucl. Instr. and Meth. **139** (1976) 233.

[Fer89] J. Fernández-Niello and C.H. Dasso, Phys. Rev. **C39** (1989) 2069.

[Fis77] H. Fischer, D. Kamke, H.J. Kittling, E. Kuhlman, H.Plicht and R. Schormann, Phys. Rev. **C15**, (1977) 921.

[Fre83] W.S. Freeman, H. Ernst, D.F. Geesaman, W. Henning, T.J. Humanic, W. Kühn, G. Rosner, J.P. Schiffer, B.

Zeidman and F.W. Prosser, Phys. Rev. Lett. **50** (1983) 1563.

[Fre83a] W.S. Freeman, H. Ernst, D.F. Geesaman, W. Henning, T.J. Humanic, W. Kühn, J.P. Schiffer, and B. Zeidman, Phys. Rev. **C28** (1983) 919.

[Fro65] N. Froman and P.O. Froman, *JWKB Approximation* (North-Holland Publishing Company - Amsterdam, 1965).

[Ful73] H.W. Fulbright, R.G. Markham and W.A. Lanford, Nucl. Instr. and Meth. **108** (1973) 125.

[Gav80] A. Gavron, Phys. Rev. **C21** (1980) 230.

[Gil85] S.Gil, R. Vandenbosch, A. Lazzarini, D.-K. Lock, and A. Ray, Phys. Rev. **C31** (1985) 1752.

[Gil90] S.Gil, D. Abriola, D.E. Digregorio, M, di Tada, M. Elgue, A. Etchegoyen, M.C. Etchegoyen, J. Fernández Niello, A.M.J. Ferrero, A.O. Macchiavelli, A.J. pacheco, J.E. Testoni, P.Silveira Gomes, V.R. Vanin, A. Charlop, A. García, S. Kailas, S.J. Luke, E.Renshaw and R.Vandenbosch, Phys. Rev. Lett. **65** (1990) 3100.

[Gil91] S. Gil, R. Vandenbosch, A. Charlop, A. Garcla, D.D. Leach, S.J. Luke and S.Kailas, Phys. Rev. **C43** (1991) 701.

[Gro70] R. Grove, I. Ko, B. Koskovar and V. Perez-Mendez, Nucl. Instr. and Meth. **99** (1970) 381.

[Dut73] H.H. Dutbrod, W.G. Winn and M. Blann, Nucl. Phys. **A213** (1973) 267.

[Har79] B.Harmatz, Nuclear Data Sheets **26** (1979) 281.

[Har81] L.H. Harwood and J.A. Nolen Jr, Nucl. Instr. and Meth. **186** (1981) 435.

[Hem75] G. Hemple, F. Hopkins and G. Schatz, Nucl. Instr. and Meth. **131** (1975) 445.

[Hen68] D.L. Hendrie, N.K. Glendenning, B.G. Harvey, O.N. Jarvis, H.H. Duhm, J. Saudinos and J. Mahoney, Phys. Lett. **26B**, (1968) 127.

[Hen73] D.L Hendrie, Phys. Rev. Lett. **31** (1973) 478.

[Hil53] D.L. Hill and J.A. Wheeler, Phys. Rev. **89** (1953) 1102.

[Hin82] D.J. Hinde, Ph.D Thesis, Australian National University 1982 (unpublished)

[Hui61] J. Huizenga and G. Igo, Nucl. Phys. **29** (1961) 462.

[Jac86] P. Jacobs, Z. Fraenkel, G. Mamane and I. Tserruya, Phys. Lett. **B175** (1986) 271.

[Jah82] U. Jahnke, H.H. Rossner, D. Hilscher and E. Holub, Phys. Rev. lett. **48** (1982) 17.

[Jam88] A.N. James, T.P. Morrison, K.L. Ying, K.A. Connell, H.G. Price and J. Simpson, Nucl. Instr. and Meth. **A267** (1988) 144.

[Kem35] E.C. Kemble, Phys. Rev. **C17** (1935) 111.

[Kon87] Y. Kondõ, B.A. Robson, J.J.M. Bokhorst. D.J. Hinde, J.R. Leigh, Phys. Rev. **C35** (1987) 828.

[Lan84] S. Landowne and S.C. Pieper, Phys. Rev. **C29** (1984) 1352.

[Lan85] S. Landowne, in *Fusion Reactions Below the Coulomb Barrier*, Lecture Notes in Physics **219**, edited by S.G. Steadman (Springer-Verlag, Berlin, Herdelberg, New York and Tokyo 1985), p. 182.

[Lee74] I.Y. Lee, J.X. Saladin, C. Baktash, J.E. Holden and J. O'Brien, Phys. Rev. Lett. **33**, (1974) 383.

[Lee75] I.Y.Lee, J.X. Saladin, J. Holden, J. O'Brien, C. Baktash, C. Bemis, Jr., P.H. Stelson, F.K. McGowan, W.T. Milner, J.L.C. Ford, Jr., R.L. Robinson and W. Tuttle, Phys. Rev. **C12**, (1975) 1483.

[Lei81] J.R. Leigh, D.J. Hinde and W. Galster, Nucl. Instr. and Meth. **186** (1981) 541.

[Lei86] J.R. Leigh, et al, Proceedings of XIII Winter School, Zakopane, Poland April (1986).

[Lei88] J.R. Leigh, J.J.M. Bokhorst, D.J. Hinde and J.O. Newton, J. Phys. **G14** (1988) L55.

[Lei93] J.R. Leigh, N. Rowley, R.C. Lemmon, D.J. Hinde, J.O. Newton, J.X. Wei, J. Mein, C. Morton, S. Kuyucak and A. Kruppa, Phys. Rev. **C47** (1993) R437.

[Lei93a] J.R. Leigh, M. Dasguta, C.R. Morton, D.J. Hinde, R.C. Lemmon, J.O. Newton, J.X. Wei and N. Rowley, Invited talk to RIKEN International Workshop, 18-22 February, 1993, Tokyo, Japan. Proceedings *RIKEN International*

Workshop On Heavy-Ion Reaction with Neutron-Rich Beams, to be published by World Scientific Press.

[Lem93] R.C. Lemmon, J.R. Leigh, J.X.Wei, C.R. Morton, D.J. Hinde, J.O. Newton. J.C. Mein, M. Dasgupta and N. Rowley, *Strong Dependence of Sub-barrier Fusion On The Nuclear Hexadecapole Deformation*, submitted to Phys. Lett. **B** (1993).

[Lin84] R. Lindsay and N. Rowley, J. Phys. **G10** (1984) 805.

[Löb83] K.E.G. Löbner, D. Evers, R. Pengo, U. Quade, K. Rudolf, S.J. Skorka and I. Weidl, in Proceedings of XXI Winter Meeting on Nuclear Physics, Bormio, (1983) p. 292.

[Lyo86] L. Lyons, *Statistics for Nuclear and Particle Physicists*, (Cambridge University Press, London New York New Rochelle Melbourne and Sydney, 1986).

[Mar78] B. Martin, H. Stelzer, in *Experimental mathods in Heavy Ion Physics*, Lecture Notes in Physics **83**, edited by K. Bethge (Springer-Verlag, Berlin, Herdelberg and New York, 1978), p. 150.

[Maz83] C. Mazur and M. Ribrag, Nucl. Instr. and Meth. **212** (1983) 203.

[Mos84] U. Mosel, in *Treatise on Heavy-Ion Science*, Vol. 2, Fusion and Quasi-Fusion Phenomena, edited D.A. Bromley (Plenum Press, New York, 1984) p. 3.

[Mur86] T. Murakami, C-C. Sahm, R. Vandenbosch, D.D. Leach, A. Ray and M.J. Murphy, Phys. Rev. **C34** (1986) 1353.

[Nag86] M.A. Nagarajan, A.B. Balantekin, N. Takigawa, Phys. Rev. **C34** (1986) 894.

[New88] J.O. Newton, D.J. Hinde, R.J. Charity, J.R. Leigh, J.J.M. Bokhorst, A. Chatterjee, G.S. Foote, and S. Ogaza, Nucl. Phys. **A483** (1988) 126.

[Nor70] L.C. Northcliffe and R.F. Schilling, Nuclear Data Table, **A7** (1970) 256.

[Pen83] R. Pengo, D. Evers, K.E.G. Löbner, U. Quade, K. Rudolph, S.J. Skorka and I Weidl, Nulc. Phys. **A411** (1983) 255.

[Pof83] N. Poffe, N. Rowley and R. Lindsay, Nucl. Phys. **A410** (1983) 498.

[Ram86] S. Raman, C.H. Malarkey, W.T. Milner, C.W. Nestor, Jr. and P.H. Stelson, At. Data Nucl. Data Tables **36** (1986) 1.

[Ras71] J. Rasmussen and K. Sugawara-Tanabe, Nucl. Phys. **A171** (1971) 711.

[Rei82] W. Reisdorf, F.P. Hessberger, K.D. Hildenbrabd, S. Hofmann, G. Münzenberg, K.-H. Schmidt, J.H.R. Schneider, W.F.W. Schneider, K. Sümmerer and G. Wirth, Phys. Rev. Lett. **49** (1982) 1811.

[Rei85] W. Reisdorf, F.P. Hessberger, K.D. Hildenbrabd, S. Hofmann, G. Münzenberg, K.-H. Schmidt, J.H.R. Schneider, W.F.W. Schneider, K. Sümmerer and G. Wirth, Nucl. Phys. **A438** (1985) 212.

[Rho83] M.J. Rhoades-Brown and V.E. Oberacker, Phys. Rev. Lett. **50** (1983) 1435.

[Row89] N. Rowley, A. Kabir and R. Lindsay, J. Phys. **G15** (1989) L269.

[Row91] N. Rowley, in: *Proceedings Workshop on Heavy Ion Collisions At Energies Near the Coulomb Barrier*, Daresbury, 1990, (Institue of Physics, Bristol, Philadelphia and New York, 1991) p. 177.

[Row91a] N. Rowley, G.R. Satchler and P.H. Stelson, Phys. Lett. **254B** (1991) 25.

[Row93] N. Rowley, J.R. Leigh, J.X, Wei and R. Lindsay, *Obtain Average Angular Momenta From Excitation Functions Near The Coulomb Barrier*, submitted to Phys. Lett. **B** (1993).

[Sal77] M.Salomaa and H.A. Enge, Nucl. Instr. and Meth. **145** (1977) 279.

[Sat79] G.R. Satchler and W.G. Love, Phys. Rep. **55** (1979) 183.

[Sch88] R. Schicker, N. Alamanos, P. Braun-Munzinger, T. Stachel and L. Waters, Nucl. Instr. and Meth. **A269** (1988) 585.

[Sco76] W. Scobel, H.H. Gutbord, M. Blann and A. Mignerey, Phys. Rev. **C14** (1976) 1808.

[Sha74] A.H. Shaw and J.S. Greenberg Phys. Rve. **C10** (1974) 263.

[Shi86] K. Shima, T. Mikumo and H. Tawara, Atomic Data and Nuvl. Data Tables **34** (1986) 358.

[Sig74] P. Sigmund and K.B Winterbon, Nucl. Instr. and Meth. **119** (1974) 541.

[Sik64] T. Sikkeland, Phys. Rev. **135** (1964) B669.

[Spe77] R.H. Spear, D.C. Kean, M.T. Esat, A.N.R. Joye and M.P. Fewell, Nucl. Instr. and Meth. **147** (1977) 455.

[Ste71] F.S. Stephens, R.M. Diamond and J. de Boer, Phys. Rev. Lett **27** (1971) 1151.

[Ste76] H. Stelzer, Nucl. Instr. and Meth. **133** (1976) 409.

[Ste83] H. Stelzer, in Proceedings of the symposium on Commemorating the 100 Anniversary of Hans Geiger's Birth, (Berlin 1982), *Detectors in Heavy-Ion Reactions*, Lecture Notes in Physics **178**, edited by W. von Oertzen (Springer-Verlag, Berlin, Heidelberg, New York and Tokyo, 1983) p. 25.

[Ste84] A.M. Stefanini, G. Fortuna, A. Tivelli, W. Meczynski, S. Beghini, C. Signorini, S. Lunardi and M. Morando, Phys. Rev. **C30** (1984) 2088.

[Ste86] S.G. Steadman and M.J. Rhoades-Brown, Annu. Rev. Nucl. Part. Sci **36** (1986) 649.

[Ste88] P.H. Stelson, Phys. Lett. **B205** (1988) 190.

[Ste89] P.H. Stelson, in *Heavy-ion Reaction Dynamics in the Tandem Energy Region*, eds. Y. Sugiyama, A. Iwamoto and I. Ikezoe, (University Academic Press, Tokyo, 1989) p.49.

[Ste90] P.H. Stelson, H.J. Kim, M. Beckerman, D. Shapira and R.L. Robinson, Phys. Rev. **C41**, (1990) 1584.

[Ste91] P.H. Stelson, in: *Proceedings Workshop on Heavy Ion Collisions At Energies Near the Coulomb Barrier*, Daresbury, 1990, (Institue of Physics, Bristol, Philadelphia and New York, 1991) p. 191.

[Ste92] A.M. Stefanini, Nucl. Phys. **A538** (1992) 195c.

[Sto78] R.G. Stokstad, Y. Eisen, S. Kaplanis, D. Pelte, U. Smilansky and I. Tserruya, Phys. Rev. Lett. **41** (1978) 465.

[Sto80] R.G. Stokstad, Y. Eisen, S. Kaplanis, D. Pelte, U. Smilansky and I. Tserruya, Phys. Rev. **C21** (1980) 2427.

[Sto80a] R.G. Stokstad, W. Reisdorf, K.D. Hildenbrand, J.V Kratz. G. Wirth, R. Lucas and J. Poitou, Z. Phys. **295** (1980) 269.

[Sto81] R.G. Stokstad, E.E. Gross, Phys. Rev. **C23** (1981) 281.

[Tho59] T.D. Thomas, Phys. Rev. **116** (1959) 703.

[Tri89] R.E. Tribble, R.H. Burch and C.A. Gagliardi, Nucl. Instr. and Meth. **A285** (1989) 441.

[Uda85] T. Udagawa, B.T. Kim and T. Tamura, Phys. Rev. **C32** (1985) 124.

[Van73] R. Vandenbosch and J.R. Huizenga, *Nuclear Fission*, (Academic Press, New York and London, 1973).

[Van83] R. Vandenbosch, B.B. Back, S. Gil, A. Lazzarini and A.Ray, Phys. Rev **C28** (1983) 1161.

[Van86] R. Vandenbosch, T. Murakami, C-C. Sahm, D.D. Leach, A. Ray and M.J. Murphy, Phys. Rev. Lett. **56** (1986) 1234.

[Van91] R. Vandenbosch, in: *Proceedings Workshop on Heavy Ion Collisions At Energies Near the Coulomb Barrier*, Daresbury, 1990, (Institue of Physics, Bristol, Philadelphia and New York, 1991) p. 269.

[Van92] R. Vandenbosch, Annu. Rev. Nucl. Part. Sci. **42** (1992) 447.

[Vaz74] L.C. Vaz, J.M. Alexander, Phys. Rev. **C10** (1974) 464.

[Vaz78] L.C. Vaz, J.M. Alexander, Phys. Rev. **C18** (1978) 2152.

[Vaz81] L.C. Vaz, J.M. Alexander and G.R. Satchler, Phys. Reports **69** (1981) 373.

[Wah64] L. Wahlin, Nucl. Instr. and Meth. **27** (1964) 55.

[Wei37] V. Weisskopf, Phys. Rev. **52** (1937) 295.

[Wei91] J.X. Wei, J.R. Leigh, D.C. Weisser, J.O. Newton, S. Elfstrom, J.P. Lestone, J.X. Chen, D.G. Popescu and D.J. Hinde Nucl. Instr. & Meth. in Phys. Res. **A306** (1991) 557.

[Wei91a] J.X. Wei, J.R. Leigh, D.J. Hinde, J.O. Newton, R.C. Lemmon, S. Elfstrom, J.X. Chen and N. Rowley, Phys. Rev. Lett. **67** (1991) 3368.

[Wie1898] W. Wien, Ann. Physik. **65** (1898) 440.

[Wie02] W. Wien, Ann. Physik. **8** (1902) 260.

[Wil80] J. Wilczynski, K. Siwek-Wilczynska, J. Van Driel, S. Gonggrijp, D.C.J.M. Hageman, R.V.F. Janssens, J. Lukasiak and R.H. Siemssen, Phys. Rev. Lett. **45** (1980) 606.

[Won73] C.Y. Wong, Phys. Rev. Lett. **31** (1973) 766.

[Wuo91] A.H. Wuosmaa, R.R. Betts, B.B. Back, M.P. Carpenter, H. Esbensen, P.B. Fernandez, B.G. Glagola, Th. Happ, R.V.F. Janssens, T.L. Khoo, E.F. Moore, F. Scarlassara, Phys. Lett. **B263** (1991) 23.

[Zai84] V.P. Zaikov, E.A. Kral'kina, N.F. Vorobjev, I.S. Dmitriev, V.S. Nikolaev and Ya.A. Teplova, Nucl. Instr. and Meth. **B5** (1984) 10.